38th conference with international participation

COMPUTATIONAL MECHANICS 2023

PROCEEDINGS OF
COMPUTATIONAL MECHANICS 2023

October 23 - 25, 2023

HOTEL SRNÍ
CZECH REPUBLIC

FACULTY
OF APPLIED SCIENCES
UNIVERSITY
OF WEST BOHEMIA

PILSEN REGION

ŠM

IFToMM

cea cm   Central European Association
for Computational Mechanics

Sponsor of the conference

DOOSAN Škoda Power

PREFACE

The proceedings contain 66 conference papers presented at the 38th conference **Computational Mechanics 2023**, which was held at the Hotel Srní in Srní, Czech Republic, on October 23 – 25, 2023. This annual conference, which was attended by more than eighty participants from the Czech Republic, Slovakia and from abroad, was organised by the Department of Mechanics, Faculty of Applied Sciences of the University of West Bohemia under the auspices of

- Miloš Železný, the Dean of the Faculty of Applied Sciences,
- Rudolf Špoták, the President of the Pilsen Region,
- Czech Society for Mechanics,
- Czech National Committee of IFToMM,
- Central European Association for Computational Mechanics.

The main objective of this traditional conference is to bring together academicians, researchers and industrial partners interested in relevant disciplines of mechanics including

- solid mechanics,
- dynamics of mechanical systems,
- mechatronics and vibrations,
- reliability and durability of structures,
- fracture mechanics,
- mechanics in civil engineering,
- fluid mechanics and fluid-structure interaction,
- thermodynamics,
- biomechanics,
- heterogeneous media and multiscale problems,
- experimental methods in mechanics,

to create an opportunity for meeting, discussion and collaboration among the participants. As in the previous years, the three best papers presented at this conference were awarded the Czech Society for Mechanics Award for young researchers under 35 years of age.

To all conference participants, we offer the possibility to publish their peer-reviewed full papers in the international journal **Applied and Computational Mechanics** indexed by Scopus. This journal has been published by the University of West Bohemia since 2007 (see https://www.kme.zcu.cz/acm/).

We would like to express our gratitude to all the invited speakers for their significant contribution to the conference and the time and effort they put. Considerable acknowledgement belongs also to the members of the Organising Committee for their important work.

We strongly believe that all participants of the CM2023 enjoyed their stay in the beautiful nature of the Šumava region in a meaningful way. Finally, we would like to invite you all to come to the next conference CM2024.

<table>
<tr><td align="center">**Jan Vimmr**
University of West Bohemia
Chairman of the Scientific
Committee</td><td align="center">**Vítězslav Adámek**
University of West Bohemia
Chairman of the Organising
Committee</td></tr>
</table>

SCIENTIFIC COMMITTEE

Chairman:
Jan Vimmr
University of West Bohemia, Faculty of Applied Sciences, Czech Republic

Members:
Miroslav Balda
Research and Testing Institute Plzeň, Czech Republic

Jiří Burša
Brno University of Technology, Faculty of Mechanical Engineering, Czech Republic

Jan Dupal
University of West Bohemia, Faculty of Applied Sciences, Czech Republic

Václav Dvořák
Technical University of Liberec, Faculty of Mechanical Engineering, Czech Republic

Jiří Fürst
Czech Technical University in Prague, Faculty of Mechanical Engineering, Czech Republic

Miroslav Holeček
University of West Bohemia, New Technologies Research Centre, Czech Republic

Jaromír Horáček
Institute of Thermomechanics, Czech Academy of Sciences, Czech Republic

Michal Kotoul
Brno University of Technology, Faculty of Mechanical Engineering, Czech Republic

Jiří Křen
University of West Bohemia, Faculty of Applied Sciences, Czech Republic

Vladislav Laš
University of West Bohemia, Faculty of Applied Sciences, Czech Republic

Justín Murín
Slovak University of Technology in Bratislava, Faculty of Mechanical Engineering, Slovak Republic

Milan Naď
Slovak University of Technology in Bratislava, Faculty of Materials Science and Technology in Trnava, Slovak Republic

Jiří Náprstek
Institute of Theoretical and Applied Mechanics, Czech Academy of Sciences, Czech Republic

Miloslav Okrouhlík
Institute of Thermomechanics, Czech Academy of Sciences, Czech Republic

Luděk Pešek
Institute of Thermomechanics, Czech Academy of Sciences, Czech Republic

Jindřich Petruška
Brno University of Technology, Faculty of Mechanical Engineering, Czech Republic

Jiří Plešek
Institute of Thermomechanics, Czech Academy of Sciences, Czech Republic

František Pochylý
Brno University of Technology, Faculty of Mechanical Engineering, Czech Republic

Pavel Polach
Research and Testing Institute Plzeň, Czech Republic

Eduard Rohan
 University of West Bohemia, Faculty of Applied Sciences, Czech Republic

Josef Rosenberg
 University of West Bohemia, Faculty of Applied Sciences, Czech Republic

Milan Růžička
 Czech Technical University in Prague, Faculty of Mechanical Engineering, Czech Republic

Milan Sága
 University of Žilina, Faculty of Mechanical Engineering, Slovak Republic

Petr Sváček
 Czech Technical University in Prague, Faculty of Mechanical Engineering, Czech Republic

Zbyněk Šika
 Czech Technical University in Prague, Faculty of Mechanical Engineering, Czech Republic

Michael Valášek
 Czech Technical University in Prague, Faculty of Mechanical Engineering, Czech Republic

Jaroslav Zapoměl
 VŠB – Technical University of Ostrava, Faculty of Mechanical Engineering, Czech Republic

Vladimír Zeman
 University of West Bohemia, Faculty of Applied Sciences, Czech Republic

Table of Contents

Damage detection study for a pedestrian cable-stayed bridge using ANSYS

J. Bayer[a], M. Kawulok[a,b], S. Urushadze[a]

[a]*Institute of Theoretical and Applied Mechanics of the Czech Academy of Sciences, Prosecká 809/76, 190 00 Prague 9, Czech Republic*
[b]*Department of Structural Mechanics, Faculty of Civil Engineering, VSB–Technical University of Ostrava, Ludvíka Podéště 1875/17, 708 00 Ostrava–Poruba, Czech Republic*

1. Introduction

Cable stayed bridges are elegant, statically indeterminate non-linear structures with a rather complex structural behaviour which makes them sensitive to vibrations [2, 5]. They have, as a rule, individual traits, and therefore their analysis is always a challenge [2, 3, 5]. Because of rather complex loads and the high utilization of material properties, there is also a rich variety of failure scenarios and possible problems [2-4]. This applies also to management and maintenance plans of these bridges [3]. In connection to development of new testing techniques for bridges at ITAM [1], a theoretical damage detection case study was launched for a cable stayed bridge over the Vltava River at Lužec. The aim of this damage detection case study is to suggest regular vibration measurement and tests that could ease or supplement the prescribed maintenance inspections of this bridge in future. Ambient vibration measurements, forced vibration test and a moving impulse load test are under consideration so far.
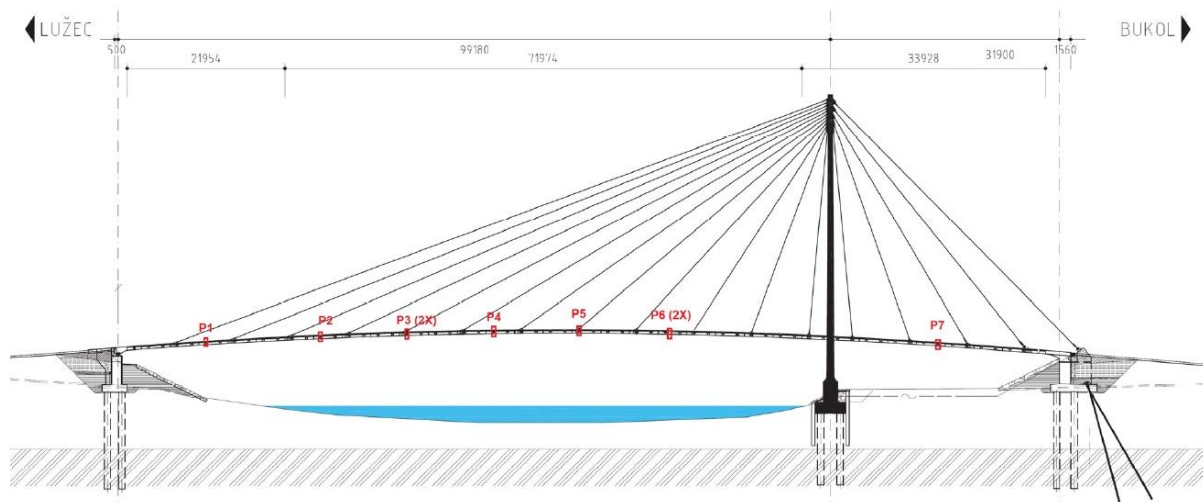
Fig. 1. Schema of the bridge structure

2. Bridge structure and analysis

The bridge (see Fig.1), with its pre-stressed reinforced concrete deck, its 100 m span, and its first natural frequency of about 0.7 Hz, is among the shorter cable-stayed bridges. An analytical model of the structure was assembled using ANSYS Workbench 2021/R2 based on project data supplied by the design office. The main components of the bridge and applied elements are shown in Table 1. The cross section of the bridge deck was assumed to be piecewise with a

constant thickness. All finite elements (FE) strictly follow the centre of gravity lines of the structure, which is achieved by eccentric "JOINT" connections. The non-linear static solution is very important because the dynamic analysis is dependent on it as on a starting point. As the final stress in the prestressing cables depends on the deformation, an iterative process had to be applied to achieve the design values. Then, the Prestressed Modal Analysis followed, providing 99 natural mode shapes.

Table 1. Main components and applied FE of the bridge

Component	FE	Material
bridge deck	Shell281	C110/130
prestressing cables of the deck	Beam189	Y1860S7
pylon	Shell281 and Beam189	C30/37 and S355
cables	Cable280	Full locked coil rope (FCL)
prestressing bars	Beam189	Y1860S7
abutment	Shell281	C50/60

3. Damage detection simulations

Global characteristics like natural frequencies and modes alone are usually not sufficient to provide damage-sensitive features applicable to monitoring [2], but there are also some more optimistic examples [2, 6] using damage indices. The bridge deck offers easily accessible measurement points for vibrations, but it is necessary to consider the limitations of an incomplete dynamic model. The first step of the damage detection case study is therefore simulation of various damage scenarios and estimation of measurable effects in the framework of applied dynamic loads and measured outputs.

4. Conclusions

The first part of the damage detection case study confirmed that partial loss of prestress of the deck and loosing of selected cables should have a measurable effect on bridge deck vibrations.

References

[1] Bayer, J., Urushadze, S., Introduction into bridge testing using a cogwheel load, Proc. of the 4th International Conference HeaMES, 2023.

[2] Caetano, E., Characterisation and assessment of damage in cable structures, Journal of Civil Structural Health Monitoring 12 (2022) 1267–1283.

[3] Pedro, J. J. O., Reis, A. J., Nonlinear analysis of composite steelconcrete cable-stayed bridges, Engineering Structures 32 (2010) 2702-2716.

[4] Polák M., Míčka T., Klier T., Plachý T., Šimler M., Experimental analysis of excessive vibrations of selected suspension bridge hinges, Proc. Of the 13th Int. Conf. on New Trends in Statics and Dynamics of Buildings, Bratislava, 2015.

[5] Virlogeux, M., State-of-the-art in cable vibrations of cable-stayed bridges, Bridge Structures: Assessment, Design and Construction 1 (3) (2005) 133-168.

[6] Wickramasinghe, W. R., Thambiratnam, D. P., Chan, T. H. T., Nguyen, T., Vibration characteristics and damage detection in a suspension bridge, Journal of Sound and Vibration 375 (2016) 254-274.

Optimization of non-collocated active spatial vibration absorbers

P. Beneš[a], J. Gregor[a], T. Vyhlídal[a], Z. Šika[a]

[a]*Faculty of Mechanical Engineering, CTU in Prague, Technická 4,160 00 Praha 6, Czech Republic*

Mechanical vibration is one of the common problems in many engineering applications. Passive and active absorbers are proven tools for their suppression. The disadvantage of simple passive absorbers is that they are limited to a narrow frequency band close to the natural frequency of the absorber. Moreover, due to the inherent damping and frictional forces in their elastic components, vibration suppression cannot be ideal. Improved results can be achieved if the mechanical properties of the absorber can be tuned ans significantly better performance can be achieved if the absorber is actively controlled. A typical example of an active vibration absorber is the delayed resonator (DR) concept proposed in the 1990s by N. Olgac and his co-workers [1]. It is based on the use of time-delayed feedback, which can be taken from position, velocity, acceleration, or a combination of these. Proper adjustment of the delayed feedback compensates for damping and changes in the stiffness of the mechanical part. Such an absorber has the properties of an ideal one.

The active vibration absorber is usually designed for a collocated absorption, where the location of the absorber is identical to the point whose vibration is to be suppressed. In the non-collocated case, the two locations differ from each other and finding the optimal absorber parameters is a more challenging task. The use of the DR concept for simple unidirectional non-collocated absorption is described in [2].

In most applications, absorbers are designed as single degree-of-freedom (DOF) systems absorbing vibration in one given direction, which is the most problematic in terms of vibration of the primary structure. Multiple such absorbers can be used simultaneously in different directions to suppress the spatial vibration of the flexible primary structure, Fig. 1. An interesting concept is to replace such a system of many single DOF absorbers by a single absorber with many DOFs [3], [4].
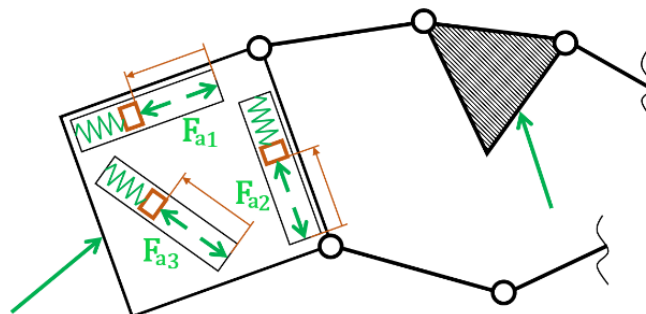
Fig. 1. Scheme of the set of single DOF absorbers attached to the primary mass

An important parameter of the absorber to optimise is its mass. It affects the amplitude of its oscillation and also the time required to reach steady state, i.e. to suppress the vibrations of the primary mass. As the mass of the absorber increases, its performance improves, but its energy requirements also increase. In the spatial case when using multiple single DOF

absorbers, a separate mass for each direction is required. This clearly shows the advantage of using a single multi DOF absorber with only one mass.

In collocated absorption, the position of the absorber is determined, but in the non-collocated case, the coordinates of the absorber location on the primary mass are important optimization parameters that must be determined considering the excitation force, the position of the reference point and the mode to be suppressed.
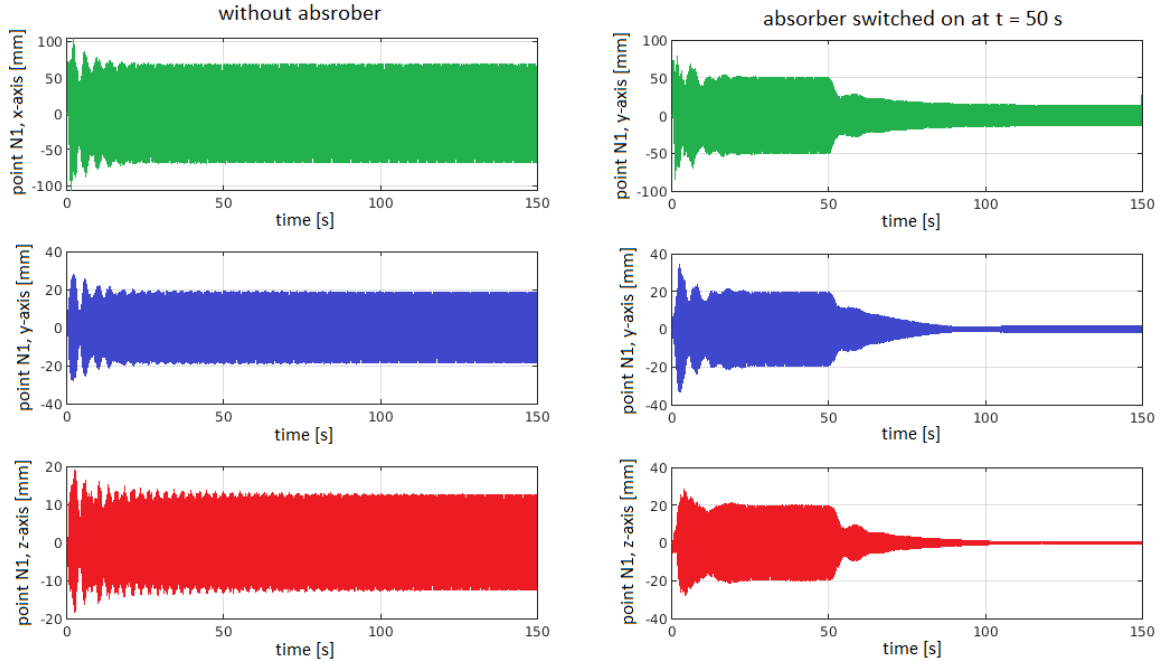
Fig. 2. Time response of the reference point to excitation by spatial periodic force without absorber (left) and with non-collocated absorber (right)

Fig. 2 shows the time response in the x, y, z directions of the reference point on a flexible frame when excited by a periodic force. In the left part of the figure is the waveform without absorber, in the right part with a non-collocated active multi DOF absorber switched on at time $t = 50$ s. It is seen that the use of the non-collocated absorber provides a significant reduction of vibration at the reference point.

Acknowledgement

References

[1] Olgac, N., Holm-Hansen, B., A novel active vibration absorption technique: Delayed resonator, Journal of Sound and Vibration 176 (1994) 93-104.
[2] Olgac, N., Jenkins, R., Time-delayed tuning of vibration absorbers for non-collocated suppression, American Control Conference (ACC), 2020, pp. 1381-1386.
[3] Šika, Z., Vyhlídal, T., Neusser, Z., Two-dimensional delayed resonator for entire vibration absorption, Journal of Sound and Vibration 500 (2021) 116010.
[4] Vyhlídal, T., Michiels, W., Neusser, Z., Bušek, J., Šika, Z., Analysis and optimized design of an actively controlled two-dimensional delayed resonator, Mechanical Systems and Signal Processing 178 (2022) 109195.

Examining vortex-induced vibration through convolutional neural networks

O. Bublík[a], V. Heidler[a], A. Pecka[a], J. Vimmr[a]

[a]*Department of Mechanics, Faculty of Applied Sciences, University of West Bohemia, Univerzitní 8, 301 00 Plzeň, Czech Republic*

1. Introduction

Phenomena like flutter, vortex-induced vibration, or buffeting can manifest during fluid-structure interaction (FSI), potentially leading to structural failure. As a result, FSI problems have garnered significant attention in fields such as the nuclear industry, aeronautics, and turbomachinery. The computational demands of simulating practical FSI problems are substantial, with fluid flow simulations often constituting the most resource-intensive aspect. To significantly alleviate these computational demands, we propose using a neural network to predict fluid flow, replacing traditional computational fluid dynamics (CFD) solvers. Convolutional Neural Networks (CNNs) were initially developed for image pattern recognition [3]. Guo et al. [4] were pioneers in employing CNNs to predict steady fluid flow, demonstrating that their CNN could predict velocity fields four orders of magnitude faster than a CPU-based solver and two orders of magnitude faster than a GPU-accelerated lattice Boltzmann CFD solver while maintaining error levels below 3%. Building upon this, Hennigh [5] extended the concept to predict unsteady fluid flows. In these groundbreaking studies, CNNs were trained to predict flow fields with varying geometries but consistent flow parameters, such as Reynolds number and angle of attack. Subsequent research by Bhatnagar et al. [1] and Thuerey et al. [7] developed CNN models capable of predicting complete velocity and pressure fields around aerofoils of diverse shapes, considering parameterized Reynolds numbers and angles of attack. This paper aims to apply CNNs to fluid-structure interaction (FSI) problems. It is worth noting that most prior research utilizing neural networks for fluid flow prediction assumed stationary boundaries. However, for FSI applications, CNNs must predict flow fields with moving boundaries. To address this challenge, we have designed and trained a CNN specifically tailored to predict unsteady, incompressible fluid flow with moving boundaries.

2. Neural network architecture and training dataset

In order to forecast the behavior of unsteady, incompressible fluid flow around a mobile object, we employ a specialized convolutional encoder-decoder neural network known as U-Net, as introduced by Ronneberger et al. [6]. This architecture is visualized in Fig. 1. The neural network takes as input a three-dimensional array with dimensions of $128 \times 32 \times 8$. This array contains eight distinct values for each grid point, which encompass the following information: the x and y coordinates of the grid points at time instances t_n and t_{n+1}, the corresponding boundary indicator, fluid velocity components u and v, as well as the pressure p at time t_n. Including grid point coordinates is essential due to the non-Cartesian nature of the mesh. Since
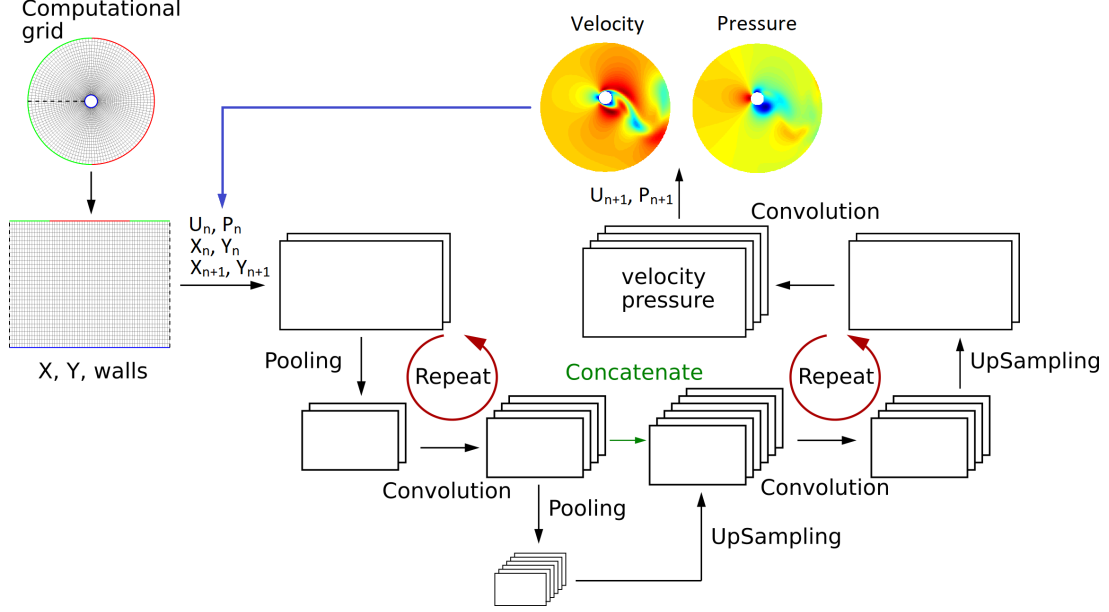
Fig. 1. Illustration of the network architecture

the mesh undergoes deformation, providing grid point positions at two distinct time steps is imperative. The boundary indicator is represented as a binary value equal to 1 if the grid point resides on the boundary of the blade profile and 0 if it is situated within the fluid domain. The network's output comprises pressure and velocity fields computed at the grid points for time t_{n+1}.

3. Structure model and fluid-structure interaction

We examine the interaction between laminar fluid flow and a solitary rigid body, which is elastically attached and can only move horizontally. Additionally, our simulation focuses solely on a 2D cross-sectional representation. The dynamics of this elastically-mounted body are encapsulated by the one-degree-of-freedom (1-DOF) linear mass-spring-damper model

$$\ddot{y} + 2\,\zeta\,\omega_n\,\dot{y} + \omega_n^2\,y = \frac{L}{m}.$$

In this context, where y represents horizontal displacement, we define several vital parameters: ζ as the damping ratio, ω_n as the undamped angular natural frequency (where $\omega_n = 2\pi f_n$ and f_n is the undamped natural frequency), m as the mass, and c and k as the damping and stiffness coefficients, respectively. Additionally, L represents the lift force. The relationship between the damped natural frequency and the undamped natural frequency is expressed as follows:

$$f_d = f_n\sqrt{1 - \zeta^2}.$$

We discretize this equation using the BDF2 method, which is a 3-level implicit method.

To ensure the accurate interaction between the fluid flow and the solid structure, two conditions must be met at the fluid-solid interface: the equilibrium of forces and geometric consistency. Assuming that no external forces are acting on the body apart from aerodynamic forces, the equilibrium of forces can be expressed as follows:

$$L = \oint_\Gamma \left(\sigma_{xx}\,n_x + \sigma_{yx}\,n_y\right)\mathrm{d}S.$$

6

Here Γ is the boundary of the body, n is the unit outer normal to the boundary and σ is the aerodynamic stress tensor.

4. Numerical results

After conducting training sessions for a Convolutional Neural Network (CNN) using data from fluid flow around a cylinder subjected to prescribed harmonic motion with varying amplitudes and frequencies, we integrated the CNN with a structural solver. This integrated system was then employed for Fluid-Structure Interaction (FSI) simulations. The validation of the CNN-based FSI solver involved a thorough comparison of its outcomes with those of a Computational Fluid Dynamics (CFD)-based FSI solver. Notably, the CNN-based and CFD-based FSI solvers shared the exact structural solver and coupling algorithm; the primary difference lay in their respective fluid solvers. In our case, we utilized FlowPro [2] as the fluid solver, which also served as the source for generating the training dataset.

To validate the performance of the CNN-based FSI solver, we conducted multiple simulations with various natural frequencies and damping ratios for the structural component. The fluid parameters remained constant across all simulations. Specifically, we selected a Reynolds number of 100. We opted for damping ratios of 0.375 and 0.45. For each damping ratio value, we executed a series of simulations with different natural frequencies for the structure and subsequently visualized the resulting amplitudes and frequencies.

In Fig. 2, we compare amplitude characteristics obtained from the CNN-based and CFD-based FSI solvers for specific damping ratios. In essence, we depict the cylinder's amplitude response for various natural frequencies near the resonance frequency. Notably, we normalize the damped natural frequency f_d by the Strouhal frequency f_{St}, representing the vortex-shedding frequency for a stationary cylinder, and we normalize the amplitude A by the cylinder's diameter D. It is important to emphasize that f_{St} and D remain consistent throughout all simulations.

Fig. 3 illustrates the steady-state oscillation frequency f of the cylinder about the damped natural frequency f_d of the structure. Both axes are normalized by f_{St}. The horizontal black line signifies the Strouhal frequency f_{St}, which, due to normalization, equates to 1. The inclined black line corresponds to the natural frequency of the cylinder f_d, which, also due to normalization, aligns with the function $y = x$. The blue circles represent frequencies obtained from the CFD-based FSI solver, while the red squares represent frequencies obtained from the CNN-based FSI solver. For natural frequencies near the Strouhal frequency, i.e., when $f_d/f_{St} \approx 1$, the vortex-shedding frequency deviates from its typical value and begins to follow the structure's
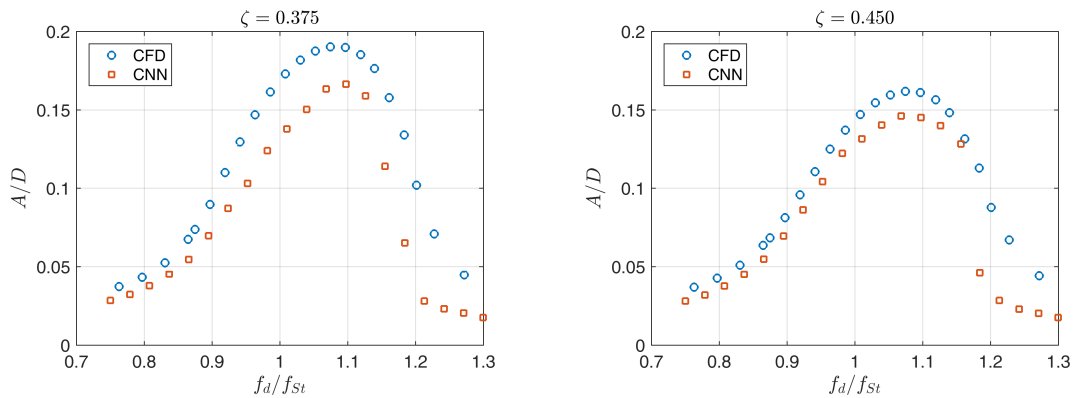
Fig. 2. Cylinder amplitudes A depending on the damped natural frequency f_d for various damping ratios ζ. The blue circles are the CFD-based results while the red squares are the CNN-based results
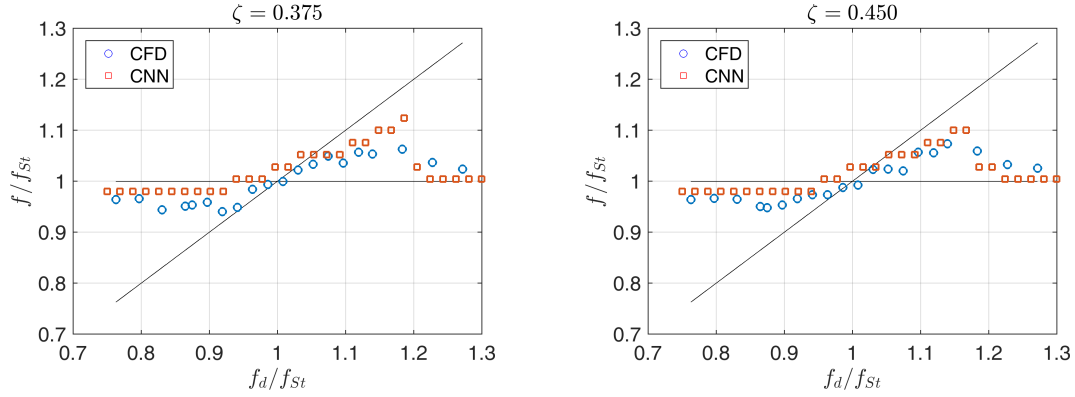
Fig. 3. Steady-state oscillation frequency f depending on the damped natural frequency f_d for various damping ratios ζ. The blue circles are the CFD-based results while the red square are the CNN-based results

natural frequency. This phenomenon indicates that within a specific region around resonance, the frequencies follow the inclined line instead of the horizontal line, commonly called "lock-in".

5. Conclusions

The findings demonstrate that the CNN-based Fluid-Structure Interaction (FSI) solver effectively captures the "lock-in" phenomenon in the vortex-induced vibration of a cylinder. Furthermore, the quantitative results closely align with those obtained from the CFD-based FSI solver. The CNN-based FSI solver also exhibits a remarkable speed advantage, two orders of magnitude faster than its CFD-based counterpart. This speedup is expected to be even more pronounced when applied to larger-scale problems.

Acknowledgment

References

[1] Bhatnagar, S., Afshar, Y., Pan, S., Duraisamy, K., Kaushik, S., Prediction of aerodynamic flow fields using convolutional neural networks, Computational Mechanics 64 (2) (2019) 525-545.

[2] Bublík, O., Pecka, A., Vimmr, J., FlowPro: Multipurpose CFD software written in Java, Proceedings of the 20th conference Computational Mechanics, Srní, University of West Bohemia, 2018.

[3] Fukushima, K., Neocognitron: A self-organizing neural network model for a mechanism of pattern recognition unaffected by shift in position, Biological Cybernetics 36 (4) (1980) 193-202.

[4] Guo, X., Li, W., Iorio, F., Convolutional neural networks for steady flow approximation, Proceedings of the ACM SIGKDD International Conference on Knowledge Discovery and Data Mining, 2016, pp. 481-490.

[5] Hennigh, O., Lat-Net: Compressing lattice Boltzmann flow simulations using deep neural networks, 2017. doi: 10.48550/arXiv.1705.09036

[6] Ronneberger, O., Fischer, P., Brox, T., U-net: Convolutional networks for biomedical image segmentation, 2015. doi: 10.48550/arXiv.1505.04597

[7] Thuerey, N., Weißenow, K., Prantl, L., Hu, X., Deep learning methods for Reynolds-averaged Navier-Stokes simulations of airfoil flows, AIAA Journal 58 (1) (2020) 25-36.

Effect of pre-stress on modification of modal properties of planar structures

P. Bucha[a], L. Rolník[a], M. Naď[a]

[a]Faculty of Materials Science and Technology in Trnava, Slovak University of Technology in Bratislava,
Ul. J. Bottu 25, 917 24 Trnava, Slovak Republic

Planar structures such as discs and plates are structural components widely used in structural and manufacturing applications. In the case of dynamic loading of a given planar structure, it is important that structure has the required modal properties. To obtain suitable modal properties of planar structures, there are several methods, which are usually based on the application of additional structural elements, attached to the basic planar structure. By using such structural modifications of the original planar structure, a redistribution of mass and stiffness properties and also the change of its modal properties is achieved. In order to achieve the required modal properties of planar structures, a method based on the creation of pre-stress in the plane of the structure is presented in this article.

A specific case of planar structures such as a circular disk are saw blades, which are widely used for wood cutting and shaping. In the cutting process, there are occasional large transverse displacements of the circular saw blade, which are caused by resonant states. To improve dynamic stability, i.e. elimination of resonance states by modifying its modal properties, it is possible to use the creation of pre-stressed areas in the plane of the circular saw blade. The influence of the parameters of the pre-stressed areas created in the circular saw blade on the modification of its modal properties is investigated and analyzed in this paper.

One of the methods for the creating of stress in-plane of circular saw blade is rolling a certain area of the blade surface. In the rolling process, the disc is compressed in rolled zone between two opposing rollers. During such rolling, a permanent plastic deformation is created in the rolled part of circular saw blade. As a result of this permanent deformation, the compressed material creates residual stress in the plane of the circular saw blade.

The values of natural frequencies for one and two plastic zones (Fig.1), their various rolling positions and for various rolling depth of the annulus are obtained by modal analysis using finite element method (FEM). The role of residual stresses obtained by rolling is assessed from the change in natural frequencies and modal shapes.
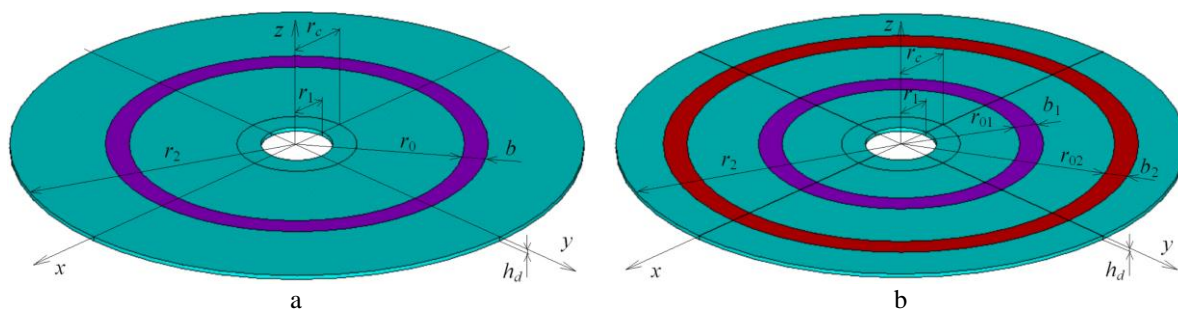
Fig. 1. The circular disc with plastically deformed zones: a - one plastic zone; b - two plastic zones

We consider circular saw blade of outer radius r_2, inner radius r_1 and thickness h_d (Fig.1). The radius r_c specify where the saw blade is clamped by flanges. For case with one plastically deformed zone (Fig.1a) are dimensions of determined by inner radius r_0 and width b and for two plastically deformed zones (Fig.1b), the dimensions of annulus are r_{01}, b_1 and r_{02}, b_2.

In a structure in which residual stress and strain exist, the stress-strain state can be generally expressed by the relation

$$\boldsymbol{\sigma} = \mathbf{D}(\boldsymbol{\varepsilon} - \boldsymbol{\varepsilon}_0) + \boldsymbol{\sigma}_0, \tag{1}$$

where $\boldsymbol{\sigma}$ - stress vector, $\boldsymbol{\varepsilon}$ - strain vector, $\boldsymbol{\sigma}_0$ - residual stress vector, $\boldsymbol{\varepsilon}_0$ - residual strain vector and $\mathbf{D}$ - elasticity matrix.

The FE formulation of equation of motion for a free vibration of circular saw blade without existence residual stresses is expressed by

$$\mathbf{M}\ddot{\mathbf{q}} + \mathbf{K}\mathbf{q} = \mathbf{0} \tag{2}$$

and eigenvalue problem has the form

$$(\mathbf{K} - \omega_i^2\mathbf{M})\boldsymbol{\psi}_i = \mathbf{0},$$

where $\mathbf{M}$ - mass matrix, $\mathbf{K}$ - stiffness matrix, $\mathbf{q}$ - vector of nodal displacements, $\ddot{\mathbf{q}}$ - vectors of nodal accelerations, ω_i - i^{th} natural angular frequency, $\boldsymbol{\psi}_i$ - i^{th} mode shape of circular saw blade.

By creating plastic zones in the circular saw blade body, a certain form of structural modification occurs, which leads to a change in the distribution of the spatial properties (mass, stiffness) of the saw blade. It is evident, that the mass distribution of circular saw blade after rolling is not changed, but the bending stiffness can be considerably changed. The finite element equation of motion for a free vibration of circular saw blade with existence residual stresses represented by equation (1) is generally expressed in the shape

$$\mathbf{M}\ddot{\mathbf{q}}_m + (\mathbf{K} + \Delta\mathbf{K}_\sigma)\mathbf{q}_m = \mathbf{0} \tag{3}$$

and then eigenvalue problem has the form

$$(\mathbf{K} + \Delta\mathbf{K}_\sigma - \omega_{m,i}^2\mathbf{M})\boldsymbol{\psi}_{m,i} = \mathbf{0}, \tag{4}$$

where parameters taking into account the stress distribution in the body of circular saw blade induced by rolling $\Delta\mathbf{K}_\sigma$ - modifying stiffness matrix, $\ddot{\mathbf{q}}_m$ - modified vectors of nodal accelerations, $\mathbf{q}_m$ - modified vector of nodal displacements, $\omega_{m,i}$ - i^{th} modified natural angular frequency, $\boldsymbol{\psi}_{m,i}$ - i^{th} mode shape of circular saw blade.

To determine the change in the stiffness of the disk after rolling and to determine the distribution of residual stresses in the plane of the circular saw blade, the thermal stress method is used. The thermal expansion embedded to annular zones induces the stress distribution in circular saw blade, which is analogous to the stress distribution initiated by rolling. The dependence between the temperature and the indentation depth of the rolled surface can be approximately described by the equation

$$\Delta T \approx \frac{\mu}{\alpha h_d}\Delta z, \tag{5}$$

where μ - Poisson´s number, α - temperature expansion coefficient, h - thickness of circular saw blade and Δz - indentation depth of the rolled surface.

The geometrical dimensions and material properties considered circular saw blade (Fig.1) are given in Table 1.

Table 1. The dimensions and material properties of circular saw blade

r_1 [mm]	r_2 [mm]	r_c [mm]	h_d [mm]	$b = b_1 = b_2$ [mm]	E [GPa]	ρ [kg/m^3]	μ [-]
15	120	25	1.8	10	210	7800	0.3

The distributions of radial and tangential residual stresses in the plane of the circular saw blade are shown in Fig.2, i.e. with one plasticized annular zone (Fig.2a) and with two plasticized annular zones (Fig.2b).
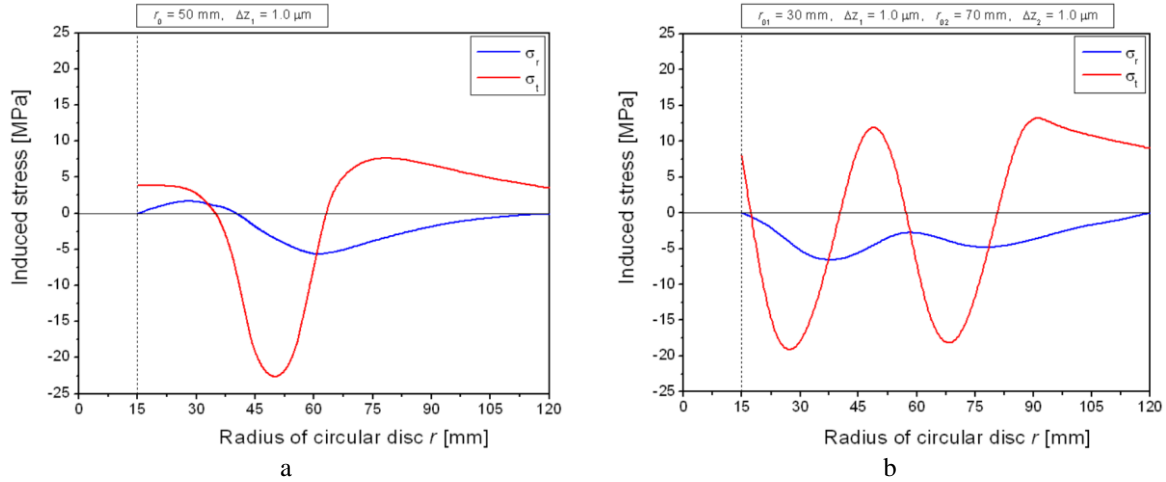
Fig. 2. Distribution of radial σ_r and tangential σ_t residual stresses initiated in disc plane: a - one plasticized zone; b - two plasticized zones

The values of natural frequencies of the modal shapes 0/1, 0/0, 0/2, 0/3 (nodal circles/nodal lines) depending on the rolling depth and the position of the plasticized annular zone for a circular saw blade (Fig.1a) are shown in Fig.3. Width of plasticized zone is $b = 10$ mm.
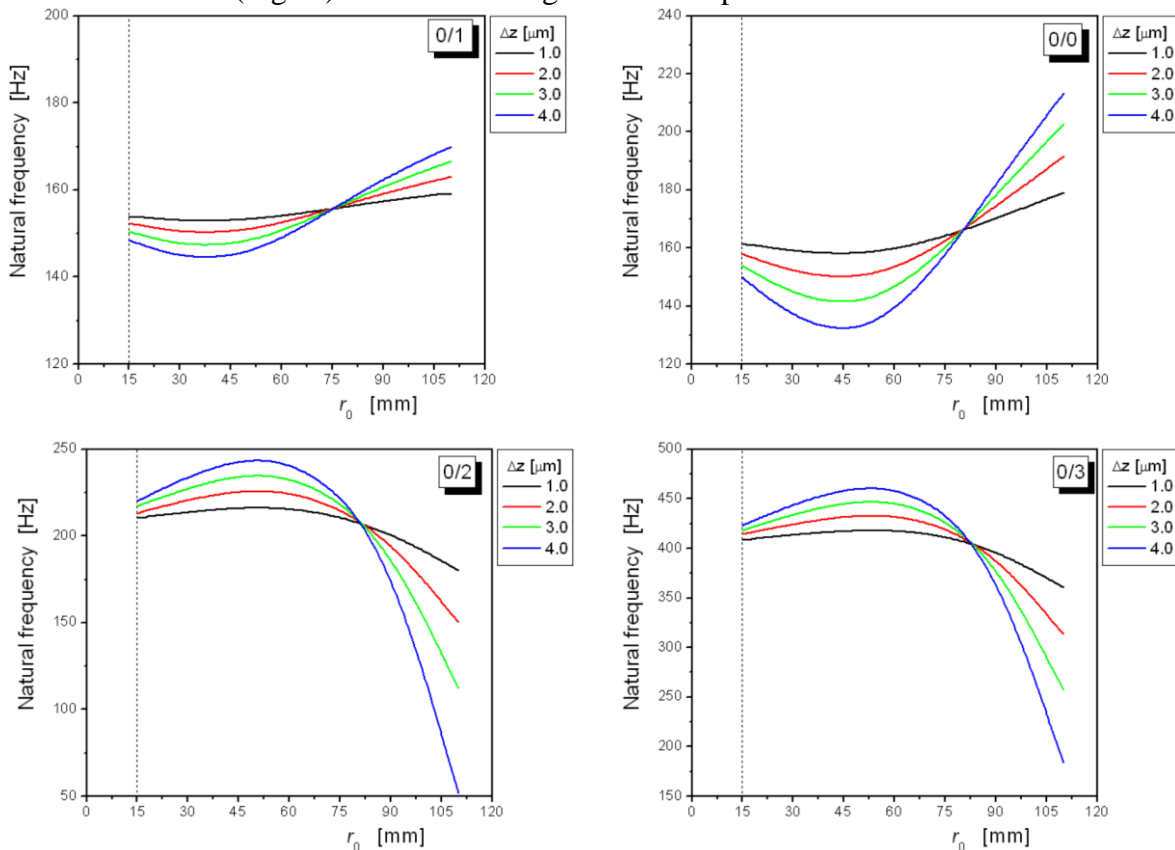
Fig. 3. Dependency of natural frequencies on position of plasticized zone for the first four modal shapes (circular saw blade with one plasticized annular zone)

The tendency of frequency curves for mode shapes 0/1 and 0/0 differs from tendency of frequency curves for mode shapes 0/2 and 0/3. The natural frequencies of the modal shapes 0/2 and 0/3 are increasing with r_0 until the maximum values near $r_0 \cong 55$ mm are reached; then they

11

are decreasing. Contrary to this, the natural frequencies of the modal shapes 0/1 and 0/0 are decreasing with r_0 and for $r_0 \cong 46$ mm reach the minimum and then they increase.

The results for values of natural frequencies of circular saw blade with two plasticized annular zones (r_{01} has constant value 30 mm, radius r_{02} varies from 30 mm to 120 mm and width of both plasticized zones is $b_1 = b_2 = 10$ mm) are shown on Fig 4.
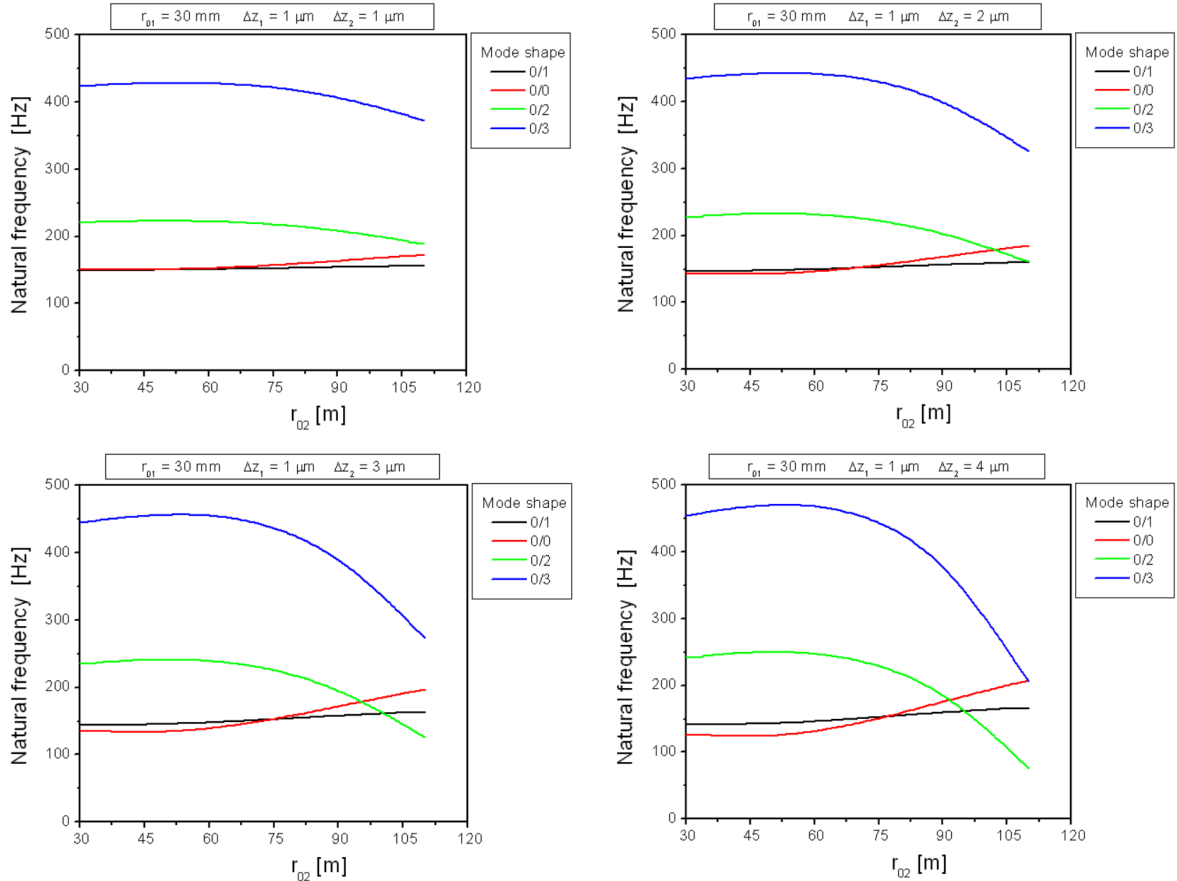
Fig. 4. Dependency of natural frequencies of the first four modal shapes on position of plasticized zone (circular saw blade with two plasticized annular zones)

The effect of two plasticized annular zones on modal properties of circular saw blade is similar as for case with one plasticized zone.

Based on the obtained results, it can be concluded that this method of structural modification can be used to solve the dynamic stability of mechanical systems and is very effective, for example, in modifying the modal properties of circular saw blades.

Acknowledgements

References

[1] Kuratani, F., Yano, S., Vibration analysis of a circular disk tensioned by rolling using finite element method, Archive of Applied Mechanics 70 (2000) 279-288.
[2] Naď, M., Modification of modal characteristics of vibrating structural elements, Scientific Monographs, Köthen, 2010.
[3] Sága, M., Žmindák, M., Dekýš, V., Sapietová, A., Segľa, Š., Selected methods for the analysis and synthesis of mechanical systems, VTS ZU, Zilina, 2009. (in Slovak)

Subcritical behaviour and stability of a rigid rotor supported by undulated journal bearings

M. Byrtus[a], V. Lukeš[a], J. Rendl[b], E. Rohan[a,b]

[a]Department of Mechanics, Faculty of Applied Sciences, University of West Bohemia, Technická 8, 301 00 Plzeň, Czech Republic
[b]NTIS – New Technologies for the Information Society, Faculty of Applied Sciences, University of West Bohemia, Technická 8, 301 00 Plzeň, Czech Republic

Journal bearings are widely used as a support for high-speed or heavy rotating machines. Among their main advantages are simple construction, low wear, damping capacity and ability to withstand shock loads. However, the journal bearing can be a source of self-excited subsynchronous vibration of the rotating parts. This behaviour is also called fluid-induced instability. The criterion and method for system stability analysis were studied in [3]. The undesirable behaviour can be suppressed by global geometry modifications leading to lemon bore bearings, multi-lobe bearings, offset-halve bearings and tilting pad journal bearings. If different bearing types are insufficient to improve the system stability, the local changes in the geometry by adding grooves, pressure dams, or, nowadays popular, textures are performed. The textures (undulation) can improve the bearing load capacity due to the fluctuation of the developed hydrodynamic pressure. The hydrodynamic pressure is governed by the Reynolds equation. In the case of an indented bearing shell, the solution of the Reynolds equation is tricky. The finite difference [3, 6] and the finite volume methods are the most used numerical methods for solving this equation. These methods are suitable for plain journal bearing, but they become time-costs inefficient for undulated bearing shells. For the textured bearing, the numerical solution requires a significantly higher number of considered nodes in the computational mesh to obtain valid results, see [6]. This contribution presents a computational approach employing the homogenisation method [4, 5] applied to the problem of hydrodynamic lubrication in the journal bearing with textures, where the homogenisation procedure is performed utilising the SfePy tool [1] – simple finite elements in Python. The SfePy tool is further linked with the continuation toolbox MATCONT [2].

First, a parameterization of the bearing model coupled with the rotor is introduced, Fig. 1. The rotor position can be described by coordinates $\boldsymbol{\Xi} = (\Xi_1, \Xi_2)$ in the Cartesian system xz, or by the polar coordinates $\boldsymbol{\xi} = (\rho, \alpha)$ with $\rho > 0$ denoting the eccentricity, and $\alpha \in]-\pi, +\pi[$ denoting the angular deviation from the reference position. Clearly

$$\boldsymbol{\Xi} = \rho(\cos\alpha, \sin\alpha) \,, \quad \rho = |\boldsymbol{\Xi}| \,. \tag{1}$$

Let $\boldsymbol{x} = (x_1, x_2) \in \Omega \subset \mathbb{R}^2$ describe the position in the plane of the rectified bearing gap. Consider $\Omega =]-s, s[\times]0, L[$, where $s = \pi R$ is the half-circumference given by the bearing shell radius R, and L is the bearing width. Due to the bearing eccentricity, the bearing median gap height h_0 is given by

$$\begin{aligned} h_0(\boldsymbol{x}) &= h^0 - \rho\cos(\theta - \alpha) \,, \quad \theta \in]-\pi, \pi] \,, \\ x_1 &= R\theta = s\theta/\pi \,, \quad x_2 \in]0, L[\,, \end{aligned} \tag{2}$$
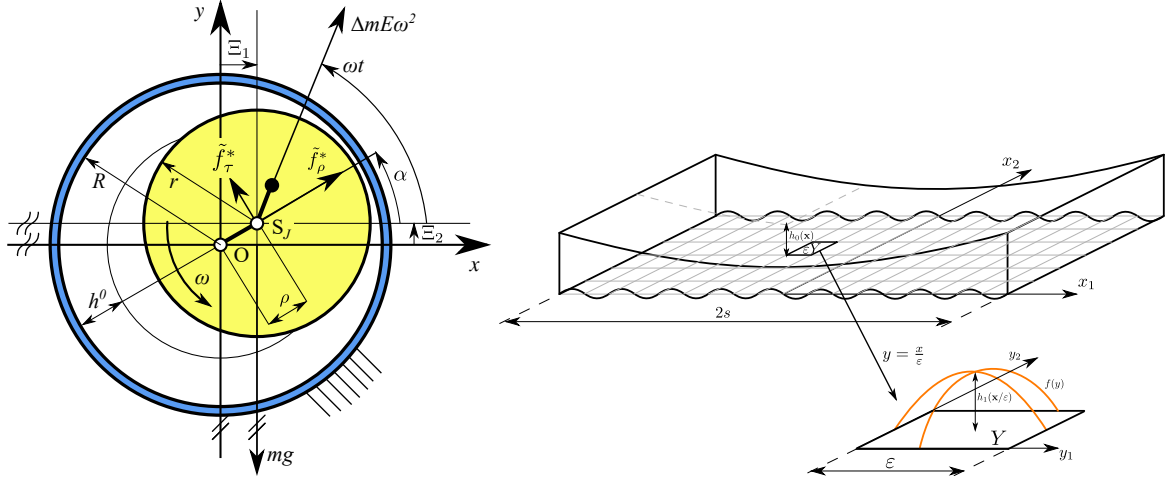
Fig. 1. A scheme of the considered rotor-bearing system with denoted forces (left) and the bearing surface area with undulation (left)

where $h^0 = R - r$ is a nominal bearing gap, given by the bearing shell and rotor radii.

The rotor dynamic is driven by

$$\boldsymbol{M}\ddot{\boldsymbol{\Xi}} = \tilde{\boldsymbol{f}}(\boldsymbol{\Xi}, \alpha, p) + \boldsymbol{g}(\omega, \phi) \quad \text{with } \phi(t) = \omega t \ , \tag{3}$$

where $\boldsymbol{M} = m\mathbf{I}$ is the mass matrix, vector $\tilde{\boldsymbol{f}}$ is given by pressure p by virtue of the Reynolds equation, and $\boldsymbol{g}$ is the rotor unbalance. Recall that the rotor angle position α and eccentricity ρ are related to the Cartesian rotor position (1). The force $\tilde{\boldsymbol{f}}^* = (\tilde{f}_\rho^*, \tilde{f}_\tau^*)$ is defined in the $\rho - \tau$ (radial, tangential) coordinate system as follows

$$\begin{aligned}
\tilde{f}_\rho^*(p, \alpha, t) &= \int_0^L \int_\theta p(t, x_1(\theta), x_2) \cos(\theta - \alpha) R \mathrm{d}\theta \mathrm{d}x_2 \ , \\
\tilde{f}_\tau^*(p, \alpha, t) &= \int_0^L \int_\theta p(t, x_1(\theta), x_2) \sin(\theta - \alpha) R \mathrm{d}\theta \mathrm{d}x_2 \ ,
\end{aligned} \tag{4}$$

where $\theta =\ ] - \pi, 0[$ so that, in the Cartesian system (Ξ_1, Ξ_2),

$$\tilde{\boldsymbol{f}} = \boldsymbol{R}(\alpha)\tilde{\boldsymbol{f}}^* \ , \quad \text{where} \quad \begin{aligned} \tilde{f}_1 &= \tilde{f}_\rho^* \cos \alpha - \tilde{f}_\tau^* \sin \alpha \ , \\ \tilde{f}_2 &= \tilde{f}_\rho^* \sin \alpha + \tilde{f}_\tau^* \cos \alpha \ , \end{aligned} \quad \text{thus,} \ \boldsymbol{R}(\alpha) = \begin{bmatrix} \cos(\alpha) & -\sin(\alpha) \\ \sin(\alpha) & \cos(\alpha) \end{bmatrix}. \tag{5}$$

Here, the perfectly balanced rotor supported by an undulated journal bearing is taken into account. The dynamic behaviour of the system described generally by (3) is investigated using two methods: numerical integration in the time domain and numerical continuation of equilibrium solution with respect to a chosen bifurcation parameter (nondimensional rotor speed $\overline{\omega}$). Both methods need to compute the pressure field in the bearing gap to determine the hydrodynamic forces which depend on the actual position and velocities of the journal center. Firstly, for a given bearing undulated geometry, the homogenized coefficients need to be calculated. Then, these homogenised coefficients are used to determine the pressure field in the bearing gap in the homogenised model of the Reynolds equation. For illustration, the pressure distribution in the bearing gap in plain journal bearing and undulated journal bearing is shown and compared in Fig. 2.

The rotor dynamic model (3) is transformed into nondimensional form and nondimensional rotor speed and rotor eccentricity are defined as $\overline{\omega} = \omega\sqrt{h_0/g}$ and $\overline{\rho} = \rho/h_0$, where $\rho =$
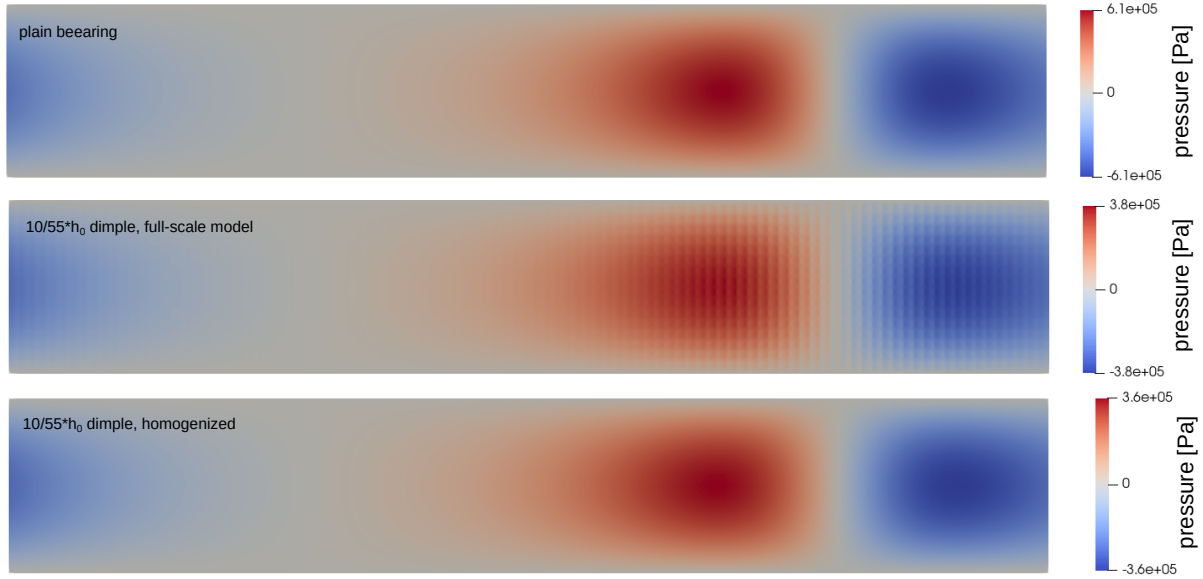
Fig. 2. Comparison of pressure distribution in the bearing gap for $\overline{\omega} = 1.5$, $\rho = 0.5h_0$ and $\alpha = 1.396$ rad; for plain bearing (top), undulated bearing with dimple height equalled to $10/55h_0$ – full-scale model (middle), homogenized model (bottom)

$\sqrt{\Xi_1^2 + \Xi_2^2}$. When neglecting the unbalance, the dynamic response of the model is formed by an equilibrium which is either stable or unstable. Based on this fact, the stability of the system is determined computationally and briefly described by the following steps:

- Initialisation: determination of parameters of homogenised model of Reynolds equation.

- Numerical integration in the time domain of the model (3) for given initial conditions of rotor position and velocity and for given nondimensional rotor parameters: rotor speed $\overline{\omega}$ and rotor bearing parameter λ. The homogenized Reynolds equation is solved in every time-integration step to determine the hydrodynamic forces.

- Finding steady-state (equilibrium) solution $\hat{\boldsymbol{\Xi}}(\overline{\omega}, \lambda)$ using the numerical integration.

- The continuation of equilibrium solution $\hat{\boldsymbol{\Xi}}(\overline{\omega}, \lambda)$ is performed with respect to parameter $\overline{\omega}$.

- In each continuation step, the stability of the solution is determined based on the properties of eigen-values of the linearized model in the equilibrium point.

- Determination of special bifurcation points. In case of equilibria continuation, Hopf's bifurcation points can be detected. These are points where the stability of the equilibrium solution is lost. Simultaneously, as the equilibrium loses its stability, a stable (or unstable) limit cycle solution can be born at Hopf's point.

- Moreover, Hopf's bifurcation points form so-called Hopf's (stability) curve, see Fig. 3 green curve. This curve can be found using codim-2 continuation of the equilibrium solution starting from Hopf's bifurcation point and the continuation is performed in two parametric space $(\overline{\omega}, \lambda)$. On the Hopf's curve, there can be detected Generalized Hopf's bifurcation point which splits the curve into two parts. The first part is formed by Hopf's points from which a stable super-critical limit cycle solution can arise. The second part is formed by Hopf's points from which an unstable sub-critical limit cycle solution arises. For more details, see Fig. 3
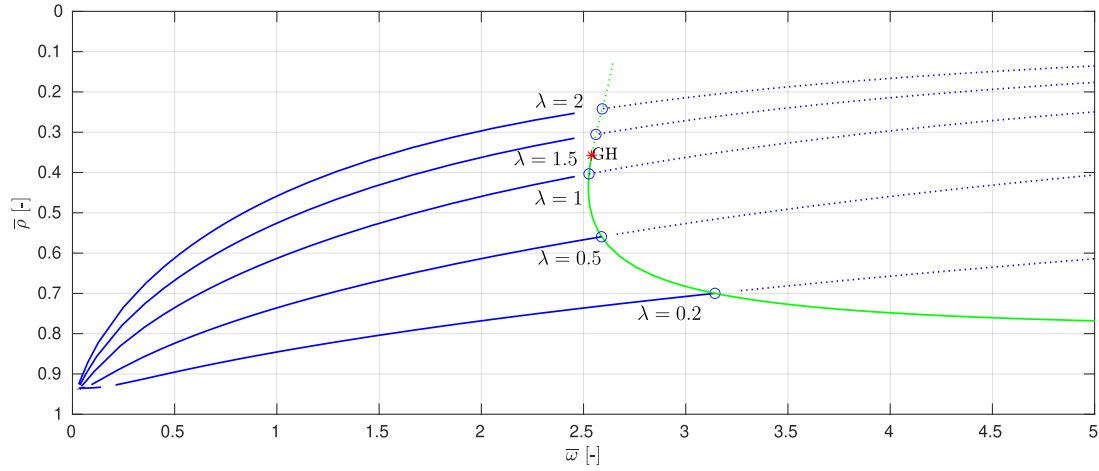
Fig. 3. Stability chart; '——' stable equilibria; '- -' unstable equilibria; ○ Hopf's bifurcation points; ∗ Generalized Hopf's bifurcation point; '——' super-critical Hopf's curve; '- -' sub-critical Hopf's curve

The work presents a novel approach which uses the homogenisation method for analysis of the pressure field in the undulated journal bearing described by the Reynolds equation in tasks of journal bearing dynamics. Based on this, a weakly-coupled dynamic model of a rotor supported by undulated journal bearings is formulated. A corresponding computational model integrates the homogenised model created in the Python-based SfePy tool into the Matlab-based continuation tool MATCONT. This method enables to perform computationally efficient dynamic analyses of weakly-coupled models.

Acknowledgements

References

[1] Cimrman, R., Lukeš, V., Rohan, E., Multiscale finite element calculations in Python using SfePy, Advances in Computational Mathematics 45 (4) (2019) 1897-1921.

[2] Dhooge, A., Govaerts, W., Kuznetsov, Y. A., Meijer, H. G. E., Sautois, B., New features of the software MATCONT for bifurcation analysis of dynamical systems, Mathematical and Computer Modelling of Dynamical Systems 14 (2) (2008) 147-175.

[3] Dyk, Š., Rendl, J., Byrtus, M., Smolík, L., Dynamic coefficients and stability analysis of finite-length journal bearings considering approximate analytical solutions of the Reynolds equation, Tribology International 130 (2019) 229-244.

[4] Prat, M., Plouraboué, F., Letalleur, N., Averaged Reynolds equation for flows between rough surfaces in sliding motion, Transport in Porous Media 48 (2002) 291-313.

[5] Rom, M., König, F., Müller, S., Jacobs, G., Why homogenization should be the averaging method of choice in hydrodynamic lubrication, Applications in Engineering Science 7 (2021) No. 100055.

[6] Smolík, L., Rendl, J., Omasta, M., Byrtus, M., Šperka, P., Polach, P., Hartl, M., Hajžman, M., Comprehensive analysis of fluid-film instability in journal bearings with mechanically indented textures, Journal of Sound and Vibration 546 (2023) No. 117454.

Updating of jet trainer aircraft FE model according to results of ground vibration test

J. Čečrdle[a]

[a]Czech Aerospace Research Centre (VZLU), Beranových 130, 199 05 Praha Letňany, Czech Republic

Computational (FEM) models of aircraft structures used for aeroelastic analyses must be validated according to experimental results. Flutter analyses have ultimate character and accuracy, and reliability of flutter results are strongly dependent on the accuracy and reliability of the input modal data. Therefore, the model updating according to the ground vibration test (GVT) results is required. Basically, updating is a problem of multidisciplinary optimization (MDO). The Bayesian Least Squares Estimation Method is frequently employed. The objective function (OBJ) is expressed as

$$OBJ = \{\Delta R\}^T [W_R] \{\Delta R\} + \{\Delta P\}^T [W_P] \{\Delta P\} \,. \tag{1}$$

It represents the weighted sum of the error in design responses $\{\Delta R\}$ and the difference in design variables $\{\Delta P\}$. $[W_P]$ and $[W_R]$ are then diagonal scatter matrices for design variables and for design responses, respectively. The solution is iterative, expressed as

$$\{P_u\} = \{P_0\} + [G]\{-\Delta R\} \,, \tag{2}$$

where $\{P_u\}$ is the vector of design variables after updating; $\{P_0\}$ is the vector of design variables before updating; $\{\Delta_R\}$ is the design response change vector and $[G]$ is the gain matrix calculated according to Bayesian Estimation Theory as

$$[G] = ([W_P] + [S]^T [W_R][S])^{-1} [S]^T [W_R] \ \text{or} \ [W_P]^{-1} [S]^T ([W_R]^{-1} + [S][W_P]^{-1}[S]^T)^{-1}, \tag{3}$$

where $[S]$ is the sensitivity matrix representing rates of design response changes with respect to change in design variables.
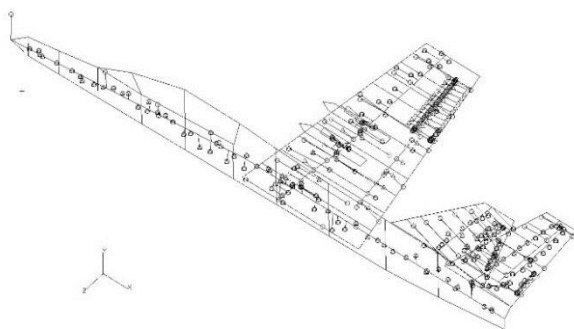
Fig. 1. FEM model (jet trainer aircraft)
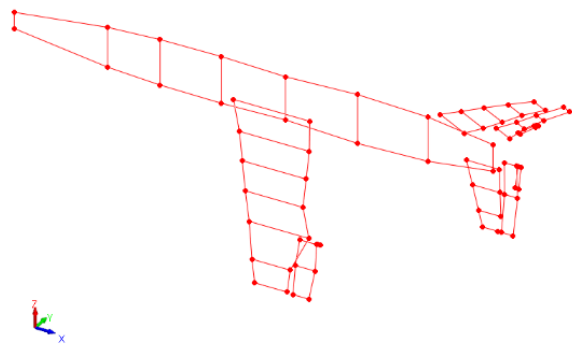
Fig. 2. GVT model (jet trainer aircraft)

Updating is usually performed in several steps in which the strategy is appropriately modified according to the situation. The key issue is the appropriate selection of design variables and design responses and setting of scatter values. FEM model has a character of a dynamic stick model. Stiffness model includes mass-less beam-like elements (structural parts) and scalar springs (specific connections, control surface actuation, etc.). Inertia model includes lumped mass elements with the appropriate moments of inertia. The model usually includes a single side only with either symmetric or antisymmetric boundary condition. The example is shown in Fig. 1. GVT data are reduced and adjusted. Provided that uniaxial sensors are used; the deformations are to be recalculated to the triaxial scheme. The appropriate selection of points is important as it affects the correlation criterion of mode shapes. Fig. 2 shows the example of the grid of experimental points.

Compared to the inertia data, the stiffness data based on the virtual prototype are considered as less accurate and reliable, thus, the stiffness data are used as design variables. The data, which are not considered as design variables must be validated and adjusted prior the updating. Therefore, the preparatory activities include the adjustment of control surfaces and tabs mass data according to the weighing. In addition, the total inertia data are adjusted according to the prototype weighing. Finally, effective stiffness of tabs actuation is updated according to the static stiffness measurements.

Design variables include beam-like elements vertical bending stiffness, in-plane bending stiffness and torsional stiffness and scalar spring stiffness modeling control surface actuations and structural part connections. Design responses (i.e., natural frequencies, MAC-values) include bending and torsional modes of the main structural parts and flapping modes of control surfaces. Modes are split into symmetric and antisymmetric modes and the updating is performed for both groups separately. Therefore, separate models with the diverse final values of design variables for symmetric and antisymmetric case are obtained.

Table 1. Experimental modes (symmetric) selected for updating

#	title	f_0 [Hz]
01	1st symmetric wing bending	14.603
02	Symmetric aileron flapping	14.970
03	1st fuselage vertical bending	18.130
04	Symmetric elevator flapping (fixed stick)	24.101
05	1st symmetric tailplane bending	27.979
06	2nd fuselage vertical bending	35.263
07	1st symmetric wing torsion	38.461
08	2nd symmetric wing bending	51.943
09	1st symmetric wing in-plane bending	60.224
11	2nd symmetric wing torsion	70.131
12	1st symmetric tailplane in-plane bending	76.146
14	1st symmetric tailplane torsion	87.698

Mode pairing (FEM and GVT) is performed manually by a visual comparison of mode shapes using the specific graphic format showing node lines and modal deformation of structural parts. Although MAC-values are used as design responses, automated pairing of modes according to MAC-values is not applicable as it may lead to inappropriate pairing, because the aircraft structure is very complicated dynamical system with the high modal density.

First, updating of the baseline configuration is performed. As the next step, correlation analysis of the updated model for additional mass configurations with the corresponding GVT

data is performed and, provided that the results are not satisfactory, further updating using additional design variables is performed. As the result, the diverse models for each mass configuration may be obtained. Note that the possibility to include the GVT data of multi-mass configuration into updating process and take a single model for multiple mass configurations is not recommended. Contrary to that, updating considering only a subset of major modes, contributing to a specific flutter instability, is feasible.

Model updating is demonstrated on the example of the new Czech jet trainer aircraft. GVT included a single (baseline) mass configuration for which a complete set of modes has been measured. Additional configurations included specific pod-based configurations or specific conditions of the control system. For these additional configurations, just appropriate modes were measured, e.g., pod-modes, control system transfer functions, etc.
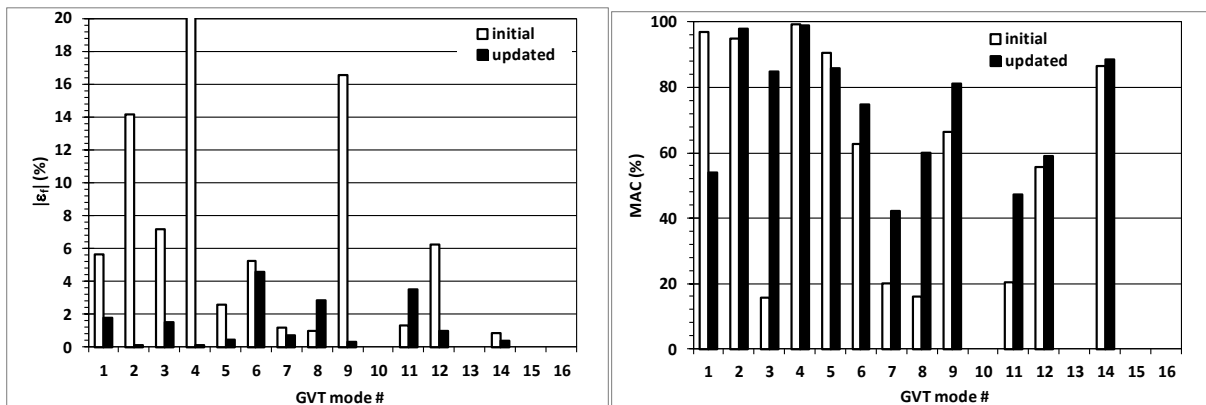
Fig. 3. Comparison of initial and final model, baseline configuration, a) frequency error, b) MAC-values

As the example, updating of the symmetric model is presented here. Experimental results of the baseline configuration included 16 symmetric modes, from which 12 modes were selected for updating. The list of the selected experimental modes is shown in Table 1.
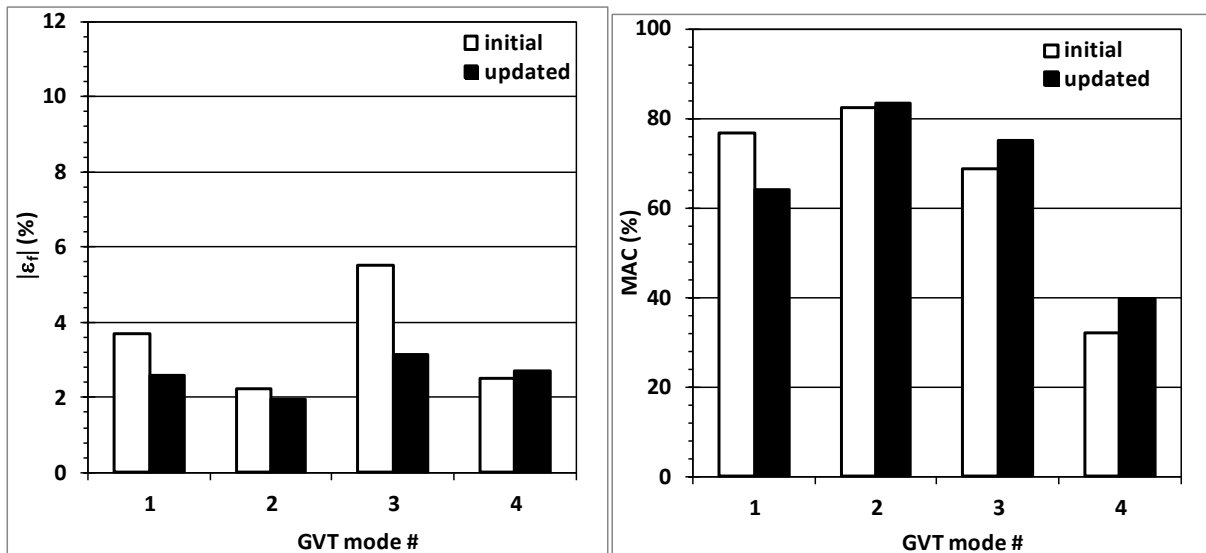
Fig. 4. Comparison of initial and final model, wing modes, a) frequency error, b) MAC values

Comparison of the initial and final pairing of modes is shown in Fig. 3. Pair numbers correspond to the GVT-mode numbers according to Table 1. Fig. 3a demonstrates relative error in natural frequencies. The final errors are less than 4.5 %. This is excellent result. Fig. 3b shows a comparison of the initial and final state in terms of MAC values. The results are also good, all MAC values increased or remained. The only exception is the mode # 01 (1st symmetric wing bending) for which the low MAC value is caused by the aileron points.

Nevertheless, provided that the MAC is considered excluding the aileron points, the value increase to 97.6 %. The reason is the cross-influence of 1st symmetric wing bending and aileron flapping modes, the frequencies of which are very close one another.

In addition, updating to the subset of four wing modes (1st wing bending, 1st fuselage vertical bending, 2nd fuselage vertical bending and 1st wing torsion), which are the main modes contributing to the wing flutter, was also performed. As the initial state, the model updated for the baseline configuration was used, except for the wing stiffness, for which the initial stiffness was used. The results are shown in Fig. 4. The improvement of the model agreement with the GVT results is not as significant as for the previous example. The main advantage here is the much lower change in wing stiffness parameters compared to the global updating of the baseline configuration.

Changes in design variables during updating are presented in Fig. 5 by showing the wing stiffness distribution in the spanwise direction expressed as the cross-sectional inertia. Bending and torsional stiffness for the initial state and for the two presented updated states are shown. As apparent from the figure, the changes in design variables for the global updating is very significant, especially in the root area in which the influence of the local flexibility of the wing and fuselage connection is simulated. Also, stiffness hump roughly at the 1/3 of spanwise station is significant. This hump is caused by 2nd bending and torsional modes, which are included into the design space for the global updating. Contrary to that, the changes of the wing stiffness parameters for updating to the wing modes are low and character of stiffness spanwise distribution was kept. The reason is that just 1st wing bending, and torsional modes were included into this updating.
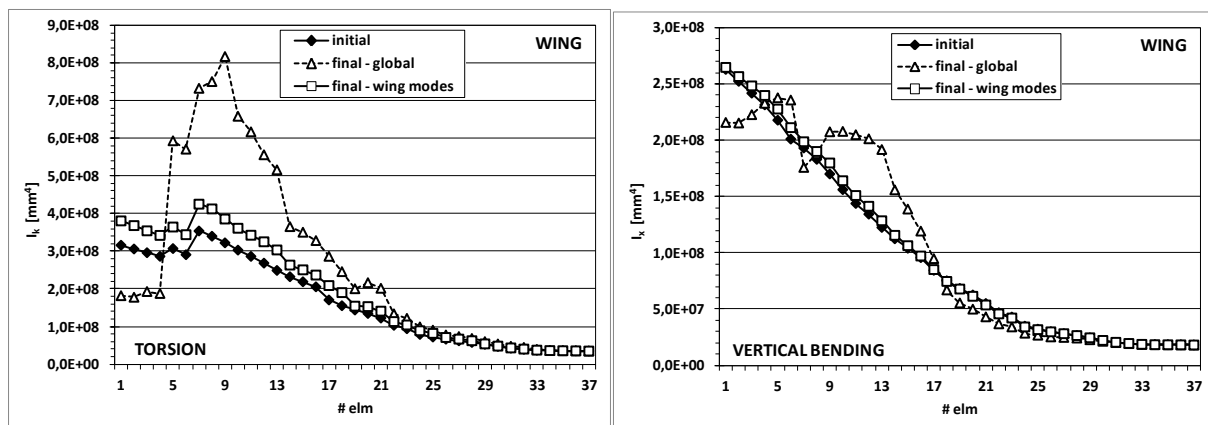
Fig. 5. Design variables change, initial state, final state – global, final state – updating to wing modes, a) wing torsional stiffness, b) wing bending stiffness

To conclude, modal parameters of updated models got much closer to the target GVT data. Updated models are prepared for the final phase of flutter calculations of the subjected aircraft.

Acknowledgements

References

[1] Čečrdle, J., Updating of finite element model of aircraft structure according results of ground vibration test, Proceedings of the Institution of Mechanical Engineers, Part G: Journal of Aerospace Engineering 230 (7) (2016) 1348-1356.

Dynamics of a cantilever beam with piezoelectric sensor: Parameter identification

R. Cimrman[a,b], R. Kolman[a,c], L. Musil[a], V. Kotek[a], J. Kylar[a]

[a]*Institute of Thermomechanics, Czech Academy of Sciences, Dolejškova 1402/5, 18200, Praha 8, Czech Republic*
[b]*New Technologies Research Centre, University of West Bohemia, Univerzitní 8, 301 14 Plzeň, Czech Republic*
[c]*College of Polytechnics Jihlava, Tolstého 16, 586 01 Jihlava, Czech Republic*

The piezoelectric materials are electroactive materials often applied for real-time sensing or structural health monitoring. Mathematical models of such structures contain several material parameters that need to be identified from experiments. The (proportional) damping coefficients are an example of such parameters, difficult to obtain in another way.

Our aim was to develop a computer model of a simple experiment performed in our laboratory [6] involving dynamics of a cantilever beam with an attached piezoelectric sensor excited by a suddenly removed weight, see Figs. 1–2. The sensor was connected to an oscilloscope that measured the voltage on the top side of the sensor, the bottom side was grounded. We had been interested in correctly simulating the experiment for various materials of the beam and/or in identifying parameters that were unknown or uncertain in advance. Preliminary simulations revealed that the oscilloscope had a finite resistance, motivating us to augment the model presented in [4]. The new model is briefly summarized below.

Let us denote by Ω_E the elastic part and by Ω_P the piezoelectric part of a body with $\Omega \subset \mathbb{R}^3$, see Fig. 1. The weak formulation of the model is as follows. Let $V_0^u(\Omega) = \{\boldsymbol{u} \in [H^1(\Omega)]^3, \boldsymbol{u} = \boldsymbol{0} \text{ on } \Gamma_u\}$, $V_0^\varphi = \{\varphi \in H^1(\Omega), \varphi = 0 \text{ on } \Gamma_{p0}\}$. We seek $\boldsymbol{u}(t)$, $\varphi(t)$, $\bar{\varphi}(t)$ such that

$$\int_\Omega \rho \boldsymbol{v} \cdot \ddot{\boldsymbol{u}} + \int_\Omega \boldsymbol{\varepsilon}(\boldsymbol{v})^T \boldsymbol{C} \boldsymbol{\varepsilon}(\boldsymbol{u}) + \alpha \int_\Omega \rho \boldsymbol{v} \cdot \dot{\boldsymbol{u}} + \beta \int_\Omega \boldsymbol{\varepsilon}(\boldsymbol{v})^T \boldsymbol{C} \boldsymbol{\varepsilon}(\dot{\boldsymbol{u}})$$

$$- \int_{\Omega_P} \boldsymbol{\varepsilon}(\boldsymbol{v})^T \boldsymbol{e}^T \boldsymbol{\nabla}\varphi - \int_\Omega \boldsymbol{v} \cdot \boldsymbol{b} = 0 \qquad \forall \boldsymbol{v} \in V_0^u(\Omega) , \quad (1)$$

$$\int_{\Omega_P} (\boldsymbol{\nabla}\psi)^T \boldsymbol{e} \boldsymbol{\varepsilon}(\boldsymbol{u}) + \int_{\Omega_P} (\boldsymbol{\nabla}\psi)^T \boldsymbol{\kappa} \boldsymbol{\nabla}\varphi - \int_{\Gamma_{pQ}} (\boldsymbol{\kappa}\boldsymbol{\nabla}\varphi) \cdot \boldsymbol{n}\psi$$

$$+ \int_{\Gamma_{pQ}} (\boldsymbol{\kappa}\boldsymbol{\nabla}\psi) \cdot \boldsymbol{n}(\varphi - \bar{\varphi}) = 0 \qquad \forall \psi \in V_0^\varphi(\Omega) , \quad (2)$$

$$\int_{\Gamma_{pQ}} (\boldsymbol{\kappa}\boldsymbol{\nabla}\dot{\varphi}) \cdot \boldsymbol{n} + \bar{\varphi}/R = 0 , \qquad (3)$$

$$\boldsymbol{u} = 0 \qquad \text{on } \Gamma_u \times [0, T] , \quad (4)$$

$$\varphi = 0 \qquad \text{on } \Gamma_{p0} \times [0, T] , \quad (5)$$

$$\boldsymbol{u}(0) = \boldsymbol{u}^0, \ \dot{\boldsymbol{u}}(0) = 0, \ \varphi(0) = \varphi^0 \qquad \text{in } \Omega , \quad (6)$$

where $\boldsymbol{u}$ is the mechanical displacement vector inducing the Cauchy strain $\boldsymbol{\varepsilon}$, φ is the electric potential, $\bar{\varphi}$ is the unknown potential on the top side of the sensor Γ_{pQ}, ρ is the density. $\boldsymbol{C}$ is the matrix of elastic properties (under constant electric field intensity in Ω_P), α, β are the
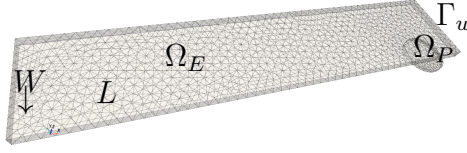
Fig. 1. The computational mesh. A weight is attached to the bottom side at the point W at time $t = 0$ s. Dynamic quantities are recorded in the point L
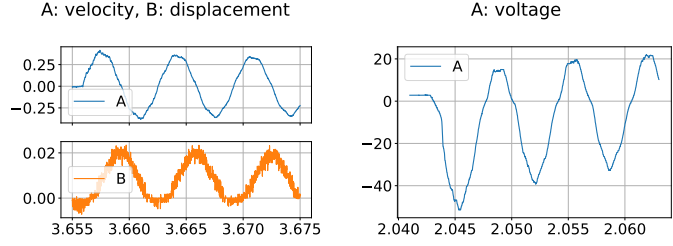
Fig. 2. The experimental data: (left) laser vibrometer, (right) oscilloscope

proportional damping coefficients, e the piezoelectric modulus, κ the permittivity under constant deformation and n is the unit outward normal. The structure is loaded by the self-weight volume forces b. The initial conditions u^0, φ^0 correspond to a static loading of the body by a localized surface force of a weight (280 g) attached, using a nylon string, at point W in Fig. 1. The external circuit is modeled by (3) with R being the oscilloscope resistance. The last two terms in (2) correspond to the weak enforcement of the Dirichlet boundary condition $\varphi = \bar\varphi(t)$ on Γ_{pQ} using the non-symmetric Nitsches method [8] without the penalty term [2]. The finite element discretization of (1)–(3) uses

$$u(\boldsymbol\xi) = \mathbf{N}_u(\boldsymbol\xi)\mathbf{u}\,, \quad \varphi(\boldsymbol\xi) = \mathbf{N}_\varphi(\boldsymbol\xi)\mathbf{p}\,, \quad \bar\varphi = 1\bar p\,, \tag{7}$$

where $\mathbf{N}_u(\boldsymbol\xi)$, $\mathbf{N}_\varphi(\boldsymbol\xi)$ are the displacement and the potential shape functions, respectively. The implicit second order Newmark method [7] is used to discretize the dynamical part (1), while the central difference scheme is used for (3). Because we want to perform a sensitivity analysis of the time-dependent system on several problem parameters, we present the discrete equations in the extended form with the unknowns vectors $\mathbf{u}$, $\dot{\mathbf{u}}$, $\ddot{\mathbf{u}}$, $\mathbf{p}$, $\dot{\mathbf{p}}$, $\bar p$ of the time step n, the $n-1$ time step quantities indicated by the superscript ^{0}

$$\ddot{\mathcal{U}}: \qquad \mathbf{M}\ddot{\mathbf{u}} + \mathbf{C}\dot{\mathbf{u}} + \mathbf{K}\mathbf{u} - \mathbf{B}^T\mathbf{p} - \mathbf{b} = 0\,, \tag{8}$$

$$\mathcal{P}: \qquad \mathbf{B}\mathbf{u} + (\mathbf{D} - \mathbf{F} + \mathbf{F}^T)\mathbf{p} - \mathbf{F}^T\mathbf{1}\bar p = 0\,, \tag{9}$$

$$\bar{\mathcal{P}}: \qquad \mathbf{1}^T\mathbf{F}\dot{\mathbf{p}} + \frac{1}{2R}(\bar p + \bar p^0) = 0\,, \tag{10}$$

$$\dot{\mathcal{U}}: \qquad \dot{\mathbf{u}} - \dot{\mathbf{u}}^0 - (1 - \gamma_N)\Delta t\ddot{\mathbf{u}}^0 - \gamma_N\Delta t\ddot{\mathbf{u}} = 0\,, \tag{11}$$

$$\mathcal{U}: \qquad \mathbf{u} - \mathbf{u}^0 - \Delta t\dot{\mathbf{u}}^0 - (\tfrac{1}{2} - \beta_N)\Delta t^2\ddot{\mathbf{u}}^0 - \beta_N\Delta t^2\ddot{\mathbf{u}} = 0\,, \tag{12}$$

$$\dot{\mathcal{P}}: \qquad \dot{\mathbf{p}} + \frac{1}{\Delta t}\mathbf{p}^0 - \frac{1}{\Delta t}\mathbf{p} = 0\,, \tag{13}$$

where $\mathbf{M}$ is the mass matrix, $\mathbf{C}$ is the damping matrix, $\mathbf{K}$ is the stiffness matrix, $\mathbf{B}$ is the piezoelastic coupling matrix, $\mathbf{D}$ is the electrostatic potential matrix and $\mathbf{b}$ is the volume forces vector. The surface flux matrix $\mathbf{F} = \int_{\Gamma_{pQ}} \mathbf{N}_\varphi^T \boldsymbol{n}\boldsymbol\kappa\mathbf{N}_\varphi'$ is used to impose weakly the Dirichlet boundary condition $\varphi = \bar\varphi$ on Γ_{pQ}, $\mathbf{1}$, the matrix of ones, is used to sum the rows of $\mathbf{F}$, performing thus the integration of (3). The Newmark scheme is expressed by (11), (12), β_N, γ_N are its parameters, the central difference scheme by (13) and the average in the second term of (10). When computing the direct problem, $\dot{\mathbf{u}}$, $\mathbf{u}$, $\dot{\mathbf{p}}$ expressed from (11)–(13) are substituted into (8)–(10), resulting in three primary unknowns $\ddot{\mathbf{u}}$, $\mathbf{p}$, $\bar p$ to compute in each time step by solving a linear system.

The parameter identification is done by fitting a time series of measured data – in our case the velocity component $v_z(t)$ measured by a laser vibrometer in the point L – to the corresponding simulated quantity $\dot{u}_z(L,t)$ by a nonlinear least-squares solver (`least_squares()` function from SciPy [10]). This solver can compute the Jacobian matrix of the objective function F numerically or use a user-supplied function returning partial sensitivities. For our linear problem, we do not expect to achieve a faster elapsed time with a semi-analytical Jacobian matrix (see below) than with the default 2-point finite difference scheme, because the number of linear systems to solve is the same and computing the Jacobian analytically involves some additional calculations. Nevertheless it allows us to test our automatically differentiated terms based on JAX [1] and provides a proof-of-concept for future nonlinear extensions of the model.

The state problem (8)–(13) in an abstract form (see also [9]) can be written as

$$\Phi(\boldsymbol{\alpha}, \mathbf{y}, \mathbf{y}^0) = 0 \,, \quad \mathbf{y} \equiv [\mathbf{u}, \dot{\mathbf{u}}, \ddot{\mathbf{u}}, \mathbf{p}, \dot{\mathbf{p}}, \bar{p}]^T \,, \tag{14}$$

where $\boldsymbol{\alpha}$ are the parameters to be identified. Our aim is to calculate the partial sensitivities $\frac{\partial \dot{u}_z(L,t)}{\partial \alpha}$. By differentiating (14) w.r.t. $\boldsymbol{\alpha}$ a recurrent relation

$$\frac{\partial \Phi}{\partial \mathbf{y}} \frac{\partial \mathbf{y}}{\partial \boldsymbol{\alpha}} = -\left(\frac{\partial \Phi}{\partial \boldsymbol{\alpha}} + \frac{\partial \Phi}{\partial \mathbf{y}^0} \frac{\partial \mathbf{y}^0}{\partial \boldsymbol{\alpha}}\right) \tag{15}$$

is obtained allowing us to compute $\frac{\partial \mathbf{y}}{\partial \boldsymbol{\alpha}}$ in all time steps, initialized by using the initial conditions. Then $\frac{\partial \dot{u}_z(L,t)}{\partial \alpha}$ are simply a component in $\frac{\partial \mathbf{y}}{\partial \boldsymbol{\alpha}}$.

To briefly demonstrate the parameter identification, below we identify the parameters β (the stiffness proportional damping parameter), E (the Young's modulus of the beam) and u_0 (a scalar multiplier of the initial condition $\boldsymbol{u}^0$), using preliminary data for $t = [0, 0.02]$ s with the following (initial) material parameters:

- Steel elastic beam: $\rho = 7800$ kg/m^3, $E = 210$ GPa, $\nu = 0.3$.
- Piezoelectric disc: $\rho = 7800$ kg/m^3, the vacuum permittivity $\varepsilon^0 = 8.8541878128 \cdot 10^{-12}$ F/m and

$$\text{in Voigt notation: } \boldsymbol{C}^P = \begin{bmatrix} 127.2050 & 80.2122 & 84.6702 & 0.0000 & 0.0000 & 0.0000 \\ 80.2122 & 127.2050 & 84.6702 & 0.0000 & 0.0000 & 0.0000 \\ 84.6702 & 84.6702 & 117.4360 & 0.0000 & 0.0000 & 0.0000 \\ 0.0000 & 0.0000 & 0.0000 & 22.9885 & 0.0000 & 0.0000 \\ 0.0000 & 0.0000 & 0.0000 & 0.0000 & 22.9885 & 0.0000 \\ 0.0000 & 0.0000 & 0.0000 & 0.0000 & 0.0000 & 23.4742 \end{bmatrix} \text{GPa},$$

$$\boldsymbol{e} = \begin{bmatrix} 0.00000 & 0.00000 & 0.0000 & 0.0000 & 17.0345 & 0.0 \\ 0.00000 & 0.00000 & 0.0000 & 17.0345 & 0.0000 & 0.0 \\ -6.62281 & -6.62281 & 23.2403 & 0.0000 & 0.0000 & 0.0 \end{bmatrix} \text{C/m}^2, \boldsymbol{\kappa} = \varepsilon^0 \begin{bmatrix} 1704.4 & 0.0 & 0.0 \\ 0.0 & 1704.4 & 0.0 \\ 0.0 & 0.0 & 1433.6 \end{bmatrix} \text{F/m} .$$

All results were obtained using the Open Source finite element software SfePy [5, 3]. The convergence of the identification procedure is shown in Fig. 3 (left), where the evolution of the parameters and the l^2 norm of the objective function are depicted. The initial and identified time histories of $\dot{u}_z(L,t)$ are shown in Fig. 3 (right), together with the experimental data. The initial parameters correspond to reference values (a steel beam) and the attached weight loading. The results indicate some discrepancies in the experiment: the initial deflection of the beam should have been higher, see u_0, to explain the amplitude of the data, and the elastic beam Young's modulus E lower to match the principal frequency of the data. Note that the decreased Young's modulus E does not explain the initial amplitude by itself. Based on that, new experiments are being undertaken, where e.g. the influence on the applied initial load of cutting the nylon string of the weight is decreased, and the material parameters of the beam are determined experimentally instead of using reference material data from a data sheet. Finally, the proportional damping coefficient was determined to be about 1.92×10^{-5} s.
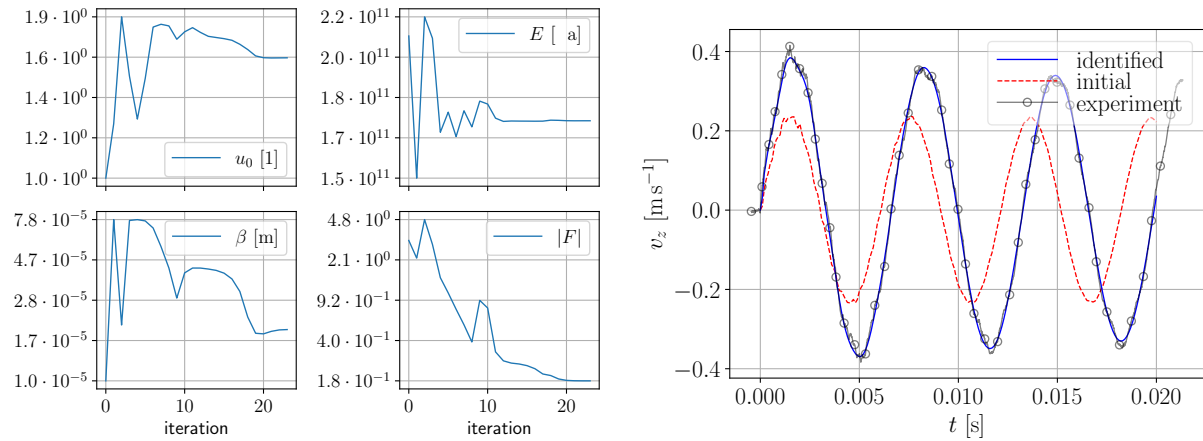
Fig. 3. Parameter identification: (left) the evolution of parameters and objective function during the objective function calls; (right) experiment, original and identified $\dot{u}_z(L,t)$

Acknowledgement

References

[1] Bradbury, J., Frostig, R., et al., JAX: Composable transformations of Python+NumPy programs, https://github.com/google/jax, 2023. Ver. 0.4.14.

[2] Burman, E., A penalty-free nonsymmetric nitsche-type method for the weak imposition of boundary conditions, SIAM Journal on Numerical Analysis 50 (4) (2012) 1959-1981.

[3] Cimrman, R., Fast evaluation of finite element weak forms using python tensor contraction packages, Advances in Engineering Software 159 (2021) No. 103033.

[4] Cimrman, R., Kolman, R., Musil, L., Kotek, V., Kylar, J., Dynamics of a cantilever beam with piezoelectric sensor: Finite element modeling, Proceedings of the 29th International Conference Engineering Mechanics 2023, Milovy, May 9-11, 2023, (editors) V. Radolf, I. Zolotarev, Institute of Thermomechanics of the Czech Academy of Sciences, 2023, pp. 51-54.

[5] Cimrman, R., Lukeš, V., Rohan, E., Multiscale finite element calculations in Python using SfePy, Advances in Computational Mathematics 45 (2019) 1897-1921.

[6] Kolman, R., Kylar, J., Kotek, V., Cimrman, R., Musil, L., Dynamics of a cantilever beam with piezoelectric sensor: Experimental study, Proceedings of the 29th International Conference Engineering Mechanics 2023, Milovy, May 9-11, 2023, (editors) V. Radolf, I. Zolotarev, Institute of Thermomechanics of the Czech Academy of Sciences, 2023, pp. 119–122.

[7] Newmark, N. M., A method of computation for structural dynamics, Journal of the Engineering Mechanics Division 85 (3) (1959) 67-94.

[8] Nitsche, J., About a variation principle for solving the Dirichlet problem when using subspaces that are not subject to boundary conditions, Abhandlungen aus dem Mathematischen Seminar der Universität Hamburg 36 (1) (1971) 9-15. (in German)

[9] Rohan, E., Cimrman, R., Sensitivity analysis and material identification for activated smooth muscle, Computer Assisted Mechanics and Engineering Sciences Vol. 9, No. 4 (2002) 519–541.

[10] Virtanen, P., Gommers, R., Oliphant, T. E., Haberland, M., Reddy, T., Cournapeau, D., Burovski, E., Peterson, P., Weckesser, W., Bright, J., van der Walt, S. J., Brett, M., Wilson, J., Millman, K. J., Mayorov, N., Nelson, A. R. J., Jones, E., Kern, R., Larson, E., Carey, C. J., Polat, I., Feng, Y., Moore, E. W., VanderPlas, J., Laxalde, D., Perktold, J., Cimrman, R., Henriksen, I., Quintero, E. A., Harris, C. R., Archibald, A. M., Ribeiro, A. H., Pedregosa, F., van Mulbregt, P., SciPy 1.0: fundamental algorithms for scientific computing in Python, Nature Methods 17 (33) (2020) 261-272.

Optimizing car tailgate design through truss topology optimization

P. David[a], T. Mareš[a]

[a]Department of Mechanics, Biomechanics and Mechatronics, Faculty of Mechanical Engineering, Czech Technical University in Prague, Technická 4, 160 00 Prague, Czech Republic

1. Introduction

This study addresses the role of truss topology optimization in improving car tailgate designs within the automotive industry. Initially, the principles of truss topology optimization are briefly reviewed. The study then presents a completed analysis focusing on truss topology optimization to develop a more efficient tailgate structure. This includes defining the problem by outlining the solution domain, applied loads, and boundary conditions. Future work aims to integrate this optimized truss design with a parametric design approach that is adaptable to sheet metal forming processes. The paper concludes by discussing the preliminary results and their potential implications for enhancing tailgate reinforcements, as well as outlining the intended methodology for the next phase of the research.

Topology optimization (TO) stands as an invaluable tool for contemporary engineering, focusing on achieving the best or nearly optimal distribution of materials within a specified design area. Over recent decades, there's been a surge of interest in this domain, largely driven by the initiative to cut down the weight of structural elements, while at the same time improving their structural performance. Using TO can potentially lead to savings in terms of material, fuel, manufacturing and other related costs. Historically, TO has been synonymous with elaborate designs that are predominantly feasible through additive manufacturing (AM). While AM remains the most widely used manufacturing technique of results received by TO, it is possible to incorporate TO into the design process of components, which are to be manufactured by traditional approaches [1, 2].

In this research, our objective centres on optimizing the positioning of reinforcements within a car's tailgate. To do so, we employ truss topology optimization (TTO) to identify the candidate areas of potential need for reinforcement. An introductory overview of TTO is provided, followed by a methodology to tackle a specific problem formulation. Next, we shift to modelling and pre-processing, where we describe relevant parts of the modelling environment of our custom TTO software developed in Python, the design space, and we conclude this section with a simple optimization setup with preset boundary conditions, loads and other inputs. Finally, we wrap up this study with a discussion of our preliminary results and we draw up how we intend to use the results of the TTO for the design of the reinforcements.

2. Truss topology optimization

TTO is a relatively mature technology, with its origins in the early 20th century. It would take until late 1960's, however, when first problem formulations and algorithms started to emerge.

The most widely used approach to a TTO problem (and a TO problem for that matter), is the so-called "Ground structure approach", where the design space is discretized by a structure, within which one seeks the optimal substructure with respect to loads, boundary conditions, etc. [1, 2].

There are many different possible TTO problem formulations, each with its own strengths and weaknesses. In this study, we use the formulation of compliance minimization, constrained by maximum volume to construct the structure and by fulfilling the equilibrium equations. The design variables are the cross-sectional areas of the individual bars. In our case, compliance takes the form of the work of external forces, that is $\delta = \mathbf{f}^T \mathbf{u}$, where δ is the work of external forces, $\mathbf{f}$ is the external force vector and $\mathbf{u}$ is the displacement vector. For linear-elastic material, this cost function can be substituted by the complementary strain energy, which can be written for the truss case as $c = \sum_{e=1}^{n} \frac{N_e^2 L_e}{2EA_e}$. The inclusion of the maximum volume constraint yields

$$\arg \min_{\mathbf{A} \in \mathcal{A}} c(\hat{\mathbf{N}}) = \sum_{e=1}^{n} \frac{N_e^2 L_e}{2EA_e},$$
$$\mathcal{A} = \{\mathbf{A} | \sum_e A_e L_e \leq V\}, \tag{1}$$

where N_e is the inner force inside the bar e, similarly L_e denotes the bar's length, E is Young's modulus, A_e is the cross-sectional area, V is the pre-set volume, and finally $\mathcal{A}$ denotes the set from which design variables can be drawn. To fulfil the conditions of equilibrium, we use the principle of minima of the complementary energy. This, coupled with (1), gives the final formulation

$$\arg \min_{\mathbf{N} \in \mathcal{N}} \min_{\mathbf{A} \in \mathcal{A}} c(\mathbf{N}) = \sum_{e=1}^{n} \frac{N_e^2 L_e}{2EA_e},$$
$$\mathcal{A} = \{\mathbf{A} | \sum_e A_e L_e \leq V\}, \tag{2}$$
$$\mathcal{N} = \{\mathbf{N} | \mathbf{B}\mathbf{N} - \mathbf{P} = 0\},$$

where $\mathcal{N}$ denotes the set of all statically admissible solutions. The optimization problem as defined by equation 2 can be solved, e.g. by the Lagrange multipliers method. The Lagrangian takes the form of

$$\mathcal{L}(\mathbf{A}, \mathbf{N}, \lambda, \mu) = c(\mathbf{N}) + \lambda^T(\mathbf{B}\mathbf{N} - \mathbf{P}) + \mu(\mathbf{A}^T \mathbf{L} - V), \tag{3}$$

which after deriving with respect to the variables and setting as equal to zero, gives us the necessary conditions of optimality. From these, we can derive the following optimization loop:

1. Set $A^{\{0\}}$ as arbitrary positive vector.
2. Compute displacements as $\mathbf{u}^{\{k\}} = \mathbf{K}^{-1}(A^{\{k\}})\mathbf{f}$.
3. Using the displacements, compute inner forces $N^{\{k\}}$ and find cross-sectional areas for next iteration as $A_e^{\{k+1\}} = \frac{V N_e^{\{k\}}}{\sum_{p=1}^{M} N_p L_p}$ $(l = 1, 2, ..., L)$.
4. Repeat steps 2–3 until a specified convergence criterion is met [3].

3. Modelling and preliminary results

The described TTO algorithm was developed in a custom Python code, which is to be used for the optimized placement of stiffeners of the car's tailgate. The model of the tailgate, which also acts as the design space can be seen in Fig. 1 (left). A mesh was generated in Abaqus, where the
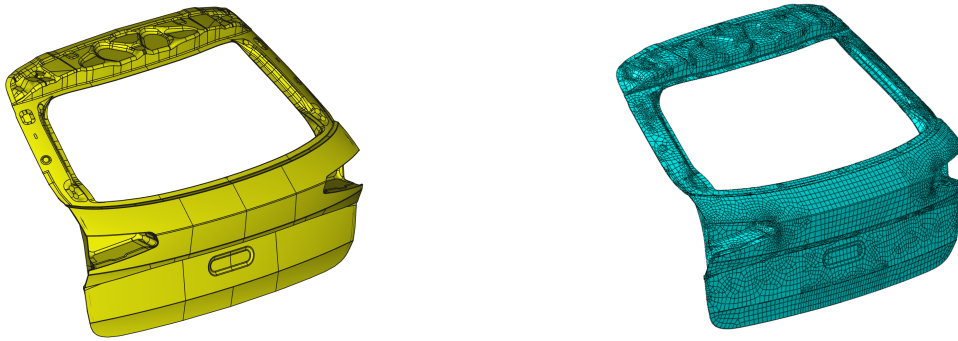
Fig. 1. The car's tailgate model (left); the mesh created by Abaqus (right)

nodes of the mesh were then exported and used as the nodes of the truss structure in the TTO model. The mesh is depicted in Fig. 1 (right).

The ground structure was instantiated by interconnecting all nodes in a small neighbourhood, which was set as 30 mm in this specific case. The approximate dimensions of the tailgate model are 1 300 mm in width and 800 mm in height. This procedure yields the ground structure as shown in Fig. 2 (left). On the right of the same figure is the depiction of the boundary condition of a simple test problem. The nodes that are red have all three degrees of freedom fixed and the green nodes have each a force of 100 N in the vertical direction acting on them. The initial cross-sectional area of all bars was set as $10\,\mathrm{mm}^2$, and the desired volume fraction was set as 10 %.

Fig. 2. The ground structure (left) and the boundary conditions (right). The clamped boundary conditions are the red nodes, the nodes with external forces are green

The first optimization result can be see in Fig. 3 (left). The sizes of few bars greatly skew the results and in turn the graphical representation, so the subsequent runs were performed with a maximum cross-sectional area constraint. The result with the maximum area constrained at $50\,\mathrm{mm}^2$ is shown in Fig. 3 (right).

Both of the runs took approximately one hour to complete, which is mainly driven by the suboptimal ground structure. It can be expected that with a better mesh and interconnectivity of the ground structure, fewer bars could be used to represent the problem without a significant loss of accuracy, thus leading to significant performance boost. In terms of programming, we were also forced to use sparse matrix representation of the stiffness matrix, further reducing the speed of the optimization.
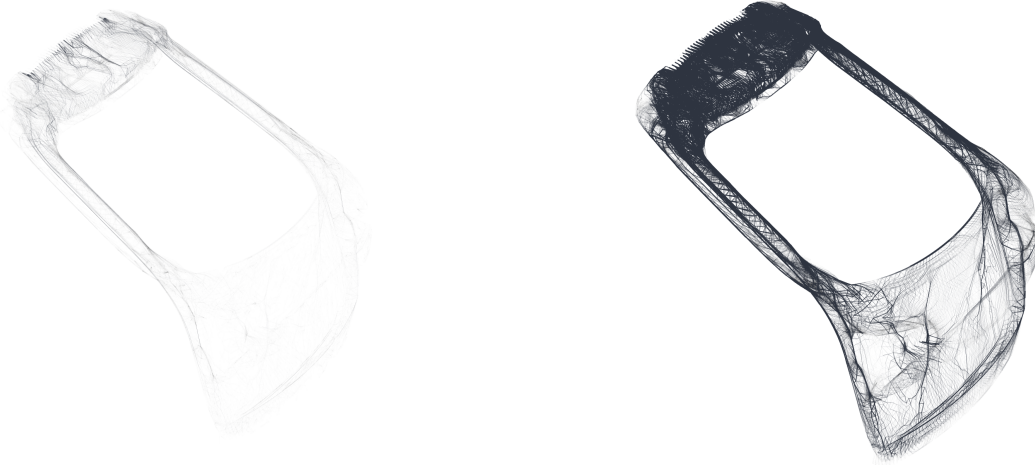
Fig. 3. The result with unconstrained maximum area (left) and the same run with maximum area constrained at $50\,\text{mm}^2$ (right)

4. Discussion and further development

In this work, we have briefly described the concept of topology optimization with the focus on trusses in particular. Next, we have shown one possible optimization formulation of compliance minimization with a volume constraint. Then, we have derived an optimization loop, solving the presented optimization formulation, leveraging the Lagrange's multiplier technique. After that, we moved onto presenting the particular problem we were to solve, consisting of optimized stiffener placement in a car's tailgate. We used our custom program, which deploys the presented optimization loop, to solve a simple static test problem.

The preliminary results of our optimization runs show great potential in terms of identification of optimized stiffener placement in a car's tailgate. Next step is the interpretation of the TTO results. Our idea is to map the TTO results on the boundary surfaces of the design space. Then, design stiffeners for the spots where bar concentration is higher than a given threshold. The stiffeners would then be fine-tuned in a parametric FEM model. All of this is subject to future work.

Acknowledgements

References

[1] Bendsøe, M. P., Sigmund, O., Topology optimization: Theory, methods, and applications, Springer Science & Business Media, 2003.
[2] Christensen, P. W., Klarbring, K., An introduction to structural optimization, Springer Science & Business Media, 2008.
[3] Mareš, T., Fundamentals of structural optimization, Knižnice konstrukční optimalizace – Svazek II., Praha, 2006. (in Czech)

Blowing through connection edges of a Y-shaped inlet channel for flow distortion reduction

D. Demovič[a], F. Brož[a]

[a]*Department of Aerospace Engineering, Faculty of Mechanical Engineering, Czech Technical University in Prague, Karlovo náměstí 13, 121 35 Praha, Czech Republic*

1. Motivation

In jet or ducted-fan powered single or two-seat aircraft, a Y-shaped inlet channel is a common design that often results from the dimensional constraints. The challenge of the Y-shaped design is the double curvature of the inlet channel, which is prone to unfavourable pressure gradients. If not managed, this inlet design brings risk of high total pressure loss as well as flow field non-uniformity (often quantified in terms of flow distortion) entering the fan. With particular focus on a ducted-fan propulsion unit, flow distortion at the engine face plane is detrimental to propulsor efficiency, stability and durability. In terms of the dynamic impact on the rotor, the effect of flow distortion can be compared to the effect of unsteadiness [1]. Therefore, methods to reduce this distortion are sought.

Key mechanisms that adversely affect the inlet channel characteristics are flow separation and secondary flow structures. These mechanisms are enhanced by the presence of unfavourable pressure gradient. Both passive and active flow control techniques in front of regions with high adverse pressure gradient have previously been subject of research interest to mitigate the resulting undesirable flow distortion [2–4]. However, common passive methods (vortex generators, grids etc.) result in additional form drag and active methods introduce extra complexity due to necessary actuators.

In this study, we focus on an alternative method to reduce flow distortion, which uses the ducted-fan design to its advantage. Blowing directly through slots in the connection edges of the two halves of the inlet channel is proposed. Use of naturally present pressure differential between the engine bay and the channel interior is suggested and investigated.

2. Principle and implementation of a rectangular blowing slot

For the case study on ducted-fan propulsion, the UL-39 aircraft, developed at the Department of Aerospace Engineering at CTU Prague, was chosen for availability of previous experimental and CFD data. There is an engine bay between the two intake limbs. The inflow of air to this engine bay goes under the boundary layer splitter of the main intake. Analysis suggests that there will be a pressure differential between the engine bay and the area just downstream of the limbs connection edge. This pressure differential can drive a flow through a cut-out slot that would replace the sharp connection edge (see Fig. 1 (left), with 1 representing the engine bay and 2 the blowing flow direction). It is deemed that the resulting jet of air can inject momentum in the azimuth range close to the channel plane of symmetry where it is otherwise at its lowest due to the inlet channel aerodynamics. A possible implementation of a rectangular blowing slot is shown in a 3D-model on the right part of Fig. 1.
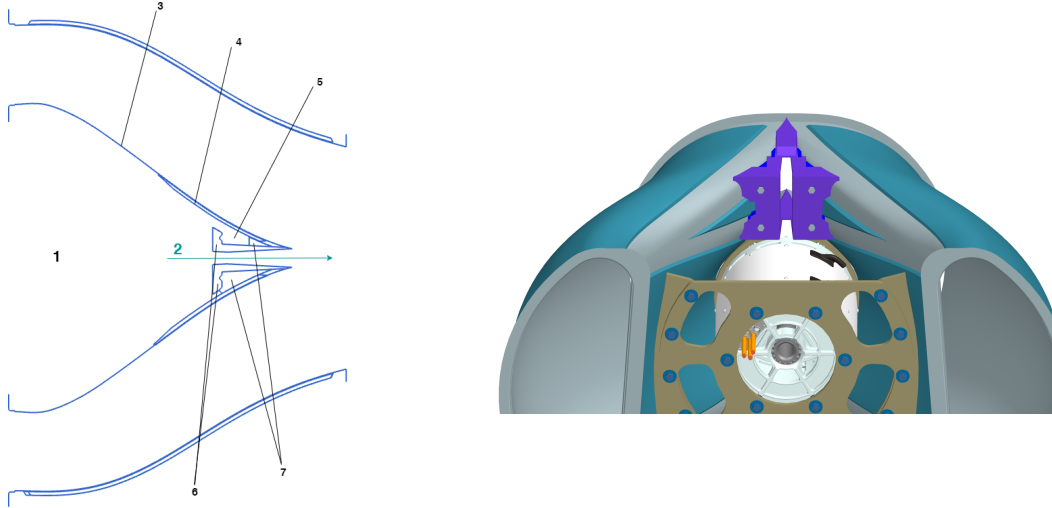
Fig. 1. Visualisation of the connection edge blowing slot by a 2D-cut (left) and a 3D model (right)

3. Analytical justification of proposed blowing based on CFD and experimental results

CFD analysis was carried out during the process of multi-criterial optimisation of the inlet channel shape. CFD calculations of the inlet channel were performed for rotor RPM of 8 000 and forward airspeeds in the range from 25 m/s to 75 m/s, with steps of 5 m/s. The calculation in ANSYS Fluent was carried out in two stages. The complete (simplified) aircraft was analysed to determine realistic flow conditions at the channel inlet plane with external and internal aerodynamics combined. At the other end of the inlet channel, detailed CFD analysis of the fan stage flow was performed. These combined for the first stage. Then in the second stage, the results of stage 1 were used as boundary conditions for a more detailed inlet channel calculation. A RANS solver with ideal-gas properties was used with a k–ω SST turbulence model. Symmetry boundary condition was used at the inlet channel symmetry plane.

We can use a simplified method to obtain the necessary slot thickness in order to supply the flow with momentum of the same order as the momentum deficit. The momentum deficit is obtained from CFD results in the annular area in the plane of pre-stator probes (96 mm downstream of connection edge). In front of the connection edge is the engine bay, with air entering under the boundary-layer splitter. The external flow will be decelerated to practically zero velocity in the engine bay. The pressure inside is thus expected to be between stagnation and static pressure of the flow at the front edge of the splitter. The exact value depends on the associated dynamic head loss of the engine bay entry. The Reynolds number at the front edge of the splitter is about Re $= 11 \times 10^6$ for the chosen reference airspeed of 60 m/s, so the boundary layer at this location is likely fully turbulent. From Cengel and Cimbala [5], we can extract a formula for momentum thickness of the boundary layer for a flat plate, and use it as an estimation for the momentum thickness at the inlet plane

$$\frac{\theta}{x} = \frac{0.016}{\mathrm{Re}_x^{1/7}}. \tag{1}$$

The distance of the inlet plane from the nose cone of the fuselage is 2.73 m, so we can calculate the approximate momentum thickness for forward velocity of 60 m/s. This turns out to be about 4.3 mm. With the average gap between the fuselage and the splitter being approximately 50 mm, the momentum thickness is less than 10 % of the gap, as shown in Table 1. The conclusion from this simple analysis is that air entering the engine bay will have an average initial velocity that will not be far away from the free-stream velocity. Therefore, we can introduce a loss

Table 1. Boundary layer momentum thickness vs. splitter gap size

$g\,[\text{mm}]$	$x\,[\text{m}]$	$v\,[\text{m/s}]$	$\text{Re}_x\,[-]$	$\theta\,[\text{mm}]$	$\theta/g\,[-]$
50	2.73	60	11×10^6	4.30	0.086

factor, which determines what fraction of the free-stream dynamic pressure is lost on entry to the engine bay. We define this as

$$LF = \frac{P_t - P_{t,EB}}{P_t - P_s}, \tag{2}$$

where P_t and P_s are the total and static pressure at front edge of the splitter (taken from experimental measurements), while $P_{t,EB}$ being the total (same as static assuming zero velocity in engine bay) pressure in the engine bay. We can turn this formula around and express the engine bay pressure in terms of the unknown loss factor

$$P_{t,EB} = P_t - LF \cdot (P_t - P_s). \tag{3}$$

The velocity of the blowing jet can then be estimated with use of experimentally measured static pressure behind the slot $P_{s,BS}$, treating the flow as incompressible and having the slot pressure loss incorporated already in the loss factor above

$$v_{sl} = \sqrt{\frac{2(P_{t,EB} - P_{s,BS})}{\varrho}}. \tag{4}$$

The momentum flux inserted into the flow by blowing (through one slot) can be then calculated as

$$\dot{p}_{in} = \varrho \cdot l \cdot t \cdot v_{sl}^2. \tag{5}$$

The momentum deficit to be supplied can be estimated from the mass flow through the annular area $\dot{m}$ and standard deviation of velocity based on mass flow average v_{SD}

$$\dot{p}_{def} = \dot{m} \cdot v_{SD}. \tag{6}$$

This momentum deficit, although calculated across the half annular area (one slot needs to compensate for half of the annular area because there will be two of them), is localised mainly in sectors close to the plane of symmetry, i.e., behind the connection edges. This can be seen from velocity contours in Ansys CFD Post in Fig. 2. Finally, equating $\dot{p}_{in}$ and $\dot{p}_{def}$ to each other, we get the expression for an estimate of the necessary slot thickness to provide the desired linear momentum flux by natural blowing to compensate for the deficit given by the inlet geometry

$$t = \frac{\dot{m} \cdot v_{SD}}{\varrho \cdot l \cdot v_{sl}^2}. \tag{7}$$

We can tabulate the necessary thickness calculated and the slot jet velocity against the loss factor. The results form Table 2.

The mass flow average velocity in the annular plane behind the slot is 63.9 m/s, so for the whole span of loss factors from 0 to 1, the predicted jet velocity will be higher. The actual maximum allowable slot thickness is 40 mm due to space constraints of the engine bay. It appears promising that the maximum thickness is the same order of magnitude as the necessary thickness calculated with this approach for the entire span of engine bay loss factors and thus blowing has a potential to effectively reduce flow distortion.
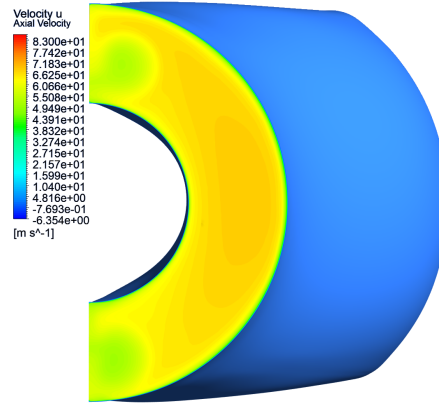
Fig. 2. Axial velocity contours in plane of pre-stator probes

Table 2. Dependence of slot velocity and necessary thickness on loss factor

$LF\,[-]$	$v_{sl}\,[\text{m/s}]$	$t\,[\text{mm}]$
0	89.5	35.2
0.2	85.4	38.7
0.4	81.1	43.0
0.6	76.5	48.3
0.8	71.6	55.0
1.0	66.4	64.0

4. Conclusions

The analytic study suggests that the jet velocity achieved by blowing through a rectangular slot in the connection edge of a Y-shaped inlet duct, using purely pressure differential between the engine bay and the channel, will be high enough to compensate for the otherwise lower velocity close to the plane of symmetry. Furthermore, the order of momentum supplied by this blowing has the same order of magnitude as the momentum deficit in the annular area behind the limbs connection. Therefore, using such blowing could effectively reduce flow distortion at the propulsor aerodynamic inlet plane. Further CFD work is currently being performed and concentrates on the loss factor influence.

References

[1] Davis, W. F., Scherrer, R., Aerodynamic principles for the design of jet-engine induction systems, Report NACA-RM-A55F16, NASA Ames Research Center Moffett Field, 1956.
[2] Paul, A. R., Joshi, S., Jindal, A., Maurya, S. P., Jain, A., Experimental studies of active and passive flow control techniques applied in a twin air-intake, The Scientific World Journal 2013 (2013) No. 523759.
[3] Paul, A., Pritanshu, R., Ranjanupadhyay, R., Jain, A., Passive flow control in twin air-intakes, Proceedings of the WASET International Conference on Mathematical and Computational Methods in Science and Engineering, Paris, France, 2011.
[4] Yadav, K., Paul, A., Hegde, N., Jain, A., A comparison of circular and slotted synthetic jets for flow control in a twin air intake, Defence Science Journal 70 (2) (2020) 113-121.
[5] Cengel, Y. A., Cimbala, J. M., Fluid mechanics: Fundamentals and applications, 3rd edition, McGraw-Hill, New York, USA, 2014.

Uncertainties in gear mesh excitation of electric drives

K. Dráždil[a,c], J. Otta[b]

[a]ZF Engineering Plzeň s.r.o., Univerzitní HQ Plant, Univerzitní 1159/53, 301 00 Plzeň, Czech Republic
[b]ZF Friedrichshafen AG, 88038 Friedrichshafen, Germany
[c]Department of Mechanics, Faculty of Applied Sciences, University of West Bohemia, Univerzitní 8, 301 00 Plzeň, Czech Republic

1. Introduction

Nowadays, virtual validation enhances development by digitally testing products, reducing physical prototypes, and accelerating time-to-market, while also considering uncertainties from manufacturing and assembling, which are essential for ensuring real-world reliability and performance.

This paper investigates the impact of uncertainties on flank line deviations in gears and their influence on the vibroacoustic system response used in an electric drive simulation. The overall system's response is based on multi-stage toolchain including non-linear quasi-static finite element (FE) analysis, gear mesh simulation, and linear dynamic FE analysis in the frequency domain, as depicted in Fig. 1.
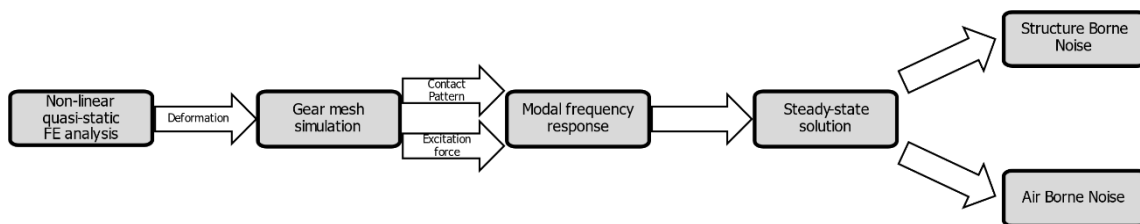
Fig. 1. Simulation toolchain

This representation is better for parametric studies and offers a significant speed advantage over the traditional time-domain representation in Multi-Body System.

2. Simulation toolchain

The current approach relies on comprehensive FE models of the electric drive system containing components like housings, electric motor, drive shafts, gears, bearings, and other relevant internal parts, as depicted in Fig. 2. This modelling enables a precise representation of mass and stiffness distribution, along with the dynamic interactions between the electric motor and the transmission.

2.1 Non-linear quasi-static finite element (FE) analysis
The nonlinear quasi-static problem described by

$$\mathbf{K}(\mathbf{x}, \mathbf{p})\mathbf{x} = \mathbf{f}(\mathbf{p}), \tag{1}$$

where the stiffness matrix $\mathbf{K}(\mathbf{x}, \mathbf{p})$ is dependent on the response vector $\mathbf{x}$ and on the vector of parameters $\mathbf{p}$ as well as the excitation force vector $\mathbf{f}(\mathbf{p})$, can be solved by any of commercial solvers. The vector of parameters $\mathbf{p}$ expressing uncertainties can be decomposed into structural parameters $\mathbf{p}_S$ resulting from design factors such as assembling tolerances and imperfections,

as well as excitation parameters $\mathbf{p}_E(\mathbf{p}_S)$ arising from gear mesh interactions (interdependence of excitation and structure), i.e. $\mathbf{p} = [\mathbf{p}_S \quad \mathbf{p}_E(\mathbf{p}_S)]$.

The flank line deviations $\mathbf{x}_{FLD}$ resulting from the deformation of the internal components under the loading conditions are visually depicted in Fig. 3. These deviations can be formulated as a function of the local deflections of gears $\mathbf{x}_{r1}, \mathbf{x}_{r2}$, which contribute to the deformation within the gear mesh

$$\mathbf{x}_{FLD}(\mathbf{p}_S) = \mathbf{x}_{FLD}(\mathbf{x}_{r1}(\mathbf{p}_S), \mathbf{x}_{r2}(\mathbf{p}_S)). \tag{2}$$
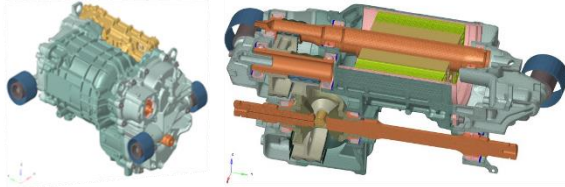
Fig. 2. (a) FE model of electric drive
(b) Section cut of the FE model
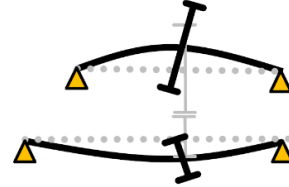
Fig. 3. Gear misalignment

2.2 Gear mesh simulation

Having laid the foundation for analysing the local deformations of the gears in the earlier section, the assessment of the gear mesh follows to derive the gear mesh forces essential for subsequent vibroacoustic simulations.

Gear mesh excitation forces are dependent on local deflections of gears causing gear mesh errors contributing to the continuous periodic transmission error (TE), as illustrated in Fig. 4.

Fig. 4. (a) Example of periodic gear mesh excitation (b) Fourier coefficients

Subsequently, the continuous periodic gear mesh force $\mathbf{f}_G(\mathbf{p}, t)$ can be approximated by partial sum of its expansion into a Fourier series, with each term corresponding to the excitation orders originating from the gear mesh [2] as

$$\mathbf{f}_G(\mathbf{p}, t) \cong \sum_{k=1}^{N} c_{zk}(\mathbf{p}, t)\big[x_M + x_{fk}(\mathbf{p}, t)\big] \cong \sum_{k=0}^{N} F_k^G(\mathbf{p}) \cos(k\omega t), \tag{3}$$

where $c_{zk}(t)$ denotes the time-dependent gear mesh stiffness, x_M stands for the mean value of TE, $x_{fk}(t)$ represents quasi-static TE, F_k^G denotes complex Fourier coefficients dependent on $\mathbf{p}$ and $\omega = 2\pi/T$ stands for basic angular frequency. Damping effects are neglected.

Gear body deflections result in imperfect gear engagement, requiring quasi-static tooth contact analysis based on the contact theory, [3]. To save a computational demand, this simulation focuses exclusively on the gear mesh, accounting for variations in the gear mesh and input torque.

The analysis is essential for evaluating both, the distribution of contact pressure and the gear mesh excitation forces, which are important for subsequent simulations. Fig. 5 shows an

example of how the load is distributed on the tooth flank, including the load path for a specific set of parameters referred to as **p.**
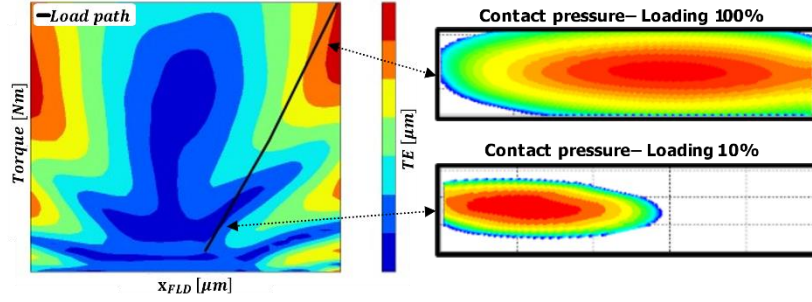
Fig. 5. (a) Example of F_1^G in dependency on the gear body deflections and input torque (b) Contact pressure on gear flank for 10 % and 100 % of loading for 1 given parameter set **p**

2.3 Linear dynamic FE analysis in the frequency domain
The complexity of the vibroacoustic model is comparable to models from Section 2.1. Its mathematical model can be represented by the equation of motion in matrix form

$$\mathbf{M}\ddot{\mathbf{x}}(t) + \mathbf{B}\dot{\mathbf{x}}(t) + \mathbf{K}\mathbf{x}(t) = \mathbf{f}_G(\mathbf{p}, t), \tag{4}$$

where $\mathbf{M}, \mathbf{B}, \mathbf{K}$ are constant linearized mass-, damping- and stiffness matrices and $\mathbf{f}_G(\mathbf{p}, t)$ represents the excitation force from (3). The model linearization is based on contact linearization of non-linear model based on contact-pressure method, [4], followed by the linearization of bearings, which involves determining bearing stiffness according to the ISO 16281 standard.

Due to linearity of the system, equation (4) can be solved exclusively for unit force excitation $\mathbf{1}_F$, which depends on the contact pattern results obtained from Chapter 2.2. Hence, the transfer function $\mathbf{g}(\mathbf{p}, \omega)$ can be expressed as follows

$$\mathbf{g}(\mathbf{p}, \omega) = \sum_{k=1}^{M} \frac{\boldsymbol{\phi}_k \boldsymbol{\phi}_k^{\mathbf{T}}}{\Omega_k^2 - \omega^2 + 2iD_k\Omega_k\omega} \mathbf{1}_F, \tag{5}$$

where Ω_k stands for k-th eigenfrequency, D_k represents k-th modal damping and $\boldsymbol{\phi}_k$ is k-th eigenvector. Real system response to harmonic excitation $\mathbf{f}(t)$ from equation (3) can be then reconstructed as a weighted sum of transfer function $\mathbf{g}(\mathbf{p}, \omega)$

$$\mathbf{x}(\mathbf{p}, t) = \sum_{k=1}^{N} F_k^G(\mathbf{p})\mathbf{g}(\mathbf{p}, \omega) \cos(\omega t - \psi_k), \tag{6}$$

where ψ_k is phase offset for k-th order of gear mesh excitation.

3. Application

The comprehensive FE model of the electric drive system, as described in Chapter 2, comprises approx. 35 million degrees of freedom (DOFs), including 115 000 contact DOFs. The nonlinear quasi-static analysis of this model requires an average computation time of 2.5 hours.

Uncertainties arising from assembly and manufacturing process as bearing clearances, fitting clearances between components, bearing seat positions, axial pretension of bearings are covered in parameter vector **p** with 42 parameters.

In order to cover this extensive high-dimensional parameter space, the Modified Extensible Lattice Sequence method, [1], was employed, generating a total of 1300 samples that can be executed on an HPC cluster within one weekend.

An example of simulation results is presented in Fig. 6 and 7. Fig. 6a illustrates the dependency of tooth flank deviation on the deflection of the gears, as shown in (2). Fig. 7a displays the distribution of load path along with excitation orders and Fig. 7b represents the NVH system response, as elaborated in (6).

Pareto diagram is employed to identify critical factors shaping flank line deviations x_{FLD}, as depicted in Fig. 6b. For this specific configuration, the dominant factors are bearing clearances near the gears along with the spline tolerance on the rotor shafts. In contrast, parameters such as bearing seat positions or axial pretension of bearings have minimal impact on the quality of flank line deviations x_{FLD}.

As observed, the parameter associated with Bearing L5 exhibits a positive correlation, whereas Bearing L2 demonstrates a negative correlation. From this, it can be inferred that the values for the Bearing L5 parameter should be increased, while the values for Bearing L2 should be decreased.
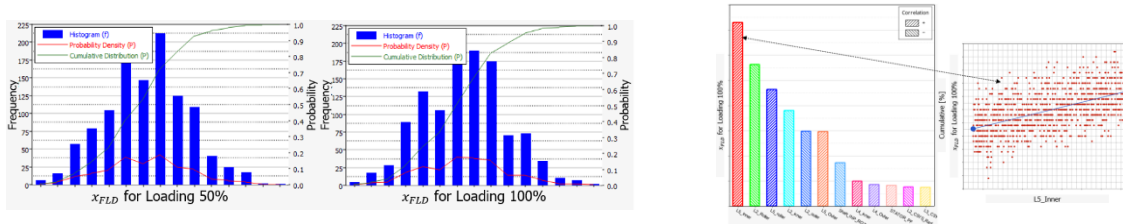
Fig. 6. (a) Histograms of flank line deviations x_{FLD} for different load levels (b) Pareto diagram of flank line deviations x_{FLD} for loading 100 % along with scatter plot of parameter L5_inner with a positive linear trend

Fig. 7. (a) Load path distribution together with probability distribution of the gear tilting (b) An example illustrating the propagation of system response-induced structure-borne noise, assessed within coupling positions to the car frame, arising from variations in gear mesh excitation

Acknowledgements

References

[1] Altair HyperStudy, https://2021.help.altair.com/2021/hwdesktop/hst/topics/design_exploration/methods_doe_r-1.htm.
[2] Börner, J., Noise excitation caused by gears, ZF internal material, 2017.
[3] Fuentes, A., Litvin, F. L., Gear geometry and applied theory, Cambridge University Press, Cambridge, 2004.
[4] PERMAS, User's Reference Manual 450 v19, INTES Publication, Stuttgart, 2022.

Time periodic solution of linear vibrating systems with time dependent stiffness using periodic collocation

J. Dupal[a]

[a]Department of Mechanics, Faculty of Applied Sciences, University of West Bohemia, Univerzitní 8, 301 00 Plzeň, Czech Republic

This paper deals with approach to solution of periodic response of systems having periodic time dependent stiffness. The methodology is prepared for systems with $n < \infty$ degrees of freedom (DOF) but we restrict to 1 DOF systems in this presentation. Let suppose that presented system can be described by equation

$$m\ddot{q}(t) + b\dot{q}(t) + \left[k_0 - \mu\tilde{k}(t)\right]q(t) = f(t), \quad q(t) = q(t+T), \quad \tilde{k}(t) = \tilde{k}(t+T), \quad f(t) = f(t+T), \tag{1}$$

where all symbols are well known and used and it is not necessary to explain them. As the first stage of investigation let us build periodic Green function (PGF), which is a response of the system without time dependent stiffness $\tilde{k}(t)$ to Dirac train of impulses with period T. This PGF has form

$$H_T(t) = \frac{1}{T} \sum_{k=-N}^{N} L_k e_k(t), \quad T = \frac{2\pi}{\omega}, \quad e_k(t) = e^{ik\omega t}, \quad L_k = \left(-k^2\omega^2 m + ik\omega b + k_0\right)^{-1}. \tag{2}$$

Solution can be written in form

$$q(t) = \mu\int_0^T H_T(t-s)\tilde{k}(s)q(s)ds + \int_0^T H_T(t-s)f(s)ds, \tag{3}$$

where

$$H_T(t) = \frac{1}{T} \sum_{k=-N}^{N} L_k e_k(t-s) = \frac{1}{T} \sum_{k=-N}^{N} L_k e^{ik\omega t} e^{-ik\omega s} = \frac{1}{T} \sum_{k=-N}^{N} L_k e_k(t) e_{-k}(s). \tag{4}$$

The time periodic dependent stiffness can be expressed by relations over whole time scale or over only one period respectively can write [1]

$$\tilde{k}(t) = \sum_{l=1}^{m} \sum_{j=-N}^{N} k_l \delta(t - t_l - jT), \quad \sum_{l=1}^{m} k_l \delta(t - t_l), \tag{5}$$

where m is number of time steps over one period and N is number of upper respected harmonic contribution. After substitution relations (4) and (5) into (3) and after some rearrangements and respecting relation

$$\int_{-\infty}^{\infty} g(t)\delta(t - t_0)dt = g(t_0),$$

we can rewrite the relation (3) in compact form

$$\mathbf{q}(t) = \frac{\mu}{T}\,\mathbf{E}^T(t)\mathbf{L}\hat{\mathbf{I}}\mathbf{E}(t)\mathbf{K}\mathbf{q}(t) + \mathbf{E}(t)\mathbf{L}\mathbf{f}, \tag{6}$$

The second term was in detail subscribed in [2]. The remaining symbols present a form

$$\mathbf{e}(t) = \left[e_{-N}(t), e_{-N+1}(t), ..., e_N(t) \right]^T, \quad \mathbf{f} = \left[f_{-N}, f_{-N+1}, ..., f_N \right]^T, \tag{7}$$

$$\mathbf{E}^T(t) = \begin{bmatrix} e_{-N}(t_1), & e_{-N+1}(t_1), & ..., & e_N(t_1) \\ e_{-N}(t_2), & e_{-N+1}(t_2), & ..., & e_N(t_2) \\ \vdots & \vdots & \ddots & \vdots \\ e_{-N}(t_m), & e_{-N+1}(t_m), & ..., & e_N(t_m) \end{bmatrix} = \begin{bmatrix} \mathbf{e}^T(t_1) \\ \mathbf{e}^T(t_2) \\ \vdots \\ \mathbf{e}^T(t_m) \end{bmatrix} \in \mathbf{C}^{m,2N+1}, \tag{8}$$

$$\mathbf{L} = \begin{bmatrix} L_{-N} & & & \\ & L_{-N+1} & & \\ & & \ddots & \\ & & & L_N \end{bmatrix} \in \mathbf{C}^{2N+1,2N+1}, \quad \hat{\mathbf{I}} = \begin{bmatrix} & & & 1 \\ & & 1 & \\ & \cdot^{\cdot} & & \\ 1 & & & \end{bmatrix} \in \mathbf{R}^{2N+1,2N+1}, \tag{9}$$

$$\mathbf{q}(t) = \left[q(t_1), \quad q(t_2), \quad ..., \quad q(t_m) \right]^T \in \mathbf{R}^{m,1}, \tag{10}$$

$$\mathbf{K} = \Delta t \begin{bmatrix} k_1 & & & \\ & k_2 & & \\ & & \ddots & \\ & & & k_m \end{bmatrix} = \Delta t \begin{bmatrix} \tilde{k}(t_1) & & & \\ & \tilde{k}(t_2) & & \\ & & \ddots & \\ & & & \tilde{k}(t_m) \end{bmatrix} = \mathbf{R}^{m,m}. \tag{11}$$

The individual terms of the vector correspond to Fourier coefficients whose can be expressed in form

$$f_k = \frac{1}{T} \int_0^T f(s) e_{-k}(s) ds, \quad k = -N, -N+1, ..., N.$$

The final expression of the response follows from (6) and has form

$$\mathbf{q}(t) = \left[\mathbf{I} - \frac{\mu}{T} \mathbf{E}^T(t) \mathbf{L} \hat{\mathbf{I}} \mathbf{E}(t) \mathbf{K} \right] \mathbf{E}^T(t) \mathbf{L} \mathbf{f}, \tag{12}$$

where $\mathbf{I} \in \mathbf{R}^{2N+1,2N+1}$ is identity matrix. The properties of the matrix in brackets are significant for stability assessment [3] and existence of total solution of (1). The details of stability assessment and existence of solution will be explained during the presentation.

Acknowledgement

Refrences

[1] Babitsky, V. I., Krupenin, V. L., Vibration of strongly nonlinear discontinuous systems, Springer, Berlin, 2001.
[2] Dupal, J., Zajíček, M., Analytical periodic solution and stability assessment of 1 DOF parametric systems with time varying stiffness. Applied Mathematics and Computation 243 (2014) 138-151.
[3] Dupal, J., Zajíček, M., Existence of analytical solution, stability assessment and periodic response of vibrating systems with time varying parameters, Applied and Computational Mechanics 14 (2) (2020) 123–144.

Analysis of autoparametric double pendulum

Š. Dyk[a], J. Rendl[a], L. Smolík[a], R. Bulín[a]

[a]*NTIS – New Technologies for the Information Society, Faculty of Applied Sciences, University of West Bohemia,
Univerzitní 8, 301 00 Plzeň, Czech Republic*

Rott's pendulum [3] is a special case of a double pendulum that possibly exhibits autoparametric resonances. As shown in Fig. 1, the basic lumped-mass model consists of two subsystems – the left one is mass m located at the end of the massless angled arm that is pivoted in P_1 and the right one is a simple mathematical pendulum with mass m attached to the left arm in pivot P_2. If pivots P_1 and P_2 are aligned horizontally in the rest position, it yields strong quadratic coupling between both pendula. If, moreover, the eigenfrequencies of both pendula are tuned in the particular integer ratio, most often 1:2, internal resonance with a slow energy exchange between both subsystems occurs.
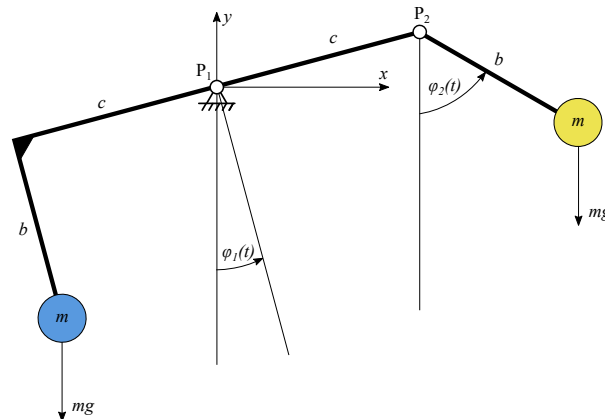
Fig. 1. Scheme of the lumped-mass Rott's pendulum

Denoting the angular position of both pendula φ_1, φ_2 and geometric parameters b, c as depicted in Fig. 1, the system in the nondimensional form can be formulated in the following form:

$$\begin{bmatrix} 1 + 2\alpha^2 & -\alpha \sin(\varphi_1 - \varphi_2) \\ -\alpha \sin(\varphi_1 - \varphi_2) & 1 \end{bmatrix} \begin{bmatrix} \ddot{\varphi}_1 \\ \ddot{\varphi}_2 \end{bmatrix} + \begin{bmatrix} \sin \varphi_1 \\ \sin \varphi_2 \end{bmatrix} + \begin{bmatrix} \alpha \cos (\varphi_1 - \varphi_2)\dot{\varphi}_2^2 \\ -\alpha \cos (\varphi_1 - \varphi_2)\dot{\varphi}_1^2 \end{bmatrix} = \mathbf{0},$$

(1)

where the geometric tuning parameter $\alpha = c/b$ and temporal derivatives are expressed with respect to nondimensional time $\tau = \Omega t$ for $\Omega = \sqrt{\frac{g}{b}}$. Initial states are given by nonzero initial positions of both pendula [2].

For the analysis, the energy-based method introduced in [4, 5] was used. This method divides the total energy of the system to term corresponding to the energy of the simple (here pendular) motions of subsystems, and a coupling energy. In the studied case, we formulated following expression for total energy (Hamiltonian)

$$E = E_1 + E_2 + E_C,$$

(2)

where E_i are energies of both pendula $i = 1, 2$ (including both kinetic and potential energy of the pendula) and a coupling energy E_C. It is shown that the states with slow energy exchange are characterised by a minimum coupling energy. This is used for in-depth analysis of such a Hamiltonian system: a set of internal resonances $1 : \kappa$, $\kappa = 2, 3, 4, 5$ is revealed with respect to initial energy E, see Fig. 2.
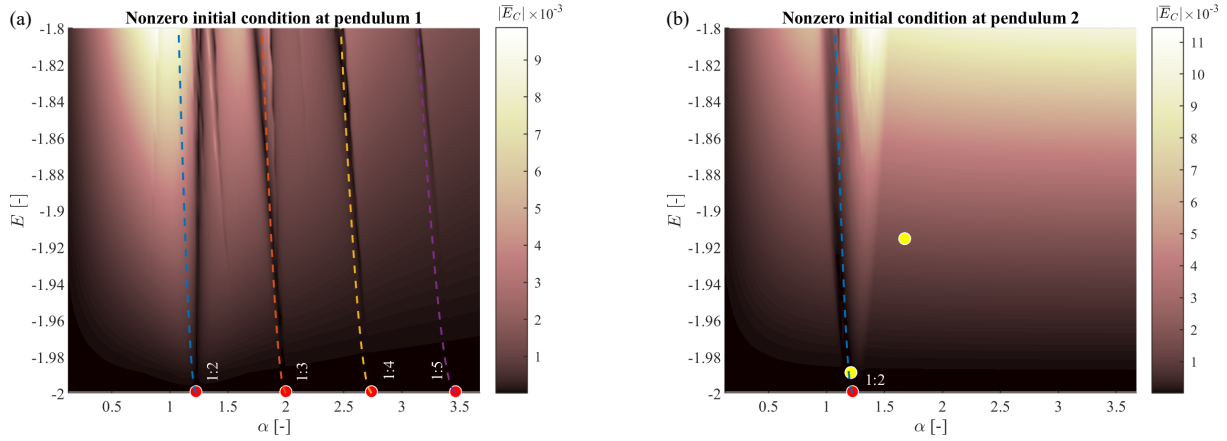
Fig. 2. Temporal averages of the coupling energy $\overline{E}_C = \overline{E}_C(\alpha, E)$ as a function of the geometric tuning parameter α and initial energy E. Dashed lines correspond to analytically obtained internal resonances $1 : \kappa$, $\kappa = 2, 3, 4, 5$

Moreover, we have shown how the coupling energy behaves for higher energy levels characterised by the chaotic and spinning motion of subsystems. To reveal chaotic regimes, fast Lyapunov indicators (FLI) are used as suggested in [1].

The energy-based method appears to be a robust method for the analysis of autoparametric systems. The great advantage is its applicability for all the motion regimes (regular periodic, quasiperiodic, chaotic motion) and is not limited to small amplitudes or a usage of the lower-order approximations of motion equations.

Acknowledgement

References

[1] Anurag, Chakraborty, S., Locating order-chaos-order transition in elastic pendulum, Nonlinear Dynamics 110 (1) (2022) 37-53.

[2] Kovacic, I., Zukovic, M. Radomirovic, D., Normal modes of a double pendulum at low energy levels, Nonlinear Dynamics 99 (2020) 1893-1908.

[3] Rott, N., A multiple pendulum for the demonstration of non-linear coupling, Zeitschrift für angewandte Mathematik und Physik ZAMP 21 (1970) 570-582.

[4] de Sousa, M. C., Marcus, F., Caldas, I. L., Viana, R. L., Energy distribution in intrinsically coupled systems: The spring pendulum paradigm, Physica A: Statistical Mechanics and its Applications 509 (2018) 1110-1119.

[5] de Sousa M. C., Schelin, A., Marcus, F., Viana, R. L., Caldas, I. L., Internal energy exchanges and chaotic dynamics in an intrinsically coupled system, Physics Letters A 453 (2022) No. 128481.

Compressional behaviour of plain woven fabric

J. Ezenwankwo[a], I. Petríková[a], J. Žák[a]

[a]*Department of Applied Mechanics, Technical University of Liberec, Studentská 1402/2 461 17 Liberec 1, Liberec, Czech Republic*

1. Introduction

Many times in operation, woven fabrics and textile materials, in general, often undergo both transverse and longitudinal compression. How filaments interact with one another during abrasive compression for multifilament yarns can significantly affect their response to those types of loads. Several research articles have performed experimental works on the compressive behaviour of monofilament and multifilament woven fabric [1, 2, 4]. On the other hand, many authors have used empirical and finite element method (FEM) in modelling the behaviour of fabrics in compression [3]. Primarily, the FEM of a unit cell (UC) is investigated in compression; the UC was assumed to be symmetric in both the warp and weft direction. The result of the work was compared with three analytical models. Early empirical works have developed models showing the relationship between applied initial and final compressive force, p_0 and p, respectively, and the fabric's initial and new thicknesses, T and T_0, respectively,

$$p = p_0 \, e^{-\frac{T-T_0}{b}}, \tag{1}$$

$$\log T = \log a - b \log p, \tag{2}$$

$$T = a + \left[\frac{b}{p+p_0}\right], \tag{3}$$

where p_0 is the initial compressive load, T_0 the initial thickness at p_0; and *a, b* are individual constants derived from experiments. All three equations show the relationship between applied load and thickness; the first equation employs an exponential function (Kawabata et al.), the second equation a logarithmic function (Young et al.) and the third equation, an inversely proportional function (Holmes et al.). However, in recent times, several works have been published on the compressional behaviour of woven fabrics using newer and modified numerical methods and FEM [3]. The Kawabata Evaluation System is now employed in measuring low-stress mechanical properties, including surface properties, friction between yarns, compression, shear, bending and tension.

2. Experimental setup

2.1 Fabric thickness measurement

The experimental method involves first measuring the thickness of the sample. Table 1 below shows the fibre geometrics obtained from a simple laboratory measurement using digital callipers. In literature, there exist a number of techniques for measuring fibre thickness. An example is to place the fabric between two thin plates of known thicknesses. A 100 gf/cm^2 weight (equivalent to 9.8066 kPa) is mounted on the upper plate to give it enough pressure to straighten out creases and crimps in the yarns that make up the fabric, and to capture precisely the thickness of the fabric, and not merely regions with lone yarns. Excessive weight would

press the sample below its actual thickness. Fig. 1 shows the laboratory measurement of the sample. Ten samples were cut and measured, and the average was evaluated as 0.38471 mm, using DNV ISO 5084:1996 standards at standard environmental conditions of 20 ± 2 °C and 65 ± 2 % for temperature and humidity, respectively. The calibration is done by zeroing the caliper with the flat stiff metal plate, placing the fabric under the plate, and taking the reading.

Fig. 1. Fabric thickness measurement setup *(a)* analogue, *(b)* digital

2.2 Compression measurement

The thickness measurement defines the fibre material geometrics when modelling in Texgen (mesoscale) or DFMA - Digital Fabric Mechanics Analyser (microscale). Other physical parameters include yarn width, yarn spacing and height, which play a crucial role in the mechanical behaviour of the yarns and fabric.
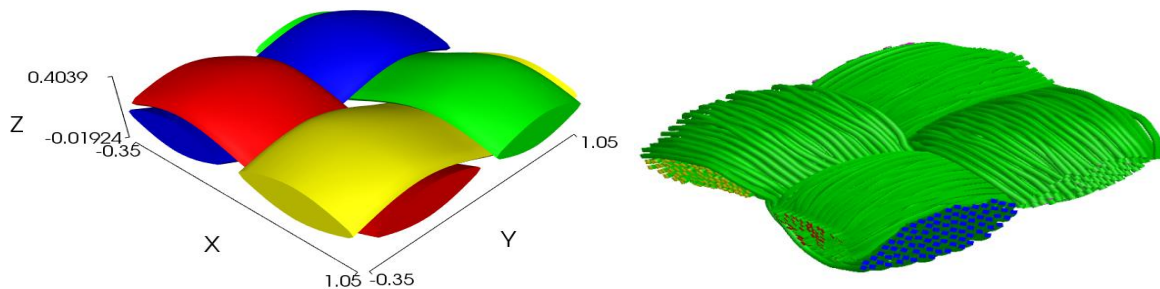
Fig. 2. Fabric model *(a)* TexGen (mesoscale), *(b)* DFMA (microscale)

3. Building the simulation

The simulation was tried in four different software including Abaqus, Ansys – Explicit Dynamics, Comsol Multiphysics – Time-Dependent Analysis and Marc Mentat – Transient Dynamics. The latter provided the most efficient, easiest and most realistic way to model the system. Into Marc, the model is imported as a .step file. The model is assumed to be symmetric to simplify the simulation system requirement. Thus, a double symmetry body is cut from the full model, so only a quarter of the whole model is used, as shown in Fig. 3. The idea is to perform a compression of up to 75 % of the fabric thickness. The faces A and B are constrained for translation in their respective lateral direction because these are the planes of symmetry of the model. The material properties are set as structural steel for the compression plate and the bottom sheet metal, whereas the material for the yarn is specified in previous experiments. The element size is set at 0.018396 mm. The model comprises four bodies and three contact regions: the yarn-to-yarn bonded breakable contact, the frictionless contact with the lower yarn and the bottom metal sheet. The model is compressed up to 70 % of its original fabric thickness, so the compression depth is 0.3983 mm. To reach the area of plastic deformation of the yarn will involve providing plastic data, which was not available at the time of the simulation; this helped inform the decision to limit the simulation to the region of linear deformation. Two symmetry

boundary conditions are created to account for the two symmetry planes in the *x* and *y* axes. The displacement load is chosen over velocity because it is more precise regarding the compression level, and it more realistically captures the slow time step of a compression process against impact simulation that requires only a few microseconds. It is essential to set the compression plate as a rigid, undeformable block and the flat bottom plate be constrained at the ground side and have a bonded (glued) interaction with the lower yarn.
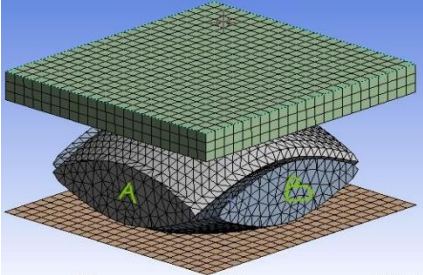
Fig. 3. Dual symmetry model mesh

4. Results and discussion

The simulation is run with results for 50 steps. The output number 3004 in Marc indicates a good convergence with no errors in the simulation. Fig. 4 below shows the initial and final compression positions.
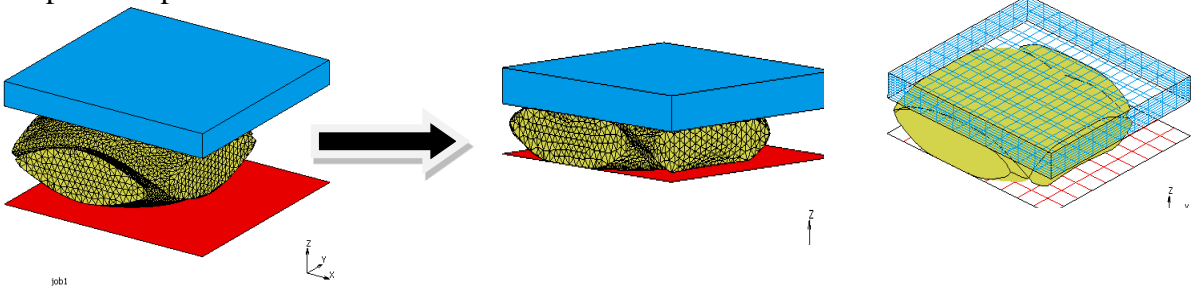
Fig. 4. Deformed and undeformed model
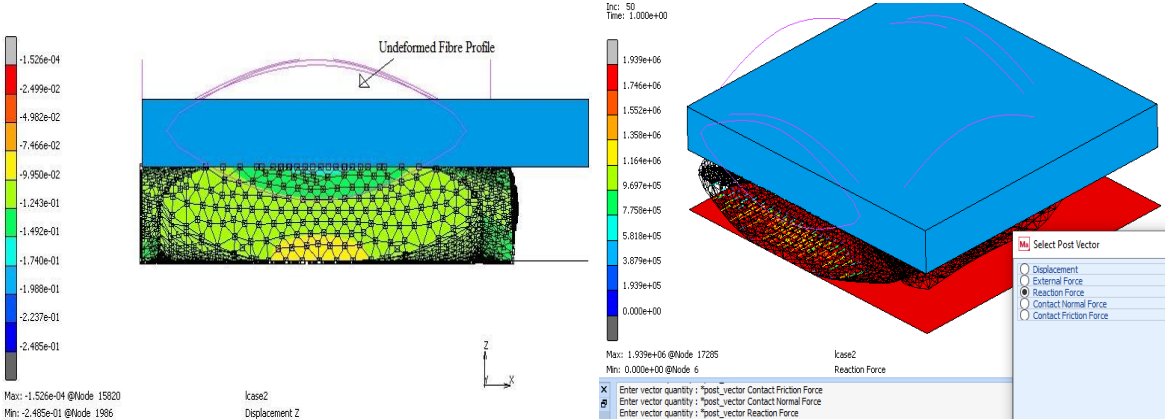
Fig. 5. Contour plots of deformed and undeformed model

43
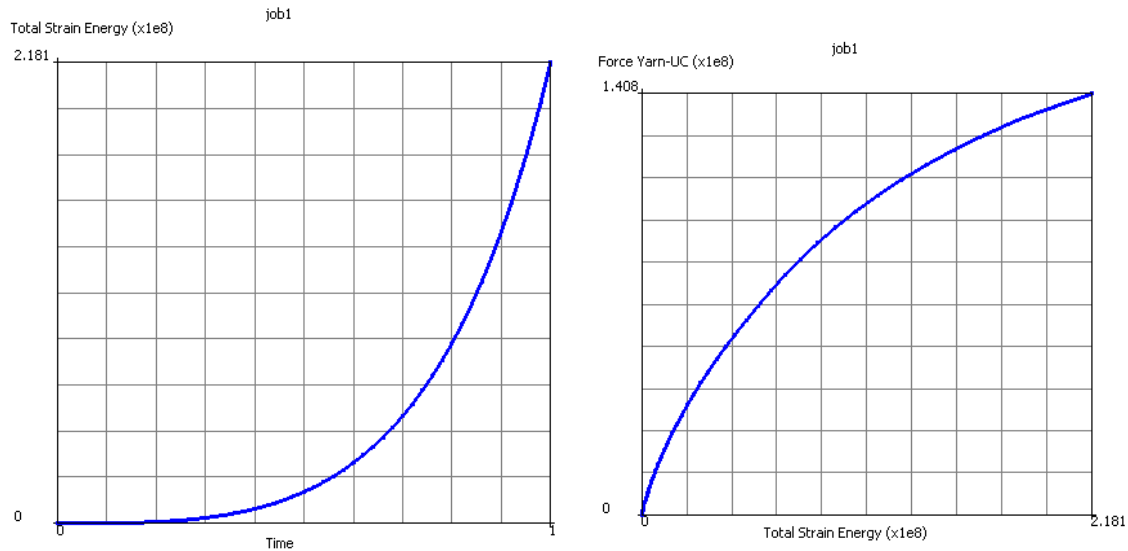
Fig. 6. Strain energy, time and total applied force by displacement

Fig. 5 shows the contour plot of the global displacement in the *z*-direction. The negative sign depicts the reverse direction, and the undeformed profile is switched on to appreciate the compression action further. For the vectors deliverables, the global displacement, reaction force, contact normal force and contact frictional force. Fig. 6 captures the plots of strain energy versus time and then force. The strain energy depicts a combination of energies arising from such entities as tension, compression and bending in a given unit cell. Further work will involve analytical models.

Acknowledgement

References

[1] Elder, H. M., The tensile, compressive and bending moduli of some monofilament materials, Journal of Textile Institute 57 (1966) 8-14.
[2] Holmes, B. R. I., Compression of textile fabrics under multiple applied loads, Journal of Textile Institute 72 (1981) 270-275.
[3] Thompson, A. J., Bassam, E. S., Ivanov, D., Belnoue, J. P.-H., Hallet, S. R., High fidelity modelling of the compression behaviour of 2D woven fabrics, International Journal of Solids and Structures 154 (2018) 104-113.
[4] Ukpomwam, J. O., Compressibility analysis of wet abraded woven fabrics, Journal Test. Eval. 21 (1993) 312-321.
[5] Young, J. J., Tae, J. K., Analysis of compressional deformation of woven fabric using finite element method, Textile Institute 92 (2001) 1-15.

Adaptation of methods for cyclo-stationary processes for noisy structural health data

C. Fischer[a], J. Bayer[a], J. Náprstek[a], S. Urushadze[a]

[a]Institute of Theoretical and Applied Mechanics of the Czech Academy of Sciences, Prosecká 76, 190 00 Prague, Czech Republic

1. Introduction

In structural health analysis, various techniques, including indirect measurement via monitoring vehicles, often yield data with significant randomness and insufficient frequency separation. Conversely, the desired attributes under scrutiny are periodic in nature. Thus, methodologies designed to identify cyclo-stationary properties within noisy data can be adapted for such scenarios, assuming an adequate length of the recorded data.

The concept of determining a bridge's natural frequency by utilizing a passing vehicle has been a pursuit since the publication of a mathematical solution for a suspended mass on a beam, [6]. For a comprehensive overview of progress in this area, consider referring to a recent review of the Vehicle Scanning Method (VSM), previously known as 'drive-by identification' [4].

However, it is essential to recognize that the idealized scenario presented in the closed-form solution, upon which VSM is built, is often impractical in real-world bridge situations. Several challenges arise, including the fact that the suspended mass cannot directly roll on the road or rail—it typically needs to be either pulled by another vehicle or equipped with its own drive. Furthermore, most bridges cannot be accurately represented as simple supported beams. Additionally, damping effects cannot always be disregarded, and both the vehicle and the bridge exhibit non-zero vibrations as the scanning vehicle enters the bridge.

These limitations prompted the development of finite element (FE) pre-processing-based solutions. These solutions involve the use of specialized elements to simulate the interaction between the vehicle and the bridge. They employ the Vehicle-Bridge Interaction (VBI) element [7], the MINE element [5] or FE software programs implementing kinematic formulations, such as LS-Dyna. These FE-based approaches aimed at creating models that reliably replicate the simplified experimental setups in order to compare numerical results and measured data [1].

The experimental bridge model corresponds to the outline in Fig. 1. It is made of a steel U-profile $0.21 \times 0.05 \times 0.004$ m with $L = 3.98$ m and a total mass of 33.3 kg. These values imply two first natural frequencies 6.99 and 27.63 Hz. Other structural parameters include viscous proportional damping ($\alpha = 0.2$, $\beta = 2.5 \times 10^{-5}$) and damping ratio of $c_s = 0.01$ for the spring dash pot, the spring mass $m_s = 245$ g and the vehicle mass $m_v = 631$ g.

In the experimental case, the measured data display a pronounced random component, which effectively obscures the frequency characteristics of the idealized experimental model. The frequency content of the signal measured on the passing vehicle is highly influenced by the vehicle's velocity and boundary conditions, and to some extent, also by the vehicle's position on the beam. Nevertheless, for sufficiently long beams, it is reasonable to assume that the boundary and positional effects can be considered negligible.
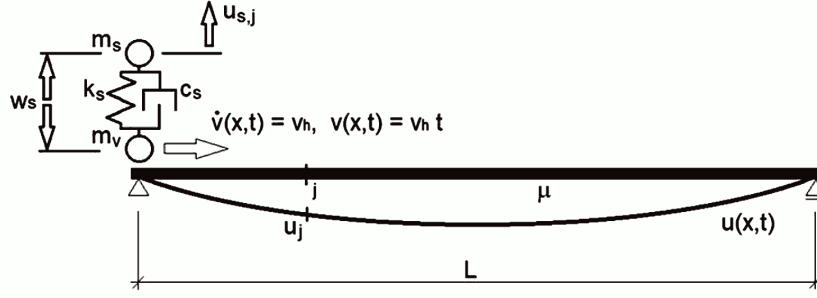
Fig. 1. Schema of the test beam and a moving sprung mass

Despite making such an assumption, the response is non-stationary and displays periodically repeating characteristics, as illustrated by the example plot of the measured response in Fig. 2. In general, this process lacks both stationarity and ergodicity. Consequently, the application of procedures commonly employed for evaluating stochastic parameters over time, as is typical in the context of stationary ergodic processes, is effectively precluded.

2. Cyclo-stationary and cyclo-ergodic processes

The periodic nature of the stochastic moments suggests the application of Cyclo-Stationary Process (CSP) theory. This approach describes situations in which consecutive quasi-periods resemble those observed in synchronously running two or more parallel realizations of the process. CSPs belong to a subclass of general non-stationary processes with periodically repeating characteristics. At the same time, it can be shown that the properties mentioned above allow non-ergodic CSPs to be understood as a 'Cyclo-Ergodic Process' (CEP), as illustrated in Fig. 3. Following the original definition of stochastic moments, they should be evaluated across individual realizations of the process. For example, by summing relevant values of $u^{(i)}(t)$, where the superscript (i) represents the realization number (e.g., black, red, blue in Fig. 3, corresponding to quasi-periods along the i axis). However, in the context of CEP, the red or blue periods along the t axis hold an equivalent stochastic value to those along the (i) axis.

The foundational works providing a theoretical background for CSP are primarily attributed to Gardner, see, e.g., [2] or recent monograph [3]. CSPs that exhibit cyclo-stationarity in second-order statistics, such as the autocorrelation function, are referred to as wide-sense CSP and are analogous to wide-sense stationary processes.

One of the key parameters characterizing a measured CSP is the length of one quasi-period (QPL). Typically, this value is not known in advance, but any a priori knowledge gained from analytical or numerical analysis can significantly enhance the identification process. When we consider the measured data as a quasi-periodic random process, the QPL becomes a stochastic
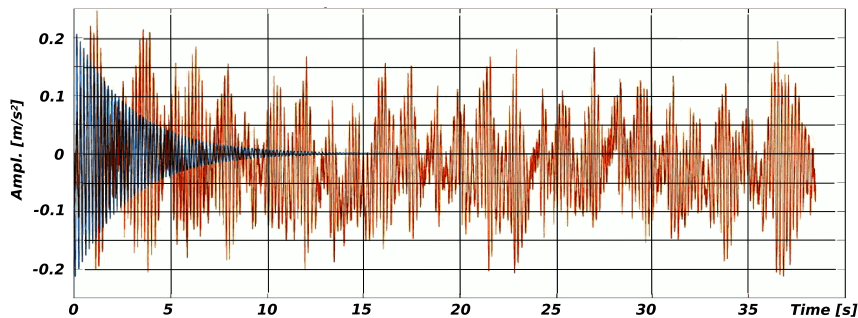
Fig. 2. Measured (red) and calculated (blue) response of the sprung mass
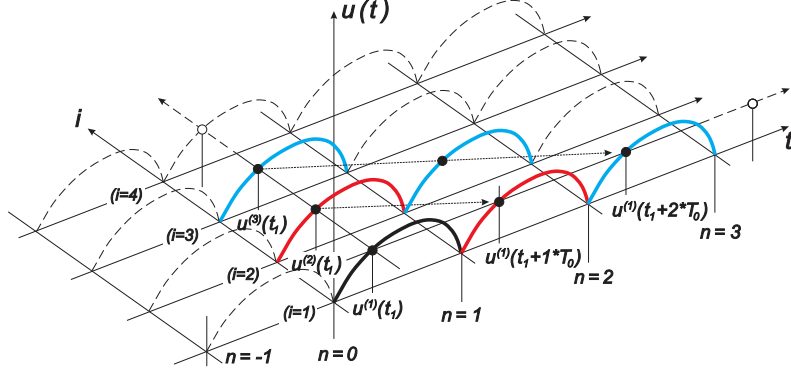
Fig. 3. Cyclo-Stationary and Cyclo-Ergodic Process; superscript in $u^{(i)}(t)$ means number of the process realization; n is number of the subsequent period of the length T_0

variable, as depicted in Fig. 4. The spread or variance of the QPL depends on various factors and tends to be sensitive on the presence of non-linear effects in the model. Consequently, these processes are referred to as Almost Cyclo-Stationary Processes (ACSP). It is evident that the variability of the QPL (within the context of a single parameter setting) should be taken into consideration. Nonetheless, it is worth noting that the variance of this statistic is typically small, allowing for a reasonable approximation of QPL variability with a suitable value.

Let each of the N quasi-periods is rescaled to the same number of steps $\delta_n = T_{0n}/N_s$. Here, δ_n represents the time increment within the n-th quasi-period, where T_{0n} is the length of the quasi-period, and N_s is a constant representing the number of steps within each quasi-period, cf. Fig. 4. This assumption allows δ_n and T_{0n} to be universally denoted as δ and T_0.

Fig. 4. TCSP – sampling with respect to QPL variability

The M-order cyclo-stationarity signifies periodically time-varying stochastic moments up to order M. In accordance with the aforementioned sampling style, primary stochastic characteristics can be defined under the CEP assumption, based on two-point statistics, as follows:

• *Mathematical mean value*:

$$m_u(t_1) = \lim_{N \to \infty} \frac{1}{2N+1} \sum_{n=-N}^{N} u(t_1 + nT_0) = m_u(t_1 + T_0). \tag{1}$$

• *Auto-correlation function*:

$$R_u(t_1, t_2) = \lim_{N \to \infty} \frac{1}{2N+1} \sum_{n=-N}^{N} u(t_1 + nT_0 + \frac{1}{2}t_2) \cdot u(t_1 + nT_0 - \frac{1}{2}t_2) = R_u(t_1 + T_0, t_2). \tag{2}$$

• *Cross-moment* of two processes $u(t)$, $v(t)$ of the $(M = r + s)$-th order:

$$C_{uv}^{rs}(t_1, t_2) = \lim_{N \to \infty} \frac{1}{2N+1} \sum_{n=-N}^{N} u^r(t_1 + nT_0 + \frac{1}{2}t_2) \cdot v^s(t_1 + nT_0 - \frac{1}{2}t_2) = C_{uv}^{rs}(t_1 + T_0, t_2), \tag{3}$$

where $r + s = M$, $t_1, t_2 \in (0, T_0)$.

In (1)–(3), both coordinates t_1, t_2 are considered within one quasi-period $(0, T_0)$. Processes $u(t), v(t)$ in (2), (3) are assumed to be centred.

The shape of the Probability Density Function (PDF) $p(u, t)$ of the $u(t)$ process depends on time $t \in (0, T_0)$. It can be deduced from a relative density of occurrence of a mean value $u_s(t)$ within a sample small interval $\Delta u(t) = u_{max} - u_{min}$ for every point $t \in (0, T_0)$

$$p(u,t) = \lim_{\Delta u \to 0} \lim_{N \to \infty} \frac{n_u(t)}{2N+1}, \quad \text{and} \quad p(u,t_1,t_2) = \lim_{\Delta u \to 0} \lim_{N \to \infty} \frac{n_u(t_1,t_2)}{2N+1}, \quad (4)$$

where $n_u(t)$ is the number of occurrences of a particular value $u(t)$ within the interval $\Delta u(t)$ at the instant t during all $2N$ quasi-periods. Similarly, $n_u(t_1, t_2)$ is the number of occurrences of a particular value of $u(t)$ at moment t_1 and another value of the process $u(t)$ at moment t_2, considering all $2N$ quasi-periods. It should be noted that the order of limits in (4) is not interchangeable.

The stochastic moments of the cyclo-stationary process can be evaluated either using the formulas in (1)–(3), or by employing their definitions with the PDF as described in (4)

$$m_u(t_1) = \int_{-\infty}^{\infty} u(t_1)p(u,t_1)\,\mathrm{d}u, \quad \text{or} \quad R_u(t_1,t_2) = \iint_{-\infty}^{\infty} u(t_1)u(t_2)p(u,t_1,t_2)\,\mathrm{d}u(t_1)\mathrm{d}u(t_2). \quad (5)$$

3. Conclusions

The theory of cyclo-stationary and cyclo-ergodic processes, along with their corresponding procedures, enables users to enhance frequency identification from data acquired through the vehicle scanning method. The assumption of cyclo-stationarity implies a restricted variability of system parameters within the recorded data, which could pose challenges in certain setups. It seems that, e.g., the wavelet-based approach may offer advantages in such situations. This topic warrants further investigation.

Acknowledgements

References

[1] Bayer, J., Analysis suggestion for vehicle scanning method, Proceeding of the conference Engineering Mechanics 2023, (editors) V. Radolf, I. Zolotarev, Prague, Institute of Thermomechanics, CAS, 2023, pp. 39-42.

[2] Gardner, W., Franks, L., Characterization of cyclostationary random signal processes, IEEE Transactions on Information Theory 21 (1) (1975) 4-14.

[3] Napolitano, A., Cyclostationary processes and time series, Elsevier, 2019.

[4] Wang, Z. L., Yang, J. P., Shi, K., Xu, H., Qiu, F. Q., Yang, Y. B., Recent advances in researches on vehicle scanning method for bridges, International Journal of Structural Stability and Dynamics 22 (15) (2022) No. 2230005.

[5] Yang, D. S., Wang, C. M., Yau, J. D., Moving internal node element method for dynamic analysis of beam structure under moving vehicle, Journal of Sound and Vibration 511 (2021) No. 116348.

[6] Yang, Y. B., Lin, C. W., Yau, J. D., Extracting bridge frequencies from the dynamic response of a passing vehicle, Journal of Sound and Vibration 272 (3-5) (2004) 471-493.

[7] Yang, Y. B., Yau, J. D., Vehicle-bridge interaction element for dynamic analysis, Journal of Structural Engineering 123 (11) (1997) 1512-1518.

Development of meso-scale discrete model for simulations of ballistic experiments

B. Fleischerová[a], J. Eliáš[a]

[a]*Institute of Structural Mechanics, Faculty of Civil Engineering, Brno University of Technology, Veveří 331/95, 602 00 Brno, Czech Republic*

Fiber-reinforced concrete panels are used for ballistic protection. During their tests, the material is loaded by a high-velocity projectile. This dynamic loading causes significant damage and fracturing in concrete. The cracks results in discontinuity in the displacement field.

In case of heterogeneous material with strain softening constitutive response, the discrete meso-scale material representation can conveniently replace the most common finite element method. Discrete models allow straightforward description of the discontinuity in the displacement field and inhomogeneities of the material are represented by an assembly of interconnected discrete units. A number of discrete models were developed by many scientists all over the world [1, 3].

The meso-scale models directly represent material heterogeneity provide material length scale and fluctuation of stresses. They are computationally expensive, but reducing kinematics by discrete representation helps to substantially decrease their computational burden.

The presented meso-scale discrete model similar to the *Lattice Discrete Particle Model* [1] is built in programming language C^{++}. The concrete is described as a two-phase material (aggregates and mortar). Individual rigid particles represent larger aggregates and surrounding matrix and are created by placing spheres randomly into the domain with a minimal mutual distance corresponding to maximum diameter of the real mineral grains. Each two neighboring particles are connected via bonds, which define a contact face. The stiffness of the bonds are modified during the deformation according to the nonlinear constitutive functions defined in vectors.

The Voronoi tesselation is used to build the geometry of the rigid particles and ensure the perpendicularity between bonds and contact faces. The particles have polyhedral geometry and at least three vertices define contacts for 3D case. For 2D case, the particles are polygons and contacts are line segments prescribed by two vertices. Edges of Delaunay simplices define connections between the particles and therefore also the mechanical elements. The elements represents both aggregates and cement matrix behavior.

Transient (dynamic) regime is used to simulate the ballistic experiments. A time discretization based on the finite difference method is usually used. Implicit time integration scheme, specifically the generalized-α method, is currently utilized by the model [2]. Unconditionally stability and reduced numerical damping are the main advantages of this time integration algorithm. The numerical energy dissipation is controlled by user-specified parameter, spectral radius ρ_{∞}. The transient regime was verified on the simple example of the cantilever beam for both 2D as well as 3D case. The model was loaded by vertical force at the free end. The results are shown by the authors in [4].

The extension of the model to include also the explicit integration scheme is under development. Explicit methods are more suitable for short time periods with high-rate loading, but the stability of the calculation depends on the time step length.

Concrete, as a natural brittle material, performs well in compression. On the other hand, its efficiency in tension is significantly lower. Therefore, the reinforcement is usually required to improve poor performance in tension. In recent decades, short randomly distributed fibers of small diameter are very popular to use. Nowadays, fiber-matrix interaction is broadly reported by many works. Although each work has its own contribution to this scientific field, most of them refer to the work of Naaman et al. [5].

The model simulates behavior of a fiber crossing a single crack. Bridging forces from the left and the right side of the fiber has to be equal. The equilibrium is satisfied during the whole simulations. Newton iterative method is used to find the equilibrium between right and left bridging force. Contribution of the fibers in the elastic regime is neglected.

The mechanical behavior of the fiber can be divided into two main stages. First, there is the debonding stage, where the fiber is still bonded with the matrix at some length. The second is the pulling-out stage, where the fiber is fully debonded from the matrix. The stages and typical curves of pullout vs. bridging force diagram are shown in Fig. 1. Non-zero parameter β_f describe softening or hardening of the material. The border between the debonding and the pulling-out stage is represented by critical pullout of the fiber ν_{crit}. During the whole simulation, the rupture condition as well as the full pullout of the fiber ($\nu = \nu_{crit}$) have to be controlled. The bridging force immediately decrease to zero for the rest of the computation in both cases.

(a) Fracture energy $G_d > 0$ (b) Fracture energy $G_d = 0$
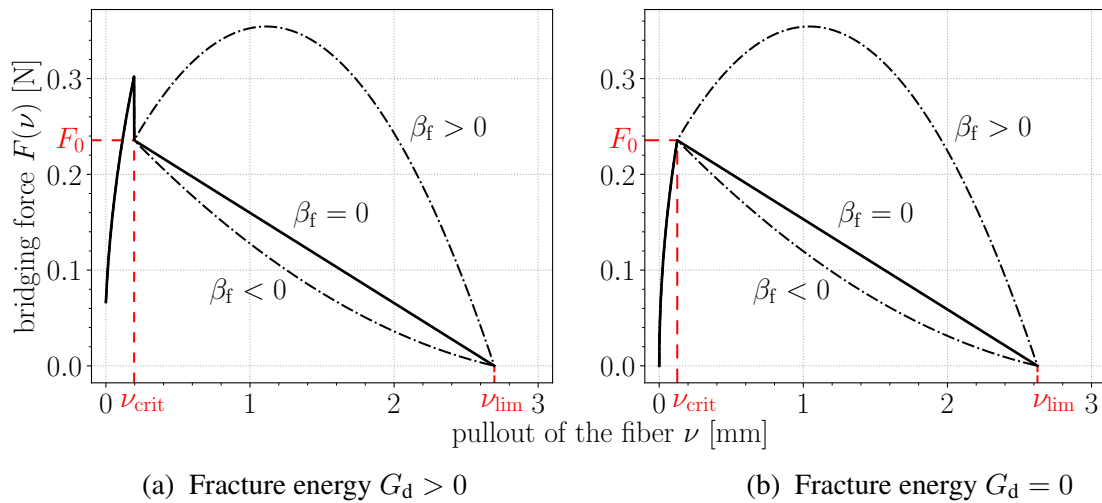
Fig. 1. Typical bridging force F(ν) versus pullout ν relationships

When the crack is closing, the linear unloading-reloading functions towards the origin ($F(\nu) = 0$, $\nu = 0$) are used to find the equilibrium between left and right side of the fiber. When the crack starts to open again, the same linear functions are used unless the crack width reaches the maximum from its previous opening.

The transient regime with fiber-reinforced concrete slabs are currently being tested. The model is loaded by prescribed displacement at one point. The convergence of the simulations as well as the obtained forces are analyzed. Boundary conditions of the model correspond to the real ballistic experiments. Also explicit integration scheme is being validated. Some partial results will be shown during the conference.

Acknowledgment

References

[1] Bolander, J. E., Eliáš, J., Cusatis, G., Nagai, K., Discrete mechanical models of concrete fracture, Engineering Fracture Mechanics 257 (2021) No. 108030.

[2] Chung, J., Hulbert, G. M., A time integration algorithm for structural dynamics with improved numerical dissipation: The generalized-α method, Journal of Applied Mechanics 6 (2) (1993) 371-375.

[3] Cusatis, G., Bažant, P., Cedolin, L., Confinement-shear lattice model for concrete damage in tension and compression, Journal of Engineering Mechanics 129 (12) (2003), doi: 10.1061/(ASCE)0733-9399(2003)129:12(1439).

[4] Fleischerová, B., Eliáš, J., Development of discrete model for dynamic simulations of concrete behavior, AIP Conference Proceedings 2887 (1) (2023) No. 020007.

[5] Naaman, A. E., Namur, G. G., Alwan, J. M., Najm, H. S., Fiber pullout and bond slip. I: Analytical study, Journal of Structural Engineering 117 (9) (1991) 2769-2790.

Numerical implementation of incremental minimization principle for materials with multiple rate-independent dissipative mechanisms

M. Frost[a], A. Moskovka[b,c], P. Sedlák[a], J. Valdman[b,d]

[a] *Institute of Thermomechanics, Czech Academy of Sciences, Dolejškova 5, 18200 Praha, Czech Republic*
[b] *Institute of Theory of Information and Automation, Czech Academy of Sciences, Pod Vodárenskou věží 4, 18200 Praha, Czech Republic*
[c] *Department of Mathematics, Faculty of Applied Sciences, University of West Bohemia, Technická 8, 30100 Plzeň, Czech Republic*
[d] *Department of Computer Science, Faculty of Science, University of South Bohemia, Branišovská 31, 37005 Č. Budějovice, Czech Republic*

1. Introduction

New experimental techniques allow for a more comprehensive examination of the mechanical response of materials, providing the opportunity for the development of more detailed material models. The incremental energy minimization approach is a compact variational formulation of the evolutionary boundary value problem for constitutive models of materials with a rate-independent response, see e.g. [3]. Although it can be easily applied to many conventional models, its main advantages arise when applied to models with multiple strongly coupled dissipation mechanisms, where the direct construction of the coupled yield conditions and flow rules may be challenging. However, the approach usually requires a more complex numerical treatment of the resulting sequence of time-incremental boundary value problems resolved via the finite element method.

2. Incremental minimization principle

In what follows, we focus on a quasi-static evolutionary boundary value problem under isothermal conditions. Let us introduce a partition of the time interval from time 0 to $\mathcal{T}$ in the form $0 = t_0 \leq t_1 \leq \cdots \leq t_N = \mathcal{T}$, $N \in \mathbb{N}$. In this time-discrete setting, the mechanical response of the system at time $t_{n+1}, n \in \{0, \ldots, N-1\}$ can then be determined by solving the incremental minimization problem

$$\inf_{\boldsymbol{\chi}} L^\tau(\boldsymbol{\chi}, \boldsymbol{\chi_n}),\tag{1}$$

where $\boldsymbol{\chi}$ represents the set of all thermodynamic descriptors of the system. The superscript τ denotes the time-discretized counterparts of time-continuous functionals of the corresponding weak formulation, and the subscript n denotes the values of the previous time step. Let us note that the minimization can be subject to some additional (kinematic and physically-based) internal constraints, see [3] for details.

The (Lagrangian) functional L^τ usually combines the incremental energy functional, E^τ, the incremental dissipation functional, D^τ, and the incremental external work functional P^τ. For many engineering-relevant solid materials, the objective function of the minimization from (1) takes the the following form:

$$L^\tau(u, \boldsymbol{\alpha}, \boldsymbol{\alpha}_n) := E^\tau(u, \boldsymbol{\alpha}, \boldsymbol{\alpha}_n) + D^\tau(\boldsymbol{\alpha}, \boldsymbol{\alpha}_n) - P^\tau(u, \boldsymbol{\alpha}, \boldsymbol{\alpha}_n).\tag{2}$$

Here, u denotes the displacement and $\boldsymbol{\alpha}$ encompasses thermodynamic descriptors of the microstructure, which can be further constrained to an admissible set $\mathcal{A}^\tau$. The most common examples include (hyper)elastic materials, where $\boldsymbol{\alpha}$ and D^τ disappear, or perfectly plastic material with $\boldsymbol{\alpha}$ being the plastic strain and D^τ being a one-homogeneous function of the difference $\boldsymbol{\alpha} - \boldsymbol{\alpha}_n$ with an imposed constraint $\operatorname{tr} \boldsymbol{\alpha} = 0$.

3. Numerical solution strategies

At least two distinct methods can be utilised to solve the rate-independent problem stated in (2). In the first case, frequently used in finite element software, the minimisation problem is split into a nested form, where a sequence of "structural" nonlinear minimization problems and "material" nonlinear minimization problems is resolved. The second approach benefits from the clear variational structure of (1) and directly applies minimization.

To illustrate these approaches, let us consider the following form of incremental functionals for a material body:

$$E_{n+1}^\tau(u, \boldsymbol{\alpha}; u_n, \boldsymbol{\alpha}_n) = \int_\Omega f_{n+1}(u, \boldsymbol{\alpha}) - f_n(u_n, \boldsymbol{\alpha}_n) \, \mathrm{d}V, \tag{3}$$

$$D_{n+1}^\tau(\boldsymbol{\alpha}; \boldsymbol{\alpha}_n) = \int_\Omega (t_{n+1} - t_n) \, \delta_{n+1}(\boldsymbol{\alpha}; \boldsymbol{\alpha}_n; t_{n+1} - t_n) \, \mathrm{d}V, \tag{4}$$

$$P_{n+1}^\tau(u; u_n) = \int_\Omega F_{n+1}^{\mathrm{vol}} \cdot (u - u_n) \, \mathrm{d}V + \int_{\Gamma_{\mathrm{N}}} F_{n+1}^{\mathrm{surf}} \cdot (u - u_n) \, \mathrm{d}S, \tag{5}$$

where f_i and δ_i stand for the *discretized* density of the thermodynamical (free energy) potential and dissipation (pseudo)potential, respectively. Moreover, the set $\Omega \subset \mathbb{R}^3$ is the geometric representation of the physical body in the space with (assumed Lipschitz) boundary $\partial\Omega$, and $\Gamma_{\mathrm{N}} \subset \partial\Omega$ represents its subset where the Neumann boundary condition is applied. The terms F_{vol}^i and F_{surf}^i represent the corresponding time discretizations of the prescribed volumetric and surface forces, respectively. Let us further assume that all necessary information on the system at $t_0 = 0$ (including $u_0, \boldsymbol{\alpha}_0$) is known and well defined. We can disregard the terms in (3)–(5), which are constant with respect to the minimization, and make profit from one-homogeneity of the dissipation (pseudo)potential to the eliminate the time increment in (4).

The nested form of the boundary problem at a time instant t_{n+1} then reads as

$$u_{n+1,p+1} = \operatorname*{argmin}_{u \in \mathcal{U}_{n+1}^\tau} \{ E_{n+1}^\tau(u, \boldsymbol{\alpha}_{n+1,p}; \boldsymbol{\alpha}_n) - P_{n+1}^\tau(u) \}, \tag{6}$$

$$\boldsymbol{\alpha}_{n+1,p+1} = \operatorname*{argmin}_{\boldsymbol{\alpha} \in \mathcal{A}_{n+1}^\tau} \{ E_{n+1}^\tau(u_{n+1,p+1}, \boldsymbol{\alpha}; \boldsymbol{\alpha}_n) + D_{n+1}^\tau(\boldsymbol{\alpha}; \boldsymbol{\alpha}_n) - P_{n+1}^\tau(u_{n+1,p+1}) \}. \tag{7}$$

Whereas the first subscript denotes the time incrementation introduced above, the second one denotes the iteration $p+1$ ($p \in \mathbb{N} \cup 0$) within the resolution process at time t_{n+1}, where the the subproblems (6), (7) are solved consecutively and repeatedly until suitable convergence criteria are met, i.e. so-called alternating minimization; $\boldsymbol{\alpha}_{n+1,0} = \boldsymbol{\alpha}_n$. After a discretization in space, the first, "structural" subproblem formally corresponds to the principle of minimum potential energy. Its solution procedure is analogous to resolving an elastic body problem, which is a rather standard problem for finite element method. The second, "material" subproblem corresponds to minimization only with respect to internal variables, i.e. finding the local thermodynamical balance, and represents the constitutive response of a material point with fixed displacement. This is usually tackled via numerical procedures specific to the particular constitutive law or with some universal tool of mathematical programming, cf. [1]. A link between the two solution procedures is provided by the material tangent stiffness operator, which must

be derived from the constitutive law as well.

In the alternative approach, the problem is tackled via "complete" minimization, i.e., minimizing all control variables at once,

$$(u_{n+1}, \boldsymbol{\alpha}_{n+1}) = \underset{u \in \mathcal{U}_{n+1}^\tau, \boldsymbol{\alpha} \in \mathcal{A}_{n+1}^\tau}{\operatorname{argmin}} \{E_{n+1}^\tau(u_{n+1}, \boldsymbol{\alpha}; \boldsymbol{\alpha}_n) + D_{n+1}^\tau(\boldsymbol{\alpha}; \boldsymbol{\alpha}_n) - P_{n+1}^\tau(u_{n+1})\}. \quad (8)$$

This monolithic approach may be especially advantageous for material models with multiple, strongly coupled rate-independent dissipative processes. In such a situation, the evolution of individual thermodynamic descriptor cannot be addressed independently, benefiting from conventional active set search strategies. Solely a single "global yield function" driving the evolution can be derived, which may render the conventional numerical treatment elaborate and dependent on the model's particular mathematical structure. In contrast, resolving directly (8) allows to avoid transferring the results from one subproblem to the other, involving the construction of the material Jacobian matrix (material tangent modulus) and its incorporation into the structural Jacobian matrix. On the other hand, it requires to cope with with a non-smooth minimization problem with non-linear constraints, which provides a complex computational challenge.

4. Conclusion

Recently, a vectorized MATLAB tool for minimization of nonlinear (mathematically well-behaved) functionals discretized by the finite element method was developed [4]. The current work builds on it and investigates both the nested and monolithic approaches for a constitutive model with two strongly coupled dissipation process occurring in shape memory alloys, cf. [2].

The principal benefits of the monolithic approach stated above are counterbalanced by some drawbacks. One is related to the limits of the variational framework: some models might require some adaptation of the sketched treat or they even might not fit to (1) at all. Second, the dimension of the "complete" minimization problem is naturally higher than in the case when the problem is split in the nested formulation, which poses a challenge for computational resources. Third, applying universal minimization methods is often less efficient than employing customized algorithms and may lead to prohibitive computational time consumption for more complex evolutionary boundary problems. However, the advance of new optimization methods and increased computational power complemented with parallelization might provide some remedies in the future.

Acknowledgements

References

[1] Frost, M., Benešová, B., Sedlák, P., A microscopically motivated constitutive model for shape memory alloys: Formulation, analysis and computations, Mathematics and Mechanics of Solids 21 (3) (2016) 358-382.

[2] Frost, M., Valdman, J., Vectorized MATLAB implementation of the incremental minimization principle for rate-independent dissipative solids using FEM: A constitutive model of shape memory alloys, Mathematics 10 (2022) No. 4412.

[3] Miehe, C. J., A multi-field incremental variational framework for gradient-extended standard dissipative solids, Journal of the Mechanics and Physics of Solids 59 (4) (2011) 898-923.

[4] Moskovka, A., Valdman, J., Fast MATLAB evaluation of nonlinear energies using FEM in 2D and 3D: Nodal elements, Applied Mathematics and Computation 424 (2022) No. 127048.

Rotation of the flap controlled by the air flow from the fan – educational mechatronic system

V. Goga[a], Š. Berta[a], J. Murín[a], J. Paulech[a]

[a]Institute of Automotive Mechatronics, Faculty of Electrical Engineering and Information Technology of Slovak University of Technology in Bratislava, Ilkovičova 3, 841 04 Bratislava, Slovak Republic

1. Introduction

The designed mechatronic system is intended to serve as an educational device for applying the control algorithm to a real physical model. The construction of the model consists of a vertical and horizontal aluminium arm, which are connected by plastic elements and metal screws. The flap rotates around a pin located on a horizontal arm. The fan attached to the vertical arm generates an air flow that rotates the flap around the pin. An infrared (IR) distance sensor which measures the horizontal displacement of the flap is placed in a suitable position from the flap. A ruler installed in the axis of the IR sensor is used for verification measurement of flap displacement. All plastic elements as well as the flap itself were designed and manufactured using 3D printing.

The physical model is completed by a simple electrical circuit installed on PCB that serves to power the system and to connect the measured signal from IR sensor and the control signal for the fan speed with the DAQ (data acquisition) measurement hardware. The DAQ hardware communicates via a USB connection with a computer and LabVIEW software, where a graphical user interface (GUI) is created. Software also enables the creation of a suitable algorithm for automatic system control.

2. Electrical circuit for the model

A computer cooling fan (ARCTIC S4028-15K) is used as an actuator of the system (basic parameters: fan speed 1150-15000 RPM, PWM controlled, 12 V DC / 0.47 A). The flap displacement is measured by IR distance sensor (SHARP GP2Y0A41SK0F) that is powered by 5 V DC and gives a voltage analog output signal.

The voltage to PWM converter module is built into the electrical circuit which creates a PWM signal for the supply voltage of the fan (0-100 %; 0-12 VDC) using a control analog voltage of 0-5 V DC. This control voltage is created either manually using a potentiometer or digitally via DAQ hardware and software. Manual or software control mode can be selected using a rocker switch.

The electric circuit is powered by a 12 V DC power adapter and a step-down voltage converter (12 V to 5 V) is designed for the needs of IR sensor and PWM module. The last part of the electrical circuit is the filter capacitor for the measured signal of IR sensor.

The physical model is completed by a simple electrical circuit that serves to power the system and to connect the measured signal from IR sensor and the control signal for the fan speed with the DAQ measurement hardware, see Fig. 1. The DAQ hardware communicates via a USB connection with a computer and LabVIEW software, where a graphical user interface (GUI) is created.
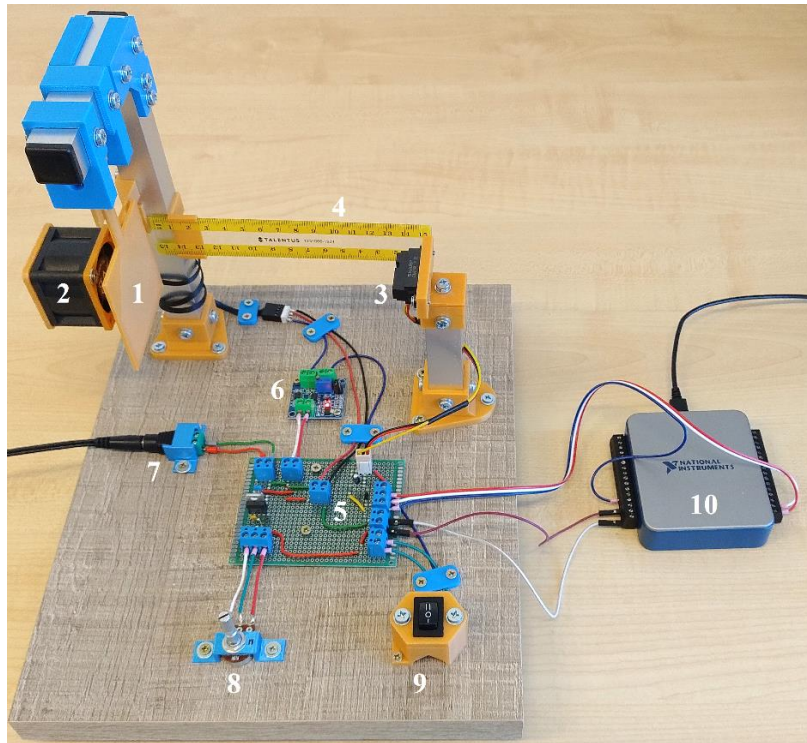
Fig. 1. Components of the mechatronic syste: 1 – flap, 2 – fan, 3 – IR sensor, 4 – ruler, 5 – PCB, 6 – PWM module, 7 – power supply connector, 8 – potentiometer, 9 – rocker switch, 10 – DAQ hardware

3. System testing

The air from the fan rotates the flap around the pin and the IR sensor measures the change in its horizontal displacement x. The sensor is located at a constant vertical distance of 75 mm from the pin. The flap rotation angle φ can be calculated according to the relationship as shown in Fig. 2. Displacement measurement is nonlinearly dependent on the electrical voltage at the sensor output as shown in Fig. 3. By approximating the measured data with a polynomial function, we obtain a function for calculating the measured distance:

$$x = 45.932\,U^3 - 323.37\,U^2 + 810.5\,U - 679.54 \tag{1}$$

The installed ruler can be used to verify the distance measurement.
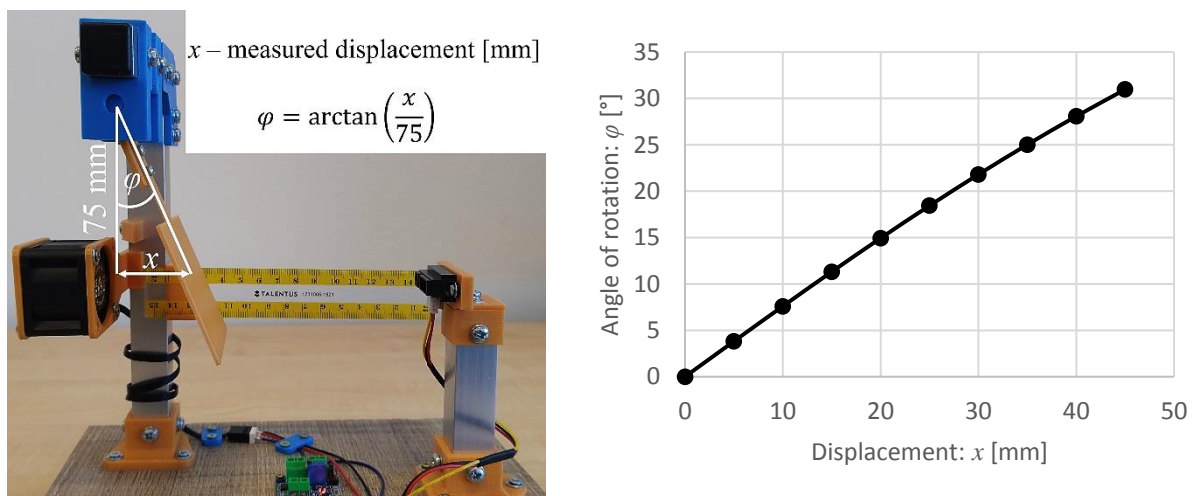
Fig. 2. Determining the flap rotation angle and its dependence on flap displacement
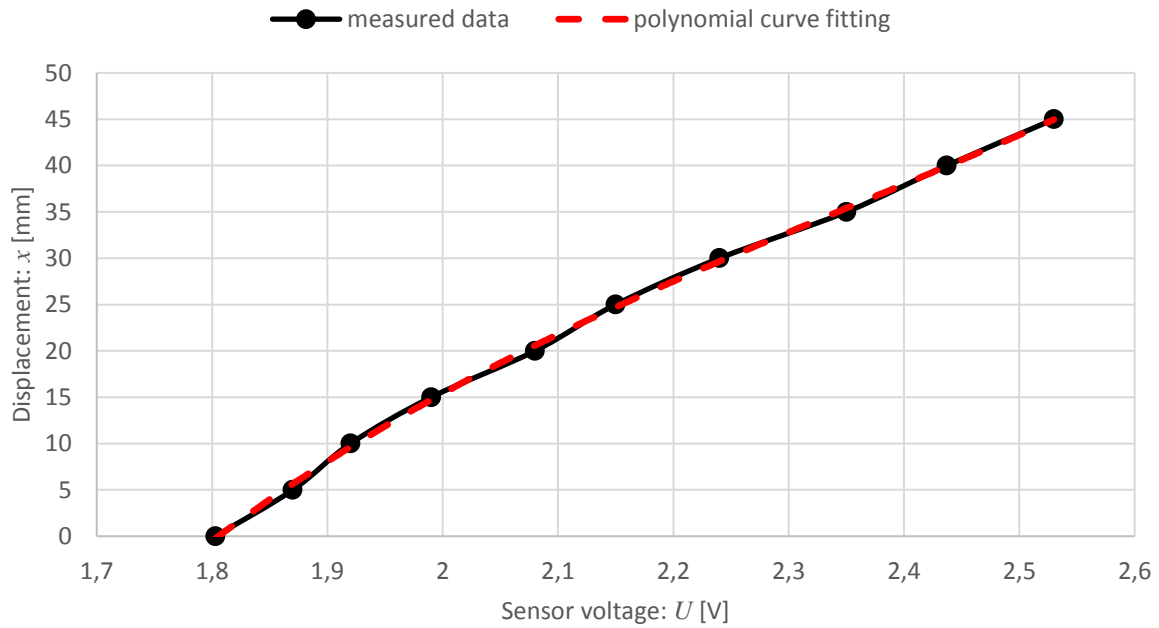
Fig. 3. Dependence of the measured distance on the output voltage of the IR sensor

Fig. 4 shows the graphical user interface (GUI) for system control created in LabVIEW software. The fan speed is set with a slider - PWM duty cycle is modified. Measured horizontal displacement of the flap and calculated value of its rotation angle are plotted on the graphs.

Due to the principle of creating the air flow by the fan as well as the flow around the flap, the whole system is considerably non-linear.
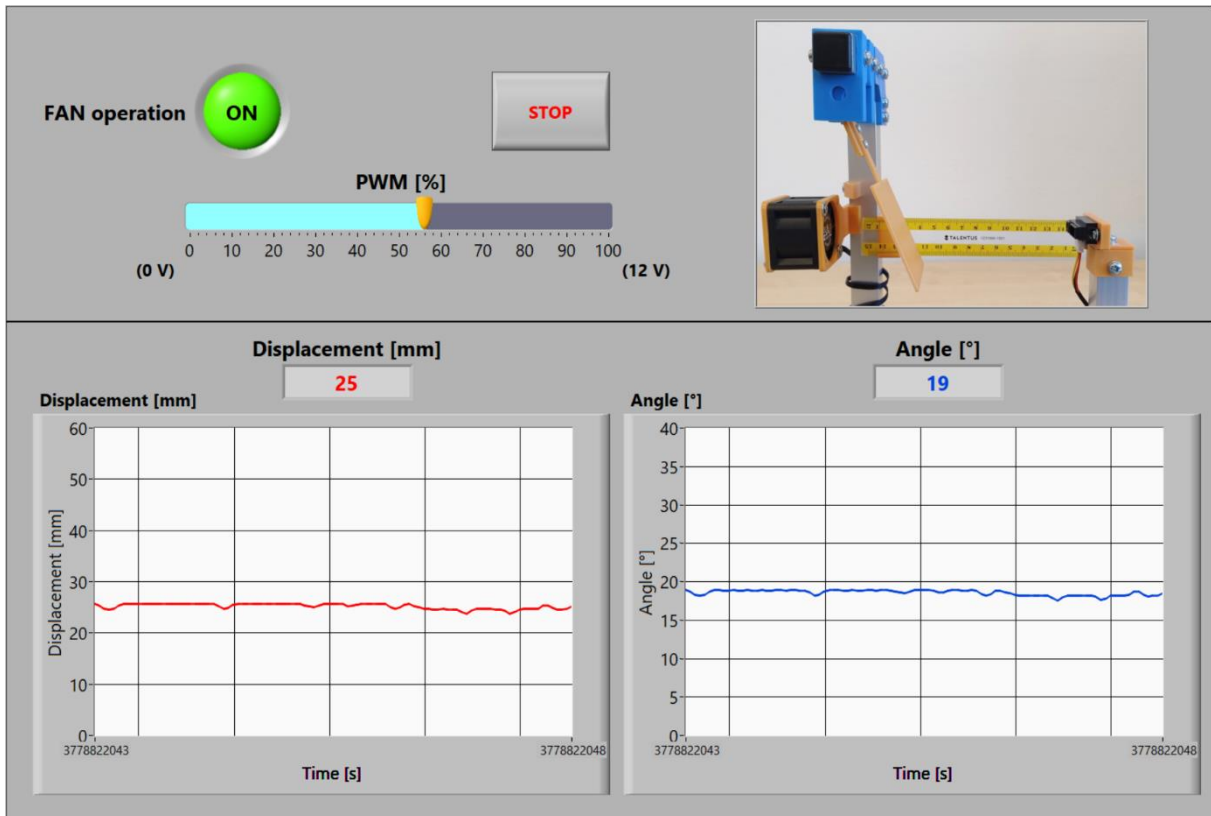
Fig. 4. Graphical user interface – LabVIEW software

4. Conclusions

A simple mechatronic system made using 3D printing and suitable electronic components was presented. This system enables practical control of the flap rotation by means of flowing air from the fan. The flap horizontal displacement change is measured by an IR distance sensor and the fan speed is controlled by a PWM signal.

A suitable controller with a programmed control algorithm can be used for the automatic control system. This model is suitable as an educational system in the field of mechatronics and cybernetics.

In the future, it would be appropriate to create a mathematical model of the system using its experimental identification.

Resolving flow around tandem cylinders with RANS-LES hybrid methods

L. Hájek[a], J. Karel[a], M. Klíma[a], D. Trdlička[a]

[a]*Department of Technical Mathematics, Faculty of Mechanical Engineering, Czech Technical University, Karlovo náměstí 13, 121 35 Praha 2, Czech Republic*

1. Introduction

Turbulence modeling is one of the more challenging but useful CFD disciplines, as turbulent flow appears in a wide variety of applications. Methods based on the Reynolds-averaged Navier–Stokes (RANS) equations have proven effective for some types of problems, but lack the ability to resolve a range of turbulent length scales for some others. This can be solved by the use of large eddy simulation (LES) models, but these come with substantial additional computational demands that make them practically unusable in some cases, even on current hardware. A possible solution to this problem are hybrid RANS-LES methods, combining lower computational requirements and a wider range of resolved turbulent scales.

Detached eddy simulation (DES) hybrid RANS-LES models recently began their transition to two equation RANS models, such as the method by Strelets [5] based on Menter's Shear Stress Transport (SST) turbulence model [4]. The delayed DES (DDES) method and its variant with improved wall modeling capability (IDDES) were also proposed for the SST model by Gritskevich et al. [1]. This paper compares all of the mentioned methods with experimental data by Jenkins et al. [2, 3] on a tandem cylinder problem – a configuration formerly proposed by the AIAA Aerospace Research Center for aircraft landing gear development.

2. Mathematical model

Under the assumption that the fluid behaves according to the thermodynamic model of an ideal gas, turbulent heat flux corresponds to the Reynolds analogy, after neglecting the effects of gravity and applying Reynolds and Favre averaging, the Reynolds-Averaged Navier–Stokes equations can take the following form:

$$\frac{\partial \rho}{\partial t} + \text{div}\,(\rho \boldsymbol{u}) = 0, \tag{1a}$$

$$\frac{\partial \rho \boldsymbol{u}}{\partial t} + \text{div}\,((\rho \boldsymbol{u}) \otimes \boldsymbol{u}) = \text{div}\,\boldsymbol{\sigma} + \text{div}\,\boldsymbol{\tau} - \text{grad}\,p, \tag{1b}$$

$$\frac{\partial \rho E}{\partial t} + \text{div}\,(\rho \boldsymbol{u} H) = \text{div}\,(\boldsymbol{\tau} \boldsymbol{u}) + \text{div}\left(\frac{c_p \mu}{\text{Pr}} \text{grad}\,T\right)$$
$$+ \text{div}\left(\boldsymbol{\sigma} \boldsymbol{u} + \left[\mu + \frac{\mu_T}{\sigma_k}\right] \text{grad}\,k + \frac{c_p \mu_T}{\text{Pr}_T} \text{grad}\,T\right), \tag{1c}$$

where t is time, ρ represents fluid density, $\boldsymbol{u}$ denotes fluid velocity with u_1, u_2, u_3 as its components, p is pressure, E specific total energy, $H = E + p/\rho$ specific enthalpy, T represents

fluid temperature, c_p is the heat capacity at constant pressure, Prandtl number and its turbulent counterpart are denoted as Pr and Pr_T, respectively, μ and μ_T are similarly dynamic laminar and eddy viscosity, σ_k is a coefficient given by a turbulence model, k represents turbulence kinetic energy, $\boldsymbol{\sigma}$ is the viscous stress tensor approximated (assuming that $\boldsymbol{S}$ is the strain tensor and $\boldsymbol{I}$ is the identity matrix) as

$$\boldsymbol{\sigma} \approx 2\mu \left(\boldsymbol{S} - \frac{1}{3}\text{div}(\boldsymbol{u})\boldsymbol{I} \right) \tag{2}$$

and $\boldsymbol{\tau}$ the Reynolds stress tensor, approximated similarly to $\boldsymbol{\sigma}$ by Boussinesq approximation. To close the system, we use the equation of state

$$p = (\gamma - 1) \left[\rho E - \frac{1}{2}\rho \left(u_1^2 + u_2^2 + u_3^2 \right) \right] \tag{3}$$

and one of the turbulence models described below.

For the SST-based turbulence models, we use the 2003 variant of the SST method [4]

$$\frac{\partial \rho k}{\partial t} + \text{div}\left(\rho k \boldsymbol{u}\right) = \text{div}\left(\left[\mu + \sigma_k \mu_T\right] \text{grad } k\right) + P_k - \rho k \frac{\sqrt{k}}{L_T}, \tag{4a}$$

$$\frac{\partial \rho \omega}{\partial t} + \text{div}\left(\rho \omega \boldsymbol{u}\right) = \text{div}\left(\left[\mu + \sigma_\omega \mu_T\right] \text{grad } \omega\right) + \frac{C_\omega \rho}{\mu_T} P_k - \beta \rho \omega^2 + 2(1 - F_1)\text{CD}, \tag{4b}$$

where ω represents the specific turbulence dissipation rate, L_T denotes the model length scale, P_k is a production term described in [4] and any model constant ϕ for the SST model is computed as $\phi = F_1 \phi^{k-\omega} + (1 - F_1)\phi^{k-\varepsilon}$ using

$$
\begin{array}{llll}
\sigma_k^{k-\omega} = 0.85, & \sigma_\omega^{k-\omega} = 0.5, & \beta^{k-\omega} = 0.075, & C_\omega^{k-\omega} = 0.553, \\
\sigma_k^{k-\varepsilon} = 1, & \sigma_\omega^{k-\varepsilon} = 0.856, & \beta^{k-\varepsilon} = 0.0828, & C_\omega^{k-\varepsilon} = 0.44.
\end{array} \tag{5}
$$

The eddy viscosity is given using the function F_2 from [4]

$$\mu_T = \frac{a_1 \rho k}{\max\left(a_1 \omega, F_2 S\right)}, \quad a_1 = 0.31. \tag{6}$$

The model length scale L_T is defined using the RANS and LES lengths

$$l_{\text{RANS}} = \frac{\sqrt{k}}{\beta^* \omega}, \quad l_{\text{LES}} = C_{\text{DES}}\Delta, \quad \hat{l}_{\text{LES}} = C_{\text{DES}}\hat{\Delta} \tag{7}$$

with Δ being the the maximum length of the cell's edges and C_{DES} is a coefficient described in [5] and $\hat{\Delta}$ is its modification which also utilizes the distance from the nearest wall [1], which give the following formulations for the SST, SST-DES, SST-DDES and SST-IDDES methods:

$$L_T^{(\text{RANS})} = l_{\text{RANS}}, \quad L_T^{(\text{DDES})} = l_{\text{RANS}} - f_d \max\left(0, l_{\text{RANS}} - l_{\text{LES}}\right),$$

$$L_T^{(\text{DES})} = \min\left(l_{\text{RANS}}, l_{\text{LES}}\right), \quad L_T^{(\text{IDDES})} = \tilde{f}_d \left(1 + f_e\right) l_{\text{RANS}} + \left(1 - \tilde{f}_d\right) \hat{l}_{\text{LES}}, \tag{8}$$

where f_d, $\tilde{f}_d$, f_e are functions described in [1].

3. Numerical model

The computation is done on our in-house parallel CFD software Orion. Implicit formulation of finite volume method is used, with linear reconstruction to obtain convective fluxes with the HLLC Riemann solver and diffusive fluxes are computed using the values on the diamond cell. Derivatives of the fluxes are computed analytically. Dual time stepping technique is utilized with local time stepping in the dual time.

4. Problem description

The tandem cylinder problem is given by two identical cylinders in a row, the first causing continuous vortex shedding, from which the vortex street passes to the front of the second cylinder, where the separated shear layer temporarily reattaches only to be separated again to form another vortex street. The Reynold number is $166\,000$, with the free stream velocity being 44 m/s. The diameter of the cylinders is $D = 0.057\,15$ m and their axes are $3.7D$ apart.

The computational grid is unstructured with $17\,725$ cells in each of the 30 layers in the z direction that are $0.025D$ thick. The grid satisfies the condition that the dimensionless wall distance $y^+ < 1$ for cells adjacent to the walls. The left domain boundary has the inlet boundary condition prescribed, while the right boundary is for the outlet. The cylinders are no-slip walls (with zero velocity at the surface).

5. Results

The results of the RANS-LES hybrid methods show good agreement with the experimental data by Jenkins et al. [2, 3]. The average pressure coefficients on the rear cylinder are shown in Fig. 1 and show that the SST-IDDES method matches the experimental data almost perfectly. The only difference are the values on the back of the cylinder (after separation occurs), which show some fluctuations in the computed values. This may be due to sampling in the statistical evaluation.

The difference between RANS and RANS-LES hybrid methods in computed vorticities is shown in Figs. 2 and 3. The lack of three-dimensional turbulent fluctuations in the results of the base RANS method is apparent.

6. Conclusions

Hybrid RANS-LES methods based on the two equation SST model showed good agreement with experimental data on the tandem cylinder problem. Even the most basic DES method was able to capture the turbulent flow better than the RANS method and the results obtained by the SST-IDDES model were the closest to the experimental data.
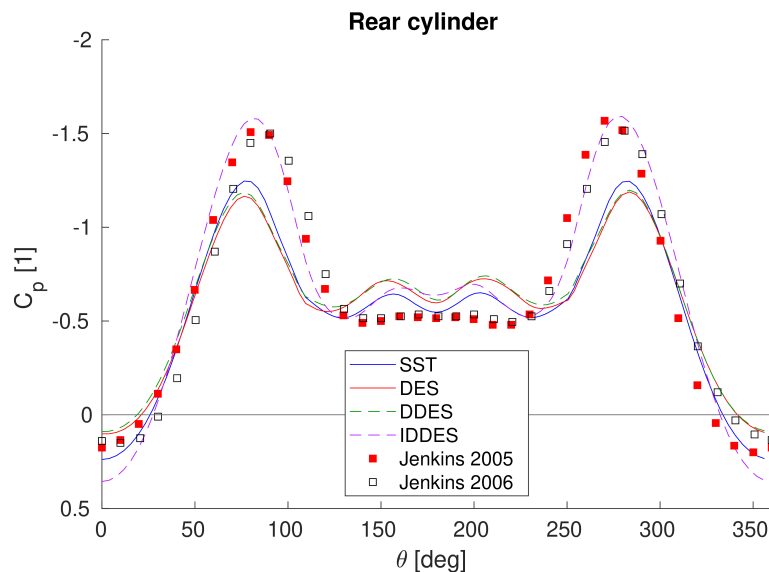
Fig. 1. Comparison of the average computed pressure coefficients on the rear (tandem) cylinder by the base RANS SST model, its RANS-LES hybrid methods and experiments [2, 3]
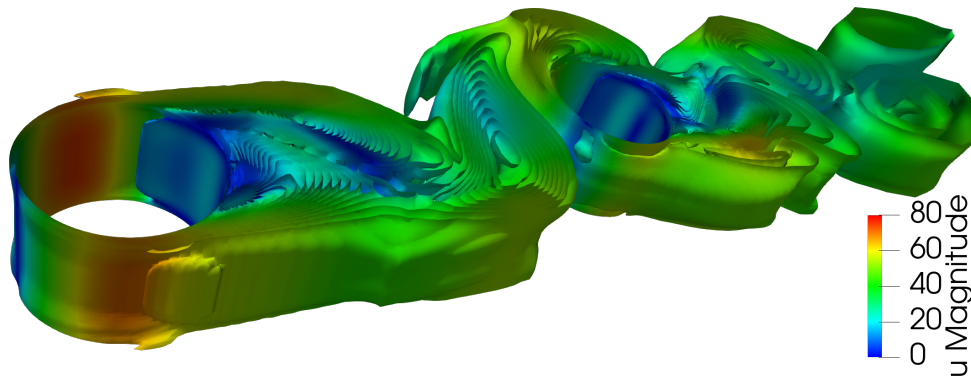
Fig. 2. Vorticity contours colored by computed velocities obtained by the RANS SST model
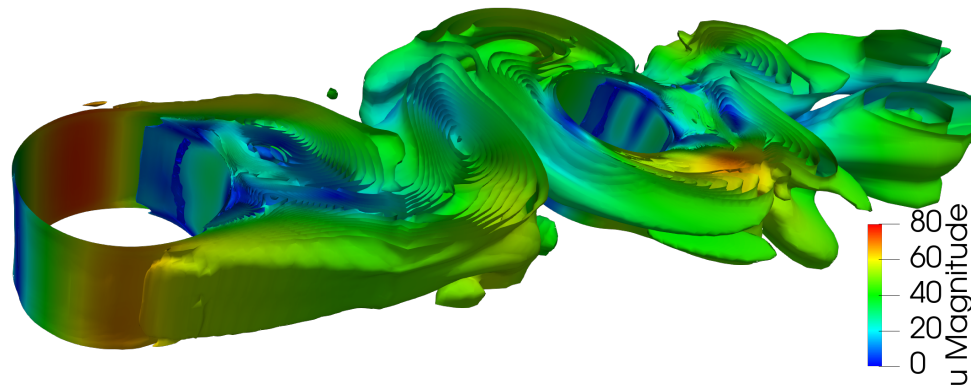
Fig. 3. Vorticity contours colored by computed velocities obtained by the DES-SST model

Acknowledgement

References

[1] Gritskevich, M., Garbaruk, A., Schütze, J., Menter, F., Development of DDES and IDDES formulations for the k–ω shear stress transport model, Flow, Turbulence and Combustion 88 (3) (2012) 431-449.

[2] Jenkins, L., Khorrami, M., Choudhari, M., McGinley, C., Characterization of unsteady flow structures around tandem cylinders for component interaction studies in airframe noise, Proceedings of the 11th AIAA/CEAS Aeroacoustics Conference, 2005.

[3] Jenkins, L., Neuhart, D., McGinley, C., Khorrami, M., Choudhari, M., Measurements of unsteady wake interference between tandem cylinders, Proceedings of the 36th AIAA fluid dynamics conference and exhibit, 2006, AIAA 2006-3202.

[4] Menter, F., Kuntz, M., Langtry, R. B., Ten years of industrial experience with the SST turbulence model, Proceedings of the 4th International Symposium on Turbulence, Heat and Mass Transfer, Begell House Inc., West Redding, 2003, pp. 625-632.

[5] Strelets, M., Detached eddy simulation of massively separated flows, Proceedings of the 39th AIAA Fluid Dynamics Conference and Exhibit, 2001, AIAA 2001-879.

Measurement of paraphysiological strain in entire bones using digital volume correlation

P. Henyš[a], E. Dall'Ara[b], S. Martelli[c,d]

[a]Institute of New Technologies and Applied Informatics, Faculty of Mechatronics, Informatics and Interdisciplinary Studies, Technical University of Liberec, Liberec, Czechia

[b]Department of Oncology and Metabolism and INSIGNEO Institute for In Silico Medicine, University of Sheffield, Sheffield, UK

[c]Centre for Biomedical Technologies, School of Mechanical, Medical and Process Engineering, Queensland University of Technology, Brisbane, Australia

[d]Medical Device Research Institute, College of Science and Engineering, Flinders University, Tonsley SA, Australia

1. Introduction

(Para)physiological bone strain is critical for studying bone pathologies and related research. Digital Volume Correlation (DVC) provides experimental measurements of internal displacements and strains within the entire bone volume. DVC algorithms calculate a deformation map by maximizing a similarity metric in images of an object under two different deformation states. Among many other studies, DVC has been successfully used to study the deformation and fracture mechanism in the entire human femur [3] and the risk of fracture and bone adaptation in metastatic vertebral bodies [5, 6]. The present study quantifies the performance of Symmetric Normalization (SyN) [7] approach for studying the deformation of the human femur under subcritical loading relative to an established method for bone analysis, BoneDVC [1].

2. Methods

The downsampled microstructural images (voxel size: 0.12 mm) of the proximal half femur of a female donor (76 years of age, T-score: -2.12) were obtained at the Australian Synchrotron (Clayton VIC, Australia) during an earlier study [4]. The femur was imaged while subjected to no load and a hip contact force direction representing a static single-leg stance loading configuration whose amplitude caused high strain levels in the internal trabecular network and a localized trabecular collapse [3].

To estimate absolute registration error, a realistic bone displacement field was created synthetically and applied to the images of the undeformed femur using the finite element approach. To create the femur-specific finite-element model, the bone was segmented from the CT images using thresholding and morphometric operations to ensure the smoothness and continuity of the mask and converted into a mesh consisting of linear hexahedral elements. A linear elastic material for bone with a uniform modulus of 1 GPa and Poisson ratio 0.3 was considered. The femur was fully constrained distally. A vertical displacement of 1 mm was applied to a patch of nodes in the superior head of the femur of 1 cm in diameter. A cubic spline interpolation was used to warp the microstructural femur image with a computed displacement field. The displacement field was scaled by factors of 1 and 10, resulting in 2 different volumes with increasing synthetic displacement. Both BoneDVC and SyN were used to compute a map $\Delta(\bar{x})$ between the images of the femur undeformed and the set of images synthetically deformed. The strain error was

defined as a difference between synthetic ε_{ref} and estimated ε

$$\delta\varepsilon := \varepsilon_{ref} - \varepsilon. \tag{1}$$

The strain was computed by projecting it onto a Discontinuous finite element space of zero-order. Considering coordinates $\bar{x}$ of reference image and image being registered x we can define a deformation map such $\Delta(\bar{x}) = x$ provided by SyN or BoneDVC. The displacement at the reference image can be expressed as $u(\bar{x}) = \Delta(\bar{x}) - \bar{x}$. Having displacement function defined on the reference domain, regularised projection of small-strain is employed in virtue of study [2]

$$\int_{\bar{\Omega}} \varepsilon : \delta r \, d\bar{\Omega} + \frac{a}{h} \int_{\partial\bar{\Omega}_e} [\varepsilon] : [\delta r] \, d\bar{s} = \frac{1}{2} \int_{\bar{\Omega}} (\nabla u + \nabla u^T) : \delta r \, d\bar{\Omega} \, , \, \delta r \, \forall V_{L2}. \tag{2}$$

The discontinuity across element interface was penalized with term containing 'jump' operator $[\cdot]$ and smoothing parameter α. Both algorithms consider the NS parameter, which gives the sampling density of the similarity metric for SyN [7] and the resolution of the numerical approximation for BoneDVC [1, 3]. The smoothing parameter α was set up to 10 or less based on zero-strain test [1, 3] and additional extensive numerical experiments. This value allows for keeping strain random error (SDER) under 500 microstrains [3].

3. Results

The highest strain errors were found concentrated in regions with smaller strain amplitudes. While SyN produced notably larger strain errors in regions with lower strains, they were relatively low and homogeneously distributed elsewhere (Fig. 1). The grid size parameter NS affected the strains estimated with BoneDVC more than the strain estimated with SyN. The error in the strain depends rather weakly on the strain amplitude. Observing the spatial distribution of strain errors, SyN generated localized errors in the femoral head and in the distal region of the femur whereas BoneDVC produced the largest error in the femoral head region (Fig. 2).
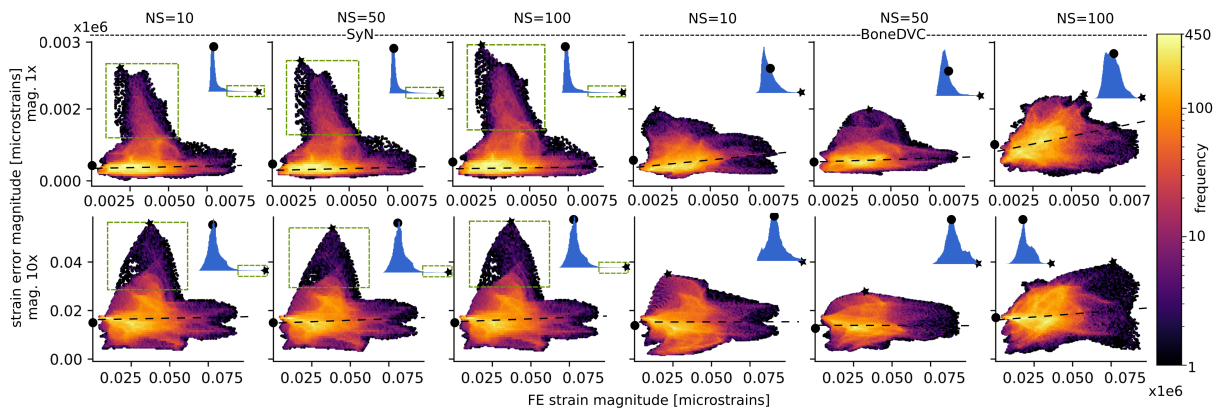
Fig. 1. The strain error dependence on imposed strain for different algorithms setups and magnitude levels. The scalar map displays the number of nodes with similar errors (frequency). A yellow color indicates a high concentration of errors with comparable values (high frequency), while a dark color signifies a low concentration (low frequency). Each line demonstrates the errors for different magnitude levels. The columns describe the sampling density of similarity metrics in the calculation. Blue histograms show error distributions with highest error marked as a black 'star' in both histograms and scatter plots. Dashed curve represents a curve estimated with linear regression. Green dashed boxes border abnormally high error peak regions located in lower amplitude regimes. Black circles represent the median of the error
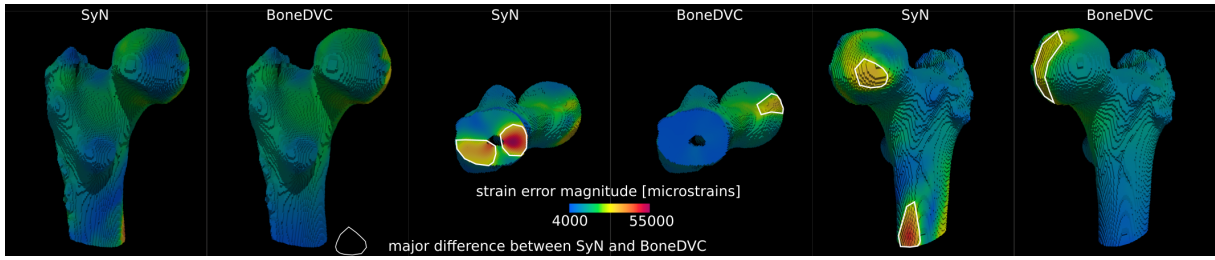
Fig. 2. Major differences in error distribution for strain computed with NS = 10 voxels and magnitude = 10 mm. There are different views of the proximal femur on the left and right

Estimation of the displacement by SyN on a finer mesh showed a strongly localized deformation in the upper part of the femur at the point of contact with the loading device, with maximum displacement equal to 2.1 mm (Fig. 3). This value is closest to the displacement of the actuator (2.66 mm) measured in the images (sample #2, from [3]). The strain map in the SyN results displayed high focal strain in correspondence of a local collapse on the internal trabeculae which was visible earlier only in the full resolution images (0.03 mm voxel size) using BoneDVC [3].
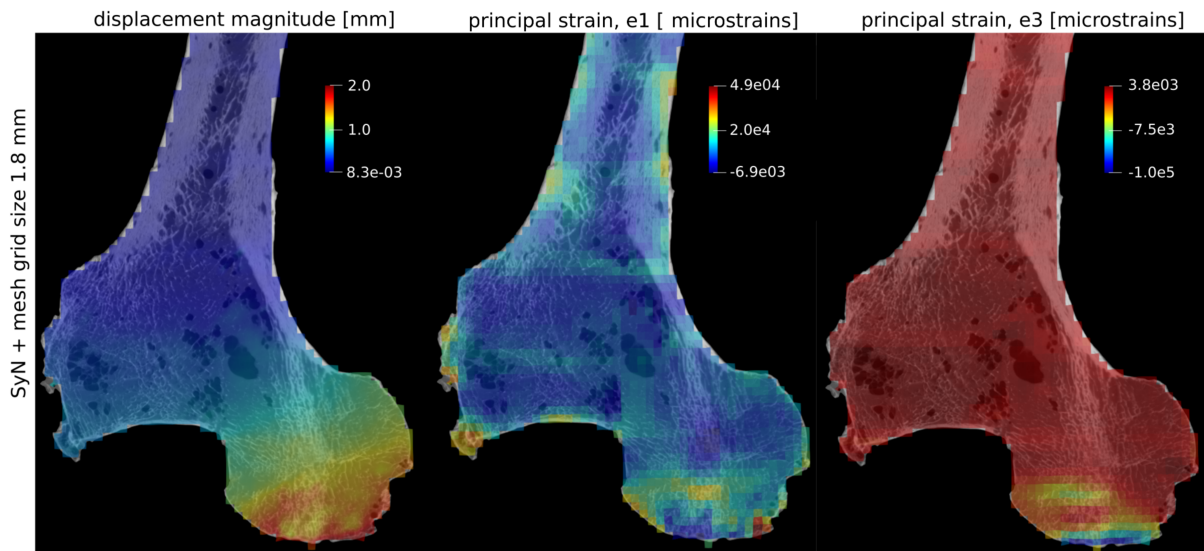
Fig. 3. Displacement and strain of femur under load computed with SyN with sampling rate NS = 50

4. Discussion

The errors in strain of two DVC approaches have been examined in a synthetic realistic displacement calculated using finite element simulation. In summary, it was found that:

- SyN provided a comparable solution to BoneDVC, although the error distribution differed either in terms of location and peak error.
- BoneDVC, in comparison, produces highly accurate strain predictions provided that the nodal spacing NS is carefully chosen balancing accuracy and computational time.
- The assessment of the absolute error should against a realistic deformation of reference allow to calibrate the smoothing parameter for noise suppression while preserving the localized features of the strain field.

Displacement and strain accuracy can be enhanced through smoothing. Generally, the range of values of α can be from zero to infinity, but in practice, the working range is much more narrow and it depends on deformation heterogeneity, mesh size and noise. It is worth noting that the smoothing effect can be partially controlled by BoneDVC's nodal resolution NS [1]. This effect was not observed in SyN where NS primarily influences computation time, but not accuracy. In fact, considering NS equal to 100 voxels resulted in a four-fold reduction in computational time, while maintaining accuracy comparable to NS equal to 1 voxel.

The error in the strain increases slightly with the strain amplitude. There are significant dispersions in the strain errors (especially in the lower strain regions for SyN). These deviations are caused locally and depend on the type of algorithm (i.e., SyN vs. BoneDVC) and also on the setup. Both used DVC methods are non-linear and thus the number of iterations and the numerical accuracy setting significantly affect the ability to correctly compute fine local strain. In both algorithms, these parameters were chosen optimally with respect to computational time.

While BoneDVC uses the optical flow equations to find the continuous deformation, SyN parameterizes the deformation map using sets of solutions of ODEs with uniquely defined initial conditions [7]. In both approaches, some type of additional regularisation is considered to ensure or improve the smoothness of the deformation map $\Delta(x)$. SyN regularises the velocities [7]. In BoneDVC, NS is the key parameter that determines the quality of the estimation because it is the parameter that directly determines at what resolution the displacement is computed. In the case of SyN, this parameter influences the sampling of the similarity metric and, according to the results in this study, does not have a significant impact on accuracy.

References

[1] Dall'Ara, E., Barber, D., Viceconti, M., About the inevitable compromise between spatial resolution and accuracy of strain measurement for bone tissue: A 3D zero-strain study, Journal of Biomechanics 47 (12) (2014) 2956-2963.

[2] Henyš, P., Vořechovský, M., Stebel, J., Kuchař, M., Exner, P., From computed tomography to finite element space: A unified bone material mapping strategy, Clinical Biomechanics 97 (2022) No. 105704.

[3] Martelli, S., Giorgi, M., Dall' Ara, E., Perilli, E., Damage tolerance and toughness of elderly human femora, Acta Biomaterialia 123 (2021) 167-177.

[4] Martelli, S., Perilli, E., Time-elapsed synchrotron-light microstructural imaging of femoral neck fracture, Journal of the Mechanical Behavior of Biomedical Materials 84 (2018) 265-272.

[5] Palanca, M., Cavazzoni, G., Dall'Ara, E., The role of bone metastases on the mechanical competence of human vertebrae, Bone (2023) No. 116814.

[6] Palanca, M., De Donno, G., Dall'Ara, E., A novel approach to evaluate the effects of artificial bone focal lesion on the three-dimensional strain distributions within the vertebral body, Plos ONE 16 (6) (2021) No. e0251873.

[7] Tustison, N. J., Cook, P. A., Holbrook, A. J., Johnson, H. J., Muschelli, J., Devenyi, G. A., Duda, J. T., Das, S. R., Cullen, N. C., Gillen, D. L., Yassa, M. A., Stone, J. R., Gee, J. C., Avants, B. B., The ANTsX ecosystem for quantitative biological and medical imaging, Scientific Reports 11 (1) (2021) No. 9068.

Performance comparison between ducted fan driven by ICE and electric motor

D. Hermann[a], J. Klesa[a], F. Brož[a]

[a]*Department of Aerospace Engineering, Faculty of Mechanical Engineering, Czech Technical University in Prague, Technická 4, 160 00 Prague, Czech Republic*

1. Introduction

Today's drive towards zero-emission operation is evident in all areas of passenger and freight transport. The origins of electrically powered aircraft can be traced back to the 1960s, when the first radio-controlled model aircraft appeared. Electricity storage technologies have made great strides in recent decades, and today's lithium based-batteries have many times the energy density. The technology of electric motors and control electronics has also advanced significantly, allowing for increased performance, downsizing and lightweighting. All of these factors have brought the use of electric power to power aircraft in all modes of transportation closer. But despite progress, the specific energy of fossil fuels remains 30–40 times greater, which is first and most important reason why the widespread application of electric propulsion in this sector will be complicated.

This paper describes a comparison of the flight performance of an ultralight aircraft with ducted fan propulsion. The author aims to find and describe the differences in performance of the UL39 ALBI II aircraft, where the fan will be driven by a piston internal combustion engine in the first case and an electric motor in the second.

2. Methods

Design point is taken from [3] and can be found in Table 1. A compressible fluid model is used because the flight velocity range is 0–$100\,\mathrm{m\,s^{-1}}$ and the upper limit is on the border between incompressible and compressible flow. And also this method could be used for faster aircraft than the ultralight category.

2.1 Fan characteristics

The aim of the first step is to find compressor characteristics [1] for what was used Numerical Propulsion System Simulation Code described in [2]. Computed characteristics can be found

Table 1. Fan design point

Fan pressure ratio Π	1.062
Fan diameter D	660 mm
Motor RPM	7 800
Fan air mass flow $\dot{m}$	$33.46\,\mathrm{kg\,s^{-1}}$
Fan efficiency η_{fan}	0.85
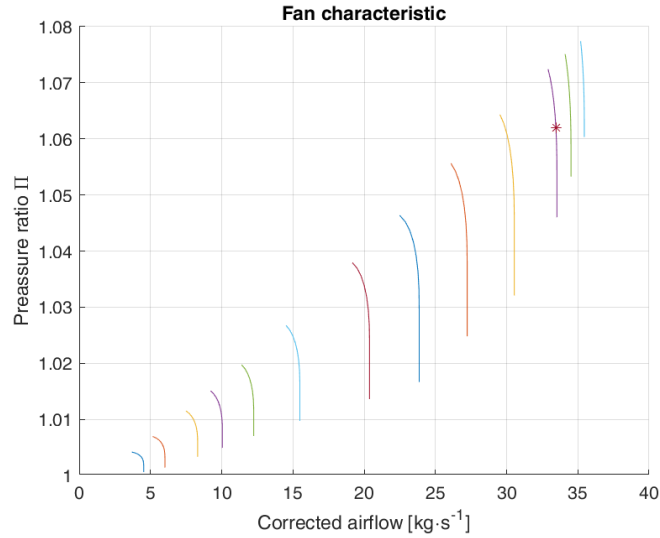
Fig. 1. Fan characteristics

in Fig. 1. The values deducted from the characteristic will be used to calculate the thrust for different values of speed and airflow.

2.2 Thrust

The values of the state variables at the inlet to the compressor channel corresponded to the values of 0m ISA and can be found in Table 2. According to the equations for compressible flow were determined values in front and behind of fan thanks to which the velocity values at the nozzle outlet v_3 could be determined. The thrust of the propulsion system is determined from the momentum conservation law

$$T = \dot{m} \cdot (v_3 - v_0), \tag{1}$$

where the air mass flow is taken from fan characteristics.

2.3 Propulsion efficiency

Propulsion efficiency is defined by the following standard formula:

$$\eta_{prop} = \frac{T \cdot v_0}{P}, \tag{2}$$

where P is engine power taken from ICE and electric motor characteristics.

Table 2. Input parameters for the propulsion system

Flight velocity range v_0	0-100 m s^{-1}
Air density ρ	1.225 kg m^3
Atmospheric pressure p_{s0}	101 325 Pa
Air temperature T_{s0}	288.15 K
Air specific heat at constant pressure c_p	1004.5 J kg^{-1} K^{-1}
Air ratio of specific heats κ	1.4
Air specific gas constant r	287.1 J kg^{-1} K^{-1}

3. Results

The results of this study are thrust curves (i.e., dependence of the thrust on the flight velocity) and propulsion efficiency for different mass air flows, RPM, and different power unit of fan, see Figs. 2–5.
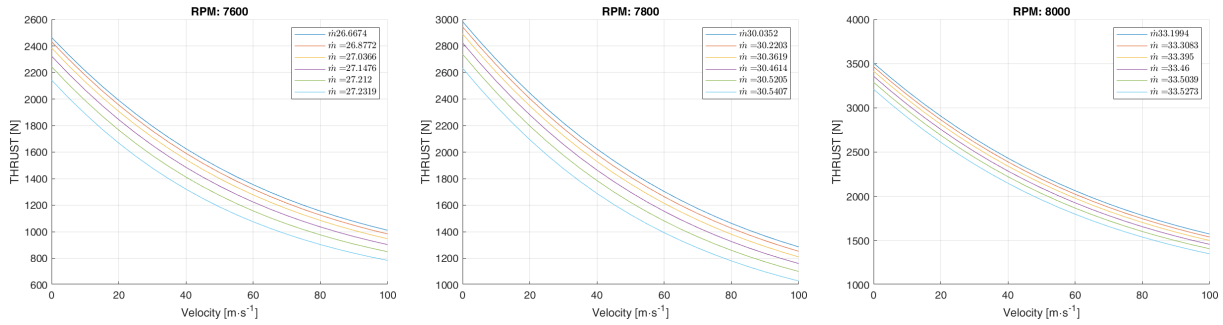
Fig. 2. Thrust curve on different RPM and airflow
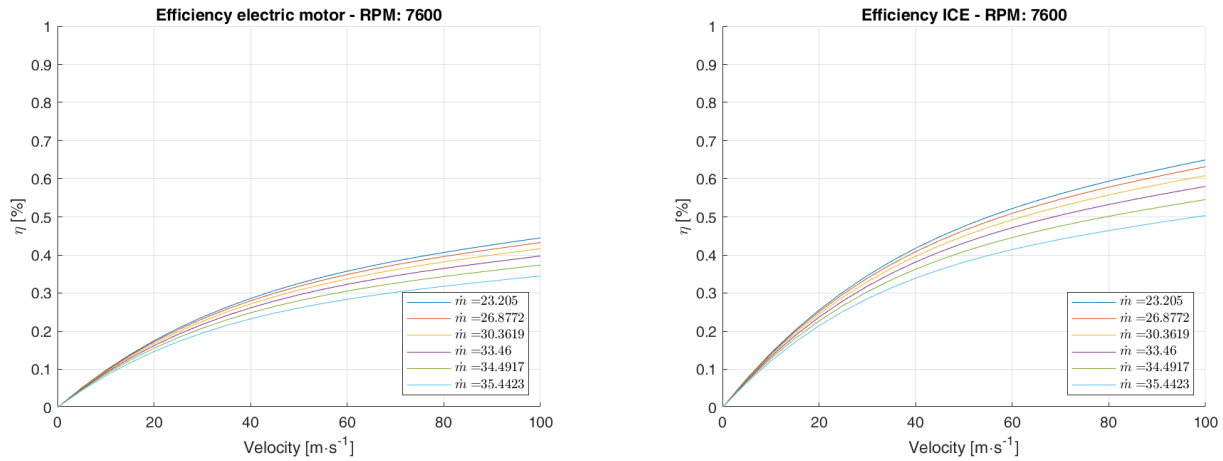
Fig. 3. Propulsion efficiency on 7 600 RPM: (left) electric motor, (right) ICE
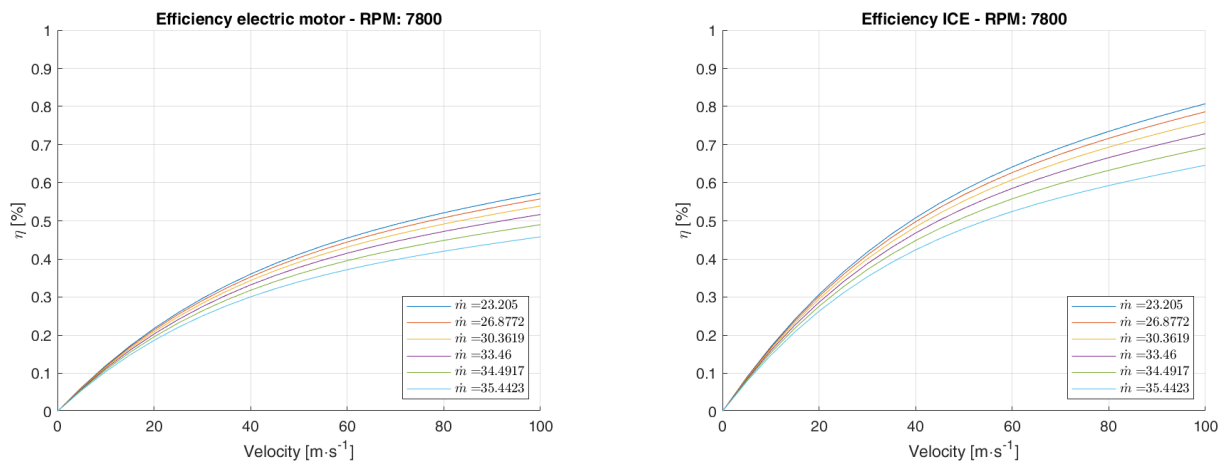
Fig. 4. Propulsion efficiency on 7 800 RPM: (left) electric motor, (right) ICE
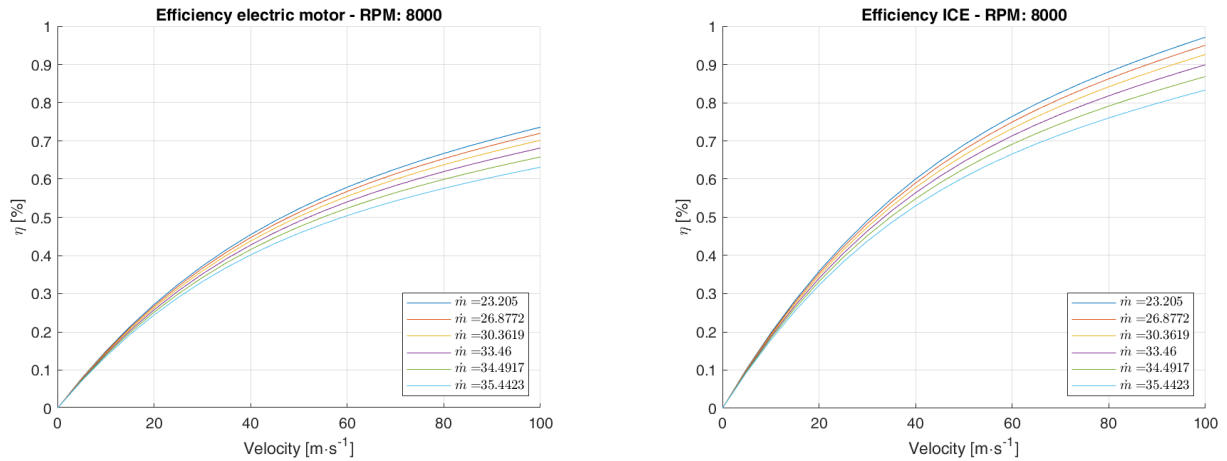
Fig. 5. Propulsion efficiency on 8 000 RPM: (left) electric motor, (right) ICE

4. Conclusion

The results show that ICE reaches higher propulsion efficiency because the power of ICE grows gradually with RPM. Whereabouts power of electric engine reaches their peak in low RPM and very slowly declining.

Acknowledgement

References

[1] Cumpsty, N. A., Compressor aerodynamics, Krieger, Malabar, 2004.

[2] Jones, S. M., An introduction to thermodynamic performance analysis of aircraft gas turbine engine cycles using the numerical propulsion system simulation code, NASA Glenn Research Center, Cleveland, 2007.

[3] Klesa, J., Determination of fan design parameters for flight-sport aircraft, Acta Polytechnica 62 (5) (2022) 549-557.

Numerical simulation of the adhesive interface

L. Horák[a], J. Krystek[a]

[a]*Department of Mechanics, Faculty of Applied Sciences, University of West Bohemia,*
Univerzitní 8, 301 00 Plzeň, Czech Republic

This work shows possible approaches to modeling crack propagation in a thin adhesive layer in a simple double cantilever beam (DCB) sample. Materials of DCB samples consist of epoxy adhesive and carbonepoxid composite. Numerical simulation is modeled based on experiments done in work [2] where increased temperature's influence on pure modes I and II was observed. The further objective is to determine the sensitivity of models parameters to maximum force and fracture toughness.

The motivation for this work is the increasing interest of the industry in adhesive bonding of composite materials due to their advantages, such as nondestructive bonding, more uniform stress distribution, and high fatigue resistance. This leads to high interest in material research and its simulation research. Adhesive can be used on large surfaces where failure on sides is not necessarily a failure of the whole part, and crack propagation is of interest. The effect of demanding operating conditions is one of the other interests in the research community.

For numerical simulation, the finite element method was used. Two main approaches to crack propagation simulations are discrete crack models or smeared crack models [5]. In this work, three discrete methods were used, namely cohesive zone model (CZM) with element deletion, extended finite element method (XFEM), and classical finite element method (FEM) with element deletion [1].

DCB sample is fabricated from two prismatic strips, which are bonded on the part of the surface, and then two loading blocks, used for transferring loads from the universal test machine, are glued to the ends. The geometry of the DCB sample is shown in Fig. 1. Loading blocks are pulled in opposite directions, and the adhesive breaks cohesively, which corresponds with pure
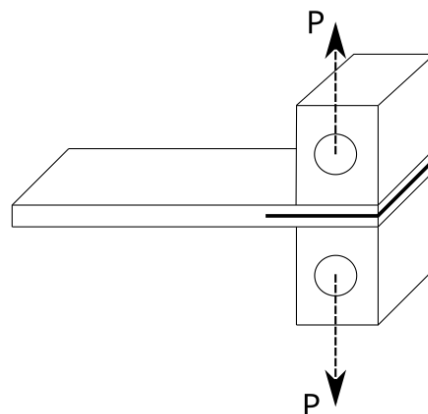
Fig. 1. Scheme of DCB sample and its loading points

mode I fracture. The effect of temperature was considered in the model by lowering all adhesive parameters in the same ratio of fracture toughness for mode I in elevated temperature ($50°$ C) and room temperature. This temperature does not have any considerable effect on composite material. For this reason, the parameters of the composite have not been modified in any way.

Models were created in Abaqus/CAE and computed in Abaqus/standard. In the next bullet points, essential parameters are described for three models.

- *CZM model:* Due to the considerable thickness of the adhesive part, CZM elements with finite thickness were used (COH2D4). Cohesive behavior was described by traction-separation parameters. Quadratic nominal stress damage (Quads) initiation criteria were used to predict damage initiation in cohesive elements, and damage evolution was described by energy-based mixed mode behavior by Benzeggagh-Kenane. Adherends were modeled by plane strain element with incompatible modes enabled (CPE4I).

- *XFEM model:* The adhesive layer was enriched by XFEM, where plane strain elements were used (C4PE). The elastic behavior of adhesive was modeled as isotropic. Maximum principal stress (Maxps) initiation criteria were used to predict damage initiation in the XFEM enriched region. The same damage evolution model was used as in CZM. Also, adherends were modeled as in CZM.

- *Ductile model:* For the last method, plane stress elements with incompatible modes enabled (CPS4I) were used. This change from previous models was done because of ductile damage initiation criteria, which is based on fracture strain. The adhesive was modeled as elastic isotropic with plasticity. Damage evolution was modeled as energy-based with a mode-independent definition. This energy had to be scaled to match previous models in Force displacement output.

Viscosity in adhesive elements for CZM and ductile damage model was specified due to convergence issue. This improved numerical stability and computational time. For the XFEM model, a stable solution and correct crack propagation was achieved with a different adhesive mesh and adherend mesh so that most of the nodes do not connect directly. Further adhesive geometry near crack initiation had to be modified for each method to get a stable solution. Material parameters for adhesive 3M$^{\text{TM}}$ Scotch-Weld$^{\text{TM}}$ Epoxy Adhesive DP490, were taken from work [4] and for composite material KORDCARBON-CPREG200T3KEP142A from [3].

For further evaluation, adhesive fracture toughness for mode I was computed according to the modified beam theory as

$$G_I = \frac{3P\delta}{2B(a + |\Delta|)}, \tag{1}$$

where P is applied load during crack propagation with crack length a. δ is load point displacement, B is width of specimen and Δ is term for correction due to possible rotation, which was set to zero.

All methods are evaluated in Fig. 2, where numerical methods are compared with the experiment. On the left figure are Force–displacement ($P - \delta$) curves, and on the right are R–curves, which are fracture thougness – crack length ($G_I - a$). Force–displacement results were obtained from the top loading point and are consistent with the experiment. Fracture toughness was computed as in experiments where crack length was measured from the loading point. R–curve was then constructed for multiple time increments throughout the simulation. Inconsistent values of fracture toughness were observed, where CZM has the largest difference from the experiment. This leads to the conclusion that the three methods are not equivalent. Further study of mesh sensitivity should be performed.
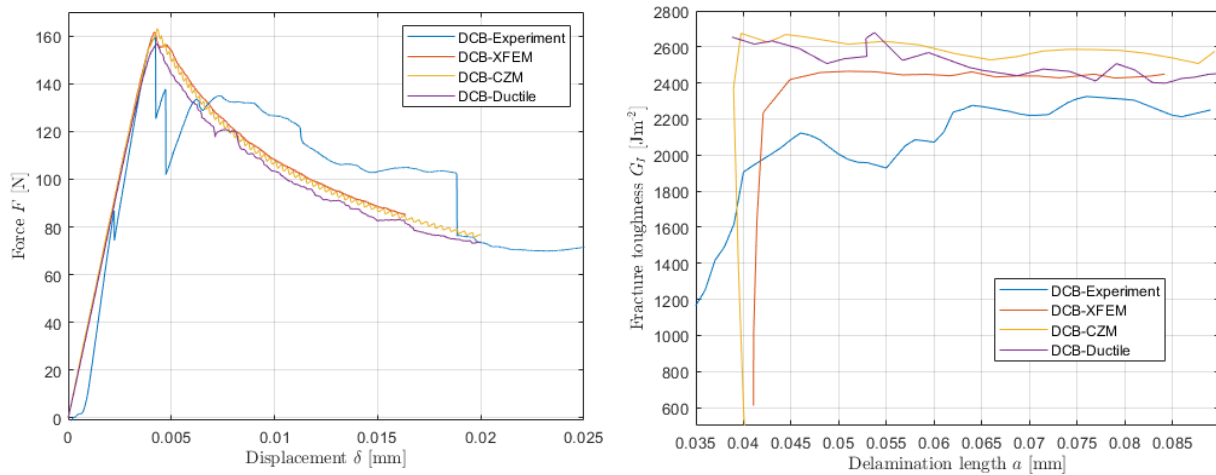
Fig. 2. Evaluation of numerical simulation and experiments: (left) force vs displacement, (right) resistance curve (R–curve)

In this work, three approaches for modeling crack propagation were compared. These methods are consistent for force–displacement evaluation but are not consistent for R–curve evaluation. Computational cost between XFEM and ductile model with element deletion were comparable, and CZM was the most efficient.

Acknowledgement

References

[1] Barbero, E. J., Finite element analysis of composite materials using Abaqus, CRC Press, Taylor & Francis Group, 2013.

[2] Horák, L., Krystek, J., Effect of temperature of adhesively bonded composite on loading of pure mode I and II, Proceedings of the 24th International Scientific Conference Applied Mechanics 2023, Piešťany, Spektrum STU, 2023, pp. 39-42.

[3] Krystek, J., Zajíček, M., Kottner, R., Identification of mechanical properties of KORDCARBON-CPREG-200-T-3K-EP1-42-A composite, Materials Science and Engineering 776 (2020) No. 012074.

[4] Sadeghi, M. Z., Weiland, J., Zimmermann, J.,Schiebahn, A., Reisgen, U., Schröder, K. U., Experimental and FE investigations on the influential parameters in positioning and measurement of strain gauges in adhesively bonded single lap joints, Elsevier, virtual conference, 2020.

[5] Verhoosel, C. V., Borst, R., A phase-field model for cohesive fracture, International Journal for Numerical Methods in Engineering 96 (1) (2013) 43-62.

Vibration attenuation properties of piezoelectric metamaterial plates

A. Hosseinkhani[a], E. Rohan[a]

[a]Department of Mechanics, Faculty of Applied Sciences, University of West Bohemia, Univerzitní 8, 301 00 Plzeň, Czech Republic

1. Introduction

Metamaterials, due to their exceptional properties beyond those of conventional materials, find applications in various fields, including vibration control. One subset of metamaterials is Phononic Crystals (PCs), which are able to manipulate the propagation of elastic waves. PCs are constructed by periodically repeating a heterogeneous structure known as a unit-cell [3]. The feature that provides the ability of wave manipulation for a PC is called bandgap. Over the bandgap frequencies, the propagation of elastic waves can be stopped completely. Bandgaps are influenced by several parameters, such as geometrical and material properties. In this regard, different geometry and material optimization techniques have been employed in the literature on metamaterials to achieve the best performance in terms of bandgap frequencies [4, 5]. Once the PCs are integrated with piezoelectric materials, more options will be available to control the bandgap properties. An electric circuit (named shunting circuit) can be attached to such materials, and the bandgap features can be changed by the use of electrical properties [2].

In this study, a heterogeneous piezoelectric 2-D plate is considered. The heterogeneity provides the periodic structure with the antiresonance property inducing a non-dissipative damping within specific frequency ranges called bandgaps, where the standing or propagating waves are suppressed. This paper examines different mechanisms for controlling bandgap properties and investigates their influences on bandgap characteristics. Finally, the bandgaps are utilized for controlling the propagation of vibrational waves along the piezoelectric plate in the frequency domain.

2. Bandgap diagram and vibration attenuation

A phononic crystal consisting of a piezoelectric matrix and solid inclusions is considered, as shown in Fig.1. The bandgap diagram and the corresponding geometrical parameters are also presented in Fig.1. The chosen material for the matrix is PZT-5A, and for the inclusion a solid-soft material with mechanical properties of $E = 4 \cdot 10^8$ Pa, $\rho = 6500 \ \text{kg/m}^3$, $v = 0.3$ is considered. In this context, 'soft inclusion' refers to a material whose elastic modulus is significantly lower than that of the matrix.

The governing equations of the solid and piezoelectric mediums are as Eqs. (1) and (2), respectively:

$$\rho \ddot{u}(r, t) - \nabla . \sigma(u) = 0, \tag{1}$$

$$\rho \ddot{u}(r, t) - \nabla . \sigma(u, \phi) = 0,$$
$$-\nabla . D(u, \phi) = 0. \tag{2}$$

The bandgap diagram is obtained from the dispersion analysis of these equations with the following Floquet-Bloch periodic boundary condition

$$u_\square(r + L) = u_k(r)e^{ikL}, \tag{3}$$

where L is the periodicity length of the structure. Detailed descriptions about the evaluation of the bandgap diagram can be found in [1].
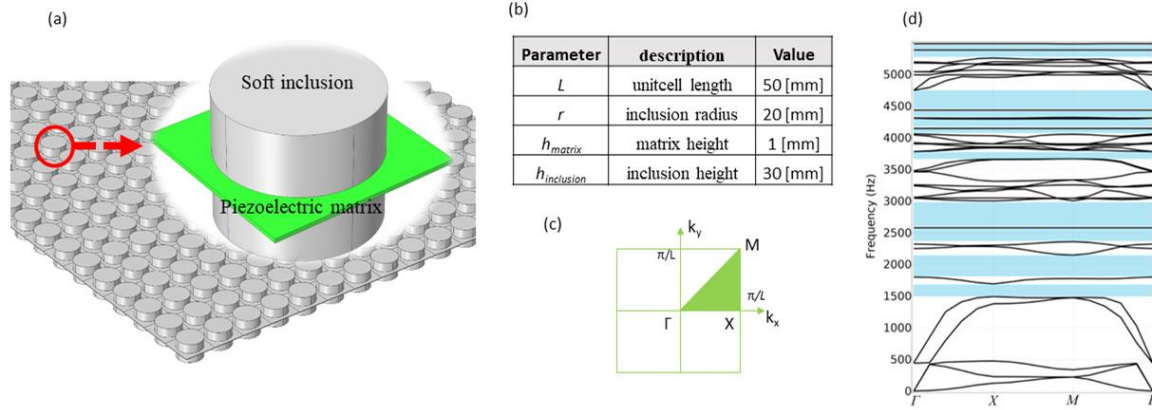
Fig. 1. (a) Schematic of the periodic structure and the unit-cell, (b) geometrical parameters (c) wave vectors and IBZ (d) the bandgap diagram

One critical geometrical parameter in this structure is inclusion height. As one example, the effects of this parameter, besides the schematic of the unit cell, are presented in Fig. 2 for three different heights:1 mm, 15 mm, and 30 mm. As it is observed, no bandgap exists for the case of 1 mm, while some narrow bandgaps have appeared as the height is increased to 15 mm. By following the increase of height, more bandgaps with wider ranges are achieved. This validates the effects of inertia that increase with increasing height. Bandgaps are also shifted to lower frequencies as the height increases.
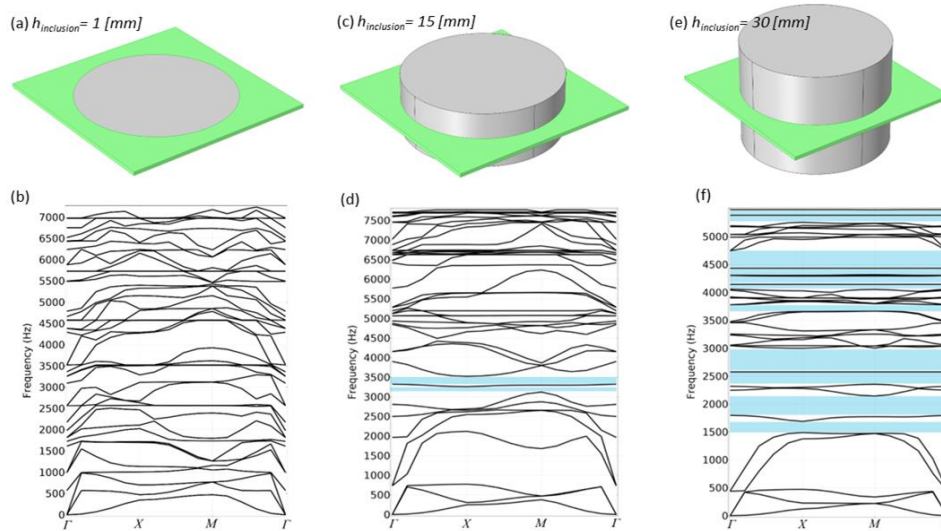
Fig. 2. Effects of inclusion height on the bandgap properties (a) $h_{inclusion}$= 1mm, (a) $h_{inclusion}$= 15 mm, (c) $h_{inclusion}$= 30mm

Then, a shunting circuit is connected to the piezoelectric element. Just a single resistor with the impedance of R (Ω) is considered to act as the shunting circuit (Fig. 3). As an example of the effect of the circuit on mechanical parameters, the elasticity matrix (c^{SU}) is calculated as the

inverse of the compliance matrix ($c^{SU}=(s^{SU})^{-1}$), and then its first component (E_{11}) is plotted versus electric resistance and frequency (Fig. 3b). As we can see, by changing the electric resistance, E_{11} changes about 50% (from $1.2 \cdot 10^{11}$ to $1.8 \cdot 10^{11}$). The shunting circuit changes the material properties and, accordingly, the bandgap properties.

(a)

(b)
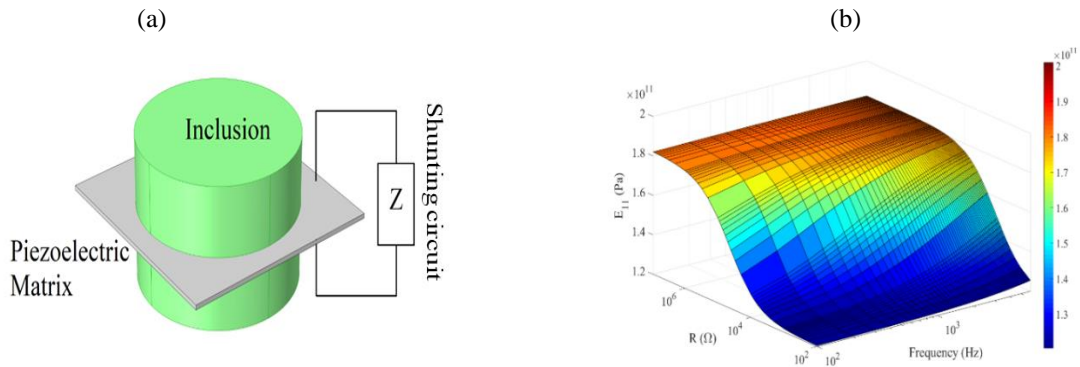
Fig. 2. (a) Schematic of the shunting circuit. (b) The variations of elasticity tensor component (E_{11}) with respect to electric resistance and frequency. (c) Variations of FBGOF and WFBG with respect to electrical resistance

Finally, the presented unit-cell is utilized in a finite structure and the vibration attenuation along the structure is investigated. Vibration attenuation is evaluated by defining the term Transmission Loss (TL) as $TL=20 \log(Y_{out}/Y_{in})$. The schematic of the finite meta-structure with the Periodic Boundary Conditions (P.B.C) and input as well as output points are depicted. TL is calculated and plotted beside the bandgap frequency ranges in Fig. 4. We can see that over the bandgaps, a big gain is achieved in TL for the meta-structure that is equivalent to no wave propagation.

(a)

(b)
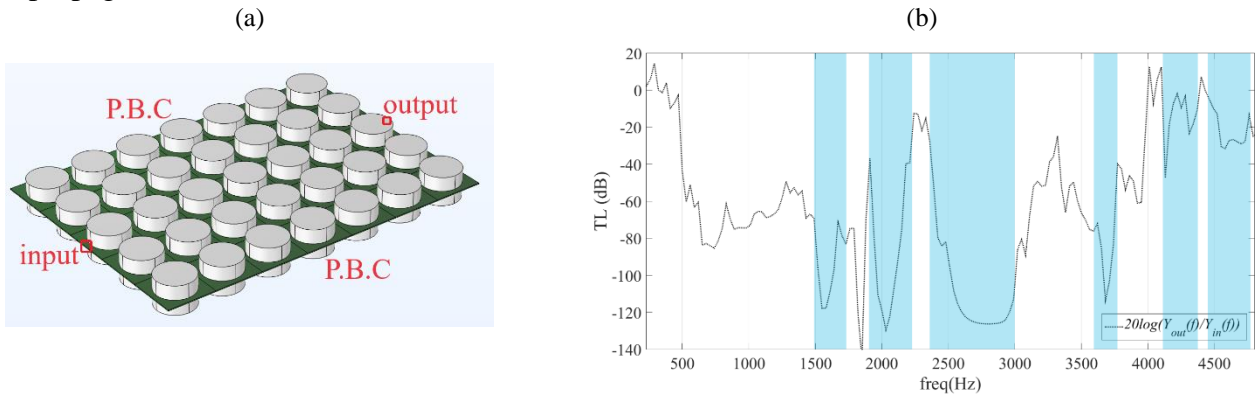
Fig. 4. (a) Schematic of the fitnie phononic crystal. (b) Transmission Loss diagram over the considered frequency range

3. Conclusion

A two-dimensional phononic crystal (a piezoelectric matrix interacting with soft inclusions) was investigated in this paper. The mechanisms of geometrical properties for controlling bandgap features and electrical properties for controlling the mechanical response were studied. The obtained results confirm the ability of such structures to control the propagation of vibrational waves, whereby more than 100 dB reduction was achieved over the bandgap frequencies.

Acknowledgement

References

[1] Deymier, P.A., Acoustic metamaterials and phononic crystals, Springer Science & Business Media, 2013.

[2] Hagood, N.W. and Flotow, A.V., Damping of structural vibrations with piezoelectric materials and passive electrical networks, Journal of sound and vibration, (146) (2) (1991) 243-268.

[3] Lu, M.H., Feng, L. and Chen, Y.F. "Phononic crystals and acoustic metamaterials." Materials today, (12) (12) (2009) 34-42.

[4] Panahi, E., Hosseinkhani, A., Frangi, A., Younesian, D., and Zega, V., A novel low-frequency multi-bandgaps metaplate: Genetic algorithm based optimization and experimental validation, Mechanical Systems and Signal Processing, (181) (2022) 109495.

[5] Vondřejc, J., Rohan, E., and Heczko, J., Shape optimization of phononic band gap structures using the homogenization approach, International Journal of Solids and Structures, (113) (2017) 147-168.

Modeling and implementation of joints in 2-D multibody dynamics considering chosen imperfections

M. Hrabačka[a], M. Hajžman[a], M. Byrtus[a], Š. Dyk[b], R. Bulín[b], L. Smolík[b]

[a]*Department of Mechanics, Faculty of Applied Sciences, University of West Bohemia, Univerzitní 8, 301 00 Plzeň, Czech Republic*
[b]*NTIS – New Technologies for the Information Society, Faculty of Applied Sciences, University of West Bohemia, Univerzitní 8, 301 00 Plzeň, Czech Republic*

Software for simulating multibody systems' (MBS) dynamics allows engineers to study and investigate mechanical and mechatronic systems' motion. It enables them to generate and solve virtual 3D models to predict and visualise motion, coupling forces, or stresses [2].

Because simulation of MBS dynamics is usually quite time demanding, MBS software must be efficient in calculations if it is to be employable in practice. This work focuses on joint formulations and their evaluation efficiency, as these expressions are evaluated many times during simulations. Moreover, the contribution investigates effects of joint imperfections (friction and clearance) on the resulting motion of a 2-D slider-crank mechanism.

The mathematical basis of the in-house developed MBS software is formed by Lagrange's equations of the first kind that represent a set of findings achieved by applying Hamilton's principle. The dynamics of a spatial system of n interconnected rigid bodies can be described according to [3] by a system of $6n + r$ differential-algebraic equations (DAEs)

$$\begin{bmatrix} \mathbf{M} & \mathbf{C_q^T} \\ \mathbf{C_q} & \mathbf{0} \end{bmatrix} \begin{bmatrix} \ddot{\mathbf{q}} \\ \boldsymbol{\lambda} \end{bmatrix} = \begin{bmatrix} \mathbf{Q}_e + \mathbf{Q}_v \\ \mathbf{Q}_d \end{bmatrix}, \tag{1}$$

where $\mathbf{M}$ is the system mass matrix, $\mathbf{q}$ is the vector of generalised coordinates of all bodies consisting of generalised coordinates $\mathbf{q}^i = [\mathbf{R}^i, \boldsymbol{\Phi}^i]^{\mathrm{T}}$ of particular bodies ($\mathbf{R}^i$ are the absolute Cartesian coordinates and $\boldsymbol{\Phi}^i$ are the orientation angles), $\boldsymbol{\lambda}$ is the vector of Lagrange multipliers, $\mathbf{Q}_e$ is the vector of generalised applied forces, and $\mathbf{Q}_v$ is the quadratic velocity vector. The constraint Jacobian matrix $\mathbf{C_q}$ and the vector $\mathbf{Q}_d$ are products of time derivatives of kinematic constraints (kinematic relationships describing mechanical joints or specified motion trajectories) represented by an algebraic system of r constraint equations

$$\mathbf{C}(\mathbf{q}, t) = \mathbf{0}, \tag{2}$$

where $\mathbf{C}$ is the constraint vector. If system (2) is twice partially differentiated with respect to time t, the kinematic acceleration equations are obtained, forming the last r equations in (1), where the vector $\mathbf{Q}_d$ can be expanded to

$$\mathbf{Q}_d = -\mathbf{C}_{tt} - (\mathbf{C_q}\dot{\mathbf{q}})_{\mathbf{q}}\dot{\mathbf{q}} - 2\mathbf{C}_{\mathbf{q}t}\dot{\mathbf{q}}. \tag{3}$$

Lower indices $\cdot_t$ and $\cdot_\mathbf{q}$ indicate partial derivatives with respect to time and with respect to generalised coordinates.

One of many possible approaches to solve the problem of MBS dynamics is, for instance, to convert system (1) of DAEs of index 1 to the underlying system of ordinary differential

equations (ODEs) and subsequent usage of some standard ODE solver. The transformation of (1) to a system of ODEs can be done via the elimination of Lagrange multipliers, obtaining

$$\ddot{\mathbf{q}} = \mathbf{M}^{-1}\mathbf{C_q^T}(\mathbf{C_q}\mathbf{M}^{-1}\mathbf{C_q^T})^{-1}[\mathbf{Q}_d - \mathbf{C_q}\mathbf{M}^{-1}(\mathbf{Q}_e + \mathbf{Q}_v)] + \mathbf{M}^{-1}(\mathbf{Q}_e + \mathbf{Q}_v). \qquad (4)$$

System (4) of ODEs can be solved directly, and it is possible to improve numerical accuracy via stabilization techniques, e.g., Baumgarte's stabilization, which can be found in [1].

(a) Kinematic constraint   (b) Contact model
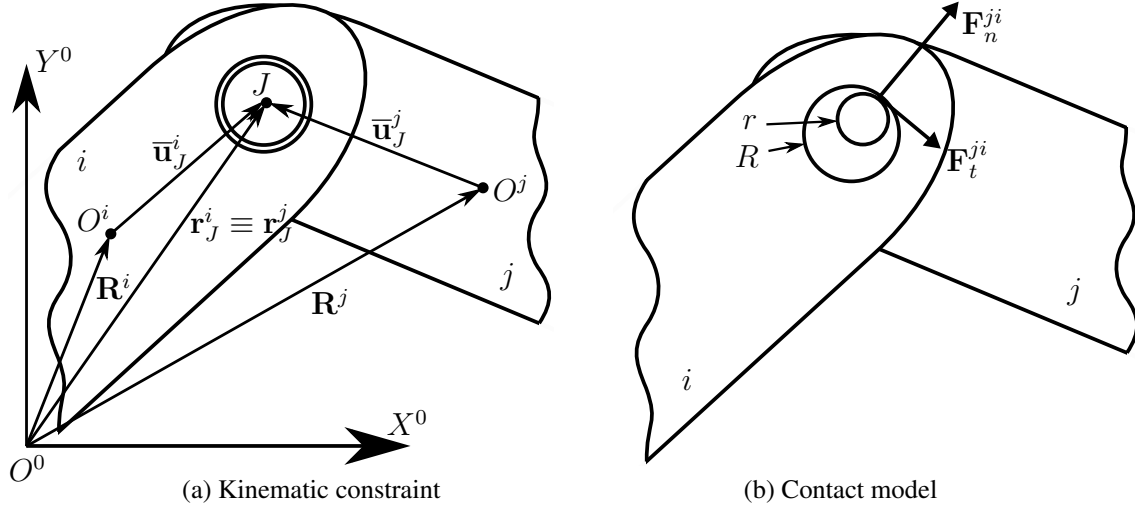
Fig. 1. Two approaches to modeling a revolute joint

There are two basic ways how to define a connection (usually called a joint) between two bodies. First approach is to use kinematic constraints representing restrictions on the relative motion between connected bodies. For instance, a revolute joint visualised in Fig. 1a eliminates relative translation between two bodies, or a prismatic joint eliminates relative rotation between two bodies. There are several other joint constraints and some of them have realistic meaning only in 3-D space such as a cylindrical joint or a spherical joint. All joints defined as kinematic constraints are included in the constraint vector $\mathbf{C}$. In Fig. 1a, a revolute joint constraint is visualised, where $\mathbf{R}^{i,j}$ are absolute coordinate vectors of linked bodies, $\overline{\mathbf{u}}_J^{i,j}$ are coordinate vectors of the joint J in local coordinate systems with origins $O^{i,j}$, and $\mathbf{r}^{i,j}$ are coordinate vectors of the joint in absolute coordinate system with origin O^0. The constraint equation is simple in case of the revolute joint: $\mathbf{r}_J^i - \mathbf{r}_J^j = 0$.

The idea of the second approach is in specifying contact forces that are generated when surfaces of two particular bodies touch each other. Similarly to the kinematic approach, there are different definitions of contact forces depending on the type of a joint. All joints that are represented by contact forces are simply included the vector $\mathbf{Q}_e$ of generalised applied forces. Fig. 1b contains visualization of a revolute joint with contact forces $\mathbf{F}_n^{ji}$ and $\mathbf{F}_t^{ji}$ applied on the body i (contact forces applied on the body j are not shown, as they can be trivially derived by applying Newton's third law), where R is the radius of the bearing, and r is the radius of the journal.

The advantage of the contact approach lies in the fact that it naturally contains parameters of joint imperfections (friction and clearance). In case of kinematic constraints, additional equation defining friction force has to be included in the model, and it is obviously impossible to include joint clearance. In this work, the first approach is used only in case of ideal joints without any imperfections. If it is needed to incorporate joint imperfection, the second approach is utilised.

During the implementation of any joint kinematic constraint to MBS software, it is necessary to have access not only to the constraint vector $\mathbf{C}$ but mainly to its derivatives $\mathbf{C_q}$ and $\mathbf{C_{qq}}$, while the second expression is included in the modified form of (3). Equation (3) also contains derivatives with respect to time t, but since joint kinematic constraints are usually scleronomic, all time derivatives of $\mathbf{C}$ are zero. Nevertheless, evaluation of $\mathbf{C_q}$ and $\mathbf{C_{qq}}$ is generally quite time consuming operation and represents a significant portion of total simulation time. On the other hand, evaluation of contact forces is not as time consuming as kinematic constraints, however, those forces bring important non-linearities to the mathematical model. This has to be taken into account when choosing and setting the numerical solver, and simulating non-linear system is generally more time consuming than solving the linear one.
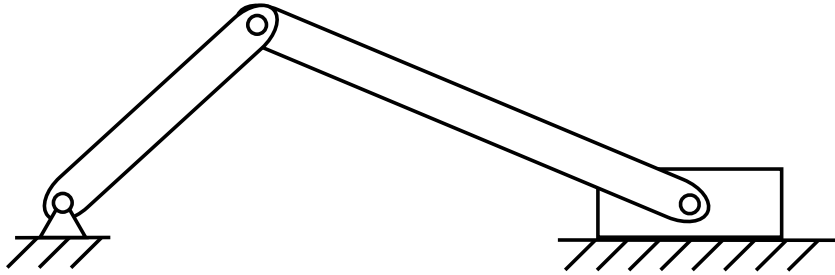
Fig. 2. A 2-D slider-crank mechanism

This work compares time demand for simulating the motion of a 2-D slider-crank mechanism, which is depicted in Fig. 2, without imperfections in two different model versions. Both versions differ in the approach used for modeling the joint between the crank and the connecting rod. All other joints (revolute between the frame and the crank, revolute between connecting the rod and the slider, prismatic between the slider and the frame) are defined as kinematic constraints in both models.

Furthermore, the effects of imperfections of the joint linking the crank and the connecting rod are investigated in a separate study. Specifically, the influence of the clearance size $R-r$ and the amount of friction are examined during various working conditions defined by the angular velocity of the crank.

Acknowledgements

References

[1] Hajžman, M., Polach, P., Application of stabilization techniques in the dynamic analysis of multibody systems, Applied and Computational Mechanics 1 (2) (2007) 479-488.
[2] Schiehlen, W., Advanced multibody system dynamics, Kluwer Academic Publishers, 1993.
[3] Shabana, A. A., Computational dynamics, Third edition, John Wiley & Sons, 2010.

The role of boundary conditions and viscosity models
in thrombosis modelling

A. Jonášová[a], S. Plánička[b], J. Vimmr[a]

[a] Department of Mechanics, Faculty of Applied Sciences, University of West Bohemia, Univerzitní 8, 301 00 Plzeň, Czech Republic
[b] NTIS – New Technologies for the Information Society, Faculty of Applied Sciences, University of West Bohemia,
Univerzitní 8, 301 00 Plzeň, Czech Republic

In the last two decades, blood flow modelling has experienced enormous growth not only due to the considerable increase in computational resources, but also due to its close cooperation with clinicians as the main providers of valuable medical data. Being the driving force in the development of various non-invasive diagnostic techniques, such as the multiscale one [5], the biomechanical research has now shifted its focus to underlaying mechanisms of acute vascular syndromes (e.g., acute cerebral and cardiac ischemic events), which are often of blood clotting nature, i.e., caused by blood clots (thrombi) blocking vessels. To better understand the role of various factors leading to thrombotic complications, the next most logical step is to perform appropriate computer simulations relevant to the studied problem. In this sense and given the various and often very complex biological and biochemical processes taking place in blood vessels prior to a thrombotic occlusion, model simplifications are often an essential part of the modelling process. On the other hand, even for a "simple" thrombosis model, one can discover very fast that the choice of the blood flow model and the accompanying boundary conditions have the power to change the course of a simulation and consequently its outcome.

To demonstrate the aforementioned simulation pitfalls, the present in-silico study is undertaken with the objective to assess the role of three keyfactors: injury extent, outlet pressure, and blood viscosity. For this purpose, the study employs an extended version of the thrombosis model previously introduced in [1] and inspired by the fundamental works [2–4]. The main parts of the model are shown in Fig. 1 and compared to the previous model [1], modified by emphasising the central role of platelets in the formation of the primary haemostatic plug. The thrombosis simulations are carried out in representative vascular geometries, including examples of venous (portal) as well as arterial (carotid) flows, i.e., each with varying degree of pulsatility and velocity magnitude. Aside from the factor of injury extent, which is approached by changing the trigger level and the size of the injury site, the effect of outlet boundary condi-
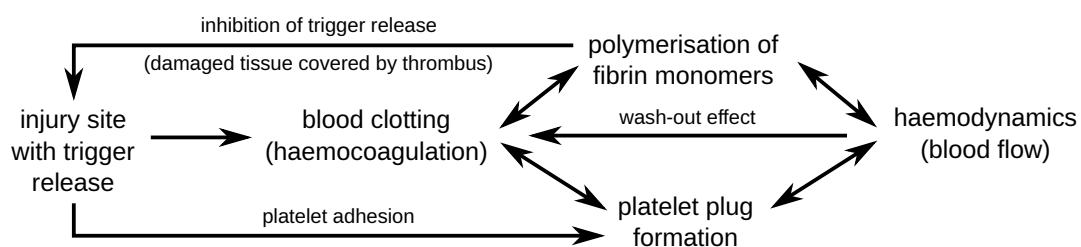
Fig. 1. Schema of the thrombosis model and its interactions with the intravascular environment
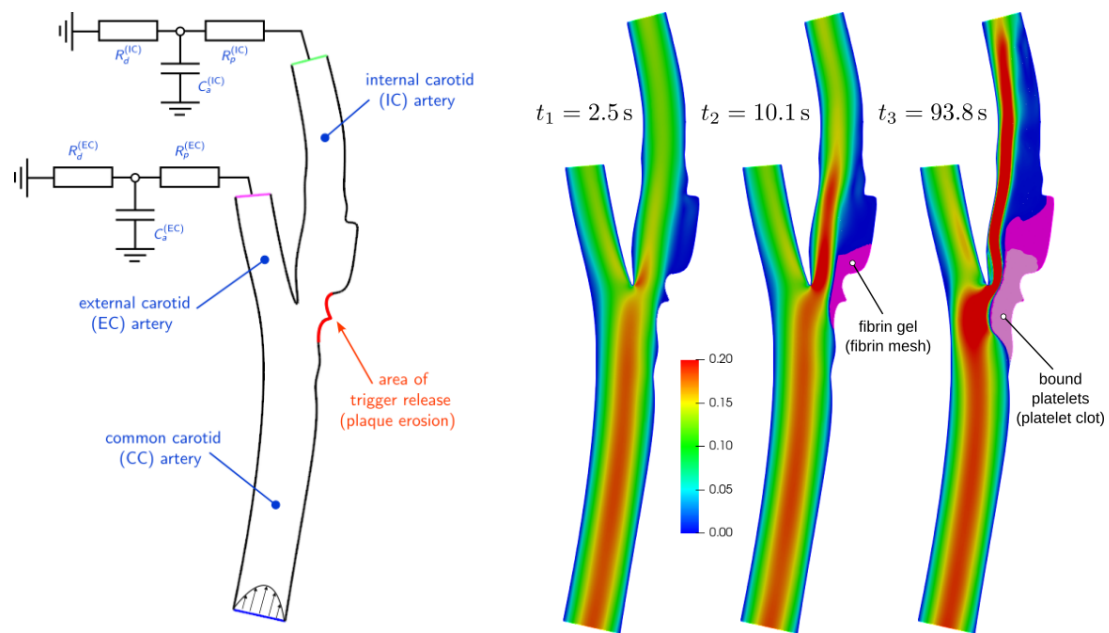
Fig. 2. (Left) Stenosed carotid bifurcation coupled with two outflow Windkessel models. (Right) Evolution of the systolic velocity field (in [m/s]) after trigger release with increasing IC blood blockage

tions is demonstrated on vascular bifurcations by assuming either a constant outlet pressure or an outflow model in the form of a Windkessel model, see Fig. 1 (left). Lastly, given the complex blood flow dynamics often seen during thrombotic events, Fig. 1 (right), the non-Newtonian effects are assessed as another keyfactor influencing the intensity of blood clotting. In this case, the Newtonian and Carreau-Yasuda models are applied with the possibility of a more advanced rheological model.

Acknowledgements

References

[1] Dušková, V., Jonášová, A., Pláničica, S., Vimmr, J., In-silico study of flow-mediated thrombosis in portal vein reconstructions, Proceedings of the conference Computational Mechanics 2021, Srní, University of West Bohemia, 2021, pp. 44-46.

[2] Link, K. G., Sorrells, M. G., Danes, N. A., Neeves, K. B., Leiderman, K., Fogelson, A. L., A mathematical model of platelet aggregation in an extravascular injury under flow, Multiscale Modeling and Simulation 18 (4) (2020) 1489-1524.

[3] Rukhlenko, O. S., Dudchenko, O. A., Zlobina, K. E., Guria, G. T., Mathematical modeling of intravascular blood coagulation under wall shear stress, PLOS One 10 (7) (2015) No. e0134028.

[4] Seo, J. H., Abd, T., George, R. T., Mittal, R., A coupled chemo-fluidic computational model for thrombogenesis in infarcted left ventricles, American Journal of Physiology–Heart and Circulatory Physiology 310 (11) (2016) H1567-H1582.

[5] Taylor, C. A., Fonte, T. A., Min, J. K., Computational fluid dynamics applied to cardiac computed tomography for noninvasive quantification of fractional flow reserve: Scientific basis, Journal of the American College of Cardiology 61 (22) (2013) 2233-2241.

Axial compressor airfoil optimization

J. Klesa^a, J. Fürst^b

^{a}*Department of Aerospace Engineering, Faculty of Mechanical Engineering, Czech Technical University in Prague,*
Karlovo náměstí 13, 121 35 Praha 2, Czech Republic
^{b}*Department of Technical Mathematics, Faculty of Mechanical Engineering, Czech Technical University in Prague,*
Karlovo náměstí 13, 121 35 Praha 2, Czech Republic

1. Introduction

The KOBRA project is focused on the development of the safety system for the gas-cooled nuclear reactor. The classical approach to the compressor airfoil family definition used for this project is introduced in [2]. The airfoils are assembled from their mean curve and thickness function. Experimental measurements of the airfoil was done by the Institute of Thermomechanics, Czech Academy of Sciences. This paper describes further development and optimization of the airfoils. The representative airfoil chosen for the investigation is representative rotor airfoil at the blade tip with relative inlet flow angle $\alpha_{IN} = 60°$ and inlet Mach number $M_{IN} = 0.8$. Mean line camber angle is $\theta = 12°$.

2. Methods

Further development of the airfoil 3 from [2] is based on the optimization of the airfoil mean line. The original aifoil 3 cascade is shown in Fig. 1. This airfoil has the mean line with the slope change of the first derivative, see Fig. 2 (right), which probably causes separation near to the leading edge in some cases. The new variant of airfoil is based on the constant flow velocity change on the airfoil.
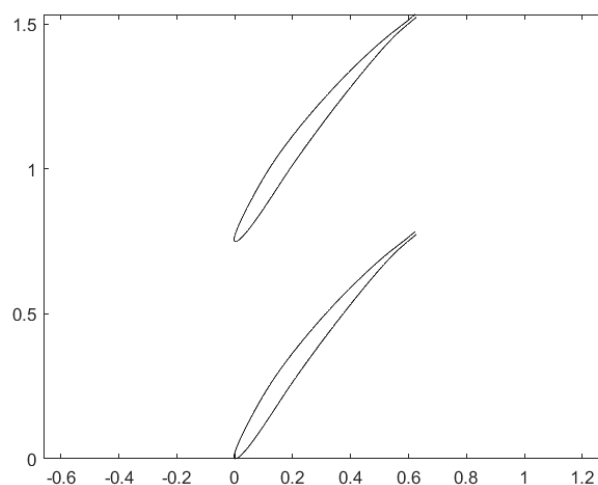
Fig. 1. Original airfoil 3 cascade with 1% leading edge thickness from [2]
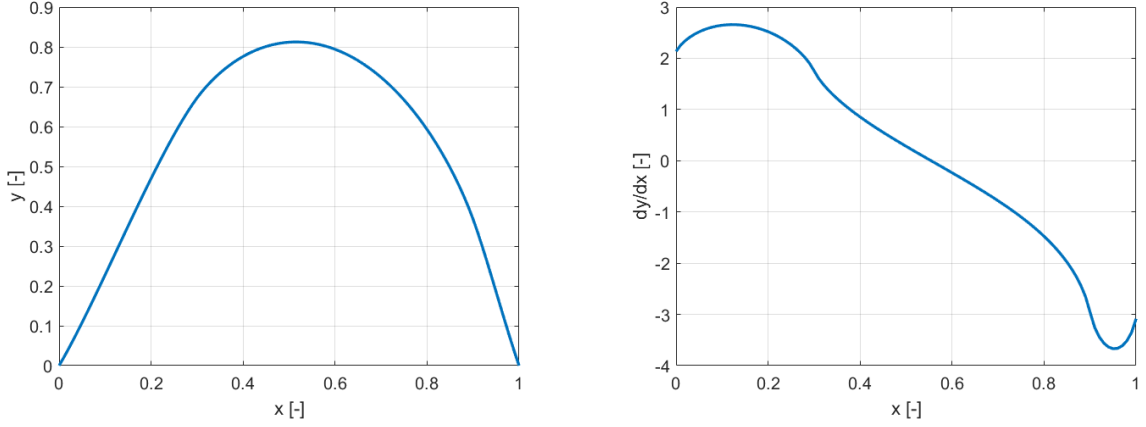
Fig. 2. Aifoil 3 mean line shape (left) and its slope (right)

The compressible flow velocity change for 1D inviscid case can be expressed in the following form (see [1]):

$$\frac{dv}{v}\left(M^2 - 1\right) = \frac{dA}{A}, \tag{1}$$

where A is the channel cross section area. The channel cross section can be expressed in the following form for the compressor cascade (constant blade length):

$$A = \frac{A_0}{\cos \alpha}, \tag{2}$$

where A_0 is the channel cross section for the axial flow and α is the flow angle measured from the compressor axis. Standard assumption for the compressor aerodynamic design is based on the constant axial velocity, i.e.,

$$v = \frac{v_{ax}}{\cos \alpha}, \tag{3}$$

where v_{ax} is the velocity component in axial direction. This means that the blade length changes so that changes in the density is compensated. Equations (2) and (3) are similar so, with some simplification, the flow acceleration with respect to the airfoil chord can be expressed by $d\alpha/dc$.

The function of $d\alpha/dc(x)$ is used as an input parameter for the airfoil mean line design. Numerical integration of $d\alpha/dc(x)$ with respect to the airfoil chord is used then to obtain desired mean line shape. Mean curve is generated directly in the final position, i.e., no airfoil rotation to the desired angle is used.

2D blade cascades were analysed by the means of the in-house CFD code at the Department of Technical mathematics, FME CTU in Prague. Cascade solidity t/c is from 0.5 to 2.0.

3. Results

The airfoil with constant $d\alpha/dc$ is presented in Fig. 3. The constant value of $d\alpha/dc$ should be favourable from the shock wave point of view so that strong shock waves should be suppressed, which should lead to low cascade losses. Results from the 2D CFD simulation are presented in Fig. 4 (cascade loss coefficient), Fig. 5 (cascade outlet angle) and Fig. 6 (flow turn angle).

4. Discussion

A modified method for the axial compressor airfoil design is presented. The method has been developed in the frame of the KOBRA project. The novel design method is based on the assumption of constant flow velocity increase on the airfoil. This should lead to lower losses and
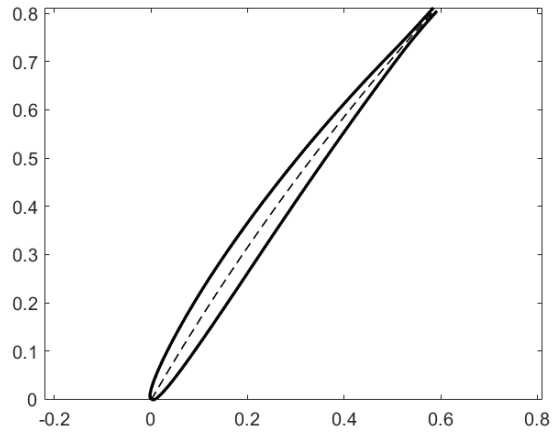
Fig. 3. Airfoil 5 with constant $d\alpha/dc$
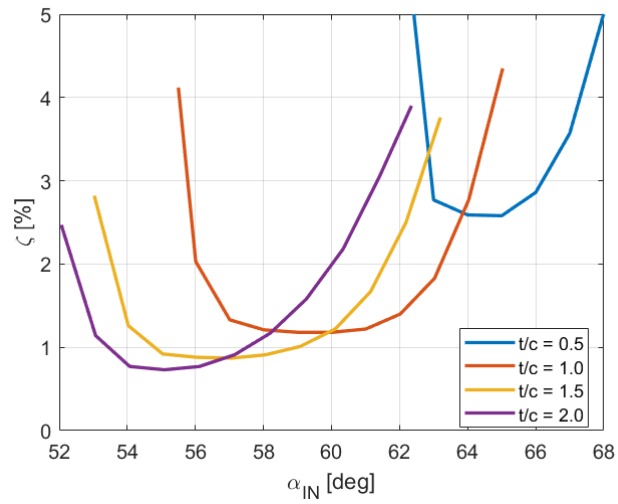
Fig. 4. Airfoil 5 with constant $d\alpha/dc$ – cascade loss coefficient ζ [%]
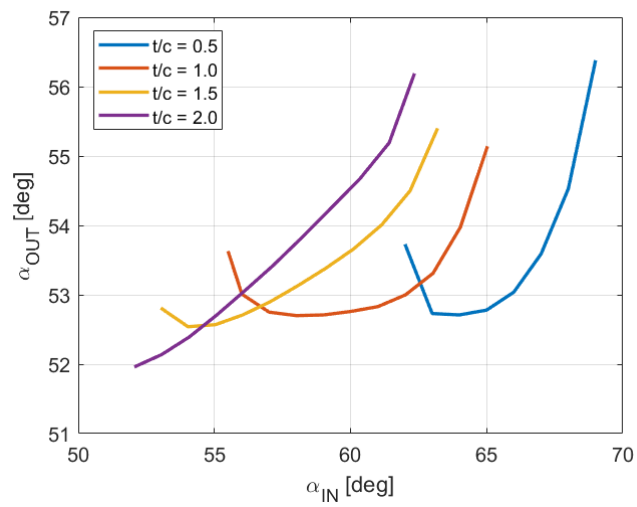
Fig. 5. Airfoil 5 with constant $d\alpha/dc$ – cascade outlet angle α_{OUT} [°]
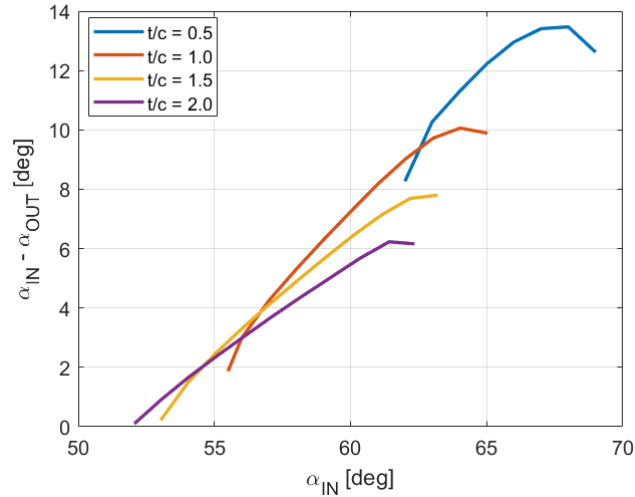
Fig. 6. Airfoil 5 with constant $d\alpha/dc$ – flow turn angle $(\alpha_{IN} - \alpha_{OUT})\,[°]$

wider operational range due to lower Mach numbers at the airfoil, and thus, less intensive shock waves. The new airfoil is designed for the sample rotor tip with the relative inlet flow angle $\alpha_{IN} = 60°$, inlet Mach number $M_{IN} = 0.8$ and camber angle is $\theta = 12°$. 2D CFD calculations with in-house code are performed for the cascade solidity t/c chosen from 0.5 to 2.0.

Acknowledgements

References

[1] Brož, V., High speed aerodynamics, 4th edition, Czech Technical University in Prague, Praha, 2001.

[2] Klesa, J., Aerodynamic design of transsonic compressor airfoil family, Proceedings of the 36th conference Computational Mechanics Conference, Srní, Czech Republic, 2021, pp. 115-117.

Dimensionless form of straight pipe pressure loss formula

M. Kořista[a]

[a]*Siemens Energy, s.r.o, odštěpný závod Industrial Turbomachinery, Brno, Olomoucká 7/9, Czech republic*

The design of the heat exchanger equipped with straight pipes solves the heat transfer and the pressure loss as a coupled problem. While so called heat transfer similitude formulas (Nusselt number criterion formulas) are commonly used in dimensionless form, the pressure loss phenomenon is traditionally analysed in the dimension form of the Darcy–Weisbach equation [4]

$$\frac{\Delta p}{L} = f_D \frac{\rho}{D_h} \frac{\overline{w}^2}{2}.$$

The Colebrook implicit equation [3]

$$1/f_C^{\frac{1}{2}} = -2 \, \log\left[2.51/\left(Re f_C^{\frac{1}{2}} \right) + \varepsilon/3.72 \right]$$

is one of possible ways to express the value of the Darcy friction coefficient of turbulent flow as the function of two dimensionless quantities the Reynolds number and relative roughness of the pipe surface

$$f_D = f_C(\text{Re}, \varepsilon) \,,$$

where the Reynolds number is defined as

$$\text{Re} = \frac{\overline{w} \, D_h \, \rho}{\mu}$$

and the relative roughness of the inner pipe surface is defined as

$$\varepsilon = k \, / \, D_h \,.$$

The formula of the mass flow rate of the fluid through the analysed pipe is added to the above equation system

$$m = \frac{\pi}{4} \, D^2 \, \overline{w} \, \rho \,.$$

The formula of magnitude of the pressure gradient along the straight pipe of constant cross section area is added to the above equation system

$$\left| \frac{\partial p}{\partial x} \right| = \frac{\Delta p}{L} \,.$$

The algebraic-only treatment of the above equation system does not allow the expression of the pressure drop as an explicit function due to the mathematical properties of the implicit Colebrook equation. Nevertheless, the explicit form of the pressure drop formula can be reached using the Lambert function from the so-called special mathematical functions category [2]. The following analysis shows the conversion of the above equation system to

the explicit dimensionless formula representing straight pipe pressure loss hydrodynamic similitude. Although the Colebrook friction coefficient equation is empirical, this theoretical analysis uses it because it is known to be very precious, and several attempts were made to convert it to an explicit form, [1] for instance.

Let's substitute the definition of the Reynolds number, magnitude of the pressure gradient along the straight pipe and formal function of relative surface roughness to the Darcy–Weisbach equation to get an interim form of the dimensionless pressure loss formulation. For the sake of simplicity let's reduce our analysis to the circular pipe only

$$D_h = D \, .$$

After some formula treatment, we get the form

$$\frac{\rho \, D^3}{\mu^2} \left| \frac{\partial p}{\partial x} \right| = f_C [\mathrm{Re}, \varepsilon(k, D)] \, \frac{\mathrm{Re}^2}{2}.$$

The received interim formula is in dimensionless form already. It is one of the possible forms (the first form) of the pressure loss hydraulic similitude of the pressure loss of the straight pipe. The right-hand side of the formula consists of the dimensionless Reynolds number and relative surface roughness only; consequently, the left-hand side of the formula must be dimensionless, too.

Let's designate the left-hand side of the above formula as the first result of this study, as a new dimensionless parameter (similitude number of "hydrodynamic diameter of the pressure loss")

$$\Phi = \frac{\rho \, D^3}{\mu^2} \left| \frac{\partial p}{\partial x} \right| .$$

The next interim step of the analysis is eliminating the pipe diameter from of the pressure loss hydraulic similitude of the pressure loss of the straight pipe. Substituting the Reynolds number equation to the mass flow rate equation and after restructuring, we get the interim formula for geometric pipe diameter

$$D = \frac{4}{\pi} \frac{m}{\mu \, \mathrm{Re}} \, .$$

Substituting the interim pipe diameter formula to the pressure loss hydraulic similitude of the straight pipe and after restructuring, we get the form

$$\left(\frac{4}{\pi} \right)^3 \frac{m^3 \, \rho}{\mu^5} \left| \frac{\partial p}{\partial x} \right| = f_C \left[\mathrm{Re}, \varepsilon \left(k, \frac{4}{\pi} \frac{m}{\mu \, Re} \right) \right] \frac{\mathrm{Re}^5}{2} \, .$$

The received interim formula is the second form of the pressure loss hydraulic similitude of the pressure loss of the straight pipe. Let's designate part of the left-hand side of the above formula as the second result of this study, as a new dimensionless parameter (similitude number of "hydrodynamic mass flow of the pressure loss")

$$\Psi = \frac{m^3 \, \rho}{\mu^5} \left| \frac{\partial p}{\partial x} \right| .$$

Eliminating the friction factor out of both formulas, the following equation for both new dimensionless quantities can be obtained

$$\Psi = \left(\frac{\pi}{4} \right)^3 \Phi \, \mathrm{Re}^3 \, .$$

The next interim step of the analysis is to express the Darcy friction factor defined by the Colebrook equation using an identity valid for the Lambert function and treat the surface roughness in the way of the new dimensionless quantity.

Logarithmic equation

$$\ln(A_W + B_W x) + C_W x = \ln D_W$$

using of the Lambert function W is identical to

$$x = \frac{1}{C_W} \, W\left[\frac{C_W \, D_W}{B_W} \, e^{\left(\frac{A_W \, C_W}{B_W}\right)}\right] - \frac{A_W}{B_W}.$$

The friction factor defined by the Colebrook equation expressed explicitly using the above shown identity is

$$f_C = \frac{1}{\left\{\frac{2}{\ln(10)} \, W\left[\frac{50 \ln(10) \, \text{Re} \, e^{\left(\frac{500 \ln(10) \, \text{Re} \, \varepsilon}{9287}\right)}}{251}\right] - \frac{1000}{9287} \, \text{Re} \, \varepsilon\right\}^2}.$$

Relative surface roughness in the above statement can be modified by substituting the pipe diameter as a function of Reynolds number

$$\varepsilon = \frac{\pi \, \text{Re} \, k \, \mu}{4 \, m}.$$

Substituting friction coefficient and relative surface roughness formulas derived above to the function of the second interim form of the hydraulic similitude of the pressure loss of straight pipe, we receive the final formula

$$\Psi = \frac{C_1 \, \text{Re}^5}{\left\{C_5 \, W\left[C_2 \, \text{Re} \, e^{(C_3 \, \text{Re}^2 \, \Omega)}\right] - C_4 \, \text{Re}^2 \, \Omega\right\}^2},$$

where the new dimensionless quantity describing the dimensionless parameter of hydrodynamic roughness of the pressure loss of the straight pipe is introduced by the formula

$$\Omega = \frac{k \, \mu}{m}.$$

Nomenclature

Variables:

D_h	[m]	hydraulic pipe diameter,
D	[m]	geometric pipe diameter (of circular pipe),
f_D	[1]	Darcy friction coefficient,
f_C	[1]	friction coefficient according to the Colebrook definition,
k	[m]	height of the roughness of the pipe surface,
L	[m]	pipe length,
m	[kg/s]	mass flow rate,
Δp	[Pa]	pressure drop of the straight pipe of the given length,
$\left|\frac{\partial p}{\partial x}\right|$	[Pa/m]	pressure gradient magnitude along the straight pipe,
$\overline{w}$	[m/s]	mean fluid velocity,
$\varepsilon = \varepsilon(k, D_h)$	[1]	relative roughness of the pipe surface,
μ	[Pa*s]	dynamic viscosity of the fluid,
ρ	[kg/m³]	fluid density.

Dimensionless hydrodynamic parameters of pressure loss in the straight pipe:

Φ	[1]	dimensionless hydrodynamic mass flow rate,
Ψ	[1]	dimensionless hydrodynamic diameter,
Ω	[1]	dimensionless surface roughness.

Logarithms, constants and symbols of identity using of the Lambert function:

ln	[-]	natural logarithm,
log	[-]	decimal logarithm,
W	[-]	main branch of the Lambert function,
A_W, B_W, C_W, D_W	[1]	constants of identity using the Lambert function.

Constants of the final formula of hydraulic similitude of the pressure loss in the straight pipe:

$C_1 = \dfrac{\pi^3}{128} \approx 0.2422\ ...$	[1]	constant,
$C_2 = \dfrac{50\ln(10)}{251} \approx 0.4586\ ...$	[1]	constant,
$C_3 = \dfrac{125\pi\ln(10)}{9287} \approx 0.0973\ ...$	[1]	constant,
$C_4 = \dfrac{250\pi}{9287} \approx 0.0845\ ...$	[1]	constant,
$C_5 = \dfrac{2}{\ln(10)} \approx 0.8685\ ...$	[1]	constant.

References

[1] Brkić, D., An explicit approximation of Colebrook's equation for fluid flow friction factor, Petroleum Science and Technology 29 (2011) 1596-1602.

[2] Brkić, D., Lambert W function in hydraulic problems, Mathematica Balkanica 26 (2012) 287-292.

[3] Colebrook, C. F., Turbulent flow in pipes, with particular reference to the transition region between the smooth and rough pipe laws, Journal of the Institution of Civil Engineers 11 (4) (1939) 133-156.

[4] Howell, G., Aerospace fluid component designers' handbook. Vol. I., TRW Systems Group, Redondo Beach CA, 1964.

About the appropriate neural network size
for the engineering applications

P. Kovář^{a,b}, A. Tater^{a,b}, J. Pařez^{b}, J. Fürst^{a}

^{a}*Department of Technical Mathematics, Faculty of Mechanical Engineering, Czech Technical University in Prague, Karlovo náměstí 13, 121 35 Praha 2, Czech Republic*
^{b}*Center of Aviation and Space Research, Faculty of Mechanical Engineering, Czech Technical University in Prague, Technická 4, 160 00 Praha 6, Czech Republic*

1. Introduction

Deep learning approaches became very popular in recent years. In terms of computational effectivity and time required for the learning process, number of degrees of freedom in the proposed neural network plays significant role. Thus, an apriori information about the appropriate neural network size for a given problem could be very promising tool in machine learning tasks.

In the contrast to the standard machine learning approaches aimed to deep learning, present contribution deals with shallow higher order neural networks. A comparison of the ability to capture more demanding engineering task using different neural networks is presented and basic idea of the neural network size estimation for the task is discussed.

2. Objective statement

Natural convection phenomenon, governed by system of Navier-Stokes equations, in the annular section representing a part of the aircraft engine where turbines are housed, was selected as the engineering complex training task. The goal is to find a neural operator $\mathcal{N}(\bullet)$ that is able to approximate temperature distribution on the outer tube T_{D_2} with permissible error and the simplest architecture as possible. In order to obtain training data set for neural network and replace experimental measurement, various numerical simulations with different geometrical setups, specifically D_1/D_2 ratios, thickness of the outer tube t_2 and temperature T_{D_1} as boundary condition on the inner tube were performed as described in detail in [5]. There is a sketch of the computational domain in Fig. 1. Based on the theoretical and experimental knowledge [4], it is necessary to assume that temperature distribution on the outer tube is also function of the angle denoted by φ.
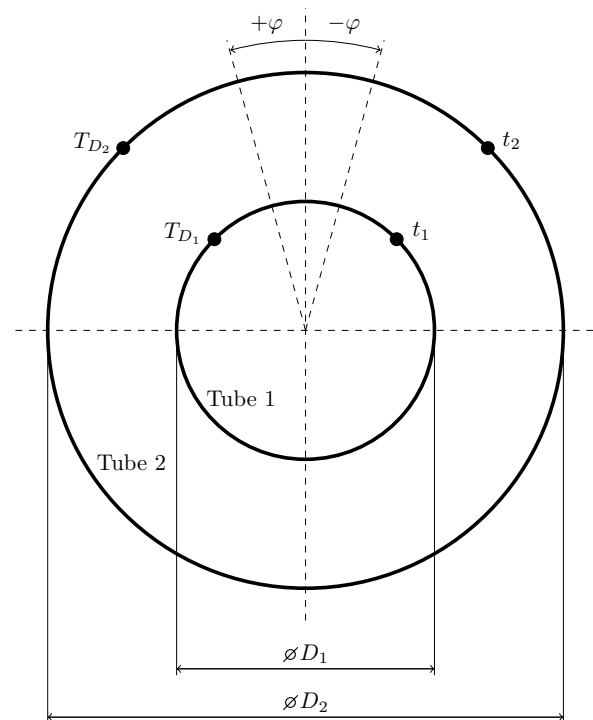
Fig. 1. Sketch of the computational domain

3. Neural networks

Referring to previous considerations, the desired function is assumed in the form

$$T_{D_2} = \mathcal{N}(\bullet) = f(D_1/D_2, t_2, T_{D_1}, \varphi). \tag{1}$$

Neural output of the neural unit is consisted of two different operations as it is shown in Fig. 2 (left). Product of the somatic operation $\widetilde{y}$, in general, can be expressed as [2]

$$\widetilde{y} = \sigma(s). \tag{2}$$

Let us assume N-th order neural unit, then product of synaptic operation can be written as [2]

$$s = w_0 x_0 + \sum_{i=1}^{n} w_i x_i + \sum_{i=1}^{n}\sum_{j=i}^{n} w_{ij} x_i x_j + \cdots + \sum_{i_1=1}^{n} \cdots \sum_{i_N=i_{N-1}}^{n} w_{i_1 i_2 \ldots i_n} x_{i_1} x_{i_2} \ldots x_{i_n}, \tag{3}$$

where $x_0 = 1$ denotes threshold and n stands for length of input feature vector.
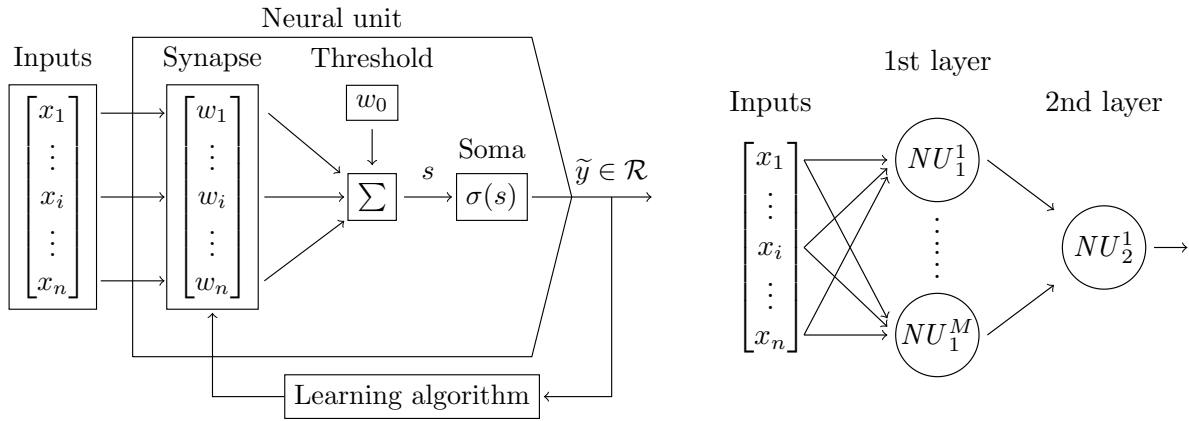
Fig. 2. Neural network: single neural unit (left); shallow neural network (right)

For clarity, let us introduce the labelling of neural networks as it is described in expression (4). It is consisted of network depth L, i.e., number of layers X_L and additional parameters which stand for size of individual layers S, i.e., number of neurons in each layer X_S, Y_S, order of somatic operation and activation function used in individual layers.

$$Name_{ANN} = LX_{L\_}SX_S Y_{S\_}OX_O Y_O \tag{4}$$

It is obvious that number of adaptable weight is dependent on number of neurons in the previous layer but it is also strongly dependent on the order of synaptic operation used in the neurons. Total number of optimizable parameters can be obtained as [1]

$$\sum_{j=0}^{N} \binom{n+j-1}{j} = \sum_{j=0}^{N} \frac{(n+j-1)!}{j!(n-1)!}, \tag{5}$$

where N denotes maximal order of synaptic operation. In Fig. 3, there is a dependency of DoFs based on the designed neural network architecture. Only shallow two layered networks are assumed, as it is indicated in Fig. 2 (right), with maximal thickness in the first layer equals to five neurons. In the output layer, there is a single neuron in all cases. Higher orders up to third only are considered.
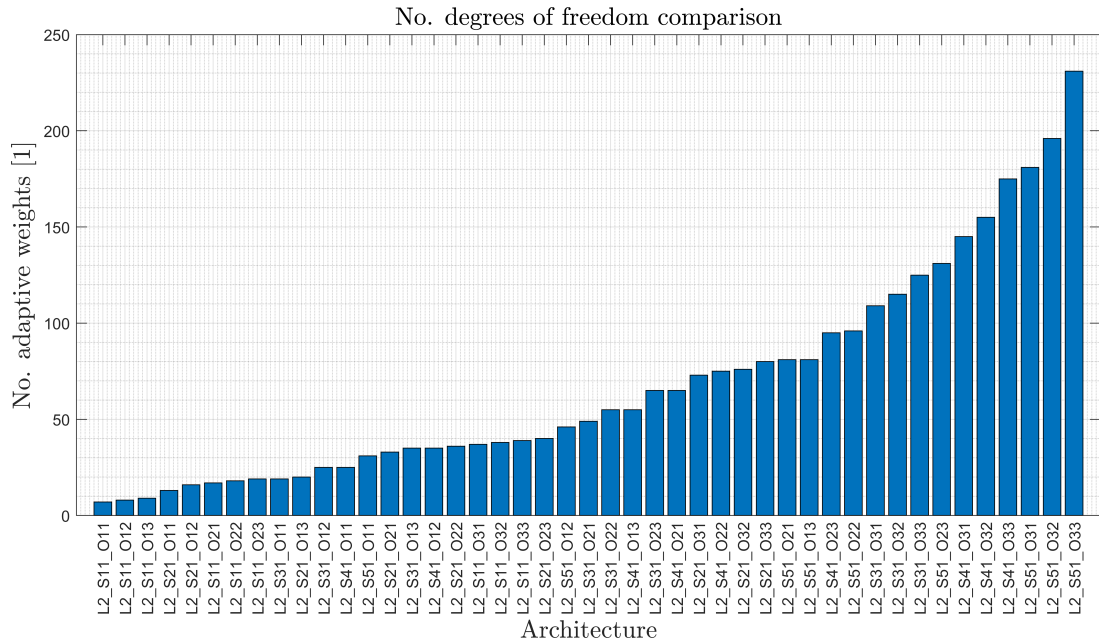
Fig. 3. Proposed neural network architectures: degrees of freedom comparison

4. Results

In Fig. 4, there are results of the learning performed on the training data set with different neural network architectures. Learning rate was set to $\mu = 0.2$ and total number of epochs to $1e3$ in all cases. Pareto front of conflicting criteria, accuracy and number of degrees of freedom, was found and as it can be seen, not all more complex compounding necessarily lead to better performance in sense of testing error value.

Four neural network architectures were found in the Pareto front. In the case of three simplest networks in this set, i.e., architectures *L2_S11_O11*, *L2_S21_O12* and *L2_S31_O13*, expected behaviour is observed. As the number of DoFs is increased, the training error is by half
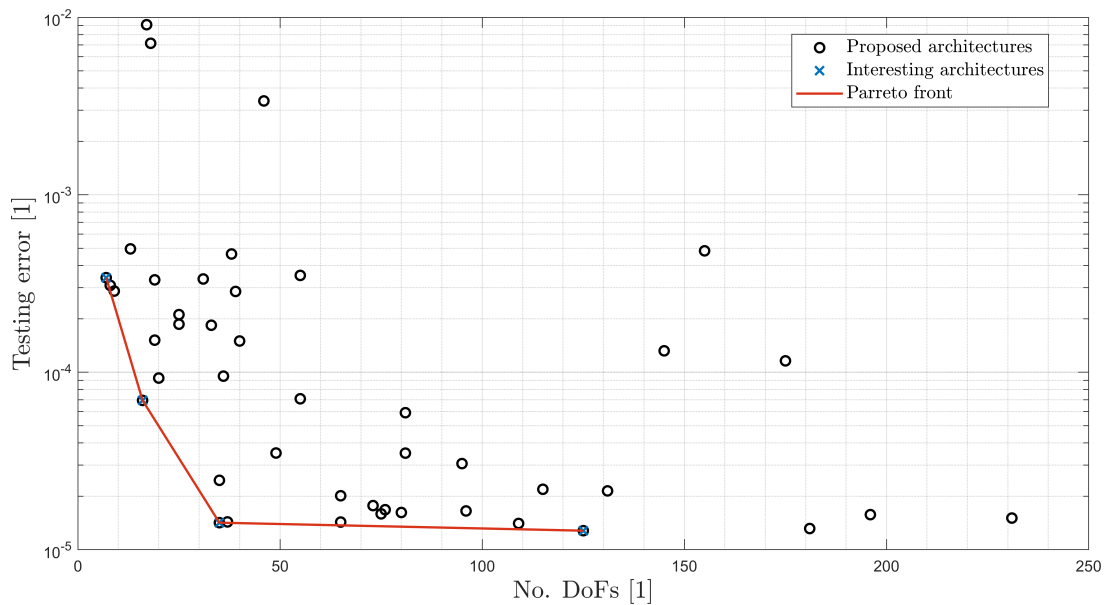
Fig. 4. Proposed neural network architectures: results of the learning

93

an order of magnitude lower as it is listed in Table 1. Different behaviour can be seen in case of the last architecture on the Pareto front. Architecture *L2_S31_O33* is more than threefold more complex but the improvement of the result accuracy is almost negligible.

Table 1. Networks in the Pareto front

Network	DoFs	Error
L2_S11_O11	7	$3.41e$-4
L2_S21_O12	16	$6.94e$-5
L2_S31_O13	35	$1.42e$-5
L2_S31_O33	125	$1.28e$-5

5. Conclusions

Learning of the real engineering task using different neural network architectures was presented. It turns out that a more complex neural network does not necessarily better approximate the given problem. Although formula for the apriori estimation of the network complexity was not found, it turned out that more than threefold simpler neural network can approximate the task almost similarly accurate.

It should be noticed that quality of the approximation is strongly dependent on the quality of the training data set. Especially in cases related to CFD simulations where the error can be estimated [6], a bound of permissible error and appropriate network size can be chosen.

More complex formula for the apriori estimation of required neural network complexity based on the complexity of the approximated task should be aim of further research. Thumbling stone of this topic is a method how the complexity of desired pattern can be quantified or if there is a relation between non-linear patterns and approximation using even or odd orders of neurons.

Acknowledgments

References

[1] Gupta, M. M., Bukovsky, I., Homma, N., Solo, A. M., Hou, Z. G., Fundamentals of higher order neural networks for modeling and simulation. In: Artificial Higher Order Neural Networks for Modeling and Simulation, IGI Global, 2013, pp. 103-133.

[2] Gupta, M. M., Liang J., Noriyasu H., Static and dynamic neural networks: From fundamentals to advanced theory, John Wiley & Sons, 2004.

[3] Kovář, P., Fürst, J., Nozzle shape optimization based on machine learning using higher order neural networks, Proceedings of the International Conference Experimental Fluid Mechanics 2022, Safari Park Dvůr Králové nad Labem, 2022, pp. 138-145.

[4] Pařez, J., Tater, A., Kovář, P., Mačák, P., Vampola, T., Influence of geometrical design on the cooling process of double annular turbine section, International Journal of Engine Research 24 (8) (2023) 3707-3719.

[5] Pařez, J., Kovář, P., Tater, A., Modelling of temperature field distribution on single annular using higher order neural network, Proceedings of the 18th Youth Symposium on Experimental Solid Mechanics, Prague, Institute of Theoretical and Applied Mechanics, AS CR, 2023, pp. 1-18.

[6] Roache, P. J., Verification and validation in computational science and engineering, Hermosa Publishers, Albuquerque, 1998.

Dynamically isotropic planar mechanism of vibration absorber

K. Kraus[a], T. Vyhlídal[b], Z. Šika[a]

[a]Department of Mechanics, Biomechanics and Mechatronics, Faculty of Mechanical Engineering, Czech Technical University in Prague, Technická 4, Praha 6, 160 00 Prague, Czech republic
[b]Department of Instrumentation and Control Engineering, Faculty of Mechanical Engineering, Czech Technical University in Prague, Technická 4, Praha 6, 160 00 Prague, Czech republic

This paper deals with dynamical isotropy of absorbers, that are designed in single-mass and multi-DoF configuration. Such tuning property has been researched for both planar and spatial cases. Vibration suppression takes place in many applications and environments. In various cases, for example in robotics and industrial environment, it might be more convenient to use absorbers [1] to suppress vibrations of the main structure over other methods for technical or practical reasons. Based on application, mass-spring absorber is attached to main structure in point of interest, tuned and actively driven if needed. Depending on absorbers count and the nature of vibrations, various algorithms can be used to drive absorber's actuators, such as PID regulation, H-inf, LQR [4], Delayed resonator [3], etc. Usually, some sort of damping takes place in the absorber structure and lots of real cases of bearing damping are far from linear. That burdens control algorithms and some way of active control might be needed to make such an absorber as ideal as possible [2]. Besides all above, for full vibration suppression in the given coordinates of desired system, considering all possible projections, the unifrequency (aka dynamical isotropy) property is a crucial feature [5].

In principle, dynamical isotropy is based on tuning of all the absorber's eigenfrequencies to single value, when using single-mass and multi-DoF configuration. That is crucial for full vibration suppression in all coordinates. There are solutions for simplified models, where only the absorber's mass is considered. The problem is that any flexible-damping-actuating structure (or legs), supporting and controlling the absorber's mass itself, has its own mass, which affects entire absorber's system. For all absorber designs, this ratio of supporting mass to the absorber's mass is non-trivial and can be very significant in some cases. Especially when using electromagnetic actuators, which usually includes heavy magnets. Therefore, it is necessary to tune and design the absorber as a whole, to be implemented in real world, which can bring some limitations.

In planar design, 3-DoF absorber's mass is joined to the system with three supporting flexible legs. Each leg consists of spring, actuator and linear bearing, and is joined using rolling bearings on each end. That gives us two more bodies per leg and each body has its own mass, moment of inertia and position of the centre of mass. Considering perpendicular design of the absorber (see Fig. 1a) and all the dynamical parameters and constraints mentioned above (in addition to dynamical parameters of the absorber's mass itself), we obtain complex problem of dynamical isotropy tuning. Although there is a solution for simplified model [5] at analytical level, equations for this new parallel seven-body system are fairly complex. Therefore, whole problem has been transformed into optimization task.

Built optimization software works with independent dynamical equations of the seven-body system and with multiple parameters mentioned above. Due to high number of such parameters, a series of subsequent optimization jobs with various subsets have been performed at first, along

with linear constraints of parameters across legs if needed. Our results had not show any non-trivial solution of such absorber in perpendicular configuration. The only result of dynamical isotropy for such case happens only when some of the leg masses tend to zero.

a) Perpendicular design of 3-DoF absorber   b) Symmetrical design of 3-DoF absorber
Fig. 1. Planar absorber kinematical configurations

Although there is convenience of the perpendicular absorber design in terms of ease of attachment to the main structure, it is not suitable candidate for dynamical isotropy tuning when implemented to real world structure. For such purpose, a symmetrical triangular symmetrical structure is considered (see Fig. 1b), although its attachment points require building of supporting structure all around the absorber's mass.

Symmetrical structure is instantly more suitable for dynamical isotropy by the fact that it already ensures both transitional eigenfrequencies of the absorber to be equal. It is conditioned by the equal dynamical and kinematical parameters of all legs and by the symmetricity of the absorber's mass and dimensions.

In order to lock scale of the absorber during optimization, mass of the absorber and its size are fixed. All other legs parameters can be tuned, such as length, angle, masses, moment of inertia, stiffness, position of CoF, as well as moment of inertia of the absorber (mass distribution). Not only we now use equal parameters across all legs, but, due to the symmetricity, not all of them must be tuned in order to achieve unifrequency. One of the main contributor to eigenfrequency is the angle of the legs, which, depending on the constellation, can equalize rotational and translational eigenfrequency of the absorber.

Acknowledgement

References

[1] Kraus, K., Šika, Z., Beneš, P., Krivošej, J., Vyhlídal, T., Mechatronic robot arm with active vibration absorbers, Journal of Vibration and Control 26 (13-14) (2020) 1145-1156.

[2] Kraus, K., Šika, Z., Krivošej, J., Experimental based tuning of active 3-DoF planar absorber, Proceedings of computational mechanics, University of West Bohemia, Plzeň, 2022, p. 54-55.

[3] Olgac, N., Elmali, H., Hosek, M., Renzulli, M., Active vibration control of distributed systems using delayed resonator with acceleration feedback, Jou. of dyn. systems, measurement, and control 119 (3) (1997) 380-389.

[4] Šika, Z., Kraus, K., Beneš, P., Vyhlídal, T., Valášek, M., Active multidimensional vibration absorbers for light robots, Proceedings of the 5th Joint International Conference on Multibody System Dynamics, Lisabon, 2018, pp. 1-12.

[5] Šika, Z., Vyhlídal, T., Neusser, Z., Two-dimensional delayed resonator for entire vibration absorption, Journal of Sound and Vibration 500 (2021) 116010.

Complex transonic phenomena in critical flow Venturi nozzle

T. Kreuzová[a]

[a]*Department of Fluid Dynamics and Thermodynamics, Faculty of Mechanical Engineering, Czech Technical University in Prague, Technická 4, 16607, Prague 6, Czech Republic*

1. Introduction

With the recent growth of hydrogen technologies, high precision measurement of flow rates at low pressure ratios is necessary. A widely used methodology for this type of measurement is the ISO 9300 standard [2]. It is in the interest of high quality measurement to recognize the nature of all the complex phenomena that occur in the flow through the critical flow Venturi nozzle (CFVN).

The axisymmetric geometry of the nozzle consists of a convergent part, which is defined as a section of a torus, and a divergent part that is created by a cone. The throat of the CFVN can be of two types – cylindrical and toroidal. The geometries are illustrated in Fig. 1.

The flow is accelerated from low subsonic velocities at the inlet of the nozzle to a supersonic flow. As the transonic conditions are reached, the flow is aerodynamically choked and the flow rate is directed solely by thermophysical properties of the gas, by stagnation conditions and by the geometry of the nozzle.

This work focuses on phenomena, which originate in compressibility of the fluid, namely the sonic line (its shape and position) and local supersonic compression in transonic expansion.

Ideal gas with properties of air (specific gas constant $r = 287.05\,\mathrm{J/(kg\,K)}$ and ratio of specific heats $\kappa = 1.4$) is considered in this work.
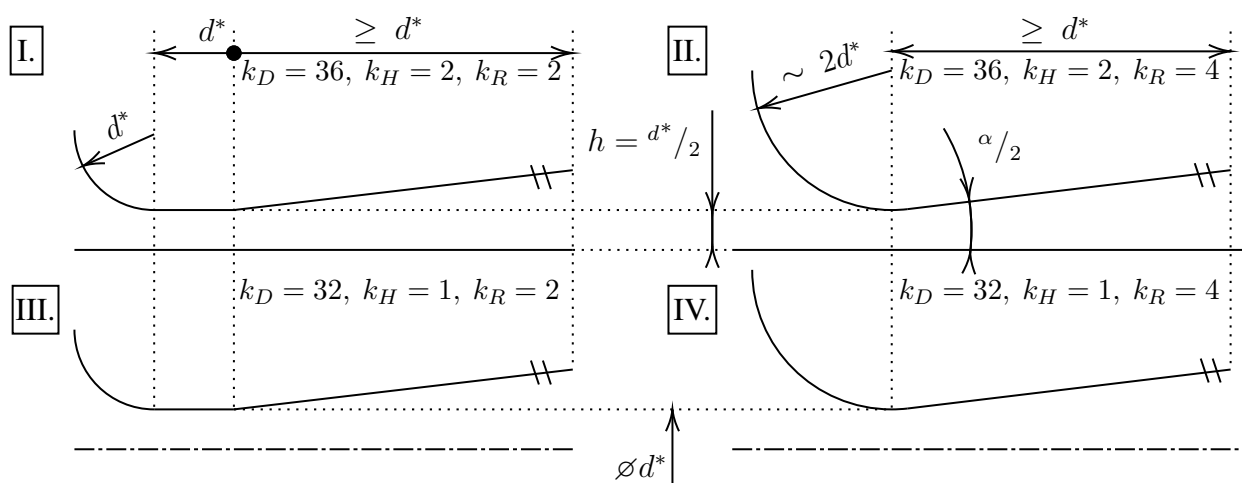
Fig. 1. Types of CFVN

2. Theoretical analysis

Thanks to the nature of transonic flow significant phenomena can be predicted based solely on theoretical background. Analytical description was developed mostly for two dimensional problems, therefore part of the theoretical analysis is performed for idealized flat asymmetrical nozzle (types I. and II. in Fig. 1[1]).

For inviscid flow, the shape and position of the sonic line can be predicted. Position of the sonic line corresponds to the minimum cross-section (throat) of the nozzle. Approximate shape of the sonic line can be determined based on analysis proposed by Shapiro in [4] for both, flat and axisymmetric, types of the nozzle. An assumption made in [4] is that in the vicinity of the sonic line, the curvature of the wall is continuous, which, in studied case, is not met (especially for types I. and III.). Still, this analysis can serve as a very good first step approximation.

The relations given in [4] are adjusted based on geometry of the nozzle, so that the resulting relations are dependent only on the heat capacity ratio (κ) and type of the nozzle. The relation is converted to dimensionless, so that it is independent of critical dimension d^* ($r^+ = {}^{2r}/_{d^*}$, $x^+ = {}^{2x}/_{d^*}$). The curve describing the sonic line is given by relation (1). Constants k_i, $i \in \{D, R, H\}$ (describing geometry and dimensionality of each problem) in relation (1) are given in Fig. 1. In Fig. 2, shapes of sonic line obtained numerically for inviscid flow and by the approximate calculation are compared. The discrepancy may be due to combination of errors of both methods.

$$r^+ = \left[(1 + k_R) - \sqrt{k_R^2 - (k_H k)^2}\right] \sqrt{\frac{k - x^+}{k(1 + k_H)}}, \qquad k = \sqrt{\frac{\kappa + 1}{k_D k_R}} \qquad (1)$$

As the inlet of the nozzle is defined by section of a torus with quite a small radius, sonic line is significantly curved. The lower the Mach number, the higher is the angle of streamline and characteristic ($\mu = \pm \arcsin M^{-1}$). These two facts allow the waves (characteristics) to interact with sonic line and be reflected by it. Expansion waves are reflected by the sonic line as compression waves, these cause local increase of the pressure and therefore slow down the transonic expansion. LSCiTE is documented in [5]. Using an interferogram obtained by inviscid numerical simulation, the LSCiTE is illustrated in Fig. 3[2].

In [3], expected frequency of the oscillations of the pressure field is given. Dimensionless

---

[1]To simplify any comparison of results, critical height of the flat nozzle is set to ${}^{d^*}/_2$.
[2]Constant of the interferogram is $0.011858 \, \text{kg/m}^3$.
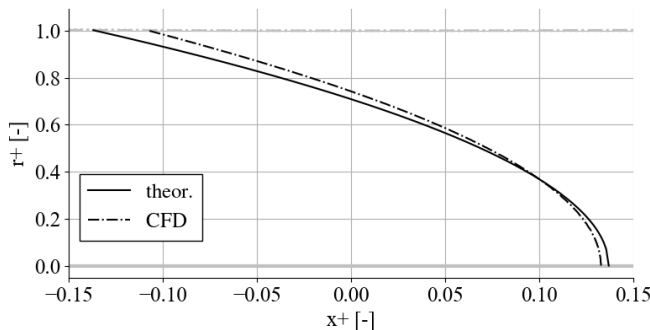
Fig. 2. Comparison of sonic line shapes (type IV.)
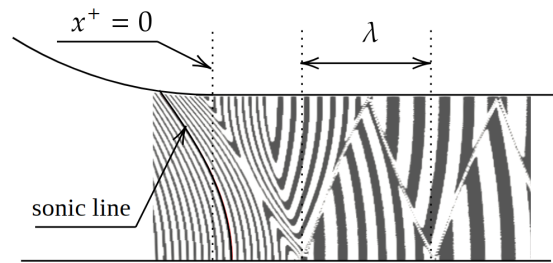
Fig. 3. Numerical interferogram with visible LSCiTE (inviscid, type I.)

wavelength of the oscillations is derived in the following form:

$$\lambda^+ = \sqrt{\frac{\kappa + 1}{2} \frac{12}{13}}. \tag{2}$$

The relation is provided only for the nozzle type I., even though similar but more complex behavior can be expected in all other types. Numerically obtained wavelength $\lambda^+ \approx 0.8$, which differs by $\approx 20\ \%$ from the theoretically predicted value. This is not surprising since the theoretical relationship is based on the very same description of the sonic line as was shown in previous part of this work and which did not match the numerical results perfectly.

3. Numerical analysis

The numerical analysis was performed using LU-SGS solver [1] implemented in OpenFOAM library. Standard boundary conditions were applied, with total pressure and total temperature set to 10^5 Pa and 303.15 K, respectively. Supersonic outlet is assumed, and therefore homogeneous Neumann BCs are prescribed for all variables. Ideal gas with properties of air is assumed. For the viscous cases the Langtry-Menter 4-equation transitional SST turbulence model was applied with boundary conditions meeting the requirements of the model. Hexahedral mesh – with refinement at the wall for viscous cases – was used. The refinement ensures that the dimensionless size of the cell at the wall is close to one ($y^+ \approx 1$) and the growth in normal direction to the wall is gradual. The value of y^+ is verified after computation, in all cases $y^+ < 2.5$. The higher values are obtained only near the inlet of the nozzle.

Results of computations with inviscid fluid can be easily compared with theoretical assumptions but need to be precised by including viscous effects. The greatest influence of viscosity can be observed in the nozzle with cylindrical throat (III. in Fig. 1), as the evenly developing boundary layer in the throat creates the minimum effective cross-section at the end of the throat. That is why LSCiTE is not observed, see Fig. 4 with comparison of results obtained with an assumption of viscous and inviscid fluid. In type IV. LSCiTE appears even in the viscous cases[3] (Fig. 5). Oscillations of the pressure field should therefore be taken in account. These perturbations can speed up the transition to turbulence which is an effect that should not be neglected as it works directly against the favorable pressure gradient, which suppresses the development of turbulent boundary layer. Moreover, as the ISO 9300 standard requires static pressure measurement behind the nozzle, it is in the best interest of precise experiment to ensure that the tap is not affected by the pressure oscillations.

---

[3]In the computed case $^\alpha/_2 = 6°$ which is maximum allowed $^\alpha/_2$ by the standard.
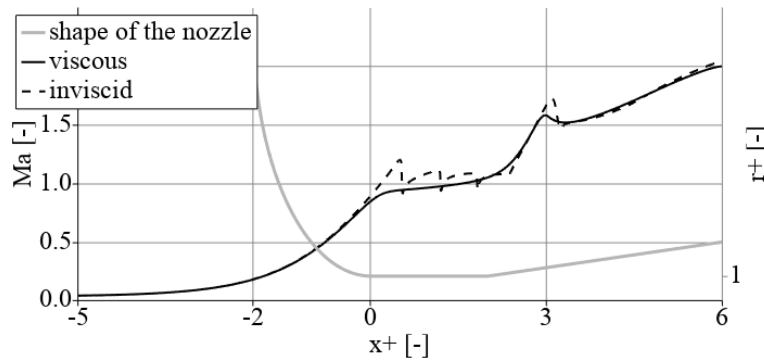
Fig. 4. Development of the Mach number along CFVN axis (type III.)
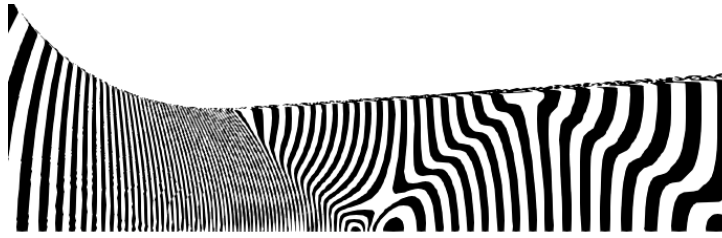
Fig. 5. Numerical artificial interferogram of meridian slice with visible LSCiTE (viscous, type IV.)

4. Conclusions

Theoretical and numerical analysis of flow field in critical flow Venturi nozzle was performed. It was shown that for proper measurement, presence of more dimensional gas dynamics effects should be taken into account. Also, it is important to point out the strong sensitivity of transonics to geometry and physical parameters changes.

For a validation of numerical computations, a set of experiments focused on more dimensional gas dynamics effects in CFVN would be necessary. Plenty of work is still left untouched in the field of (as precise as possible) turbulence modeling. Based on empirical criteria for relaminarization it can be easily shown that in major part of the nozzle, turbulence in boundary layer might be suppressed by the presence of strong favorable pressure gradient. Interference of this effect with LSCiTE should be studied.

References

[1] Fürst, J., Development of a coupled matrix-free LU-SGS solver for turbulent compressible flows, Computers & Fluids 172 (2018) 332-339.

[2] ISO 9300:2022, Measurement of gas flow by means of critical flow nozzles, International Organization for Standardization, 2022.

[3] Šafařík, P., Theoretical analysis of transonic expansion in blade cascade, Report No. Z-856/83, IT CAS, 1983.

[4] Shapiro, A. H., The dynamics and thermodynamics of compressible fluid flow, Ronald Press Company, 1953.

[5] Šťastný, M., Šafařík, P., Experimental analysis data on the transonic flow past a plane turbine cascade, Volume 1: Turbomachinery, American Society of Mechanical Engineers, 1990, Paper No: 90-GT-313.

Energy-efficient control strategy of exoskeleton of upper limb

J. Krivošej[a], J. Švadlena[a], M. Daniel[a], Z. Šika[a]

[a]*The Department of Mechanics, Biomechanics and Mechatronics, Faculty of Mechanical Engineering,*
Czech Technical University in Prague, Technická 4, Prague 6, Dejvice 160 00, Czech Republic

The current research and effort in an improvement of exoskeletons can be partly divided into two main areas, which are focused by muscle targeting on lower and upper limb exoskeletons, respectively. A systematic review, which deals with the design, actuation and control of exoskeletons, is shown in [3]. Moreover, exoskeletons can be also divided to wearable exoskeletons and stationary designs. An notable concept of stationary upper limb exoskeleton with redundant cable actuation control implemented is CAREX-7 [1]. This concept was explored further by topics such as self-identification and other topics connected with redundancy in cables as well as sensors. An interesting representative of the wearable exoskeleton is described in [4], where a semi-active approach is proposed and studied. Besides the classic mechanical strutures, there are also special cases. One of them is a lower limb exoskeleton with an active and passive variable stiffness control system based on a shape memory alloy [5].
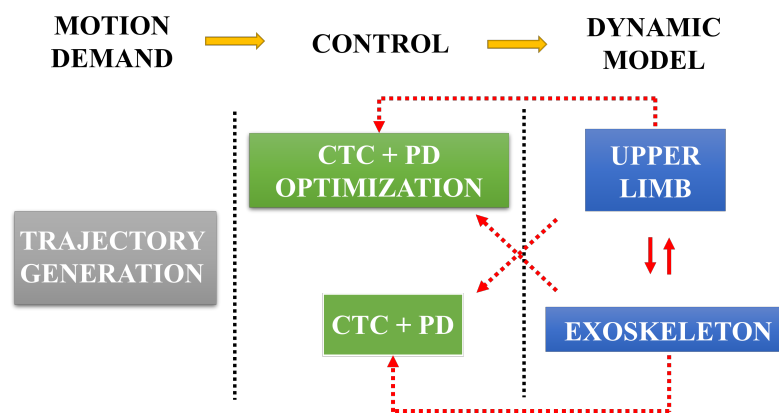
Fig. 1. Simulation scheme of biomechatronic system composed from human upper limb and exoskeleton

The paper deals with the exoskeleton of upper limb. The main focus is targeted on the wearable type of exoskeleton, where the energy-efficient control strategy is crucial. The considered approach is based on the natural motion of the upper limb with the exoskeleton mounted. In the scenarios studied, these are mainly repetitive motions, which intuitively leads to the use of energy storage elements such as springs. Tuning these elements to fully support the upper limb during the repetitive motion demands (typically a rehabilitation procedures) is the basis for a concept called "eigenmotion" [2]. The active control force is then used ideally only to overcome the dissipation in the structure and to support the upper limb motion to stay on the eigenmotion trajectory.

The arising system leads to the simulation scheme of biomechatronic system. The upper limb and upper limb exoskeleton is considered planar for simplicity and for concept verifica-

tion. The upper limb is modelled as a double pendulum with seven muscles projected to the planar geometry. The Hill's muscle model is used. The control of the upper limb is done using computed torque control together with the PD (Proportional-Derivative) regulator and optimization, which is implemented due to the muscle redundancy.

The upper limb exoskeleton is also modelled as a double pendulum and drives are placed in joints. The dynamics of the upper limb exoskeleton is given as

$$\mathbf{M}(\mathbf{q})\ddot{\mathbf{q}} + \mathbf{N}(\mathbf{q}, \dot{\mathbf{q}}) + \mathbf{D}(\dot{\mathbf{q}}) + \mathbf{K}(\mathbf{q}) + \mathbf{Q}_G(\mathbf{q}) = \mathbf{Q}_D, \qquad (1)$$

where $\mathbf{M}(\mathbf{q})$ is the mass matrix, $\mathbf{N}(\mathbf{q}, \dot{\mathbf{q}})$ is a vector of nonlinear terms, $\mathbf{D}(\dot{\mathbf{q}})$ represents damping, $\mathbf{K}(\mathbf{q})$ represents stiffness, $\mathbf{Q}_G(\mathbf{q})$ is a vector representing the gravitational forces and $\mathbf{Q}_D$ is a vector of drive forces. The connection of the upper limb and the exoskeleton is provided by very stiff springs. The simulation scheme of arising biomechatronic system is shown in Fig. 1.

The biomechatronic system consisting of upper limb and upper limb exoskeleton is proposed and studied. The exoskeleton is supposed to be a wearable one with is directly connected with the energy-efficient control strategy. The considered approach is based on the concept known as "eigenmotion". The upper limb and exoskeleton are considered planar to verify the considered approach and are based on a double pendulum. The computed torque control with PD controller are implemented to both upper limb and exoskeleton, where inner optimization is implemented to treat the muscle redundancy. Finally, the trajectory generation is done using the eigenmotion concept to follow the natural motion of the upper limb and exoskeleton together.

Acknowledgements

References

[1] Cui, X., Chen, W., Jin, X., Agrawal, S. K., Design of a 7-DOF cable-driven arm exoskeleton (CAREX-7) and a controller for dexterous motion training or assistance, IEEE/ASME Transactions on Mechatronics 22 (1) (2016) 161-172.

[2] Krivošej, J., Beneš, P., Zavřel, J., Balon, A., Halamka, V., Šika, Z., Energy efficient robots based on structures with tensegrity features and cable-driven mechanisms, Mechanism and Machine Theory 187 (2023) No. 105364.

[3] de la Tejera, J. A., Bustamante-Bello, R., Ramirez-Mendoza, R. A., Izquierdo-Reyes, J., Systematic review of exoskeletons towards a general categorization model proposal, Applied Sciences 11 (1) (2020) No. 76.

[4] Zahedi, A., Wang, Y., Martinez-Hernandez, U., Zhang, D., A wearable elbow exoskeleton for tremor suppression equipped with rotational semi-active actuator, Mechanical Systems and Signal Processing 157 (2021) No. 107674.

[5] Zhang, J., Cong, M., Liu, D., Du, Y., Ma, H., Design of an active and passive control system for a knee exoskeleton with variable stiffness based on a shape memory alloy, Journal of Intelligent & Robotic Systems 101 (2021) 1-15.

Mechanical stabilisation of sacral bone injuries

L. Lobovský[a], M. Marešová[b], T. Mandys[a], M. Salášek[c], D. Weisová[c],
J. Krystek[b], J. Křen[a,b]

[a]*NTIS – New Technologies for the Information Society, Faculty of Applied Sciences, University of West Bohemia, Univerzitní 8, 301 00 Plzeň, Czech Republic*

[b]*Department of Mechanics, Faculty of Applied Sciences, University of West Bohemia, Univerzitní 8, 301 00 Plzeň, Czech Republic*

[c]*Clinic for Orthopaedics and Traumatology of Locomotive Organs, University Hospital, alej Svobody 80, 323 00 Plzeň, Czech Republic*

In order to perform a thorough analysis of mechanical stabilisation of unstable pelvic ring injuries and to suggest their optimal treatment, a computational model based on finite element method is designed and verified using experimental data. Sacral bone fractures and especially the fractures with spinopelvic dissociation are of interest. Several osteosynthesis techniques for internal fixation of dorsal pelvis injuries are investigated. An attention is paid to minimally invasive osteosynthesis which employs transiliac internal fixation (TIFI) [3, 7], iliosacral screws (ISS) [1, 4] or lumbo-sacral fixations [5].

The conducted experimental study focuses solely on mechanical response of physical models of male pelvis with/without fracture and its treatment. These include models made of homogeneous isotropic material with linear mechanical response [8] as well as models with composite sandwich structure [9]. The latter mimics mechanical properties of real pelvic bones. On contrary to cadaveric pelves, experiments with physical models provide repeatable data and their execution and control is substantially simplified. Mechanical properties of materials, the physical models are made of, are unambiguously determined.

The experimental pelvic tests are designed so that the uncertainity in the measured data is minimal. The models are tested under a quasi-static loading in craniocaudal direction while no displacements nor rotations in acetabula are allowed. Displacements and deformations of the pelvic bones are assessed using digital image correlation [6].

The applied experimental approach enables straightforward development of the computational model which precisely reflects the performed experiments. The geometry of the computational model is derived from the computed tomography scans of the physical models. The computational problem of elastostatics is solved and a surface-to-surface contact algorithm with a finite sliding formulation is employed between the fractured bone parts. Motion of all fixator screws within the bone tissue is fully constrained. In both computations and experiments, the effect of soft tissue structures is not reflected.

The computational model is verified for experiments on pelvic ring with either unilateral linear or unilateral comminuted fracture. Absolute displacements of the loaded sacral base, relative motion of the fractured bone parts and a symmetry of bone deformations are used as a key indicator of structural stability of the tested pelvis. In order to quantify the stability of each fixation technique, the stiffness ratio between the treated and the intact pelvic structure is introduced.

The verified computational model of pelvic ring is extended so that it includes the last two lumbar vertebrae and intervertebral discs. This enables modelling of lumbo-sacral fixation tech-
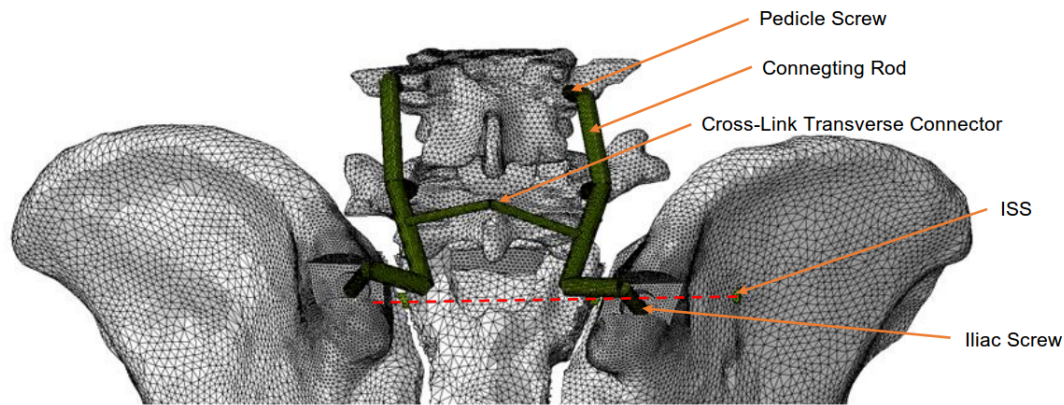
Fig. 1. Computational model of male pelvis with last two lumbar vertebrae and lumbo-sacral fixation

niques which provide superior results for unstable fractures with spinopelvic dissociation. In these cases, a lumbo-sacral fixation with a cross-link connector [2] is advantageous, Fig. 1. However, such technique requires an open surgery. This may be avoided when the cross-link connector is superseded by the ISS. The absence of the cross-link connector allows for a minimally invasive approach while the combination of the lumbo-sacral fixation with the ISS significantly increases stability of the treated pelvic structure.

Acknowledgement

References

[1] Berber, O., Amis, A. A., Day, A. C., Biomechanical testing of a concept of posterior pelvic reconstruction in rotationally and vertically unstable fractures, The Journal of Bone and Joint Surgery. British volume 93-B (2) (2011) 237-244.

[2] Cornaz, F., Widmer, J., Snedeker, J. G., Spirig, J. M., Farshad, M., Cross-links in posterior pedicle screw-rod instrumentation of the spine: A systematic review on mechanical, biomechanical, numerical and clinical studies, European Spine Journal (30) (2021) 34-49.

[3] Dienstknecht, T., Berner, A., Lenich, A., Zellner, J., Mueller, M., Nerlich, M., Fuechtmeier, B., Biomechanical analysis of transiliac internal fixator, International Orthopaedics 35 (12) (2011) 1863-1868.

[4] Giráldez-Sánchez, M. A., Lázaro-Gonzálvez, A., Martínez-Reina, J., Serrano-Toledano, D., Navarro-Robles, A., Cano-Luis, P., Fragkakis, E. M., Giannoudis, P. V., Percutaneous iliosacral fixation in external rotational pelvic fractures. A biomechanical analysis, Injury 46 (2) (2015) 327-332.

[5] Lindahl, J., Mäkinen, T. J., Koskinen, S. K., Söderlund, T., Factors associated with outcome of spinopelvic dissociation treated with lumbopelvic fixation, Injury (45) (2014) 1914-1920.

[6] Sutton, M. A., Orteu, J. J., Schreier, H. W., Image correlation for shape, motion and deformation measurements, Springer Science+Business Media, New York, 2009.

[7] Ueno, F. H., Pisani, M. J., Machado, A. N., Rodrigues, F. L., Fujiki, E. N., Biomechanical study of the sacroiliac fracture fixation with titanium rods and pedicle screws, Acta Ortopedica Brasileira 23 (3) (2015) 154-157.

[8] https://www.sawbones.com/full-male-pelvis-large-solid-foam-w-sacrum-1301.html

[9] https://www.sawbones.com/full-pelvis-large-4th-generation-composite-pelvis-fused-w-4th-generation-epoxy.html

Numerical simulations of finite compressor cascade in 2D and 3D

P. Louda[a]

[a] *Institute of Thermomechanics, Czech Academy of Sciences, Dolejškova 5, Praha 8, Czech Republic*

The recent research at Institute of Thermomechanics AS CR includes measurements of flow through a model of compressor cascade [4]. In the experiment, suction of fluid from inter-blade channels is applied using relatively large slots in both side walls, see Fig. 1. In order to understand better the effect of suction, corresponding numerical simulations are carried out which are the subject of present article. The 3D solution domain consists of inlet channel, test section, and part of settling chamber of the wind tunnel, see Fig. 1. The suction slots are vented into common chamber with discharge piping on both ends (see Fig. 1, where the chamber itself is omitted in CAD drawing). Moreover, solid plates are positioned in the wakes of outer blades. Only half of the symmetrical test section is considered in simulations. Even so, the computational domain has 1 inlet and 6 outlets. The net flow rate is not known from measurement, therefore the inlet conditions are prescribed in order to meet the target Mach number in front of the cascade. On the outlet, target Mach number behind the cascade and net suction flow rate is known. In 4 outlets, the flow rate is dynamically adjusted to target values. One possibility of flow rate boundary conditions is given by Jirásek [2]. Other approach tested is dynamically adjusting average static pressure according to the 1D Bernoulli equation. Both approaches lead to same results.
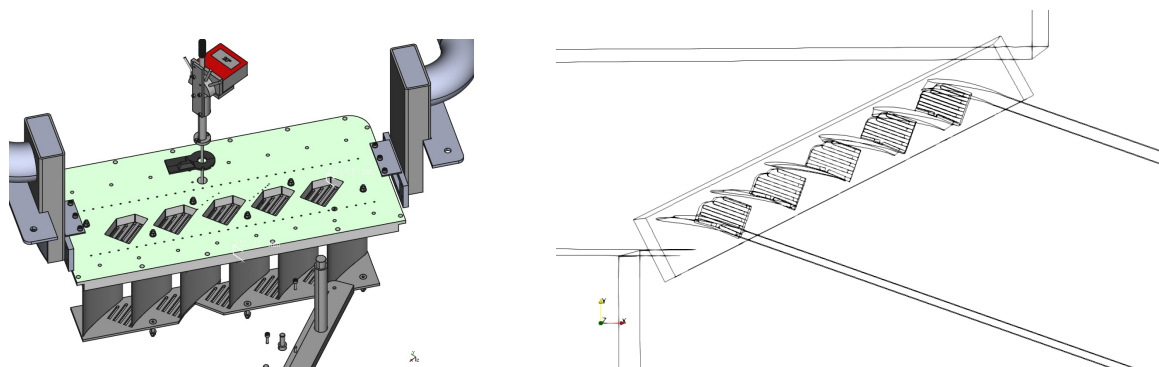
Fig. 1. Left: CAD model of the experimental cascade, right: corresponding computational domain

The mathematical model is based on Favre averaged Navier-Stokes equations for compressible flow. The turbulence is approximated by an explicit algebraic Reynolds stress model (EARSM) due to Wallin and Hellsten [1, 5].

The governing equations are discretized by an implicit finite volume method using hexahedral finite volumes in structured grid. Multi-block extension is used for complex geometry. The inviscid part of equations is approximated by the AUSMPW+ upwind method [3] with higher order interpolation in the direction of grid lines. The equations are linearized leading to block

7-diagonal algebraic system (if the boundary is neglected). The linear solver combines direct solver for 3-diagonal system with sweeps in other two directions. The implementation is in-house parallel code by the author. The grid is also generated by author's code and a zoom is shown in Fig. 2. The grid consists of approx. 5.5 mil. finite volumes in approx. 2 000 blocks. The work to parallel processes is distributed block-wise.

The simulated regime corresponds to inlet Mach number 0.892, inlet angle of $61°$ and outlet Mach number 0.627 with outlet angle $45.6°$. The isolines of Mach number in the cascade are shown in Fig. 3. One can see that there is large flow separation on 4th and 5th blade. This makes the simulation to some extend unsteady. The measurement corresponds to attached flow, however, differs somewhat in Mach number.
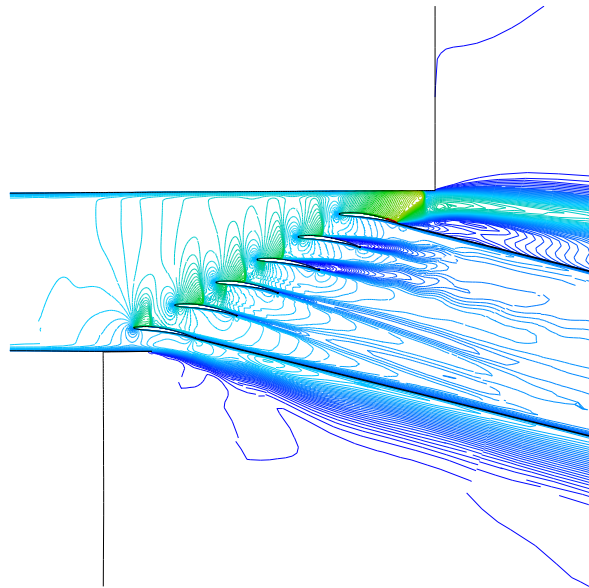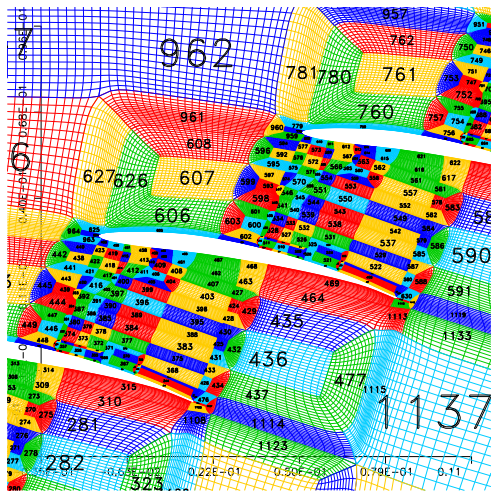
Fig. 2. Grid structure around the cascade   Fig. 3. Mach number isolines in the center-plane

The net influence of transversal flow can be expressed by means of the axial velocity density ration (AVDR) coefficient: AVDR$= \left(\int_0^t \rho_2 v_{ax2} ds\right)\left(\int_0^t \rho_1 v_{ax1} ds\right)$, where subscript 1 denotes inlet and subscript 2 outlet. The AVDR for each inter-blade channel is shown in Table 1.

Table 1. AVDR coefficients for inter-blade channels

channel	simulation	measurement
1	1.261	
2	1.208	
3	1.154	1.178
4	0.774	
5	0.794	

The distribution of Mach number in the middle of suction slots is shown in Fig. 4. It should be noted that there is reverse flow near front and rear end of most slots. The line in the same figure denotes plane, which is shown in terms of Mach number in Fig. 5.

Simultaneously, 2D simulations are carried out, as well. They enable faster evaluation of inlet parameters since inlet is not much influenced by 3-dimensionality of the flow. To some extend, they could approximated flow in center-plane without suction. However, the 2D sim-
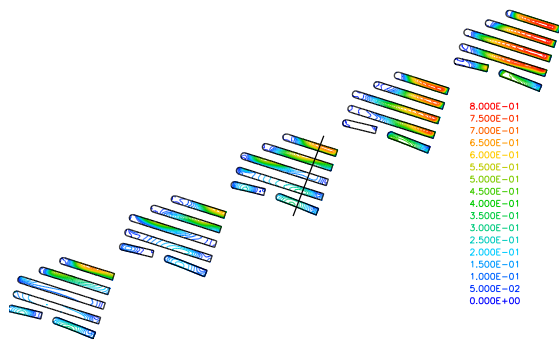
Fig. 4. Mach number in the suction slots
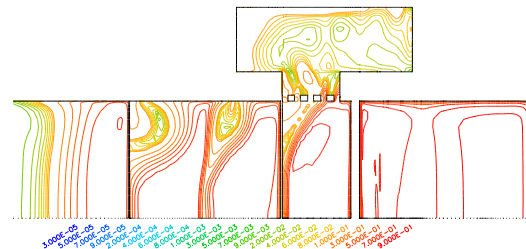
Fig. 5. Mach number of the secondary flow

ulation predicts some flow separation on all blades and it remains to be confirmed if it is the effect of suction from side walls.

As a preliminary conclusion, though, only 3D simulations probably can provide reliable results even if one considers the center-plane only. The convergence of numerical simulations is adversely affected by the need of dynamically adjusting flow rates in some outlets and by large overall dimensions of the solution domain compared to the cascade. Moreover, the parameters of flow regime in the experiment are found by trial and error. Nevertheless the simulation is the only way to visualize secondary flows in the present configuration.

Acknowledgment

References

[1] Hellsten, A., New advanced k-ω turbulence model for high-lift aerodynamics, AIAA Journal 43 (9) (2005) 1857-1869.

[2] Jirásek, A., Mass flow boundary conditions for subsonic inflow and outflow boundary, AIAA Journal 44 (5) (2006) 939-947.

[3] Kim, K. H., Kim, C., Rho, O.-H., Methods for accurate computations of hypersonic flows I. AUSMPW+ scheme, Journal of Computational Physics 174 (2001) 38-80.

[4] Luxa, M., Šimurda, D., Measurements on compressor cascade KOBRA, Research Report Z 1649/21, Institute of Thermomechanics, Czech Academy of Science, v.v.i., 2022.

[5] Wallin, S., Engineering turbulence modeling for CFD with a focus on explicit algebraic Reynolds stress models, Ph.D. thesis, Royal Institute of Technology, Stockholm, 2000.

Geometric model of nonwoven fabric
for homogenization of mechanical properties

A. Luciová[a], A. Potěšil[a,b], P. Henyš[a]

[a]Institute of New Technologies and Applied Informatics, Faculty of Mechatronics, Informatics and Interdisciplinary Studies, Technical
University of Liberec, Studentsk 1402/2, 461 17 Liberec, Czech Republic
[b]LENAM, s.r.o., Husova 725/40, 460 01 Liberec. Czech Republic

1. Introduction

Light nonwoven fabric Meftex is a functional textile material with various interesting properties, including EMS shielding properties and electrical conductivity. The functional properties of the textile are given by a thin metal surface layer on a polyester fiber core. In our application, Meftex figures a functional layer inside a more complex laminate material for electric car battery boxes. As with other automotive applications, safety requirements exist, especially on mechanical properties, which will be investigated by a computational homogenization approach. The first step for computational analysis of Meftex mechanical properties and homogenization is to create representative geometry. Geometrical modeling of Meftex fabric with different surface density is described in the paper [2], which describes the reconstruction of the geometry of a small section of a similar textile with lower areal density. Textiles with different areal densities exhibit distinct characteristics and require the introduction of different assumptions. In contrast to the mentioned article, this work aims to establish a methodology for constructing a micro-mechanical representative model rather than creating an accurate replica of a small textile segment.

2. Image processing

The structure of the Meftex consists of two layers connected by thermal bonding. In each layer, fibers are almost parallel and perpendicular between layers, which is reflected in the model. Therefore, the proposed model consists of two layers of fibers and thermal bonds. Each of these units is created independently. Image data from scanning confocal microscope were
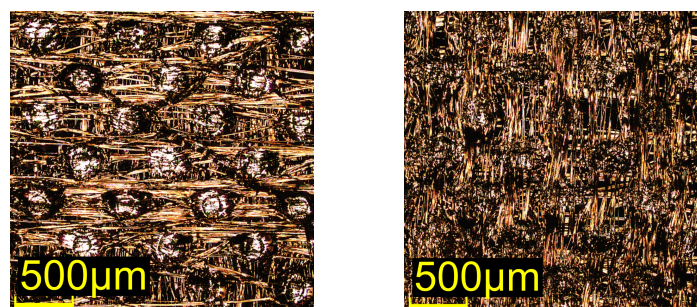
Fig. 1. Images of Meftex fabric obtained by confocal scanning microscope from front and back side

used as input, Fig. 1. The images show uneven fiber placement, where fibers are arranged in periodically spaced clusters. The objective of image analysis is to characterize and replicate this arrangement.

Fibers from the opposite side are visible through both the front and back layers, which could cause distortions in subsequent analyses. The distribution of fibers between layers was determined by orientation analysis in ImageJ software [3]. Each image was then binarized and skeletonized, Fig. 2. Each skeleton was characterized by its length and center coordinates for further analysis. Furthermore, the local mass distribution was obtained by summing over the direction of fiber orientation, Fig. 3.
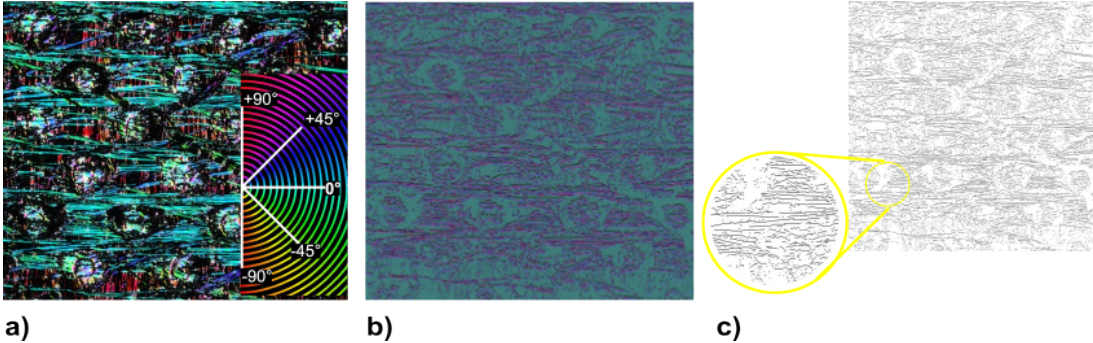
Fig. 2. Image processing procedure–orientation analysis (a), segments with uniform orientation (b), image after skeletonization (c)
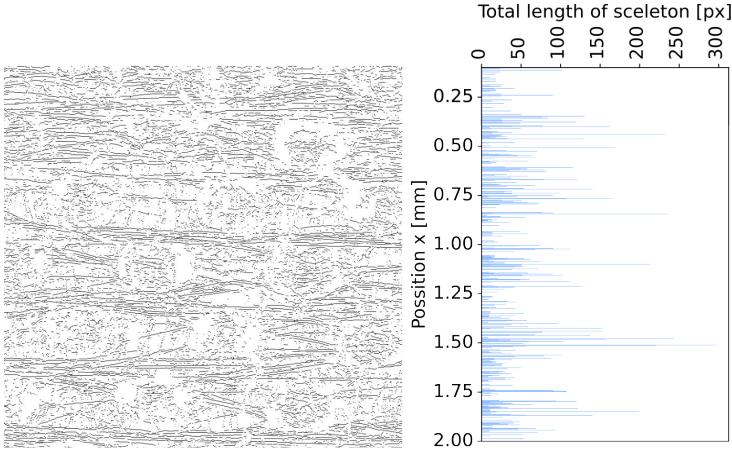
Fig. 3. Example of vertical mass distribution of one side of fabric

3. Identification of fiber placement characteristics

The mass distribution diagram shows two levels of periodicity of the structure. The fibers are arranged in periodically spaced bundles. The next level of arrangement is the distribution of fibers within these bundles. The discrete wavelet transform (DWT) was used to separate these two levels. The main reason for using the wavelet transform is its ability to decompose the signal into frequency components while preserving localization information with minimal distortion [4]. A fifth-order Daubechies wavelet was used as the basis function. Fig. 4 shows the trend and fluctuation components of the signal obtained by the wavelet transform. The fast Fourier transform (FFT) of these components was performed to characterize the periodicity of the fiber distribution.
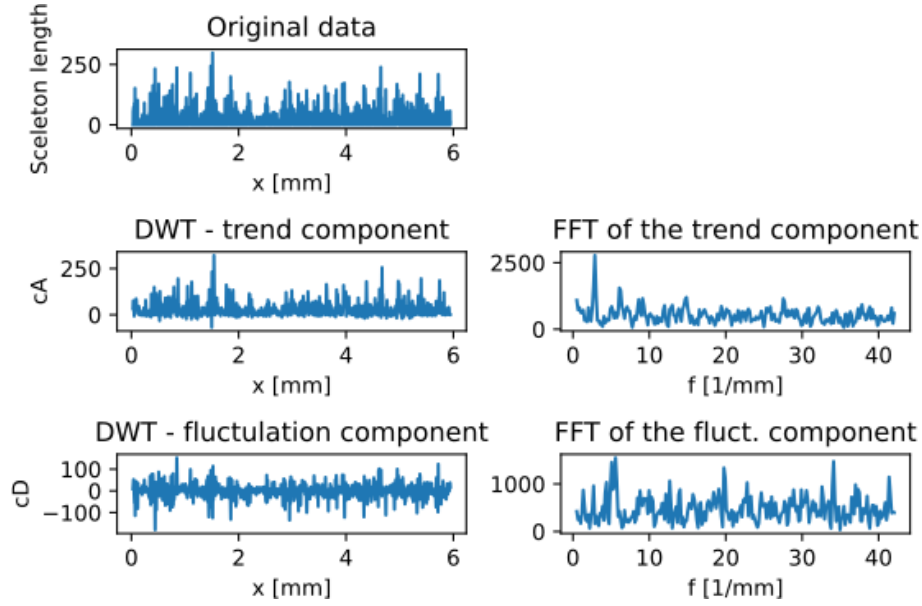
Fig. 4. Decomposition of mass distribution signal by wavelet transform and frequency spectrum of each component

The mass of a single fiber was estimated from its length, diameter, surface density of fabric, and front-to-back side skeleton length ratio. In the next step, the placement of each fiber was determined, and the transversal coordinate was chosen so that no intersections or collisions between fibers would occur. Finally, the representative geometry was built in the multi-scale modeling software MSC.Digimat [1].

4. Application

The developed geometry was used to estimate the effective elastic properties of the laminate with epoxy matrix and Meftex reinforcement. The linear elastic behavior of the material was considered, i.e.,

$$\sigma_{ij} = C_{ijkl}\epsilon_{kl}\,. \tag{1}$$

The representative geometry was discretized using the voxel mesh. Periodic boundary conditions were used. Effective elastic coefficients were computed using linear homogenization

$$\langle\sigma_{ij}\rangle = \frac{1}{V}\int \sigma_{ij}\mathrm{d}V\,. \tag{2}$$

Results are demonstrated by directional dependence of stiffness tensor component E_{11}, Fig. 5b. The FFT solver implemented in MSC.Digimat software was used for the computation [1].

5. Conclusion

The described methodology allows the construction of a geometry based on the characteristics of the periodicity of the fiber placement. Several assumptions were considered. The fibers are treated as straight, arranged in two layers with uniform orientation in one layer. As a result, the geometry is, by default, periodical, which allows the usage of periodic boundary conditions in the homogenization step. Furthermore, a constant fiber diameter is considered, and the vertical position of the fibers is chosen so that the fibers do not intersect. The usage of the developed representative geometry was demonstrated by the homogenization of its mechanical properties.
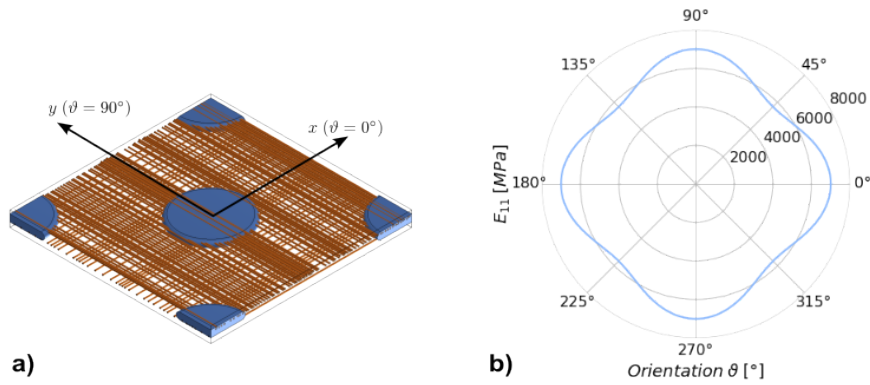
Fig. 5. Representative volume element of reconstructed geometry (a) and directional dependence of stiffness tensor component E_{11} (b)

Acknowledgements

References

[1] Hexagon, Digimat 2022.4 FE Users Guide, 2022.

[2] Hu, S., Wang, D., Kyosev, Y., Schmidt, A.-M., Kremenakova, D., Statistical fiber-level geometrical model of thin non-woven structures, Proceedings of the International Symposium "Technical Textiles – Present and Future", Sciendo, 2022, pp. 99-104.

[3] Rezakhaniha, R., Agianniotis, A., Schrauwen, J. T. C., Griffa, A., Sage, D., Bouten, C., van de Vosse, F., Unser, M., Stergiopulos, N., Experimental investigation of collagen waviness and orientation in the arterial adventitia using confocal laser scanning microscopy, Biomechanics and Modeling in Mechanobiology 11 (34) (2012) 461473.

[4] Walker, J. S., A primer on wavelets and their scientific applications, CRC Press, 2021.

Efficient methods for calculating equivalent stiffness of circular composite tubes: Insights for structural design optimisation

A. Malá[a], Z. Padovec[a], T. Mareš[a]

[a] *Department of Mechanics, Biomechanics and Mechatronics, Faculty of Mechanical Engineering, Czech Technical University in Prague, Prague, Czech Republic*

This paper presents the comparative analysis of various analytical methods used to estimate the equivalent stiffness of circular cross-section composite tubes manufactured using filament wound technology with long fibre laminates. Four computation methods, namely ABD matrices theory (ABD), minimum total potential energy theory (E), minimum complementary energy theory (C), and an averaged approach (avg), are evaluated. The comparison involves analysing a cantilever beam subjected to bending, torsion, and combined loading with varying force-to-moment ratios (as illustrated in Fig. 1).

Fig. 1. Cantilever beam loaded with bending (bending force F) and torsion (torque moment T)

These theories are derived from the extended Hooke´s law for orthotropic materials, defining the stiffness matrix of a ply in the laminate coordinates E_{ti} akin to its inversion (compliance matrix C_{ti}), as found in references like [1]. Both matrices are determined by material mechanical parameters (Young´s module in the fibre direction E_L and perpendicular to the fibre direction E_T, shear module G_{LT}, and Poisson's ratio ν_{LT}), as well as the ply orientation angle (α_i).

Important geometric parameters used in calculations include tube outer diameter (d_{out}), inner diameter (d_{in}), outer radius (r_{out}), mean radius (r), inner radius (r_{in}), the number of plies in the laminate (n), ply thickness (t), and the thickness of the tube (T_T). The index 'i' refers to '$i-th$' ply of the laminate.

The equations for determining equivalent stiffnesses, such as tensile $(EA)_{eq}$, bending $(EJ)_{eq}$, torsional $(GJ_p)_{eq}$ and shear $(GA)_{eq}$, are provided in Table 1. The cross-sectional area $\tilde{A} = \pi(r_{out}^2 - r_{in}^2)$, the moment of inertia $J = \frac{\pi(d_{out}^4 - d_{in}^4)}{64}$, and the polar moment of inertia $J_p = \frac{\pi(d_{out}^4 - d_{in}^4)}{32}$. ABD matrices theory employs matrix A for calculation, representing laminate extensional stiffness. It is defined by the equation (1) as the sum of the product of individual ply stiffnesses and the ply thicknesses. The laminate tension module E_{eqABD} and shear module

G_{eqABD} are determined by members of the A matrix in equations (2) and (3), incorporating the laminate thickness (T_T) and auxiliary variable M (4).

$$A= \sum_{i=1}^{n} E_{ti}t_i \ , \tag{1}$$

$$E_{eqABD}= \frac{M}{T_T(A(3, 3)A(2, 2)-A(2, 3)A(2, 3))} \ , \tag{2}$$

$$G_{eqABD}= \frac{M}{T_T(A(1, 1)A(2, 2)-A(1, 2)A(1, 2))} \ , \tag{3}$$

$$M=A(1,1)A(2,2)A(3,3)+2A(1,2)A(1,3)A(2,3)-A(1,1)A(2,3)^2-A(2,2)A(1,3)^2-A(3,3)A(1,2)^2 \ , \tag{4}$$

Table 1. Equations for calculating equivalent stiffnesses according to individual calculation methods

Theory	Stiffness			
	$(EA)_{eq}$	$(EJ)_{eq}$	$(GJ_p)_{eq}$	$(GA)_{eq}$
ABD	$E_{eqABD}\widetilde{A}$	$E_{eqABD}J$	$G_{eqABD}J_p$	$G_{eqABD}\widetilde{A}$
E	$\sum_{i=1}^{n} \pi(r_{outi}^2-r_{ini}^2)E_{ti}(1,1)$	$\sum_{i=1}^{n} \pi r_i^3 t_i E_{ti}(1,1)$	$\sum_{i=1}^{n} \frac{4A_{ci}^2 t_i E_{ti}(3,3)}{c_i}$	$\sum_{i=1}^{n} \pi(r_{outi}^2-r_{ini}^2)E_{ti}(3,3)$
C	$\sum_{i=1}^{n} \frac{\pi(r_{outi}^2-r_{ini}^2)}{C_{ti}(1,1)}$	$\sum_{i=1}^{n} \frac{\pi r_i^3 t_i}{C_{ti}(1,1)}$	$\sum_{i=1}^{n} \frac{4A_{ci}^2 t_i}{c_i C_{ti}(3,3)}$	$\sum_{i=1}^{n} \frac{\pi(r_{outi}^2-r_{ini}^2)}{C_{ti}(3,3)}$
avg	the average of the stiffness values obtained from the previous three methods			

The set of tubes were loaded by bending force $F = 1000$ N, torsion moment $T = 1000$ Nm, or by its combination, where the ratios $T/F = 1, \ 10, \ 100$ or 1000 with constant value of bending force $F = 1000$ N. The value of displacement for pure bending, rotation of pure torsion, and minimum equivalent energy of combined loading was shown in a dependence graph of the given value on the tube winding angle. These dependencies were plotted for tubes of different thicknesses ($t = 0.2, 0.5, 1, 2, 5, 10$ and 20 mm), which winding is composed of four layers with thicknesses $t/4$ and winding angles $\pm\alpha$.

Inner diameters of analysed tubes were $d = 5, 10, 20, 40, 80$ mm, and the tube length-to-inner diameter ratios $L/d = 1, 5, 10, 20$ and 50. Material parameters of analysed tubes were set as T700/epoxy laminate properties: $E_L = 128000$ MPa, $E_T = 5060$ MPa, $G_{LT} = 3400$ MPa and $\nu_{LT} = 0.345$.

A typical angle-to-displacement dependence for the bended beam, with a length-to-diameter ratio greater than 5, is displayed in Fig. 2. Similarly, the angle-to-rotation dependence is presented in Fig. 3. The angle-to-equivalent energy dependence for beams subjected to combined loading highly depends on the torsion moment-to-bending force ratio, which affects the position of the extremes of the given dependencies, as shown in Fig. 4. The top graph shows an example of a load with a bending force of 1000 N and a torque of 1000 Nmm, while the bottom graph shows a load with a bending force of 1000 N and a torque of 1000 Nm.
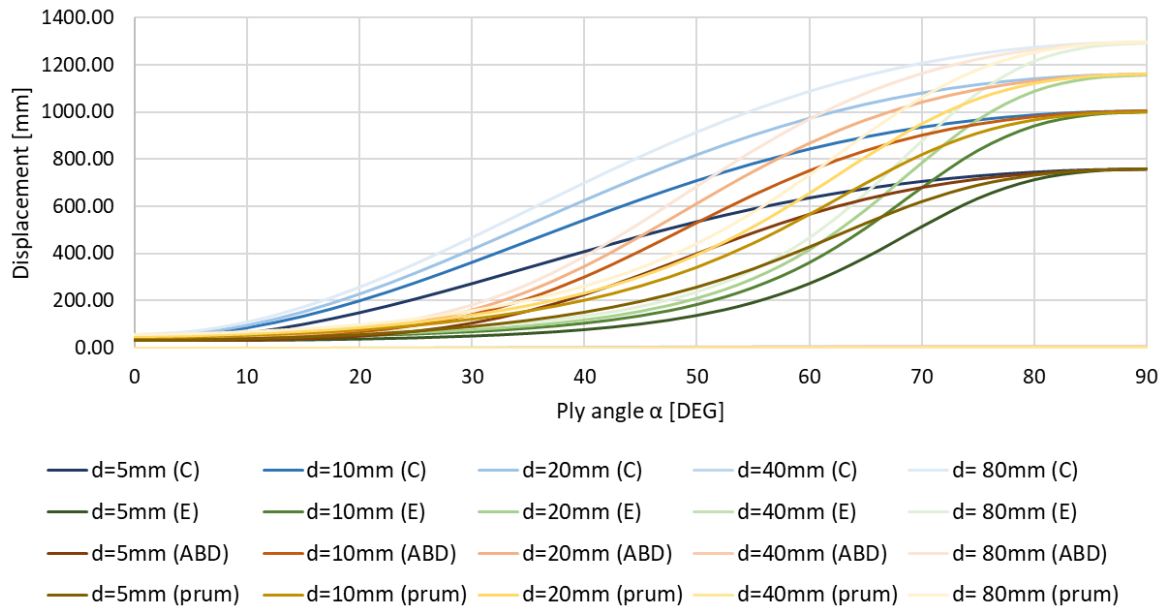
Fig. 2. A typical angle-to-displacement dependence for bended beam
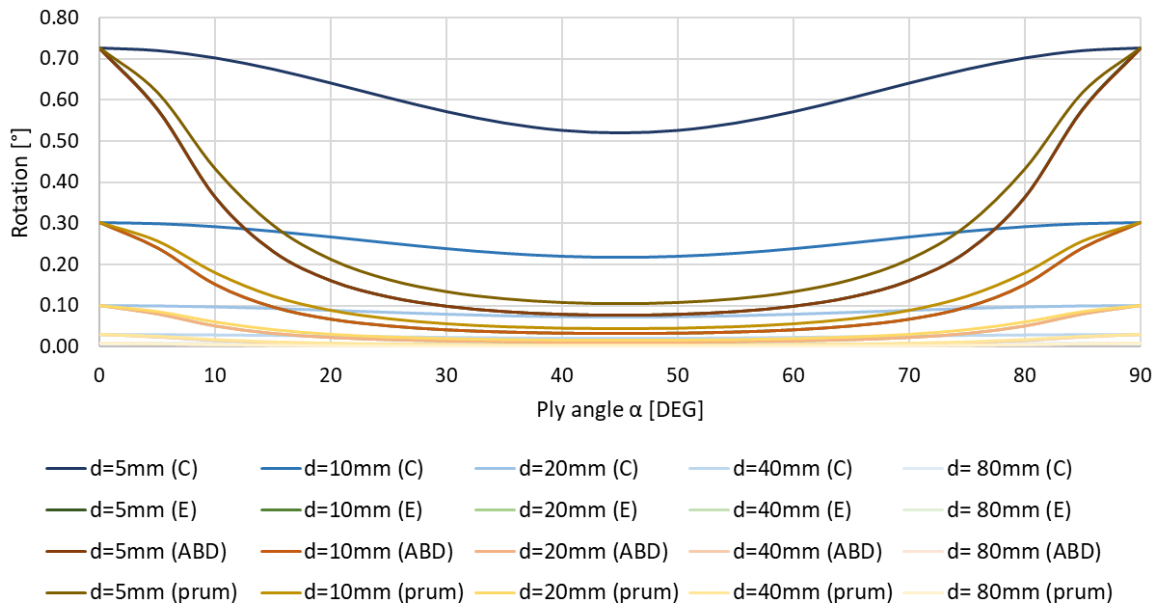
Fig. 3. A typical angle-to-rotation dependence for torsion
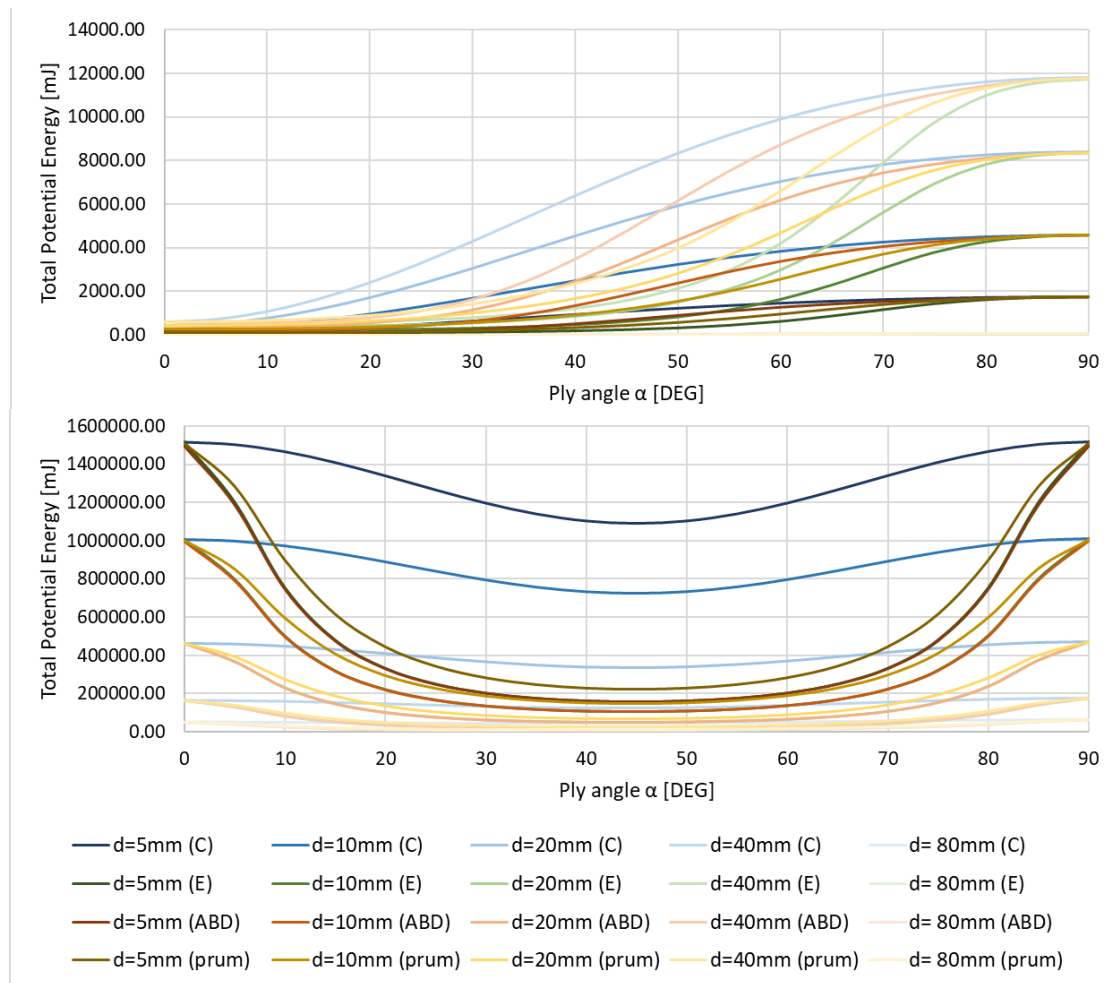
Fig. 5. Angle-to-total potential energy dependence

As evident from the aforementioned dependencies, the minimum complementary energy theory exhibits the highest absolute values, while the trends remain similar across the selected theories. This underscores the preference for utilizing the minimum complementary energy approach in optimizing the winding parameters for composite tubes. The theory's higher values correspond to lower stiffness, which enhances the safety margin in the design process. It is worth noting that extreme cases involving beams with a length-to-diameter ratio of one have been excluded from consideration for the given structures, as such geometries are no longer deemed as beams in this context.

Acknowledgement

References

[1] Jones, R. M, Mechanics of Composite Materials, second ed., Taylor & Francis Ltd., London, 1999.

Modelling of secondary suspension for electric multiple unit

T. Michálek[a], F. Jeniš[b]

[a] Department of Transport Means and Diagnostics, Faculty of Transport Engineering, University of Pardubice,
Studentská 95, 532 10 Pardubice, Czech Republic
[b] Institute of Machine and Industrial Design, Faculty of Mechanical Engineering, Brno University of Technology,
Technická 2896/2, 616 69 Brno, Czech Republic

The ride comfort is one of the most important aspects of railway vehicle dynamics from the point of view of railway users – the passengers. Increasing running speed and the requirements on barrier-free access into the vehicles, i.e. on low-floor high-capacity vehicles with traction equipment situated on the roof, make it more demanding to maintain the ride comfort at a high level. From the point of view of the railway vehicle design, the ride comfort is significantly influenced by the secondary suspension stage, i.e. the elastic and damping joints transmitting forces between the vehicle body and bogie frames and their parameters. A possible way, how to increase the ride comfort, is the application of modern technologies into the vehicle running gear, especially the actuators or semi-active dampers. Because of higher costs and demanding requirements on fail-safe function, the actuators are more complicated for application on the vehicle than the semi-active systems. However, the actuators are used nowadays in case of some locomotives in form of so-called active yaw dampers to help the individual bogies to steer into small-radius curves, and reduce the wheel/rail forces and wear in this way (see, e.g., [4]).
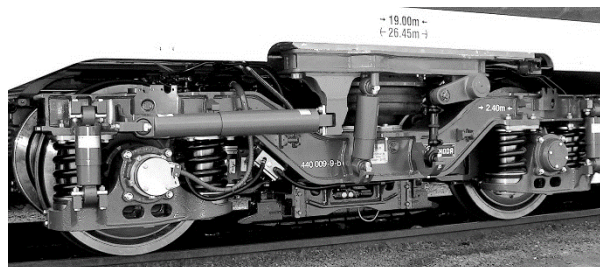
Fig. 1. Trailer bogie of a single-deck ŠKODA EMU

Potential benefits of semi-actively controlled secondary dampers – i.e. the second possible (and simultaneously cheaper as well as less demanding from the point of view of running safety and energy consumption) way to improve the ride comfort of railway vehicles by applying the innovative technologies – are investigated in framework of co-operation of Strojírna Oslavany (ST-OS), the Faculty of Mechanical Engineering of Brno University of Technology (BUT) and the Faculty of Transport Engineering of the University of Pardubice (UPCE) at solving an R&D project of the Technology Agency of the Czech Republic focused on improvement of the ride comfort of an electric multiple unit (EMU). An intermediate traction coach of the single-deck ŠKODA 10Ev EMU was selected as the object of the research work. This vehicle consists of a vehicle body and two two-axle bogies – one traction and one trailer bogie (see Fig. 1). The basic concept of both bogie types is the same – the primary suspension is realized by a couple of helical coil springs per axle box, the wheelset guiding within the bogie frame is ensured by vertical cylindrical plugs with rubber elements. The secondary suspension stage is realized by

a pair of air springs with additional rubber springs per bogie and supplemented with vertical, lateral and longitudinal (yaw) dampers (a couple of each of them per bogie) and an anti-roll bar. The longitudinal force transmission between the bogie frame and the vehicle body is ensured by a central pivot and lemniscate mechanism. Lateral and yaw movements of the bogie relative to the vehicle body are limited by relevant bump stops. All the wheelsets are braked by web-mounted brake discs; in case of the traction bogie, the relevant wheelsets are driven individually and the torque of asynchronous traction motor is transmitted on the wheelset through a tilting coupling and an axle gear box.

For purposes of investigation of dynamic behaviour of the selected vehicle and optimization of the semi-active control of the secondary lateral and vertical dampers, a multi-body model of the vehicle was created in the SJKV simulation tool at the Faculty of Transport Engineering of the University of Pardubice. At the modelling, the most challenging task was the creation of the secondary suspension model including implementation of semi-active control of the dampers. As mentioned above, the secondary suspension consists of a couple of pneumatic springs, which are placed on the (emergency) rubber springs. In case of the investigated vehicle, two additional air reservoirs are connected to each air bellow to ensure a sufficiently soft characteristics of the suspension. Because of a pneumatical interconnection of the air springs on both bogie sides, a one-point support of the vehicle body on each bogie is achieved. Therefore, the stability of the vehicle body at the inflated air springs is ensured only by the anti-roll bars. For application into the multi-body vehicle model, the vertical and horizontal stiffness characteristics of the whole air spring system were estimated on basis of results of bench tests performed by manufacturer of the springs.

The secondary dampers, which are planned to be tested on the investigated vehicle in the mode of semi-active control, are being developed in co-operation of the Faculty of Mechanical Engineering of Brno University of Technology and ST-OS. Their design is based on previously developed semi-active yaw dampers with a short response time using the magnetorheological fluid (see, e.g., [3]). In this stage of the research, the control algorithm "Skyhook linear" (see, e.g., [2]) was chosen for implementation. Generally, the concept of "Skyhook control" is based on the idea that the vehicle body is connected with the inertial reference frame (i.e. the sky) by means of an ideal viscous damper to ensure a high level of the ride comfort during excitation of the vehicle by running on real track irregularities. Therefore, the "Skyhook damper" should work with the absolute velocity of the vehicle body. In practical application, the damper is able to switch (continuously) between its maximum and minimum $F-v$ characteristic and the so-called "Skyhook linear" algorithm is based on these conditions (see, e.g., [2])

$$F(v) = \begin{cases} F_{\min}(v) & \Leftrightarrow \dot{y}_b \cdot (\dot{y}_b - \dot{y}_f) \leq 0 \\ \mathrm{sat}\left(\dfrac{\alpha \cdot F_{\max}(v) \cdot (\dot{y}_b - \dot{y}_f) + (1-\alpha) \cdot F_{\max}(v) \cdot \dot{y}_b}{\dot{y}_b - \dot{y}_f} \right) & \Leftrightarrow \dot{y}_b \cdot (\dot{y}_b - \dot{y}_f) > 0 \end{cases}$$

where $F_{\min}(v)$ and $F_{\max}(v)$ denote the minimum and maximum $F-v$ curves of the damper, $\dot{y}_b$ is the velocity of the vehicle body in relevant direction (lateral vs. vertical), $\dot{y}_f$ is the velocity of the bogie frame in this direction and the coefficient α is a tuning parameter ($\alpha = 0$ belongs to the "Skyhook linear" algorithm and $\alpha = 1$ to the simpler "ON/OFF Skyhook"). The response time of the magnetorheological dampers as well as the effect of stiffness of rubber bushing in the damper joints are considered in form of dependency of the time constant of the damper (see, e.g., [1]) on the velocity of damper deformation reflecting measurement results obtained with a damper prototype at BUT.

To demonstrate a potential contribution of the semi-active control of secondary dampers to the ride comfort improvement, a comparison of simulation results for the vehicle equipped with the original hydraulic dampers and with the semi-actively controlled lateral secondary dampers is presented in Fig. 2. The relevant simulations of vehicle running performance were performed

in a straight track at speed of 160 km/h. In the left graph, time behaviour of lateral acceleration on the vehicle body and floating RMS signal (calculated in accordance with the requirements of EN standard on on-track tests with a window of 100 m) are presented. It is evident that the acceleration observed on the vehicle with semi-actively controlled lateral dampers (grey lines) reaches a lower level; the observed maximum RMS value in this particular track section is lower about approximately 30 % in comparison with the vehicle with passive damping (black lines). In the right graph in Fig. 2, corresponding working $F-v$ characteristics of one of the lateral dampers is shown. It should be noted that significantly lower damping forces and slightly higher velocities are observed on the semi-active damper in comparison with the passive one.
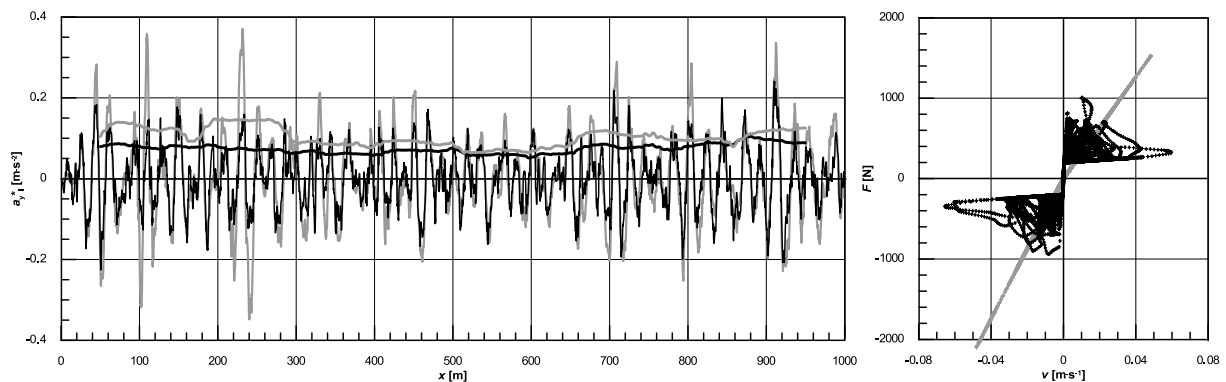
Fig. 2. Comparison of lateral acceleration (time behaviour and floating RMS) on the vehicle body (left) and working $F-v$ characteristics of a lateral secondary damper (right) at simulation of vehicle running on a straight track at 160 km/h with original passive (grey lines/dots) and semi-actively controlled lateral secondary dampers (black lines/dots)

In this contribution, selected simulation results of the initial stage of development of a semi-active damping system for a single-deck EMU are presented. In the next stage, the described simulation model will be used for optimization of efficiency of the semi-active damping system. Verification of the simulation results by on-track tests is expected to be realized in 2024.

Acknowledgements

References

[1] Jeniš, F., Kubík, M., Michálek, T., Strecker, Z., Žáček, J., Mazůrek, I., Effect of the magnetorheological damper dynamic behaviour on the rail vehicle comfort: hardware-in-the-loop simulation, Actuators 12 (2) (2023) 47.

[2] Koulocheris, D., Papaioannou, G., Chrysos, E., A comparison of optimal semi-active suspension systems regarding vehicle ride comfort, IOP Conference Series: Materials Science and Engineering 252 (2017).

[3] Kubík, M., Strecker, Z., Jeniš, F., Macháček, O., Přikryl, M., Špalek, P., Magnetorheological yaw damper with short response time for railway vehicle bogie, Actuators 2021, VDE Verlag GmbH, Berlin, 2021.

[4] Michálek, T., Zelenka, J., Reduction of lateral forces between the railway vehicle and the track in small-radius curves by means of active elements, Applied and Computational Mechanics 5 (2) (2011) 187-196.

Experimental moose test

A. A. Mokhtar[a], L. Hynčík[a,b], A. Talimian[b]

[a]Department of Mechanics, Faculty of Applied Sciences, University of West Bohemia, Univerzitní 8, 301 00 Plzeň, Czech Republic
[b]Department of Biomechanical Human Body Models, New Technologies – Research Centre, University of West Bohemia, Univerzitní 8, 301 00 Plzeň, Czech Republic

1. Introduction

For evaluation and further development of vehicle safety technologies, it is essential to be able to anticipate how human occupants will react in both precrash scenarios such as driver-induced or autonomous braking and steering maneuvers [4] and in-crash circumstances [2] In order to allow for anthropomorphic occupant reaction in pre-crash conditions, human body models are being fitted with muscle control systems [1]. These models, known as active human body models (AHBMs), must be using volunteer data, such as body kinematics and reactions, in a variety of realistic probable precrash loading conditions.

Although none of these volunteer studies have provided information on muscle activity for volunteers traveling in a regular car and subjected to maneuvers like lane changes, they have provided some understanding of the occupant kinematics and the activity of a select few muscles when the volunteers were exposed to lateral loading in a laboratory environment. Recently, [3] supplied volunteers riding in a standard automobile subjected to lane changes and lane changes with braking maneuvers with data on passengers' heads and T1 displacements, boundary conditions including seat belt forces and position, as well as vehicle dynamics. Evasive maneuver testing determines a vehicle's capacity to avoid unexpected impediments. The Moose test has been carrying it out since the 1970s. In 1997, a Swedish automotive magazine and television program flipped a Mercedes-Benz A-Class, prompting the test's naming. The test simulates situations like a reversing car or a child rushing onto the road. The goal of the current study is to illustrate, utilizing the occupants' four body part motion during moose trajectory autonomous vehicle movements.

2. Methodology

The University of West Bohemia's Ethical Review Board gave their approval to the use of human volunteers. To put it concisely, the test method for each participant involved first collecting anthropometric data. Furthermore, the experimental vehicle was equipped with Qualisys system facilities. Each predetermined anthropometry participant was equipped with clusters of reflective markers (Fig. 1), which will be fastened using fixation tape and whose movement will be monitored by the Qualisys system. An accelerometer was used to simultaneously detect and synchronize the vehicle's movement.

The experimental vehicle was driven somehow to be as close as possible to the red line passes among the path signs, see Fig. 2. The vehicle is accelerated from a stationary position until reaches to a specified speed. Then the throttle is released and the car is driven for 10 meteres. Afterwards the car speed is measured. The experiment's speed was done at 30 and 50 km/h to prevent any skidding or turning. The experiment was conducted with two cases with
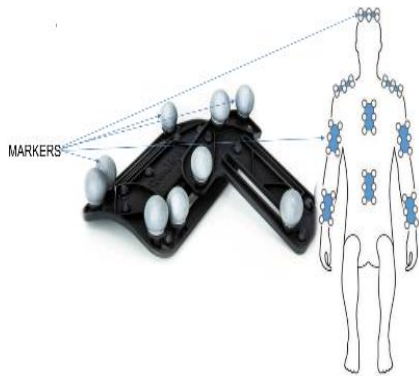
Fig. 1. Markers set-up
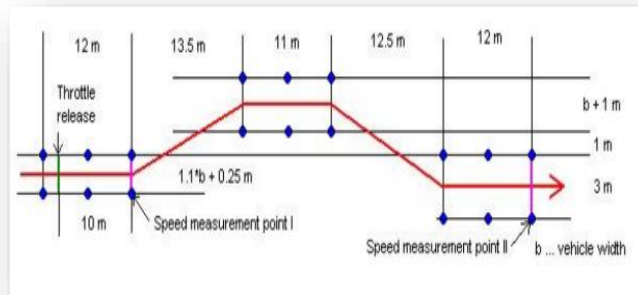
Fig. 2. Experimental vehicle trajectory

and without pedals. For the case which was done with pedals means that the accelartor pedal was not released and without pedals the accelerator pedal was released.

3. Result

The generated trajectories after being post-processed in Python to get the body parts (head, shoulder and chest) trajectories are depicted in Figs. 3 and 4 in coronal plane (-yz). The trajectory's beginning is shown by the marker. The motion domain of the various body parts is analysed at two distinct speeds (30 km/h and 50 km/h) which are then compared and investigated. As indicated in Table 1, data is collected focused on shoulder, chest, and head. The body height and weight of passenger 4 meet the criteria for 50 percentile HBM. Fig. 5 depicts a bar graph that compares passengers with and without pedals. The first half of the bar graph displays the comparison of passenger 4 with passenger 2, while the second half shows the comparison of traveler 4 with passenger 5.

The same applies for the opposite bar chart, which shows chest data as well as the right and left shoulders.
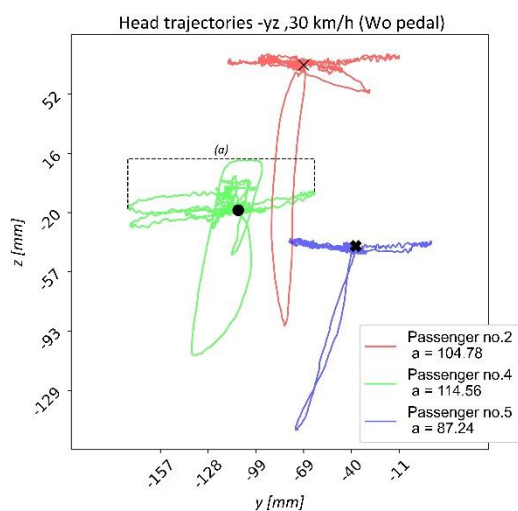
Fig. 3. Comparing the head trajectory range of passenger 2, 4 and 5 at 30 km/h
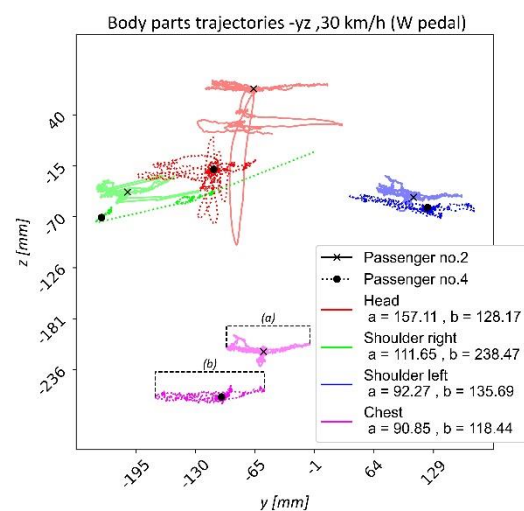
Fig. 4. Comparing the body (head, shoulders and chest) trajectories range of the passengers 2, 4 and 5 at 50 km/h

Fig. 5. Comparision of the passenger with the refernce passenger of head, chest and shoulder

Table 1. Body part motion domain

HEAD DATA

	30 kmph	30 kmph	50 kmph	50 kmph
Passengers	With Pedal (WP)	Without Pedal (WoP)	With Pedal (WP)	Without Pedal (WoP)
Passenger 2	157.11	104.78	253.92	211.8
Passenger 4	128.17	114.56	235.54	326.26
Passenger 5	106.95	87.24	211.47	157.4

CHEST DATA

	30 kmph	30 kmph	50 kmph	50 kmph
Passengers	With Pedal (WP)	Without Pedal (WoP)	With Pedal (WP)	Without Pedal (WoP)
Passenger 2	90.85	63.4	205.36	164.69
Passenger 4	118.44	96.64	172.03	193.29
Passenger 5	62.44	65.46	132.2	107.96

RIGHT SHOULDER DATA

	30 kmph	30 kmph	50 kmp	50 kmph
Passengers	With Pedal (WP)	Without Pedal (WoP)	With Pedal (WP)	Without Pedal (WoP)
Passenger 2	111.65	73.1	216.43	112.75
Passenger 4	234.47	130.55	242.28	234.46
Passenger 5	101.96	130.51	133.19	116.29

LEFT SHOULDER DATA

	30 kmph	30 kmph	50 kmph	50 kmph
Passengers	With Pedal (WP)	Without Pedal (WoP)	With Pedal (WP)	Without Pedal (WoP)
Passenger 2	92.27	69.19	233.64	164.69
Passenger 4	135.69	115.62	207.52	274.24
Passenger 5	103.58	75.64	180.19	131.19

4. Conclusion

We conducted a research to evaluate the kinematics of passengers during a vehicle motion. One female and two males of different anthropometry participated in the study after the ethics committee approval. They sit as passengers on the frontal seat and were instrumented by Qualisys markers to be monitored during the maneuver. Several measurements at the speeds of 30 km/h and 50 km/h were performed. The study analyses and compares the motion capture data as a base for validating an active human body model.

Acknowledgement

References

[1] Iwamoto, M., Nakahira, Y., Kimpara, H., Sugiyama, T., Min, K., Development of a human body finite element model with multiple muscles and their controller for estimating occupant motions and impact responses in frontal crash situations, Stapp Car Crash J. 56 (2012) 231-268.

[2] Kumar, S., Ferrari, R., Narayan, Y., Electromyographic and kinematic exploration of whiplash-type neck perturbations in left lateral collisions, Spine 29 (6) (2004) 650-659.

[3] Osth, J., Olafsdottir, J. M., Davidsson, J., Brolin, K., Driver kinematic and muscle responses in braking events with standard and reversible pre-tensioned restraints: Validation data for human models, Stapp Car Crash J. 57 (2013) 1-41.

[4] Unselt, T., Mayer, C., et al., Assessment of behavioural aspects in integrated safety systems, International Technical Conference on the Enhanced Safety of Vehicles (ESV), Washington, DC, 2011.

Temperature influence on the acoustic streaming of viscous fluid in a confining layer

F. Moravcová[a], E. Rohan[a]

[a]Department of Mechanics, Faculty of Applied Sciences, University of West Bohemia, Univerzitní 8, 301 00 Plzeň, Czech Republic

Acoustic streaming (AS) is a secondary effect of acoustic waves propagating in a bulk fluid, or near surfaces. The AS is presented as a quasi-stationary flow propelled by the attenuated energy of the acoustic waves caused by the fluid viscosity. More precisely, AS, results from the inhomogeneities in viscous flow due to non-zero divergence of the Reynolds stress associated with the kinetic energy of the velocity fluctuations. It can be induced by vibrating solid-fluid interface while considering laminar flow in confining channels [3]. In this study, we examine the influence of inhomogeneities in the temperature field on the AS and on the consequent heat transfer from the fluid to the solid, cf. [1, 2].

The AS model can be derived from the mass, momentum and energy conservation laws which yield the coupled set of equations

$$\frac{D\rho}{Dt} = -\rho\nabla \cdot \boldsymbol{v} \ , \quad \rho\frac{D\boldsymbol{v}}{Dt} = \nabla \cdot \boldsymbol{\sigma} \ , \quad \rho C_V \frac{D\Theta}{Dt} = \nabla \cdot (k\nabla\Theta) + \boldsymbol{\sigma} : \nabla\boldsymbol{v} \ . \qquad (1)$$

In (1), t is the time, $\boldsymbol{v}$, ρ and Θ denote the fields of velocity, density and temperature, respectively, C_V is the specific heat capacity at constant volume, k is the thermal conductivity, and $\boldsymbol{\sigma} = -p\boldsymbol{I} + \boldsymbol{\tau}$ is the Cauchy stress which splits into a pressure term and a viscous part. In addition, the (ideal gas) state equation closes the system (1),

$$p = R\Theta\rho \ . \qquad (2)$$

To distinguish the phenomenon of AS, flow equations (1) can be either solved directly or in a decomposed form obtained from the perturbation analysis [4], i.e., the expansion of any state variable u with respect to a perturbation parameter α,

$$u(\boldsymbol{x}, t) = u_0(\boldsymbol{x}) + \alpha u_1(\boldsymbol{x}, t) + \alpha^2 u_2(\boldsymbol{x}, t) + ... \ , \qquad (3)$$

with $\alpha \approx v_0/c_0$, where c_0 is the reference sound speed and v_0 is a characteristic flow velocity ($v_0 \ll c_0$). Upon substituting (3) in (1) and pursuing the standard split according to orders in α, two problems for the triplets $(\rho_1, \boldsymbol{v}_1, \Theta_1)$ and $(\rho_2, \boldsymbol{v}_2, \Theta_2)$ are identified being governed by the following linear equations (written in a generic form where $i = 1, 2$ refers to the 1st, or the 2nd order problem)

$$\frac{\partial \rho_i}{\partial t} + \rho_0 \nabla \cdot \boldsymbol{v}_i = M_i \ ,$$

$$\rho_0 \frac{\partial \boldsymbol{v}_i}{\partial t} + \nabla p_i - \mu_0 \nabla^2 \boldsymbol{v}_i - \left(\eta_0 + \frac{1}{3}\mu_0\right)\nabla(\nabla \cdot \boldsymbol{v}_i) = \boldsymbol{F}_i \ , \qquad (4)$$

$$C_V \left(\rho_0 \frac{\partial \Theta_i}{\partial t} + \rho_0 \boldsymbol{v}_i \cdot \nabla \Theta_0\right) - k_0 \nabla^2 \Theta_i - \nabla \cdot (k_i \nabla \Theta_0) + p_0(\nabla \cdot \boldsymbol{v}_i) = Q_i \ ,$$
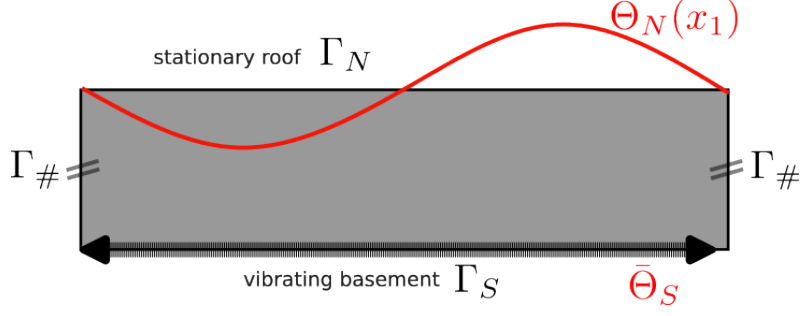
Fig. 1. The domain Ω with vibrating basement and prescribed walls temperature

supplemented by the corresponding state equations obtained from (2) using the expansions (3). The second order problem involves functions $(\rho_2, \boldsymbol{v}_2, \Theta_2)$ which are considered as time-averaged over a time-period T which equals the one of the acoustic waves; this makes disappear all T-periodic fluctuations present in the linear form and time derivatives of expressions involving the 1st order problem responses. In (4), the r.h.s. terms of the 1st order problem $i = 1$, vanish ($M_1 = 0$, $\boldsymbol{F}_1 = \boldsymbol{0}$, $Q_1 = 0$), whereas the following holds for driving forces of the acoustic streaming governed by the 2nd order problem ($\langle \cdot, \cdot \rangle$ denotes the time average),

$$M_2 = -\Big\langle \nabla \cdot (\rho_1 \boldsymbol{v}_1) \Big\rangle,$$

$$\boldsymbol{F}_2 = -\Big\langle \nabla \rho_0 (\boldsymbol{v}_1 \otimes \boldsymbol{v}_1) \Big\rangle + \Big\langle \nabla \cdot \Big(\Theta_1 \Big(d_\mu (\nabla \boldsymbol{v}_1 + (\nabla \boldsymbol{v}_1)^T) + \Big(d_\eta - \frac{2}{3} d_\mu \Big) (\nabla \cdot \boldsymbol{v}_1) \boldsymbol{I} \Big) \Big) \Big\rangle, \quad (5)$$

$$Q_2 = -C_V \Big\langle \nabla \cdot (\rho_0 \boldsymbol{v}_1 \Theta_1) + \rho_1 \boldsymbol{v}_1 \cdot \nabla \Theta_0 \Big\rangle + \Big\langle d_k \nabla \cdot (\Theta_1 \nabla \Theta_1) \Big\rangle - \Big\langle p_1 (\nabla \cdot \boldsymbol{v}_1) \Big\rangle + \Big\langle \boldsymbol{\tau}_1 : \nabla \boldsymbol{v}_1 \Big\rangle.$$

It is worth to emphasize that the material parameters are temperature dependent except of the specific heat capacity which is assumed to be constant [1]. In (5), the Taylor expansion has been used and $d_u = \frac{\partial u}{\partial \Theta}|_{\Theta_0}$ is applied with $u := \mu, \eta$.

The flow equations (1) (or (4)) are solved in a two-dimensional rectangular domain $\Omega =]0, L[\times]0, h[\subset \mathbb{R}^2$ representing a section of the infinite layer $] - \infty, +\infty[\times]0, h[$ and shown in Fig. 1. The domain Ω is bounded by $\partial \Omega$ consisting of four parts Γ_N, Γ_S and $\Gamma_\#$. Periodic conditions are prescribed on the vertical boundary segments $\Gamma_\#$. The flow is induced by harmonic oscillations of the south wall Γ_S whereas fixed north wall Γ_N is considered. The temperature at both walls is prescribed; they are stationary. Hence,

$$\begin{aligned} \boldsymbol{v}|_{x_2=0} &= \boldsymbol{v}_S(x_1) \sin\left(\frac{2\pi t}{T}\right), & \Theta|_{x_2=0} &= \Theta_S(x_1) , \\ \boldsymbol{v}|_{x_2=h} &= 0 , & \Theta|_{x_2=h} &= \Theta_N(x_1) , \end{aligned} \quad (6)$$

where $\boldsymbol{v}_S(x_1)$, $\Theta_S(x_1)$ and $\Theta_N(x_1)$ are given amplitudes. For illustration, in Fig. 2, $\boldsymbol{v}_S(x_1) = \bar{\boldsymbol{v}}_s \sin(2\pi(x_1 - x_0)/L))$, $\Theta_S(x_1) = \bar{\Theta}_S$ and (a) $\Theta_N(x_1) = \bar{\Theta}_S + \Delta \bar{\Theta}$ or (b) $\Theta_N(x_1) = \bar{\Theta}_S(1 + 1/2 \sin(2\pi(x_1 - x_0)/L))$. The influence of the the temperature gradient on the distribution of the AS is tested performing numerical simulation with (a) various values of the difference $\Delta \bar{\Theta}$ or (b) various positions x_0. The distribution (AS magnitude and streamlines) are shown is the whole domain Ω (left figure) and also distribution along a horizontal line probe $x_2 = h/2$ are plotted (right figures). In Fig. 2a), one may recognize in the middle figure which corresponds to the zero gradient $\Delta \bar{\Theta} = 0$, the solution observed for barotropic material [3]. The temperature gradient can accentuate or mitigate the AS effects.
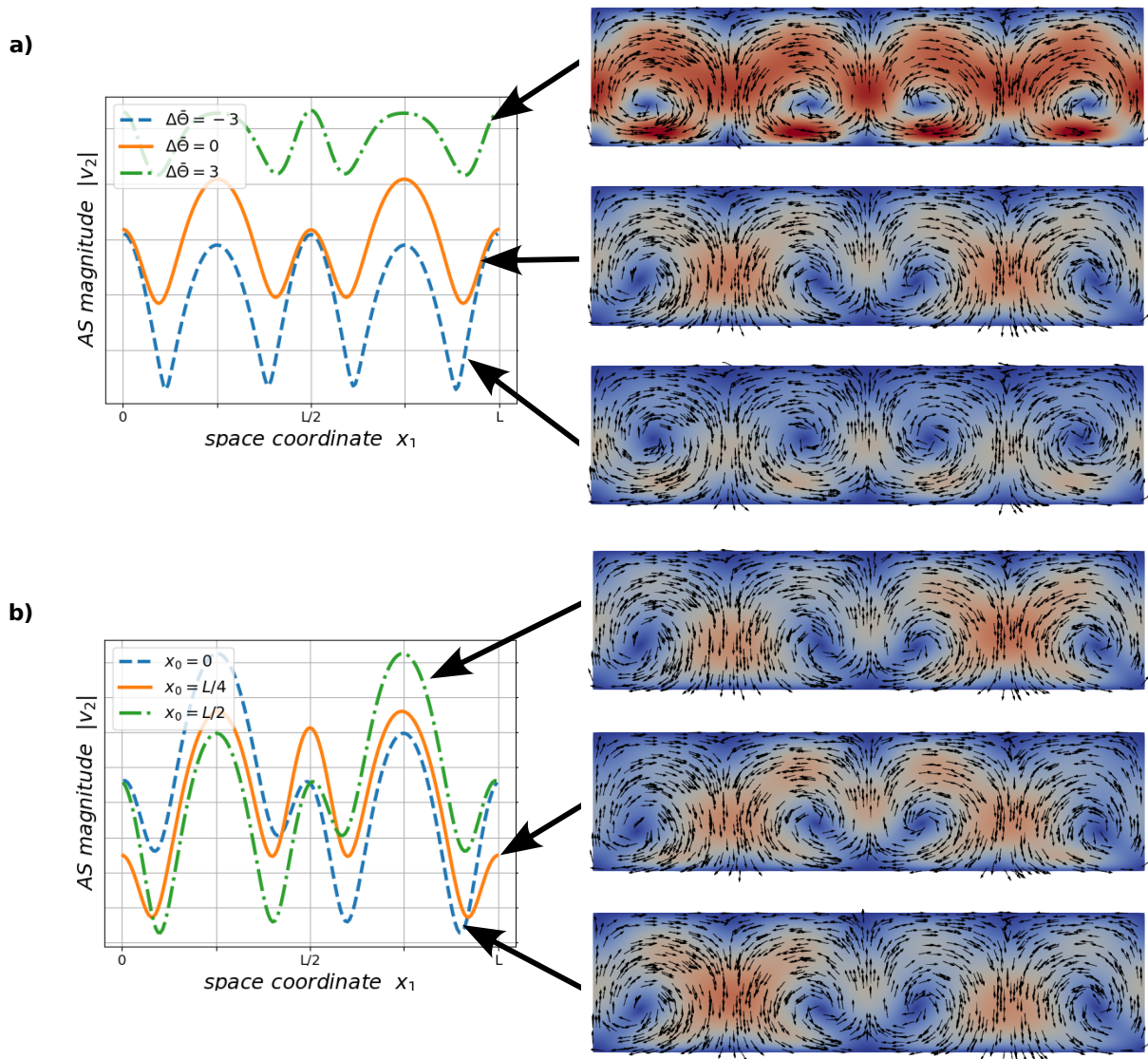
Fig. 2. Distribution of the streaming velocity $|v_2|$ along a horizontal line ($x_2 = h/2$) and in the whole domain Ω, two cases considered with the temperature prescribed on Γ_N (a) by constant different from the one on Γ_S, (b) by a sinus function

Acknowledgement

References

[1] Červenka, M., Bednařík, M., Effect of inhomogeneous temperature fields on acoustic streaming structures in resonators, Journal of the Acoustical Society of America 141 (6) (2017) 4418-4426.

[2] Loh, B.-G., Hyun, S., Ro, P. I, Kleinstreuer, C., Acoustic streaming induced by ultrasonic flexural vibrations and associated enhancement of convective heat transfer, Journal of the Acoustical Society of America 111 (2) (2002) 875-883.

[3] Moravcová, F., Rohan, E., Acoustic streaming of viscous fluid in a confining layer with vibrating walls – numerical simulations, Proceedings of the conference Computational Mechanics 2021, Srní, University of West Bohemia, 2021, pp. 157-160.

[4] Nyborg, W. L., Acoustic streaming due to attenuated plane waves, Journal of the Acoustical Society of America 25 (1) (1953) 68-75.

The effect of feed drive axes dynamics on the wearing of linear guideways

J. Moravec[a], E. Stach[a], M. Stejskal[a], M. Sulitka[a]

[a]*Department of Production Machines and Equipment (RCMT), Faculty of Mechanical Engineering, Czech Technical University in Prague, Horská 3, 128 00 Praha 2, Czech Republic*

1. Introduction

This paper treats a method developed by the authors which helps to evaluate loading linear guideways used in NC machine tools. Research was motivated by the industrial problem with total damage of linear guideways which occured during the high productive manufacturing of small parts. Method links two mechanical influences on failure of linear guideways. The count of contacts between the guideway static part (rail) and its moving part (bearing block) alongside the rail and the level of acceleration at these points. Method facilitate insight into non-constant load of linear guideway alongside its rail and takes into accounts the influence of dynamics of all three feed drive axes X, Y and Z on axis X where damaging occurs. Method helps to find appropriate set of maximal accelerations and jerks of feed drive axes X, Y and Z with lower dynamic impact on the load of guideway and with minimal penalty on machining time.

2. Outline of the problem

Fig. 1 (left) shows schema of linear guideway commonly used in machine tools. It consists of rail, bearing block and rolling element which could be ball shaped or roller shaped. In our case roller type was used. Bearing block is filled by a long life grease and equipped by seal elements to wiping down chips from machining. Damaged locations on rails are marked by the red points. Our task was to clarify the causes of damage of linear guideways used in highly productive production of duralumin parts. Two significant influences with impact on linear guideways damage were supposed. Malfunction of greasing and impact of inertial forces given by frequent acceleration and deceleration of moving axes. Both flows from extreme conditions during the part production. Cycle time of one machined part was approx. 4.5 minutes and machine was used in three-shift operation seven days in week. For the complete machining of part several tools were used. Tool changes requires fast movements to a magazine located at the back end of Y-axis (Fig. 3). Inertial and frictional forces from rapid feeds such causes additional stress to linear guideways beside the cutting forces and inertial forces from machining. Workpiece was machined under intensive flow of cooling emulsion.

3. Causes of linear guideways damage

Damaged sides of rails are shown in Fig. 1 (right). Case A shows constant wear, case B shows wear with surface fatigue but cases C and D show sharply bounded traces from rolling elements of bearing block. Inside the bearing block high degradation of seals and mixture of metal
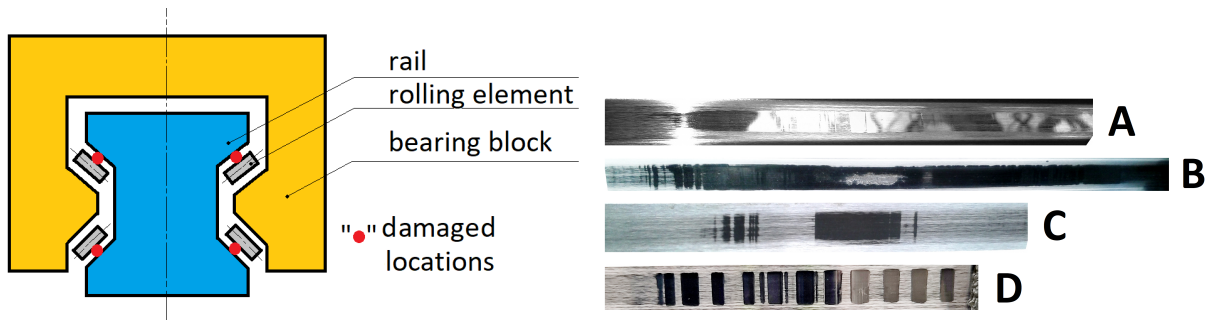
Fig. 1. Schema of linear guideway (left); damaged sides of rails (right)

chips with grease were observed. Such conditions complicate soft movement and causes further damage rollers and rails.

By this hypothesis it would be possible to interpret flat regular traces in cases A and B but short sharp, regular and relatively deep traces in cases C and D would suggest rather local force shocks. It would agree with previously noted dynamical conditions of Y-axis movement. Therefore evaluation method was based on analysis of mechanical loading from inertial forces. Many research topics related to linear guideways from the view in many aspect were published, for example experimental analysis of the wear coefficient [4], effect of grease characteristics on sound and vibration [1] or model for wear prediction [3]. Analysis of drive dynamics is in [2].

4. Graphical evaluation of influence of moving axes dynamics on linear guideways loading

Presented analysis is based purely on processing of data acquired from NC machine tool control system by its internal oscilloscope. Data for analysis are recorded as desired and real positions and velocities of feed drive axes X, Y and Z. Accelerations of axes was computed by a numerical derivation of velocities. Even though proper approach would be based on computation with forces which directly impact on wear of linear guideways only computation with axes accelerations is done. The reason is that no information about moving masses and position of center of gravity is available. So, computations with forces are imitated by computation with accelerations.

Some locations on rails were more damaged than other. This led to examine acceleration not only in time domain but also in geometrical domain along the rail. Moreover, during the working cycle some locations could be in more numerous contact between rail and bearing block than others. Count of appearance on particular coordinate is therefore taken into account by a histogram plot.

So, level of acceleration along the rail forms first 2D graph for identification where local extremes of acceleration acts (top set of Fig. 2). Count of accelerations at the partial rail points forms second 2D graph for identification how many contacts between bearing block and rail was done during the working cycle (middle set of Fig. 2). Both graphs jointed together form 3D histogram with position of particular machine axis on one axis acceleration on second axis and count of acceleration on partial rail point on third axis. For better readibility, 3D graph is converted to 2D where the third axes is represented by the color scale (bottom set of Fig. 2). Let us note the graphs that count of contacts between both parts of guideway was evaluated at 5 mm sections as a summation of values inside this interval (comparisons of histograms for counts on elementary points and for 5 mm ones are for respective axes in middle row of Fig. 2).

The most damaged guideways were on Y-axis where the high exposure of coolant and acceleration frequency from rapid feed acts together. For example, during the working cycle of
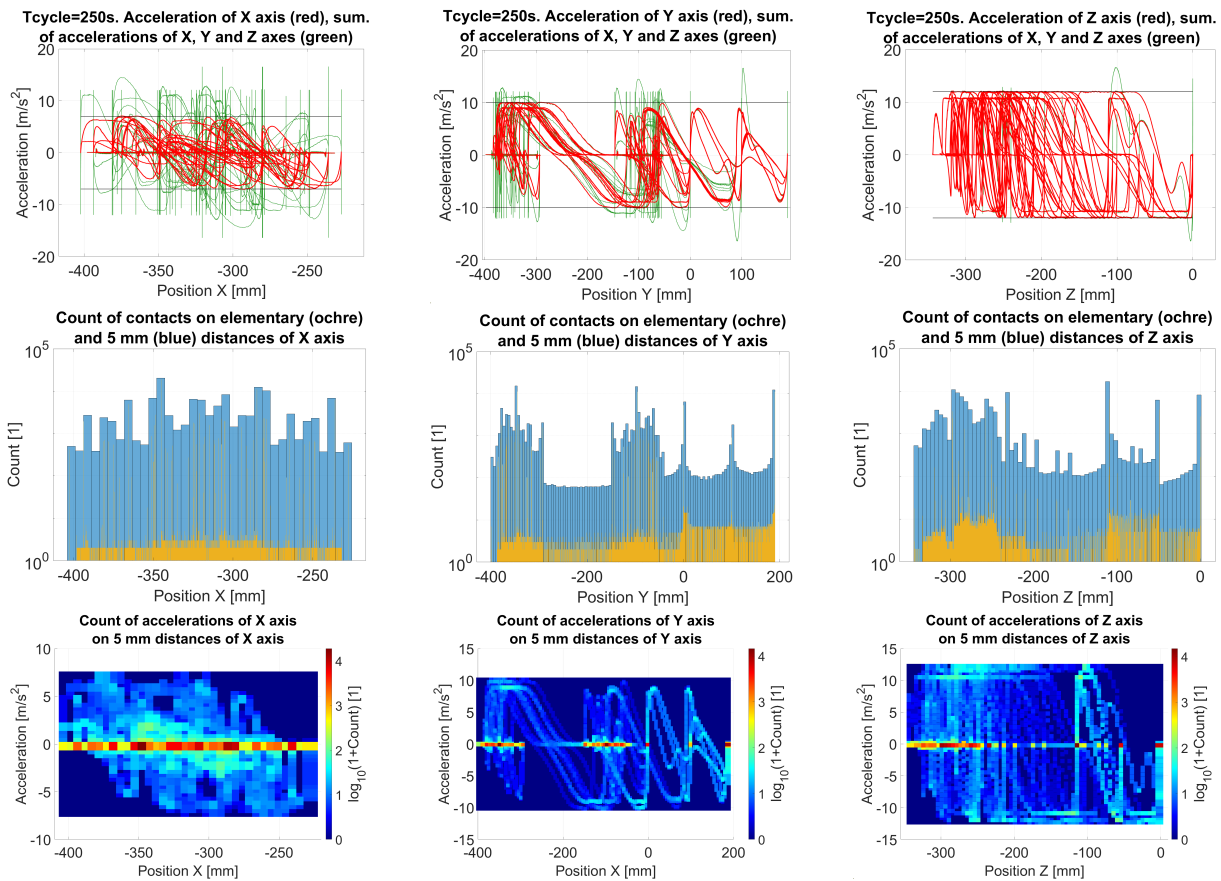
Fig. 2. Level of acceleration along rail (top row); count of acceleration at partial rail points (middle row); 3D histograms count of acceleration on partial rail distances (bottom row). Axes X, Y and Z are grouped in respective columns. Limit of axes accelerations are $7\,\mathrm{m/s^2}$ for X, $10\,\mathrm{m/s^2}$ for Y and $12\,\mathrm{m/s^2}$ for Z, maximal axes jerks are $25\,\mathrm{m/s^3}$ for X, $50\,\mathrm{m/s^3}$ for Y and $300\,\mathrm{m/s^3}$ for Z. Machining time is 250 s

250 s more than 30 accelerations (or decelerations) were to a maximum speed of 75 m/min. For this reason the main attention is paid to the analysis of Y-axis.

Fig. 3 shows a diagram of the machine in the YZ plane. From the figure, it is clear that the forces from the acceleration of Y-axis, together with the forces from acceleration in the Z-axis, create a tilting moment Mx around the X-axis. This causes stress on the guideways of Y-axis.
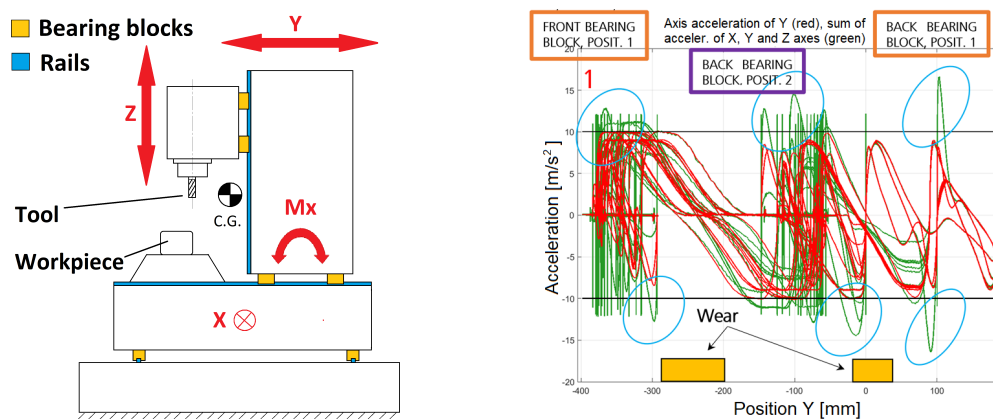
Fig. 3. Schema of machine with coordinates (left); correlation of acceleration extremes with damaged rail sections on Y-axis (right)

Therefore, in Fig. 2 (top row), two acceleration values are plotted. Reds are the accelerations in a given axis and greens are the summations of accelerations in the X, Y and Z axes which together contributes to the loading of guideways. Black lines on graphs in Fig. 2 (top row) shows limit values of axes accelerations. It can be seen that sum of accelerations significantly overlaps limit values for axes X and Y. This imply the influence of other axes to particular axis which results to high forces acting to the guideway. Moreover, histograms from the middle and bottom rows shows that contacts in the Y and Z axes are less regular than in Y-axis. Color maps further detects that higher levels of accelerations are concentrated at particular coordinates. It would clarify why are rails such damaged at these coordinates. Detail graph with correlation of acceleration extremes with damaged rail sections on Y-axis is in Fig. 3 (right).

Based on these analysis several measurements with different accelerations and jerks of axes X, Y and Z were evaluated and the most proper one, also with regard to minimal time penalty, was appicated into the control system of real NC machine tool. This set is graphically shown in Fig. 4. It is clear that sum of the accelerations X, Y and Z axes has lower level and more regular character then in the previous case. Local extremes which probably cause sharp traces on rails diminish.
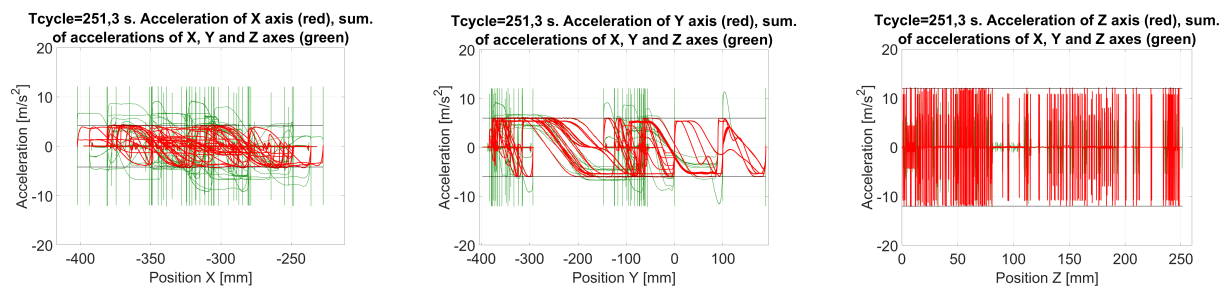
Fig. 4. Optimal set of axes accelerations and jerks with limits $4.2\,\mathrm{m/s^2}$ for X, $6\,\mathrm{m/s^2}$ for Y and $12\,\mathrm{m/s^2}$ for Z, maximal axes jerks are $25\,\mathrm{m/s^3}$ for X, $50\,\mathrm{m/s^3}$ for Y and $300\,\mathrm{m/s^3}$ for Z. Machining time is 251.3 s

5. Conclusions

Primary cause of linear guideway damage was probably influence of cooling emulsion which degrades seal and originate mixture of grease and metal chips which significantly gets worse friction in linear guideways. Another cause of guideways damage sources from high force shocks given by accelerating of all three axes in one moment. Analysis shown relativelly high influence of dynamics of neighbouring axes Z and X to the load of axis Y. Developed analysis brings results which correlates level of accelerations with damaged sections on the rails. More suitable levels of axes accelerations and jerks were chosen and applied into the NC machine tool in industry.

References

[1] Ohta, H., Tsuruoka, T., Fujinami, Y., Kato, S., Effects of grease characteristics on sound and vibration of a linear-guideway type recirculating ball bearing, Journal of Tribology 138 (2) (2016) No. 021101.

[2] Souček, P., Servomechanisms in production machines, Czech Technical University in Prague, Prague, 2004. (in Czech)

[3] Tao, W., Zhong, Y., Feng, H., Wang, Y., Model for wear prediction of roller linear guides, Wear 305 (1-2) (2013) 260-266.

[4] Wang, X.-Y., Zhou, C., Ou, Y., Experimental analysis of the wear coefficient for the rolling linear guide, Advances in Mechanical Engineering 11 (1) (2019), doi: 10.1177/1687814018821744.

Numerical minimization of energy functionals in continuum mechanics using hp-FEM in MATLAB

A. Moskovka[a,b], M. Frost[c], J. Valdman[a,d]

[a]Institute of Theory of Information and Automation, Czech Academy of Sciences, Pod Vodárenskou věží 4, 18200 Praha, Czech Republic
[b]Department of Mathematics, Faculty of Applied Sciences, University of West Bohemia, Technická 8, 30100 Plzeň, Czech Republic
[c]Institute of Thermomechanics, Czech Academy of Sciences, Dolejškova 5, 18200 Praha, Czech Republic
[d]Department of Computer Science, Faculty of Science, University of South Bohemia, Branišovská 31, 37005 Č. Budějovice, Czech Republic

1. Introduction

Energy functionals appearing in various types of problems in science and engineering can be efficiently minimized using the finite element method (FEM). In [3], we introduced several vectorization techniques for an efficient evaluation of the discrete energy gradient and, additionally, applied these techniques for the minimization of hyperelasticity in 2D and 3D using P1 finite elements (piece-wise linear nodal elements defined on triangles/tetrahedra). Recently, our approach has been successfully applied to 2D/3D problems in solid mechanics, namely the resolution of elastoplastic deformations of layered structures or superelastic and pseudoplastic deformations of shape-memory alloys [2].

The hp-FEM is an advanced numerical method based on FEM dating back to the pioneering works of I. Babuška, B. A. Szabó and co-workers in 1980s. It provides increased flexibility and convergence properties compared to the "conventional" FEM. In particular, hp-FEM on quadrilaterals (in 2D) and hexahedra (in 3D) are usually preferred in structural computations.

This contribution presents and extends results published in [1], where the energy evaluation techniques of [3] are combined with the implementation of rectangular hp-FEM [4] using some techniques, mainly for the construction of hierarchical shape basis functions, taken from [5]. The actual minimization of energies was performed using the trust-region (TR) method available in the MATLAB Optimization Toolbox which was found to be very efficient in the comparison performed in [3]. It requires the gradient of a discrete energy functional and also allows to specify a sparsity pattern of the corresponding Hessian matrix which is directly given by a finite element discretization. The gradient can be evaluated explicitly or numerically using the central difference scheme. A particular hyperelasticity problem was chosen to demonstrate the capabilities of our implementation.

2. Hyperelasticity

Boundary value problems in (non-linear) elastostatics provide examples of vector problem which can be directly dealt with our approach, see [3]. Given a (hyper)elastic body spanning the domain $\Omega \in \mathbb{R}^d$ and subjected to volumetric force, $\mathbf{f}(\mathbf{x})$, the corresponding deformation, $\mathbf{y}(\mathbf{x})$, can be obtained by minimization of the following energy functional:

$$J(\mathbf{y}(\mathbf{x})) = \int_\Omega W\big(\mathbf{F}(\mathbf{y}(\mathbf{x}))\big)\,\mathrm{d}\mathbf{x} - \int_\Omega \mathbf{f}(\mathbf{x}) \cdot \mathbf{y}(\mathbf{x})\,\mathrm{d}\mathbf{x}\,, \qquad (1)$$

where $\mathbf{F}(\mathbf{y}(\mathbf{x})) = \nabla\mathbf{y}(\mathbf{x})$ denotes deformation gradient and

$$W(\mathbf{F}) = C_1\big(I_1(\mathbf{F}) - \dim -2\log(\det\mathbf{F})\big) + D_1(\det\mathbf{F} - 1)^2 \qquad (2)$$

is so-called compressible Neo-Hookean energy density with C_1, D_1 being material constants and $I_1(\mathbf{F}) = \|\mathbf{F}\|^2$ denotes the squared Frobenius norm.

We consider a double-beam model given by the following parameters: a 2D hyperelastic domain given by a rectangle $[0,1] \times [0, 0.25]$ is subjected to a constant volumetric vector force $\mathbf{f} = (0, -2 \cdot 10^7)$ acting in a top-to-bottom direction; zero Dirichlet boundary conditions are applied on the left and right edges. We assume the Young modulus $E = 10^8$ and the Poisson ratio $\nu = 0.3$. Arbitrary, although mutually consistent physical units are considered. For illustration, Fig. 1 shows examples of the corresponding deformed mesh together with the underlying Neo-Hookean density distribution. Fig. 2 depicts a comparison of P1 elements and hp-FEM for the polynomial degrees $p = 1, 2, 3, 4$ (denoted by Q1, Q2, Q3, Q4, respectively) used in our computation. Since we do not know the exact energy value, we use J_{ref} as the smallest of all achieved energy values $J(u)$ obtained in our computation decreased by 10^2. Q2 and Q4 elements are superior to P1, Q1 and Q3 in accuracy with respect to the number of dofs. However, Q2 elements are only slightly better with respect to the evaluation times, while Q4 elements turned out to be the least efficient.
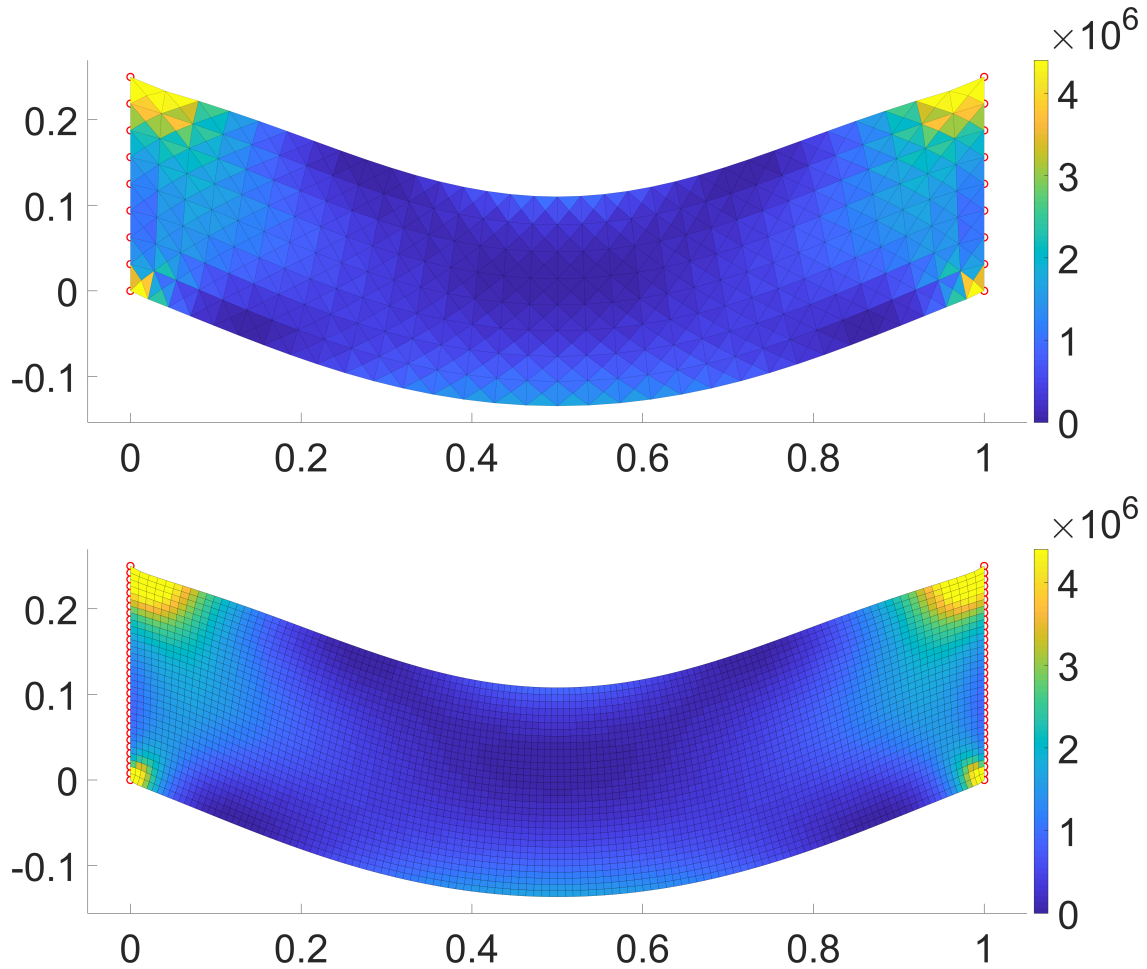
Fig. 1. Deformation and the corresponding Neo-Hookean density distributions for the 2D hyperelastic problem. The top figure corresponds to P1 elements and a computational mesh with 1 024 triangles. The bottom figure corresponds to Q3 elements and a computational mesh with 4 096 rectangles
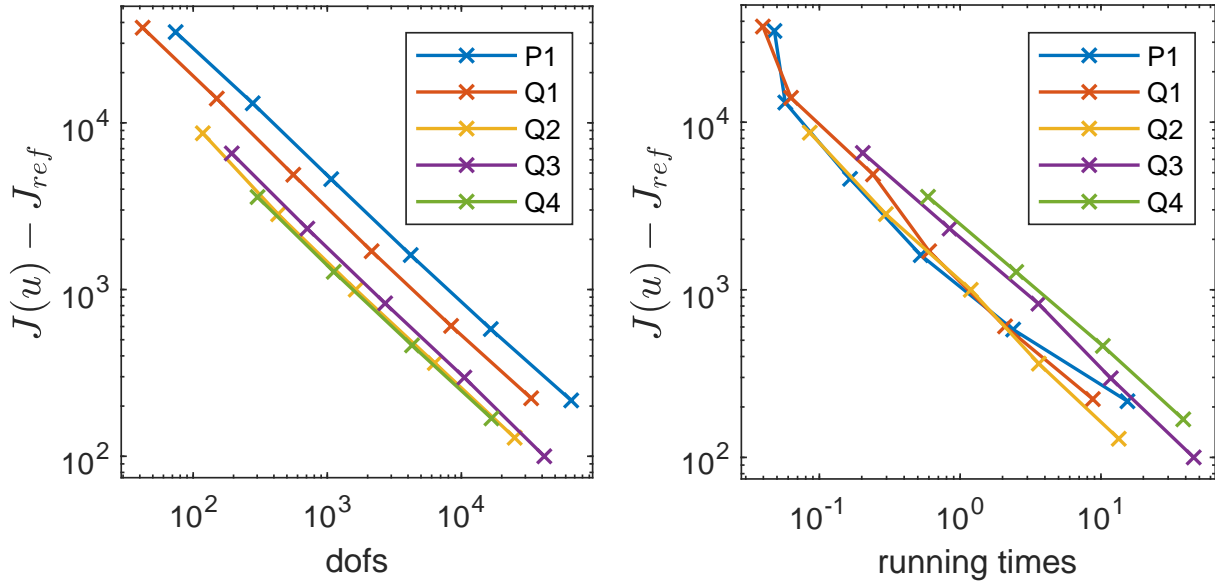
Fig. 2. Performance of hyperelasticity: comparison of elements

3. Conclusions and outlook

The hp-FEM for 2D rectangular elements was successfully incorporated into our vectorized MATLAB code and its improved convergence performance was demonstrated on the particular hyperelasticity problem.

This work contributes to our long-term effort in developing a vectorized finite element-based solvers for energy minimization problems. Since many such problems emerge in science and engineering, the code is designed in a modular way so that various modifications (e.g., in functional types or boundary conditions) can be easily adopted. Our future research directions include implementing the hp-FEM in 3D or tuning the applied minimization algorithms.

References

[1] Frost, M., Moskovka, A., Valdman, J., Minimization of energy functionals via FEM: Implementation of hp-FEM, LSSC 2023, Lecture Notes in Computer Science, doi: 10.48550/arXiv.2309.13028. (accepted paper)

[2] Frost, M., Valdman, J., Vectorized MATLAB implementation of the incremental minimization principle for rate-independent dissipative solids using FEM: A constitutive model of shape memory alloys, Mathematics 10 (2022) No. 4412.

[3] Moskovka, A., Valdman, J., Fast MATLAB evaluation of nonlinear energies using FEM in 2D and 3D: Nodal elements, Applied Mathematics and Computation 424 (2022) No. 127048.

[4] Moskovka, A., Valdman, J., MATLAB implementation of hp finite elements on rectangles using hierarchical basis functions, PPAM 2022, Lecture Notes in Computer Science (LNCS) 13827 (2023) 287-299.

[5] Szabó, B., Babuška, I., Introduction to finite element analysis, John Wiley & Sons, 2011.

Calculation of the stresses in the tapered FGM beams with varying stiffness

J. Murín[a], S. Kugler[b], J. Paulech[a], J. Hrabovský[a], V. Kutiš[a], M. Aminbaghai[c]

[a]*Department of Applied Mechanics and Mechatronics, IAMM FEI STU Ilkovičova 3, 812 19 Bratislava, Slovakia*
[b]*University of Applied Sciences Wiener Neustadt, Department of Applied and Numerical Mechanics, Wiener Neustadt, Austria*
[c]*Vienna University of Technology, Institute for Mechanics of Materials and Structures, Karlsplatz 13, A-1040 Vienna, Austria*

1. Introduction

In the contribution, the expressions will be presented for semi-analytical calculation of normal and shear stresses in the tapered Functionally Graded Material (FGM) beams with spatially variable stiffness. This variability will be caused by the longitudinal continuous variation of the solid cross-section and spatial variation of material properties. These expressions will be applied to calculate stresses in the cantilever beam with longitudinally variable square cross-section, while the material properties change continuosly in its three main axes. The beam will be loaded in tension, biaxial bending, and pure torsion. The results of the semi-analytical solution will be compared with the results of the numerical solution with 3D solid finite elements. Due to limited scope of this short article, we will present here only the expressions for calculation of the normal stresses caused by the axial force. The complete processing of the solved problem in this contribution will be carried out in the prepared article for scientific journal.

2. Calculation of the normal and shear stresses in the tapered FGM beam.

In Fig. 1a the tapered FGM beam with spatial variability of material properties is shown. Using selected homogenization methods, we obtain homogenized FGM beam with longitudinal variability of effective material properties – Fig. 1b.
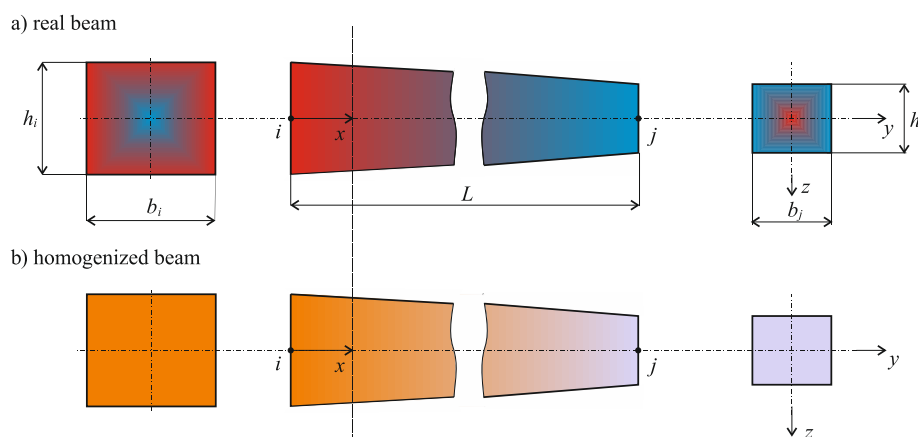
Fig. 1. Tapered FGM beam: a) real beam and b) homogenized beam

Elastostatic deformation analysis of FGM beams (calculation of displacements and rotation angles as well as the internal forces and moments) can be performed on a beam with homogenized stiffnesses [3]. However, the stress calculation must be performed on a real beam [4].

The expressions for the stress calculation in the real FGM tapered beam depend among other things also on the cross-sectional area geometry and material properties variation. FGM is created by mixing two or more components so that at each material point the material is isotropic, while its properties change in one, two or three directions.

In the presentation, at the CM2023 conference, we will focus on derivation of the expression for calculation of the normal and shear stresses distribution on an arbitrary doubly symmetric cross-sectional area of the FGM beam with spatial variation of material properties. As an example of such cross-section is the rectangle (Fig. 2a).

a)   b)
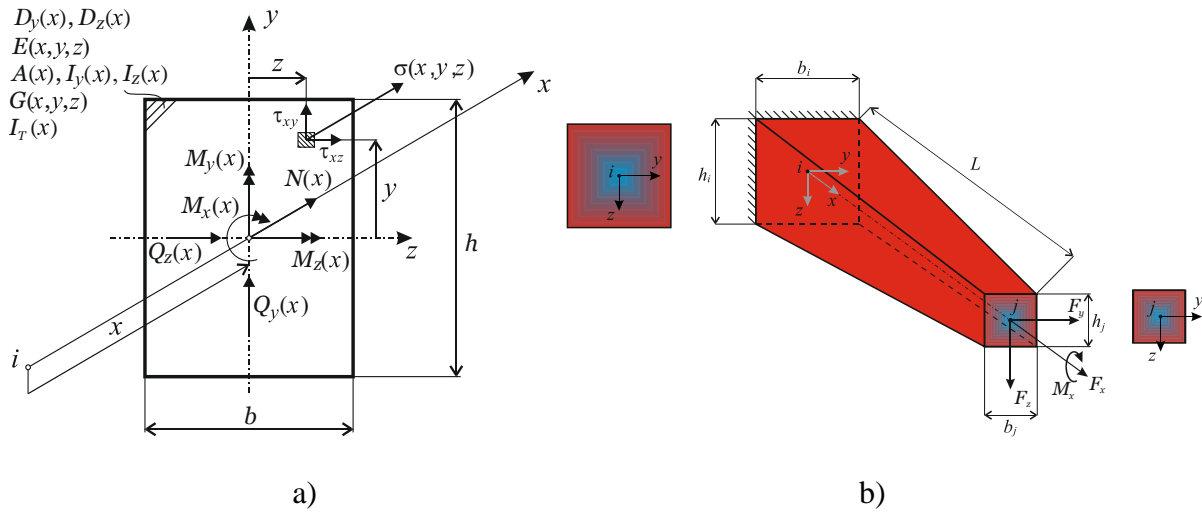
Fig. 2. To calculating the stresses in the tapered FGM beam

The tapered FGM cantilever beam with doubly symmetric rectangular cross-section at position x with doubly symmetric spatial variation of material properties is shown in Fig. 2b. At the centroid of the cross-sectional area at position x acts the normal force $N(x)$, the bending moments $M_y(x)$ and $M_z(x)$, which cause the normal stresses. The internal torsional moment is $M_x(x)$. Further, $A(x)$ is the cross-sectional area, $I_z(x)$ and $I_y(x)$ are the quadratic moments of the cross-sectional area, and $I_T(x)$ is the torsion constant.

Considered spatial variability of material properties is shown in Fig. 2b using a colour scale. On the neutral axis x of the beam is Aluminium and on the outer longitudinal surfaces of the beam is Tungsten. In each cross-section of the beam, the properties in the transverse and lateral directions change linearly from Aluminium to Tungsten. The longitudinally varying effective stiffnesses for tension-compression, bending, shear, and torsion have been obtained by the Reference Beam Method (RBM) [2].

Due to limited scope of this short article, we will present here only the expressions for calculation of the normal stresses caused by the axial force $N(x) = F_x = 100$ N. The results of their application will be presented as well, while a verification of the semi analytical results will be done by the ones obtained with the SOLID185 finite elements [1].

Considering the variation of material properties as shown in Fig. 2b, and with dimensions of the tapered beam with length $L = 0.1$ m, and $a_i = h_i = b_i = 0.01$ m at node i and $a_j = h_j = b_j = 0.005$ m at node j, the effective axial stiffness has been obtained [2]

$$EA(x) = 3.43 \times 10^7 - 3.43 \times 10^8 x + 8.57 \times 10^8 x^2 - 1.11 \times 10^{-3} x^3 \text{ [N]}. \qquad (1)$$

There, the elasticity, and shear modulus for Tungsten is $4.8 \cdot 10^{11}$ Pa, and $2.0 \cdot 10^{11}$ Pa. The elasticity, and shear modulus for Aluminium is $0.69 \cdot 10^{11}$ Pa, and $0.26 \cdot 10^{11}$ Pa.

The normal stresses at the cross-section point (x, y, z) with the elasticity modulus $E(x, y, z)$, is expressed by

$$\sigma^N(x, y, z) = \varepsilon^N(x)E(x, y, z) = \frac{N(x)}{EA(x)}E(x, y, z), \tag{2}$$

where $\sigma^N(x) = \frac{N(x)}{A(x)}$ is the effective normal stress in the homogenized cross-section while constant effective normal strain $\varepsilon^N(x) = \frac{\sigma^N(x)}{E_L^{NH}(x)}$ over the whole cross-sectional area is assumed. Here, $E_L^{NH}(x)$ is the effective elasticity modulus for tension-compression, which is a part of the effective axial stiffness $EA(x)$.

In Fig. 3 and Table 1, results of the normal stresses calculation by the FGM beam using the expression (2) is drawn: a) on the outer surfaces, and b) on the neutral axis of the beam, for $N(x) = F_x = 100$ N. Figs. 3c and 3d show a map of the normal stresses in the cross-section of the beam at a distance of $x = 0.001$ and $x = 0.05$ m obtained from the solution using SOLID 185 finite elements. The normal stresses obtained by SOLID185 finite elements, in MPa, agree very well with the ones obtained with the author's semi-analytical solution. This agreement was also achieved in cross-sections along the entire length of the beam. Some dicrepancies achieved at the free end of the beam affected by the different way of the load insertion.
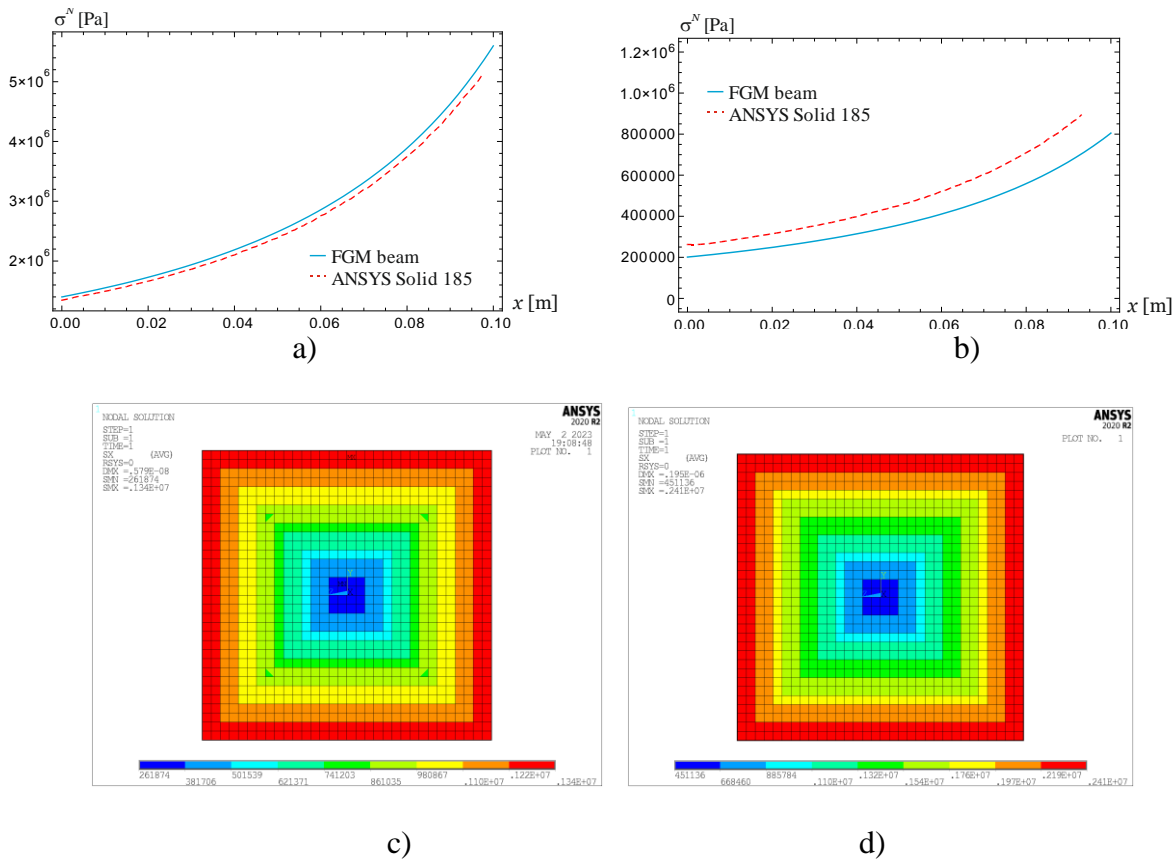
Fig. 3. Longitudinal distribution of the tensile normal stresses, in [Pa], on the outer surfaces: a) and on neutral axis, b) calculated semianalytically (FGM beam), and the maps of the stresses at distances of $x = 0.001$ m, c) and $x = 0.05$ m, d) calculated by SOLID185 finite elements

Table 1. Comparison of the normal stresses on the outer surfaces, $\sigma^N(x,y,z)out$, and on the neutral axis, $\sigma^N(x,y,z)nax$, of the beam calculated by semianalytical method and with ANSYS [1] – red numbers

x [m]	0	0.05	0.1
$\sigma^N(x,y,z)out$/SOLID 185 [Mpa]	1.40/1.34	2.49/2.41	5.6
$\sigma^N(x,y,z)nax$/SOLID 185 [Mpa]	0.20/0.26	0.36/0.45	0.80

The expressions for calculation of the stresses caused by the bending moments, shear forces, and torsion moment have been established by a similar way. In all the load cases, a very well agreement of the normal s shear stresses calculated by the author´s method and SOLID185 finite elements has been obtained.

3. Conclusions

The elastostatic analysis of FGM beams using 3D solid finite elements is very demanding in terms of the need for their fine mesh and processing of the auxiliary program for assigning real functionally graded material properties to individual finite elements. However, these procedures are suitable for comparative calculations used to assess the effectiveness and accuracy of other, more effective solutions. Presented original semi-analytical relations for calculation of normal and shear stresses in FGM tapered beams represent a sufficiently accurate and effective tool. They are also part of our new tapered FGM beam finite element with variable stiffness, which was subjected to deformation analysis of the beam shown in Fig. 2b). This cantilever in Fig. 2b) was modeled by a single FGM beam finite element. The complete processing of the solved problem in this contribution will be carried out in the prepared article for scientific journal.

Acknowledgements

References

[1] ANSYS Release 15.0, Swanson Analysis System, Inc., Johnson Road Houston, PA 1534/1300, USA.
[2] Kugler, S., Fotiu, P., Murin, J., A novel GBT-formulation for thin-walled FGM-bem-structures based on a reference beam problem, Composite Structures 257 (2021) 113158.
[3] Kutiš, V., Murín, J., Belák. J., Paulech, J., Beam element with spatial variation of material properties for multiphysics analysis of functionally graded materials, Computers and Structures 89 (2011) 1192-1205.
[4] Murin, J., Kugler. S., Hrabovsky, J., Kutiš, V., Paulech, J., Aminbaghai, M., Warping torsion of FGM beams with spatially vaeying materal properties, Composite Structures 291 (2022) 115592.

Role of air humidity in residual fatigue lifetime of railway axle

L. Náhlík[a], P. Pokorný[a], T. Vojtek[a], P. Dlhý[a], R. Fajkoš[b], O. Peter[b], P. Hutař[a]

[a]Institute of Physics of Materials, Czech Academy of Sciences, Žižkova 22, 616 00 Brno, Czech Republic
[b]BONATRANS GROUP, a. s., Revoluční 1234, 735 81 Bohumín, Czech Republic

The inspection intervals are often set according to Damage tolerance approach, where a potential crack in a railway axle is considered to ensure safe operation even if some defect is present. This work is focused on development of optimized Damage tolerance model for prediction of residual fatigue life (RFL) of railway axles with consideration of oxide debris at fracture surfaces. Correct prediction of fatigue crack growth rates is essential for RFL predictions, which in turn allows better optimization of inspection intervals. The fatigue crack growth threshold influences low growth rates, which is especially important for RFL of railway axles due to high occurrence of loading amplitudes near or below the threshold. Threshold value of railway axle steels is affected by many factors such as loading history, loading frequency, etc. The contribution shows influence of the air humidity and consequent oxide debris formation at fracture surfaces on threshold values for fatigue crack propagation in railway axle.
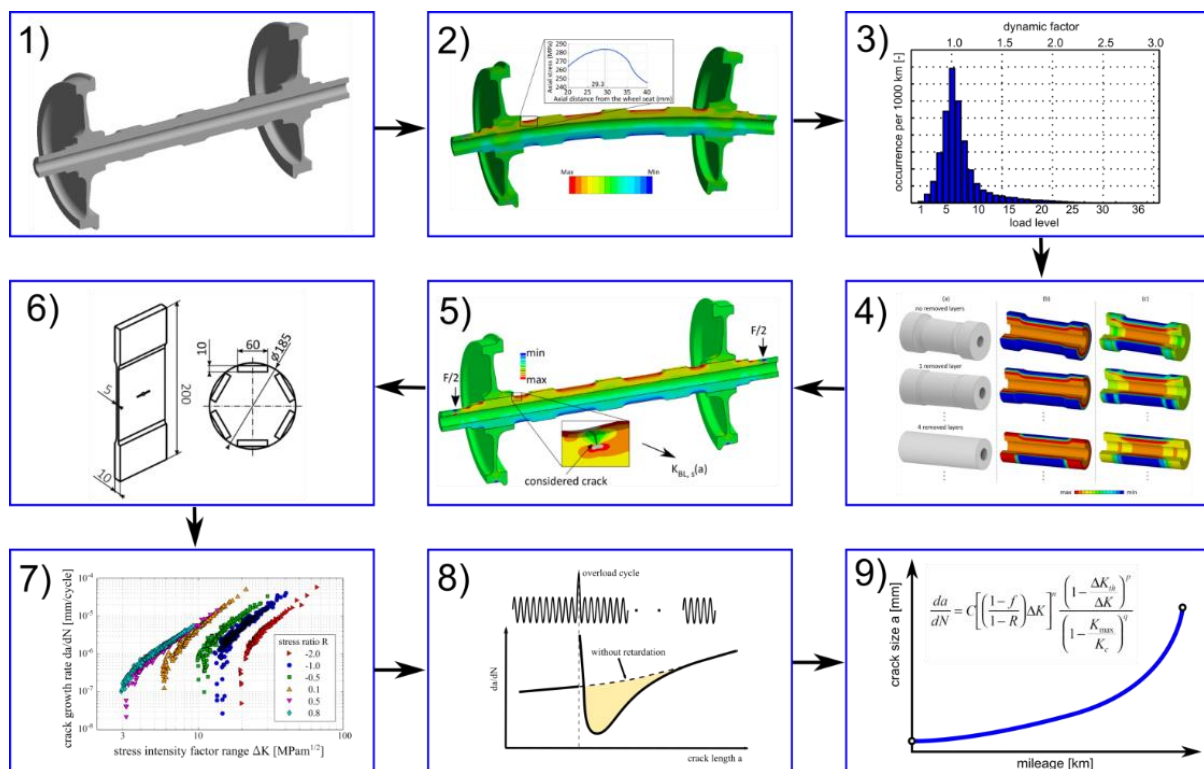
Fig. 1. Scheme of methodology of prediction of residual fatigue lifetime of railway axle

During years Institute of Physics of Materials CAS (IPM) and Bonatrans Group developed own procedure for estimation of residual fatigue lifetime of railway axles, see Fig.1. This complex methodology covers:

1) Modelling of railway axle geometry,
2) Finite element model of studied wheelset. Numerical calculations lead to the investigation of critical areas,
3) Determination of load spectrum and interference between axle and wheel,
4) Determination of residual stresses based on own experimental and numerical approaches,
5) Determination of fracture parameters of propagating fatigue crack: stress intensity factor solutions for bending load, press-fit load and implemented distribution of residual stress,
6) Preparing for an experimental campaign,
7) Experimental determination of fatigue crack propagation rates ($\mathrm{d}a/\mathrm{d}N$-ΔK curves) for all load ratios and humidity conditions in service,
8) Inclusion of other influences: e.g. retardation effects,
9) Use of NASGRO approach [1] based on Newman´s equation [2] for residual fatigue lifetime determination,
10) Validation of the results. Comparison with full scale experimental meauserements.

The contribution presented will show the influence of air humidity during determination of material properties or during train operation. Experimental data obtained under different air humidity conditions were used in the methodology introduced above and important difference in RFLs for different air conditions were obtained. It will be show that the humidity of the air belongs to the main parameters influencing fatigue crack behaviour during fatigue loading.

Collaboration between the Institute of Physics of Materials, the Czech Academy of Sciences and the Bonatrans Group has yielded exciting results. Some factors influencing the residual fatigue lifetime estimation of railway axles were found to be extremely significant. At the same time, these factors are not taken into account in traditional computational approaches. In particular, the first one is compressive residual stress, commonly induced in the surface layers of railway axles. The second one is the crack growth threshold, which is not constant, even for a constant load ratio. Its fluctuation due to air humidity can lead to changes in residual fatigue lifetime of one or two orders of magnitude. Computational models taking these effects into account have been recently developed at the Institute of Physics of Materials, as well as experimental procedures to obtain the necessary material inputs. It was found that conditions in usual fatigue testing laboratories may lead to non-conservative threshold values. This problem can be overcome by using of the original special sealed chamber for modification of air humidity. In this way, the conditions for lower threshold can be simulated, which is relevant for some conditions in operation. It will avoid using of non-conservative values in the theoretical estimations of residual fatigue lifetimes of railway axles.

Acknowledgement

References

[1] NASGRO, Fracture mechanics and fatigue crack growth analysis software, 2002.
[2] Newman, J. C., A crack opening stress equation for fatigue crack growth, Int. Journal of Fracture 24 (1984) 131-135.

Analyzing stochastic stability of a gyroscope through the stochastic Lyapunov function

J. Náprstek[a], C. Fischer[a]

[a]*Institute of Theoretical and Applied Mechanics of the Czech Academy of Sciences, Prosecká 76, 190 00 Prague, Czech Republic*

1. Introduction

Practical experience shows that the random excitation component can affect the system response and its dynamic stability not only negatively but also positively. For example, the presence of a certain artificially generated turbulence component can have a positive effect against the occurrence of resonance. Such mechanisms are usually developed heuristically and are often not sufficiently justified theoretically. On the other hand, the presence of random excitation can lead to dangerous interactions with deterministic processes and thus cause a reduction in the level of dynamic stability in conditions that do not seem serious at first sight (icing on cables or power lines, road roughness, etc.).

This contribution delves into the application of first integrals in the construction of Lyapunov functions (LF) for analyzing the stability of dynamic systems in stochastic domains. It emphasizes the distinct characteristics of first integrals that warrant the introduction of additional constraints to ensure the essential properties required for a Lyapunov function. These constraints possess physical interpretations associated with system stability. The general approach to testing stochastic stability is illustrated using the example of a 3-degrees-of-freedom system representing a gyroscope.

2. The stochastic Lyapunov function

In the sense presented by Bolotin [1], the deterministic LF, is replaced in the stochastic domain by the adjoint Fokker-Planck (FP) operator

$$\mathbf{L}\{\lambda(t,\mathbf{u})\} = \frac{\partial \lambda(t,\mathbf{u})}{\partial t} + \sum_{i=1}^{n} \frac{\partial \lambda(t,\mathbf{u})}{\partial u_i}\kappa_i + \frac{1}{2}\sum_{i,j=1}^{n} \frac{\partial^2 \lambda(t,\mathbf{u})}{\partial u_i \partial u_j}\kappa_{ij}, \tag{1}$$

where κ_i, κ_{ij} are the drift and diffusion coefficients of the n-dimensional Markov process and m depends on the system structure

$$\kappa_i = \sum_{k=1}^{m} A_{ik}(t)f_{ik}(\mathbf{u}) + \frac{1}{2}\sum_{k,l=1}^{m}\sum_{p=1}^{n}\frac{\partial f_{ik}(\mathbf{u})}{\partial u_p}f_{ip}(\mathbf{u})\cdot s_{iklp}, \quad \kappa_{ij} = \sum_{k,l=1}^{m} f_{ik}(\mathbf{u})f_{jl}(\mathbf{u})\cdot s_{ikjl}. \tag{2}$$

Equations (1)–(2) relate to the original stochastic system, the stochastic stability of which is being assessed

$$\dot{u}_i = \sum_{k-1}^{m}(A_{ik}(t)+w_{ik}(t))f_{ik}(\mathbf{u}), \quad \mathbf{u}(t_0) = \mathbf{u}_0, \tag{3}$$

where $\lambda(t, \mathbf{u})$ is the LF candidate, $A_{ik}(t)$ are the nominal values of the system coefficients, $w_{ik}(t)$ is the Gaussian white noise of cross-intensity s_{ikjl}, and $f_{ik}(\mathbf{u})$ are the continuous non-decreasing functions.

Function $\lambda(t, \mathbf{u})$ should be a continuous positive definite. Its derivatives $\partial_t \lambda(t, \mathbf{u})$ and $\partial_{\mathbf{u},\mathbf{u}} \lambda(t, \mathbf{u})$ should be continuous as well. Let $\psi(t, \mathbf{u}) = \mathbf{L}\{\lambda(t, \mathbf{u})\} < 0$ in $\mathbf{u} \in \Omega$ and $\psi(t, 0) = 0$ or $\psi(t, 0)$ is not defined. Then $\lambda(t, \mathbf{u})$ can be considered a Lyapunov function. Thus, for any $\|\mathbf{u}_0\| \neq 0$ function $\lambda(t, \mathbf{u})$ decreases for $t \to \infty$ and, consequently, the trivial solution of (3) is stable in terms of probability.

3. Construction of the Lyapunov function

Let us denote $J_1, \ldots J_s$ the following first integrals which satisfy the equations of motion,

$$J_1(\mathbf{u}) = C_1, ..., J_s(\mathbf{u}) = C_s. \tag{4}$$

The Lyapunov function can be selected as a linear combination of $J_1, \ldots J_s$ and their functions. A convenient selection of the λ may be

$$\lambda(\mathbf{u}) = \sum_{i=1}^{s} a_i \left(J_i(\mathbf{u}) - J_i(0) \right) + b_i \left(J_i^2(\mathbf{u}) - J_i^2(0) \right), \tag{5}$$

where a_i, b_i are constants of the linear combination that have to be selected so that the function (5) is positive definite.

4. Gyroscope

A rotationally symmetrical gyroscope rotates around its z axis along with its massless shaft, which is hinged at the origin of coordinates. The centroid of the gyroscope is positioned above the point where the shaft is fastened. The primary motion of the gyroscope can be affected by perturbations resulting from potential parasitic rotations around horizontal axes. The moving coordinate system x, y, z associated with the gyroscope deviates from the fixed coordinate system x_0, y_0, z_0 by the Euler angles α and β, as shown in Fig. 1.

The movement of the gyroscope, as described in [2], is characterized by five coordinates, whose values in the absence of perturbations are

$$\alpha = 0, \quad \dot{\alpha} = 0, \quad \beta = 0, \quad \dot{\beta} = 0, \quad \varphi = \varphi_0, \quad \dot{\varphi}_0 = \omega. \tag{6}$$
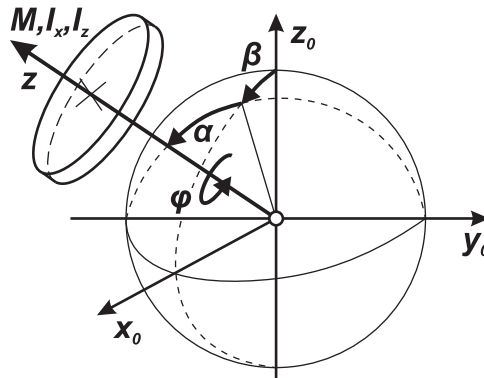
Fig. 1. Gyroscope outline with coordinates

The kinetic and potential energy of the unperturbed system can be determined as

$$T = \frac{1}{2}I_x(\dot{\alpha}^2 + \dot{\beta}^2 \cos^2 \alpha) + \frac{1}{2}I_z(\dot{\varphi} - \dot{\beta}\sin\alpha)^2,$$

$$\Pi = Mgl\cos\alpha\cos\beta,$$

(7)

where $I_x = I_y, I_z$ represent the moments of inertia of the gyroscope, M denotes its mass, and l represents the distance between the centroid and the origin. The system possesses three first integrals. The first one is given by the simple sum of both energies, as expressed in (7),

$$T + \Pi = \frac{1}{2}I_x(\dot{\alpha}^2 + \dot{\beta}^2 \cos^2 \alpha) + \frac{1}{2}I_z(\dot{\varphi} - \dot{\beta}\sin\alpha)^2 + Mgl \cdot \cos\alpha\cos\beta = C_1.$$

(8)

Since the coordinate φ is cyclic, the corresponding Lagrange equation simplifies considerably so that the second first integral is

$$\frac{\partial T}{\partial \dot{\varphi}} = I_z(\dot{\varphi} - \dot{\beta}\sin\alpha) = I_z \cdot C_2.$$

(9)

The third first integral can be introduced, for example, as the integral of the angular momentum of the gyroscope with respect to the fixed axis z_o. It can be written in the following form:

$$I_x(-\dot{\alpha}\sin\beta + \dot{\beta}\cos\alpha\sin\alpha\cos\beta) + I_z(\dot{\varphi} - \dot{\beta}\sin\alpha)\cos\alpha\cos\beta = C_3.$$

(10)

Random perturbations of the individual components will be introduced as the coordinates $\mathbf{u} = [u_1, u_2, u_3, u_4, u_5]$ in the following form:

$$\alpha = u_1, \quad \dot{\alpha} = u_2, \quad \beta = u_3, \quad \dot{\beta} = u_4, \quad \dot{\varphi} = \omega + u_5.$$

The first integrals of the movement with perturbations take the form

$$J_1(\mathbf{u}) = \frac{1}{2}I_x(u_2^2 + u_4^2 \cos^2 u_1) + \frac{1}{2}I_z(\dot{\varphi}_o + u_5 - u_4 \sin u_1)^2 + Mgl \cdot \cos u_1 \cos u_3 = C_1,$$

$$J_2(\mathbf{u}) = \omega + u_5 - u_4 \sin u_1 = C_2,$$

(11)

$$J_3(\mathbf{u}) = I_x(-u_2 \sin u_3 + u_4 \cos u_1 \sin u_1 \cos u_3) +$$
$$+ I_z(\dot{\varphi}_o + u_5 - u_4 \sin u_1)\cos u_1 \cos u_3 = C_3,$$

where only J_1 is positive definite. Therefore, the LF has the form of (5) with $b_i = 0$ and $a_1 = 1$. Assuming small values of perturbations, i.e., keeping only two terms of the $\sin, \cos$ Taylor expansions, the (approximate) LF is introduced as follows:

$$\lambda(\mathbf{u}) = -\frac{1}{2}(Mgl + a_3\omega I_z)u_1^2 + \frac{1}{2}I_x u_2^2 - \frac{1}{2}(Mgl + a_3\omega I_z)u_3^2 + \frac{1}{2}I_x u_4^2 + \frac{1}{2}I_z u_5^2 +$$
$$(\omega I_z + a_2 + a_3 I_z)u_5 - (\omega I_z + a_2 + a_3 I_z - a_3 I_x)u_1 u_4 - a_3 I_x u_2 u_3, \quad (12)$$

where coefficients a_2, a_3 remain to be determined. To ensure that the function in (12) is positive definite, it is necessary to set the coefficient of the first power of u_5 to zero, i.e.:

$$\omega I_z + a_2 + a_3 I_z = 0.$$

(13)

Such assumption changes (12) to the form

$$\lambda(\mathbf{u}) = \frac{1}{2}\underbrace{\left(\delta u_1^2 + 2a_3 I_x u_1 u_4 + I_x u_4^2\right)}_{=\lambda_1(\mathbf{u})} + \frac{1}{2}\underbrace{\left(\delta u_3^2 - 2a_3 I_x u_2 u_3 + I_x u_2^2\right)}_{=\lambda_2(\mathbf{u})} + \frac{1}{2}\underbrace{I_z u_5^2}_{=\lambda_3(\mathbf{u})}, \quad (14)$$

where $\delta = -(Mgl + a_3\omega I_z)$. The last term $\lambda_3(\mathbf{u})$ is positive definite in the variable u_5. Functions $\lambda_1(\mathbf{u})$ and $\lambda_2(\mathbf{u})$ are the quadratic forms which are positive, according to Sylvester's conditions, for non-vanishing u_1, u_4 and u_2, u_3, when

$$\Delta_1 = \delta > 0, \quad \Delta_2 = \begin{vmatrix} \delta & \pm a_3 I_x \\ \pm a_3 I_x & I_x \end{vmatrix} = I_x(\delta - a_3^2 I_x) > 0. \tag{15}$$

This implies

$$a_3 < -\frac{Mgl}{\omega I_z} \ \wedge\ \left| 2a_3 + \omega\frac{I_z}{I_x} \right| < \sqrt{\left(\frac{I_z}{I_x}\right)^2 \omega^2 - \frac{Mgl}{I_x}}. \tag{16}$$

Therefore, e.g., for a sufficiently high angular velocity of the gyroscope, that is, for $|\omega| > 2\sqrt{MglI_x}/I_z$, there exist real coefficients a_3 and a_2 that satisfy (16) and (13), respectively, so that the function $\lambda(\mathbf{u})$ defined in (12) is positive definite and can be used as the Lyapunov function.

The further analysis continues by assembly of the FP equation, see Eq. (1), using the drift and diffusion coefficients defined in (2). The stochastic equation form follows from the Lagrange equations based on the energy balance. This approach shows that when investigating the stochastic stability of the system, one can start from the characteristics of the deterministic system and examine only the characteristics of the last term of the FP operator according to (1) with respect to its contribution to the positive or negative values of the function $\psi(\mathbf{u})$.

5. Conclusion

The Lyapunov function constructed on the basis of first integrals provides a possibility to work with the stochastic part of the problem with a much greater overview and to construct mathematical models with regard to the stabilizing or destabilizing effects of parametric random noises. This type of analysis is applicable to a variety of dynamic stability problems, including naturally the problem of signal and noise separation in structural health monitoring and various indirect measuring methods.

Acknowledgements

References

[1] Bolotin, V. V., Random vibrations of elastic systems, Netherlands, Springer, 1984.
[2] Eiserman, M. A., Classical mechanics, Moscow, Nauka, 1980. (in Russian)

Calculation of stresses in filament-wound dome/cylinder joint using influence coefficients

Z. Padovec[a], D. Vondráček[a], T. Mareš[a]

[a]Department of Mechanics,Biomechanics and Mechatronics, Faculty of Mechanical Engineering, CTU in Prague, Technická 4, 160 00 Praha, Czech Republic

Presented text deals with the calculation of stresses in filament wound dome/cylinder joint where membrane stress condition is violated (cylindrical part of the vessel has different thickness than dome part). Due to this fact statically indeterminate shear force and bending moment occur in the joint (see Fig. 1 for details). These internal force effects cause inner plane resultant forces and moments acting on cylindrical part and dome of the vessel which are used for calculation of additional stresses (membrane and bending) in the joint.
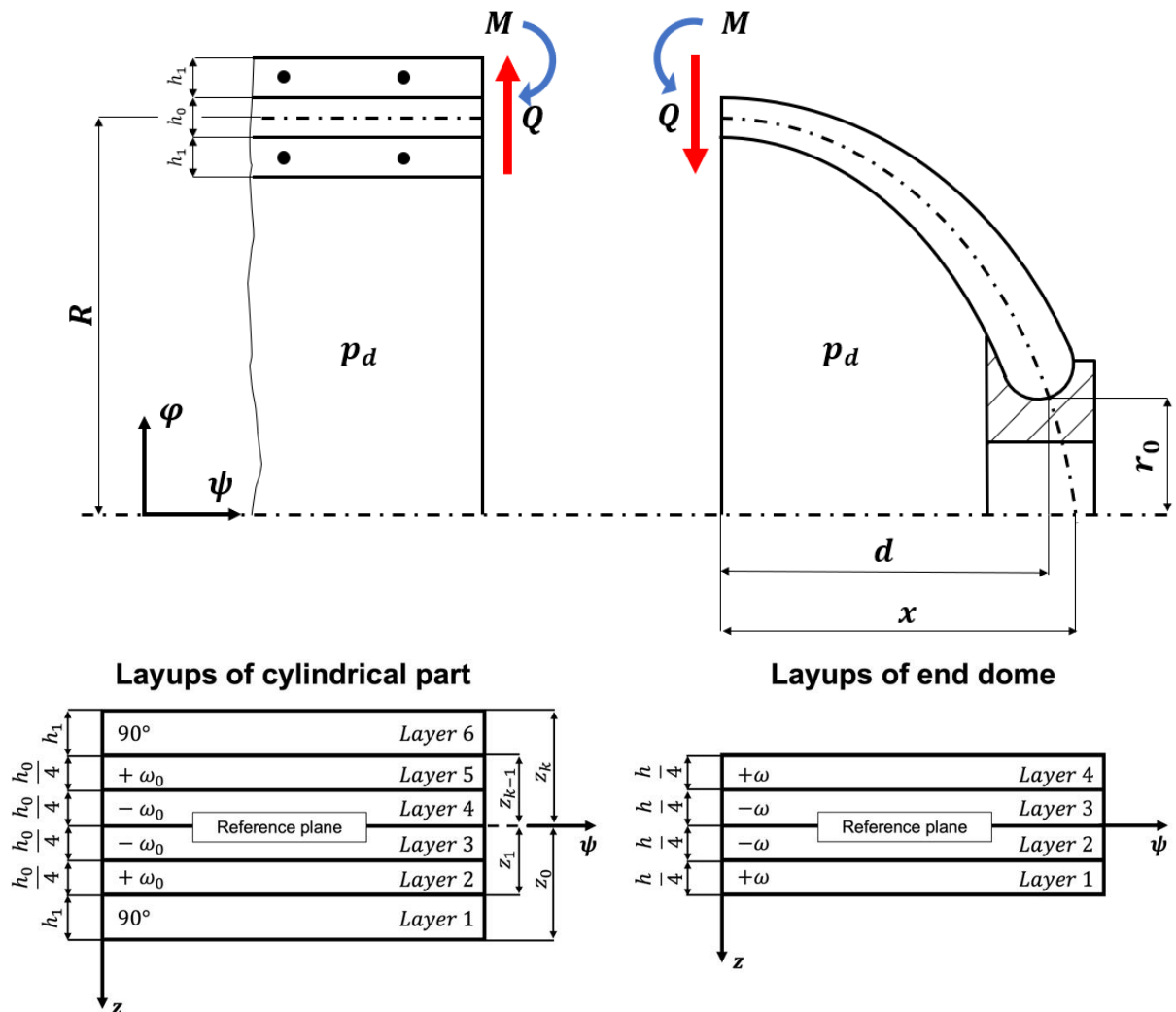
Fig. 1. Scheme of the dome/cylinder joint with internal force and composite lay-up for each part

Shear force Q and bending moment M can be calculated using influence coefficients derived in [2] as

$$M = p_d \, \frac{\left(\delta_p^C - \delta_p^D\right)\left(\vartheta_Q^D - \vartheta_Q^C\right)}{\left(\Delta_Q^C + \Delta_Q^D\right)\left(\vartheta_M^C + \vartheta_M^D\right) + \left(\Delta_M^C - \Delta_M^D\right)\left(\vartheta_Q^D - \vartheta_Q^C\right)} \; , \tag{1}$$

$$Q = M \, \frac{\vartheta_M^C + \vartheta_M^D}{\vartheta_Q^D - \vartheta_Q^C} \, , \tag{2}$$

where p_d is damage pressure and $\delta_p^{C,D}$, $\Delta_{Q,M}^{C,D}$ and $\vartheta_{Q,M}^{C,D}$ are influence coefficients [1]. Subscript indicates what is the influence factor caused by (p indicates internal pressure, Q indicates shear force and M indicates bending moment). Superscript indicates the area where the influence factor act (C indicates cylindrical part and D indicates end dome).

Inner plane resultant forces and moments are derived with the use of bending theory of cylindrical shell. Geometric equations of cylindrical shell (principal radii of curvature, normal angle to the shell midplane, etc.), equilibrium equations of the elements, equations which combine strain with displacements and curvature changes with displacements and slopes and classic lamination theory (ABD matrices and inner plane resultant forces and moments) were used for the derivation of fourth order ordinary differential equation for deflection line of the shell midplane. Boundary conditions given by shear force Q and bending moment M are used for the solution of integration constant which are used for computation of inner plane resultant forces and moments.

Strains on midplane for cylindrical part and end dome can be computed as

$$\begin{bmatrix} \varepsilon_\psi^0 \\ \varepsilon_\varphi^0 \end{bmatrix} = \boldsymbol{a} \left(\begin{bmatrix} N_\psi \\ N_\varphi \end{bmatrix}_p + \begin{bmatrix} N_\psi \\ N_\varphi \end{bmatrix}_Q + \begin{bmatrix} N_\psi \\ N_\varphi \end{bmatrix}_M \right) , \tag{3}$$

where $\boldsymbol{\varepsilon_0}$ are strains on midplane, $\boldsymbol{N_p}$ are in-plane resultant forces caused by membrane stresses, $\boldsymbol{N_Q}$ are in-plane resultant forces caused by shear force Q, $\boldsymbol{N_M}$ are in-plane resultant forces caused by bending moment M and $\boldsymbol{a}$ is the inverted tensile stiffness matrix (for cylindrical part is $\boldsymbol{a} = \left(A_{ij}^C\right)^{-1}$ and for end dome is $\boldsymbol{a} = \left(A_{ij}^D\right)^{-1}$).

The curvature changes of the midplane can be computed as

$$\begin{bmatrix} \kappa_\psi \\ \kappa_\varphi \end{bmatrix} = \boldsymbol{d} \begin{bmatrix} M_\psi \\ M_\varphi \end{bmatrix}_M , \tag{4}$$

where $\boldsymbol{\kappa}$ are curvature changes of the midplane, $\boldsymbol{M_M}$ are in-plane resultant moments caused by bending moment M and $\boldsymbol{d}$ is the inverted bending stiffness matrix (for cylindrical part is $\boldsymbol{d} = \left(D_{ij}^C\right)^{-1}$ and for end dome is $\boldsymbol{d} = \left(D_{ij}^D\right)^{-1}$).

Total strain in meridian and circumferential directions can be computed as

$$\begin{bmatrix} \varepsilon_\psi \\ \varepsilon_\varphi \end{bmatrix} = \begin{bmatrix} \varepsilon_\psi^0 \\ \varepsilon_\varphi^0 \end{bmatrix} + z_k \begin{bmatrix} \kappa_\psi \\ \kappa_\varphi \end{bmatrix} , \tag{5}$$

where z_k is the distance from the reference plane to the surface of the k-th layer (see Fig. 1). Then the stresses in the k-th layer in meridian and circumferential directions can be written as

$$\begin{bmatrix} \sigma_\psi \\ \sigma_\varphi \\ \tau_{\psi\varphi} \end{bmatrix}^k = \boldsymbol{Q}^k \begin{bmatrix} \varepsilon_\psi \\ \varepsilon_\varphi \\ 0 \end{bmatrix}^k , \tag{6}$$

where σ_ψ and σ_φ are normal stresses, $\tau_{\psi\varphi}$ is shear stress and $\boldsymbol{Q}$ is the well-known reduced stiffness matrix (for cylindrical part is $\boldsymbol{Q}^k = Q_{ij}^k$ and for end dome is $\boldsymbol{Q}^k = \overline{Q_{ij}}$).

These resulting stresses (σ_ψ, σ_φ and $\tau_{\psi\varphi}$) in coordinate system (ψ, φ) are created by superposition of the membrane stress, the stress caused by shear force Q, the stress caused by bending moment M and the stress caused by change in curvature as shown in Fig. 2 (cylindrical part) and Fig. 3 (end dome). There are six points on the cylindrical part (A_C, B_C, C_C, D_C, E_C and F_C) and two points on end dome (C_D and D_D) where peak stresses can occur (see Fig. 2 and Fig. 3) [3].
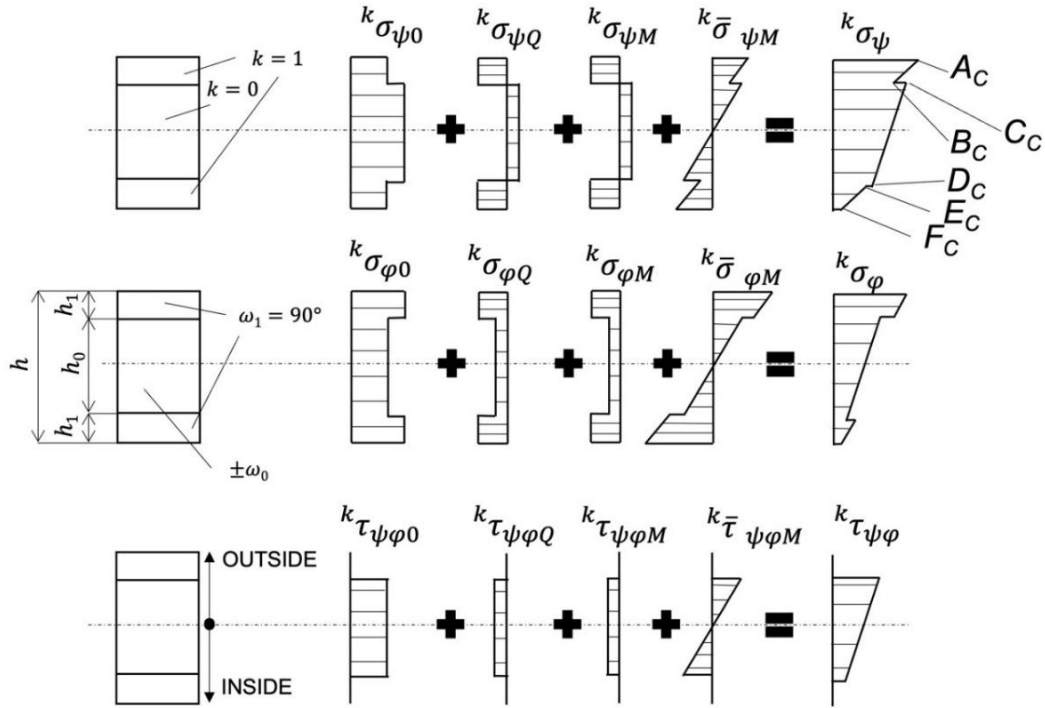
Fig. 2. Superposition of stresses for cylindrical part
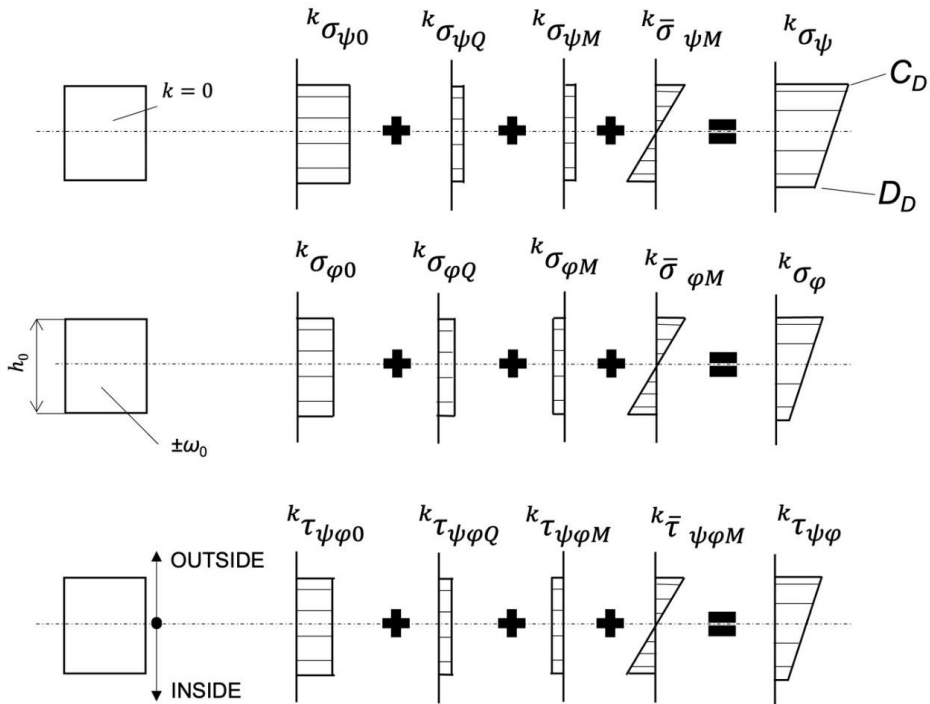
Fig. 3. Superposition of stresses for dome part

Stresses in coordination system (ψ, φ) are transformed to material coordinate system (L, T). This transformation can be written as

$$\begin{bmatrix} \sigma_L \\ \sigma_T \\ \tau_{LT} \end{bmatrix} = \begin{bmatrix} m^2 & n^2 & 2\,m\,n \\ n^2 & m^2 & -2\,m\,n \\ -m\,n & m\,n & m^2 - n^2 \end{bmatrix} \begin{bmatrix} \sigma_\psi \\ \sigma_\varphi \\ \tau_{\psi\varphi} \end{bmatrix}, \tag{7}$$

where $m = \cos \omega$ and $n = \sin \omega$. The same superposition can be used for resulting stresses $(\sigma_L, \sigma_T$ and $\tau_{LT})$ in material coordinate system (L, T). In each point shown in Fig. 2 and Fig.3 failure of the pressure vessel can occur. Therefore, all these stresses were used for failure index (FI) computation (see Fig. 4) for given internal pressure 1 MPa according to Hoffman strength criterion (see [1] for example). In Fig. 4 is presented FI for the cylinder joint with geodesic-isotensoid dome.
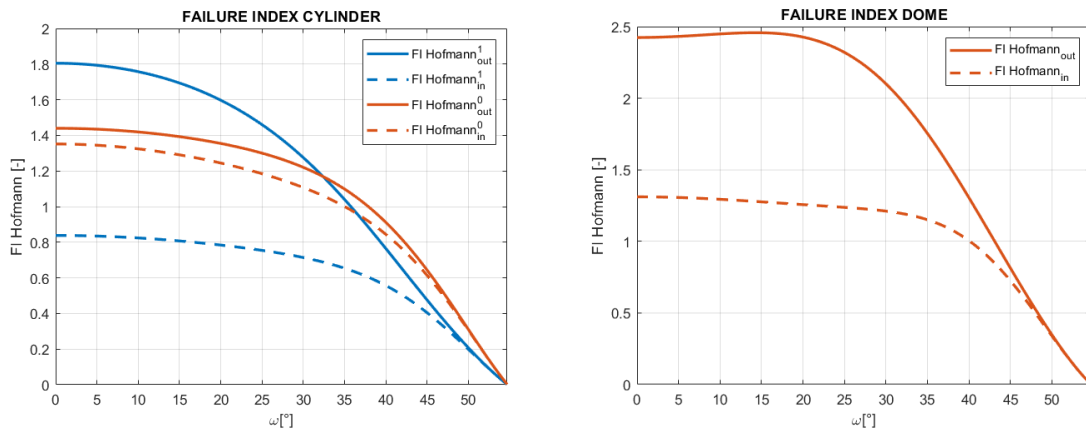
Fig. 4. FI for the cylinder joint with geodesic-isotensoid dome

This study describes a procedure for fast and efficient analysis of the junction between the cylindrical part and end dome of a filament wound pressure vessel. Analysis was done for five types of domes (sphere, geodesic-isotensoid, dome with zero transversal stress, dome with zero transversal strain and dome with identical strains). From the results we may see which dome is the best for the connection from the failure index point of view. Future work will focus on multi-criteria optimization of the dome shape according to the joint with cylinder.

Acknowledgements

References

[1] Laš, V., Mechanics of composite materials, UWB in Pilsen, Pilsen, 2008. (in Czech)
[2] Padovec, J., Stress and strain analysis in flimant wound pressure vessels from fibrous composite materials, Ph.D. Thesis, CTU in Prague, 1978.
[3] Vondráček, D., Padovec, Z., Mareš, T., Chakraborti, N., Analysis and optimization of junction between cylindrical part and end dome of filament wound pressure vessels using data driven evolutionary algorithms, Proceedings of the iMeche, Part C: Journal of Mechanical Engineering Science, Online First (2023) 1 − 14.

Comparison of co-rotational and other algorithms for geometrically nonlinear static analysis with small strains

R. Páleník[a,b], Z. Poruba[b]

[a] IT4Innovations, VSB – Technical University of Ostrava, 17. listopadu 2172/15, 708 00, Ostrava-Poruba, Czech Republic
[b] Department of Applied Mechanics, Faculty of Mechanical Engineering, VSB – Technical University of Ostrava, 17. listopadu 2172/15, 708 00, Ostrava-Poruba, Czech Republic

1. Introduction

Geometrically nonlinear problems of structural mechanics are typically solved by a fully nonlinear (NL) algorithm utilizing the total or updated Lagrangian formulation. However, in cases where the large displacements result mainly from the rigid body motion and induce only small strains, using the co-rotational (CR) algorithm is advantageous. Such an algorithm utilizes the CR formulation which yields a faster pseudolinear solution compared to its fully NL counterpart.

This paper aims to demonstrate the capabilities of the implemented CR algorithm on a practical example of an orthopaedic shoe insole. However, the purpose is not the strength analysis of the insole.

The previously published CR algorithm [3] is extended by incorporating the tetrahedral element, and strain and stress post-processing. Firstly, the CR and NL algorithm are theoretically compared, as they were implemented in MATLAB. Secondly, both the implemented algorithms are practically tested in a static analysis of the orthopaedic shoe insole discretized with tetrahedral elements. The resulting displacements, strains, and stresses are verified with finite element commercial software results.

2. Description of the CR and NL algorithm

This section provides a comparative theoretical description of two algorithms utilizing the finite element method to solve geometrically nonlinear static analysis with small strains. The CR algorithm implemented according to [2] utilizes the CR formulation, whereas the NL algorithm implemented according to Chapter 9 in [1] utilizes the total Lagrangian formulation. Both the implemented algorithms are applicable to any solid finite element with linear shape functions. Also, when coupled with a proper time-integration scheme, the algorithms can be used for a transient dynamic analysis. A linear elastic material model is assumed.

The main steps of a static analysis with the NL and CR algorithm are presented in Table 1. Both algorithms can be divided into two parts. Firstly, the nodal displacements $\mathbf{u}_{\text{new}}$ of the whole model are calculated using the conventional iterative Newton-Raphson (NR) procedure. Secondly, the element strains and stresses are computed from the resulting displacements on a per-element basis. Throughout the paper, the e subscript denotes the e-th element of the mesh.

The exceptionality and computational efficiency of the CR algorithm come from the utilization of the deformational nodal displacements $\boldsymbol{u}_{ed}$, whereas the NL algorithm uses only the standard (i.e., total) nodal displacements $\boldsymbol{u}_e$ on the element level. The deformational displacements are that part of displacements which causes strain, and they are extracted via the

polar decomposition of the deformational gradient computed in the element centroid. In the case of geometrically nonlinear problems with small strains, the large displacements are mainly caused by the rigid body motions. Therefore, the extracted deformational displacements are small, which enables linear calculation on the element level.

In the case of the NL algorithm, only the constitutional matrix $\boldsymbol{C}$ can be precomputed. Then, in each load step and each NR iteration inside of it, the NL formulation computes the element tangent stiffness matrix $\boldsymbol{K}_{te}$ and the element internal force vector $\boldsymbol{f}_{ie}$ using the Gauss quadrature integration. The integration procedure starts from the known constitutional matrix, initial element coordinates $\boldsymbol{x}_{0e}$ and the current nodal displacements $\boldsymbol{u}_e$, and it utilizes the deformation gradient, the Green-Lagrange strain tensor, and the second Piola-Kirchhoff stress tensor.

Whereas, in the case of the CR algorithm, the linear element stiffness matrix $\boldsymbol{K}_e$ can be precomputed for each element. Then, during the NR iterations, they are just modified inside the CR formulation onto $\boldsymbol{K}_{te}$. The modification contains mainly a both-sided multiplication of $\boldsymbol{K}_e$ with an orthogonal rotation matrix. The rotation matrix is obtained from the polar decomposition of the deformational gradient computed at the element centroid, and it represents the rigid body rotation of the element with respect to its initial coordinates.

Table 1. Main steps of a static analysis with the NL and CR algorithm

NL algorithm	CR algorithm
Prepare constitutional matrix $\boldsymbol{C}$	Compute linear element stiffness matrices $\boldsymbol{K}_e$
Start load steps loop, inside of it start NR iterations	
$(\boldsymbol{C}, \boldsymbol{x}_{0e}, \boldsymbol{u}_e) \xrightarrow{\text{NL formulation}} (\boldsymbol{K}_{te}, \boldsymbol{f}_{ie})$	$(\boldsymbol{K}_e, \boldsymbol{x}_{0e}, \boldsymbol{u}_e) \xrightarrow{\text{CR formulation}} (\boldsymbol{K}_{te}, \boldsymbol{f}_{ie}, \boldsymbol{u}_{ed})$
Assemble global tangent stiffness matrix $\boldsymbol{K}_t$ from $\mathbf{K}_{te}$ and global internal forces $\boldsymbol{f}_{int}$ from $\boldsymbol{f}_{ie}$ and apply boundary conditions	
Compute vector of residual forces $\boldsymbol{r} = \boldsymbol{f}_{ext} - \boldsymbol{f}_{int}$	
NR iterations of displacements: $\boldsymbol{u}_{new} = \boldsymbol{u}_{old} + \boldsymbol{K}_t^{-1}\boldsymbol{r}$	
Exit NR iterations if $\|\boldsymbol{r}\|/\|\boldsymbol{f}_{ext}\|$ is smaller than predefined NR tolerance	
Increase external forces $\boldsymbol{f}_{ext}$ up to full load and then exit load steps loop	
Extract element displacements $\boldsymbol{u}_e$ from $\boldsymbol{u}_{new}$	Use element deformational displacements $\boldsymbol{u}_{ed}$
Compute deformational gradient: $\boldsymbol{F}_e = \frac{\partial(\boldsymbol{x}_{0e} + \boldsymbol{u}_e)}{\partial \boldsymbol{x}_{0e}}$	Compute linear strain-displacement matrix: $\boldsymbol{B}_e$
Compute Green-Lagrange strain tensor: $\boldsymbol{E}_e = 1/2(\boldsymbol{F}_e{}^T\boldsymbol{F}_e - \boldsymbol{I})$, rewrite into vector $\boldsymbol{\varepsilon}_e$	Compute infinitesimal strain vector: $\boldsymbol{\varepsilon}_e = \boldsymbol{B}_e\,\boldsymbol{u}_{ed}$
Compute element stress vector: $\boldsymbol{\sigma}_e = \boldsymbol{C}\,\boldsymbol{\varepsilon}_e$	

In the second part of the NL algorithm, firstly, the element Green-Lagrange strain tensor $\boldsymbol{E}_e$ is computed from the element deformational gradient $\boldsymbol{F}_e$. Then, the element strain tensor components are rewritten to a vector form $\boldsymbol{\varepsilon}_e$ using the Voigt notation. The identity matrix $\boldsymbol{I}$ has dimensions 3×3 for 3-dimensional solid elements or 2×2 for 2-dimensional solid elements.

On the other hand, the CR algorithm is able to compute directly the element infinitesimal strain tensor components in a vector form $\boldsymbol{\varepsilon}_e$ linearly from the known deformational displacements $\boldsymbol{u}_{ed}$. The linear strain-displacement matrix $\boldsymbol{B}_e$ contains derivatives of shape functions with respect to the initial nodal coordinates.

Once the element strain tensor components are known, the element stress tensor components $\boldsymbol{\sigma}_e$, with respect to the initial configuration, are obtained easily by multiplying with $\boldsymbol{C}$. This, of course, applies only to the linear elastic material model.

Both the implemented algorithms compute its derivative quantity, $\boldsymbol{F}_e$ or $\boldsymbol{B}_e$, only in the element centroid, not in Gauss points. This is precise only for tetrahedral or triangular solid finite elements with linear shape functions because they have constant strain distribution through the whole element. However, based on the author's tests with hexahedral elements, this procedure gives satisfactorily precise results for other solid elements with linear shape functions, if a model contains relatively many small elements.

The equivalent strain and stress and all the other derived quantities on the element level are standardly computed from the element strain or stress tensor components. Optionally, the element strain and stress quantities can be averaged in nodes.

3. Numerical tests on an orthopaedic shoe insole undergoing large displacements

The orthopaedic shoe insole is discretized by 39595 tetrahedral elements with linear shape functions. The computational model contains 8896 nodes, and it is depicted in Fig. 1. The nodes marked by blue colour are fixed and 21 nodes marked by the red arrows are loaded in the direction of the z-axis. The loading force of 20 N is evenly distributed onto the loaded nodes. A linear elastic material model with Young's modulus of 1250 MPa and Poisson's ratio of 0.29 is assumed in the whole range of strains.
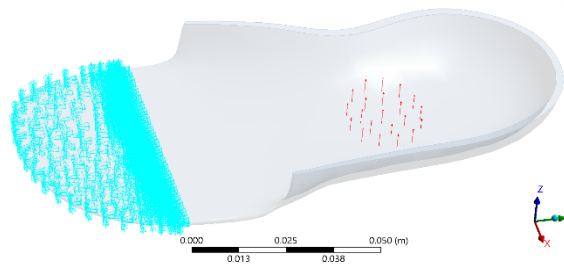
Fig. 1. Computational model: fixed nodes (blue), forced nodes (red)
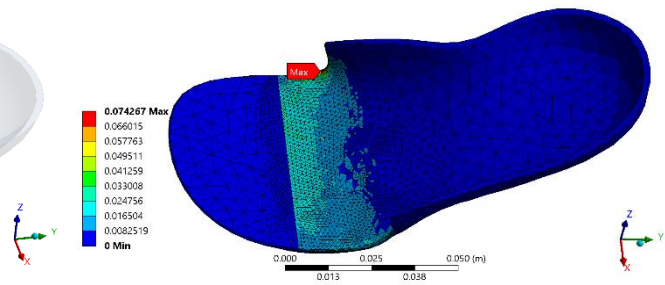
Fig. 2. Equivalent element strain (-) from commercial software

The geometrically nonlinear static analysis of the insole was performed using 3 different algorithms: the implemented CR, the implemented NL, and the one from commercial software which utilizes the updated Lagrangian formulation. The resulting maximal total displacements, maximal equivalent element strains and maximal equivalent element stresses are comparatively presented in Table 2, where the commercial software results are taken as a reference. The CR and NL algorithm results are almost identical and differ from the commercial software results by less than 2 %. To avoid the influence of the different nodal averaging techniques, the element (i.e., unaveraged) strains and stresses are compared. These are the results which directly come from the constant-strain tetrahedral finite elements. However, they are significantly higher than the nodal (i.e., averaged) results which are typically used for the strength evaluation.

Both the implemented algorithms required only one load step to reach the specified NR tolerance of 10^{-7}. Although, the NL algorithm used fewer NR iterations than the CR one, computation with the CR algorithm was about 1.2 times faster, because the CR formulation calculations are computationally less demanding. In terms of computational time, the algorithms implemented in MATLAB cannot compete with the optimized implementation in commercial software.

In Figs. 2 and 3, the distributions of equivalent element strains are displayed on a deflected insole in a true scale. The distributions obtained by different algorithms are visually indistinguishable. Although the maximal equivalent strain is almost 8 %, such high strains

appear only locally on a few elements. In most elements, the equivalent strain is lower than 3 %, which can be considered a small strain. Therefore, the CR algorithm provides very similar results to the NL one.
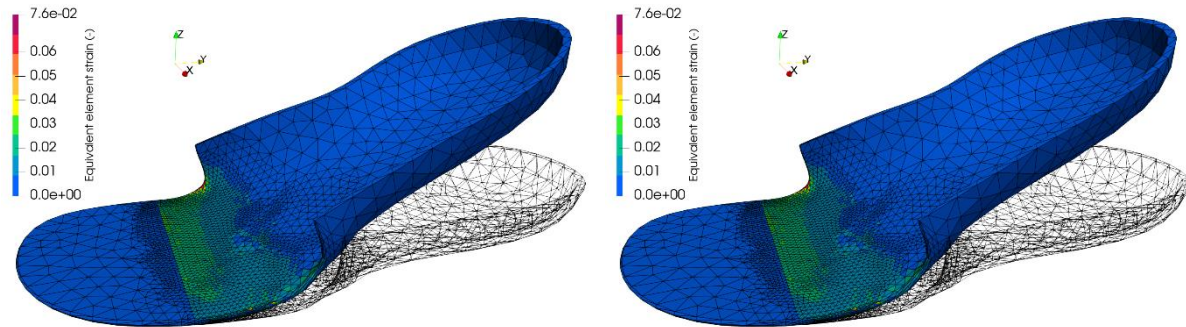
Fig. 3. Equivalent element strain (-) by NL (left) and CR (right) algorithm

Table 2. Comparison of the CR and NL algorithm results and verification with commercial software results

Algorithm	NL	CR	Commercial
Max. total displacement [m]	0.043170	0.043135	0.042643
Displacement relative error [%]	1.24	1.15	-
Max. eqv. element strain [-]	0.075667	0.075170	0.074267
Eqv. strain relative error [%]	1.89	1.22	-
Max. eqv. element stress [MPa]	94.583	93.963	92.834
Eqv. stress relative error [%]	1.88	1.22	-
Computational time [s]	1748	1475	(11)
Number of NR iterations [-]	9	10	(7)

4. Conclusion

The CR and NL algorithm were implemented and numerically tested on a practical example of an orthopaedic shoe insole undergoing large displacements. The insole was discretized by tetrahedral finite elements with linear shape functions. The resulting CR and NL displacements, element strains and stresses are almost the same, and they differ from the commercial software results by less than 2 %. The CR algorithm is faster than the NL one because it contains less computationally demanding mathematical operations. Although the CR formulation is generally limited by a small strain, it was demonstrated that the large local strain over a few elements does not noticeably damage the results, because the large local strains do not influence the final deflected shape significantly.

Acknowledgements

References

[1] Bhatti, M. A., Advanced topics in finite element analysis of structures with Mathematica and MATLAB computations. Wiley, New York, 2006.
[2] Moita, G. F., Crisfield, M. A., A finite element formulation for 3-D continua using the co-rotational technique, International journal for numerical methods in engineering 39 (1996) 3775-3792.
[3] Páleník, R., Molčan, M., Poruba, Z., Comparison of co-rotational and nonlinear finite element simulations with geometric nonlinearities, Proceedings of the 27/28th International Conference Engineering Mechanics, Milovy, 2022, pp. 301-304.

On tank hydrodynamics of recirculating aquaculture systems: Computational fluid dynamics modeling and its validation

Š. Papáček[a], M. Schuster[b], J. Urban[a]

[a] *University of South Bohemia in České Budějovice, FFPW, Institute of Complex Systems, 373 33 Nové Hrady, Czech Republic*
[b] *Research and Testing Institute Plzeň Ltd., Tylova 1581/46, Plzeň, Czech Republic*

1. Introduction

Recirculating aquaculture systems (RAS) form an important subset of aquaculture systems, providing about half the fish for human consumption worldwide. The demand for fish is rising, but fisheries are not expected to grow due to fully or over-exploited fish stocks. Therefore, there exists a strong demand in the public and private sectors of aquaculture research, which has to work toward sustainable production of high-quality fish with reduced environmental impact [3]. In the frame of the AQUAEXCEL (Aquaculture infrastructures for excellence in European fish research) project[1] we aim to bridge the gap between the the scientific community and the fish industry through the stimulation of problem-based research and enhanced knowledge transfer.

As follows, we focus on developing CFD (Computational Fluid Dynamics) based methodology for numerical simulation and further scale-up of aquaculture systems. The principal goal is to present a CFD-based simulation related to RAS tank hydrodynamics. As far as we know, only a few works are related to this area; see [7] for general agro-environmental application and [5] for a study on RAS. Here, as a proof-of-concept, we provide the steady-state flow fields of the conical-cylindrical tank used in the Hellenic Centre for Marine Research (HCMR) for larvae rearing [8].

Moreover, knowing that the numerical model validation is the paramount issue within CFD-based methodology, we further compare the experimentally measured and numerically simulated profiles of the flow field within tanks. Eventually, having a reliable method to simulate the fluid flow within the RAS tanks, we can address two important features of aquaculture tank design and operation, i.e., (i) to maximize the capability of the system for self-cleaning, and (ii) to ensure the optimal rearing conditions (including the fish exercising).

While the question of whether the tank will effectively clean or not was already extensively treated, see [9, 10] and references within there, the topic of fish exercising, which can be viewed as a sub-case of fish wellbeing is only emerging [4, 6, 11]. Here, we place the CFD-based methodology to solve the above-proposed problems once being precisely formulated.

---

2. Fluid-dynamic model of RAS

As follows, we model only one incompressible Newtonian liquid phase (fresh or sea water) in RAS.[2] Therefore, the classical system of Navier-Stokes equations and the continuity equation are used as fluid-dynamic model

$$\frac{\partial u}{\partial t} + (u \cdot \nabla)u = f - \frac{1}{\rho}\nabla p + \nu\nabla^2 u, \quad \nabla \cdot u = 0 \quad \text{in } (t_0, T) \times \Omega \tag{1}$$

with corresponding boundary conditions (reflecting the tank geometry) on $(t_0, T) \times \partial\Omega$ and initial conditions (reflecting the tank operating conditions) in Ω, and where u, p, f, ρ and ν denote the fluid velocity, the pressure, the body forces, fluid density, and kinematic viscosity, respectively.

Well-established methods exist to solve (1). Nowadays, the commercial CFD codes prefer the finite volume approach (FVM) to obtain the discretized form of (1) than other approaches like FDM or FEM (finite difference or finite element methods, respectively), especially with unstructured grids. The system of discretized equations (very large system of linear algebraic equations) is solved, usually iteratively, to find the values of velocities and pressures in all grid points. The coupled set of governing equations (1) is discretized in time for steady and unsteady calculations. In the steady case, it is assumed that time marching proceeds until a steady-state solution is reached.

The conical-cylindrical tank geometry used in this work is described in [8]. Among the three tank volumes (small of 40 liters, medium of 0.5 m³, and big of 2 m³), the 0.5 m³ tank for fish larvae tank was chosen. The mean hydraulic retention time (HRT) was set to 120 minutes, corresponding to the volumetric flow rate of 0.25 m³/hour, and the inlet velocity was 0.35 m/s. Some details about the inlet and outlet arrangement were communicated personally. The tank 3D representation, made by the CFD code ANSYS Fluent [2], is depicted in Fig. 1 (left). Computational mesh of 0.46×10^6 so-called polyhedral elements converted by merging from the originally 1.9×10^6 tetrahedral elements (besides the reduction of the total number of elements, the new polyhedral mesh is showing improved orthogonal quality and reduced skewness) was

---

[2]The simulation of solid particle movement was treated in our study [12], while the study about the incorporation of fish swimming (and respiration) is still under development.
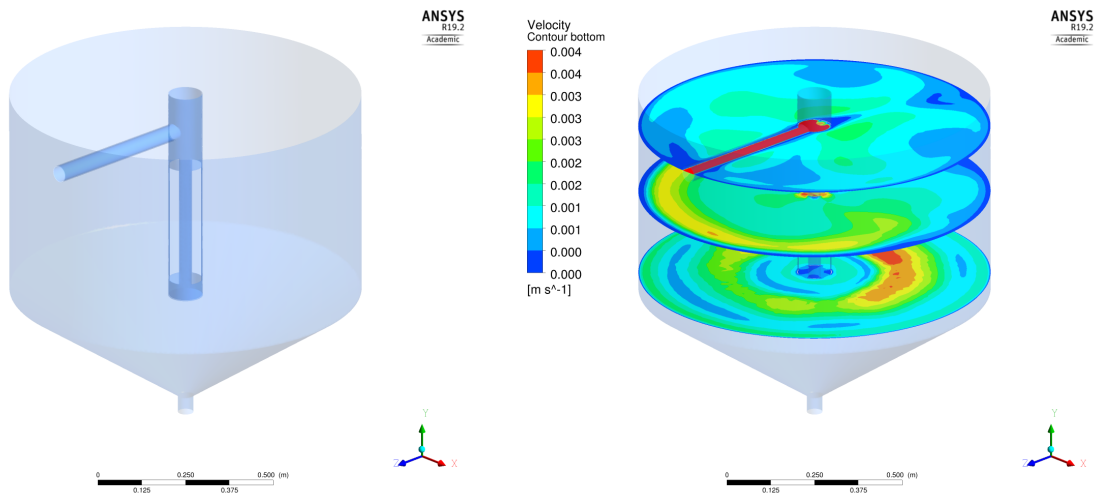
Fig. 1. (Left) Tank geometry of the RAS for rearing fish larvae at HCMR Heraklion, Greece. (Right) Velocity contours in three horizontal planes (40, 400, and 800 mm above the tank bottom)
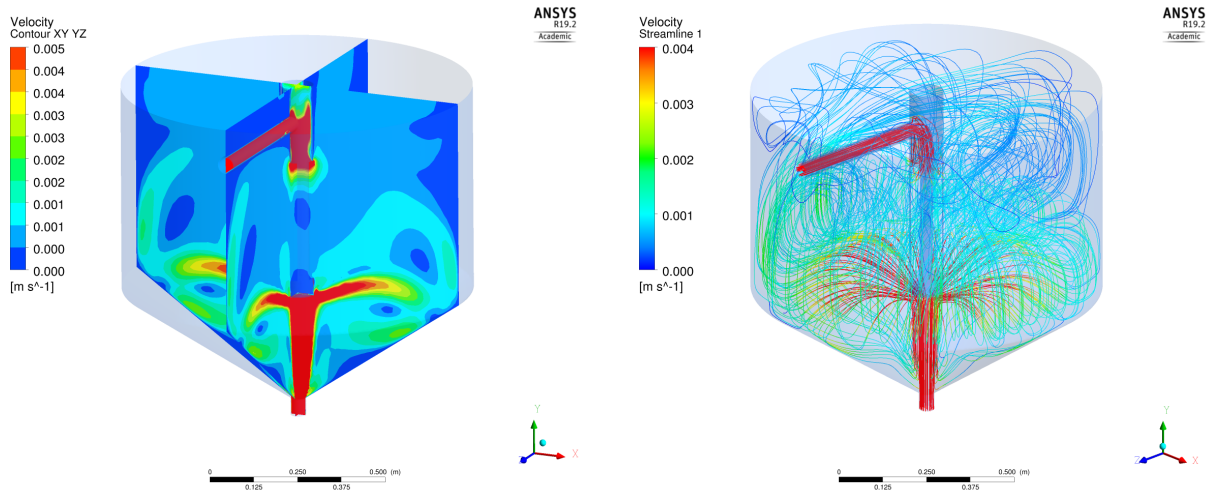
Fig. 2. (left) Velocity contours in two perpendicular axial cross-sections. (right) Streamlines illustrating the flow pattern in the HCMR tank

used for the velocity flow field calculation in the whole domain. As an illustration of CFD results, the velocity contours in three horizontal planes are depicted in Fig. 1 (right), while the velocity contours in two perpendicular axial cross-sections are shown in Fig. 2 (left) and the streamlines are plotted in Fig. 2 (right).

3. Validation of CFD simulation

The validation of the CFD model is defined as the process of determining the degree to which the model is an accurate representation of the real world from the perspective of the intended uses of the model [1]. Validation basically depends on directly comparing CFD-computed results and measured experimental results. Fluid velocity measurements were performed using a Vectrino velocimeter, a high-resolution acoustic velocimeter used to measure three-dimensional velocity in various applications from the laboratory to the ocean. The measurement technology is based on the coherent Doppler processing, having a range of ± 1 cm s^{-1} with an accuracy of ± 0.5 % of the measured value or ± 1 mm s^{-1}. The sampling volume is at a distance of 5 cm from the probe, with a diameter of 6 mm and a height of 7 mm. A specially prepared construction on the top of the tanks allowed the accurate positioning of the sensor in the tank to perform the measurements. The 0.5 m^3 tank was divided into three layers, where 12 measurements were taken at the first two layers and eight measurements at the third layer.

Afterward, the CFD results for the liquid phase velocity in the bottom, the medium, and the surface plane were used to calculate the average velocities in these planes, see Fig. 1 (right). Finally, these results were compared with the experimentally measured values published in [8] (see Table II on page 1 279).

4. Conclusions

Our work is a step towards using CFD for aquaculture tank design, optimization, and the scale-up of a laboratory system. We argue that the CFD-based methodology is an economically feasible tool, making it possible to conduct simulation studies on a desktop PC. Our CFD validation study has shown comparable results to real-world measurements, even though we do not assume the measurement is more accurate than the CFD results because the validation methodology only asserts that experimental measurements are the only true reflection of reality and

that the estimation process for error and uncertainty must be effectuated on both sides [1]. Even though CFD calculations may not be sufficiently exact, the degree of error is within reasonable bounds for engineering purposes. Thus, CFD analysis can become the standard tool for RAS design and operation, reducing research and engineering development costs.

Future work can focus both on biological and computational sides; i.e., we aim first to determine a simple description of fish swimming inside RAS and then to implement it to a suitable CFD code.

For instance, the description of the influence of the fish swimming on the flow pattern, see, e.g., [5, 9] and the quantification of fish preferences [11], in order to set up the design criteria in the optimization procedure with CFD runs embedded.

Acknowledgments

References

[1] AIAA-G-77 – Guide for verification and validation of computational fluid dynamics simulation, American Institute of Aeronautics Astronautics, 1998.

[2] ANSYS Fluent. http://www.ansys.com/Products/Fluids/ANSYS-Fluent

[3] AQUAEXCEL^{2020} – AQUAculture infrastructures for EXCELlence in European fish research towards 2020. https://aquaexcel2020.eu/

[4] Davison, W., Herbert, N. A., Swimming – enhanced growth, In: Swimming physiology of fish: Towards using exercise to farm a fit fish in sustainable aquaculture, (eds.) A. P. Palstra, J. V. Planas, Berlin, Springer, 2013, pp. 172-202.

[5] Gorle, J. M. R., Terjesen, B. F., Mota, V. C., Summerfelt, S., Water velocity in commercial RAS culture tanks for Atlantic salmon smolt production, Aquacultural Engineering 81 (2018) 89-100.

[6] Hanák, J., CFD simulation of flow in fish tanks, Master thesis, CTU Prague, Prague, 2016.

[7] Lee, I. B., Bitog, J. P. P., Hong, S.-W., Seo, I.-H., Kwon, K.-S., Bartzanas, T., Kacira, M., The past, present and future of CFD for agro-environmental applications, Computers and Electronics in Agriculture 93 (2013) 168-183.

[8] Lika, K., Pavlidis, M., Mitrizakis, N., Samaras, A., Papandroulakis, N., Do experimental units of different scale affect the biological performance of European sea bass Dicentrarchus labrax larvae? Journal of Fish Biology 86 (4) (2015) 1271-1285.

[9] Masaló, I., Oca, J., Influence of fish swimming on the flow pattern of circular tanks, Aquacultural Engineering 74 (2016) 84-95.

[10] Oca, J., Masalo, I., Flow pattern in aquaculture circular tanks: Influence of flow rate, water depth, and water inlet & outlet features, Aquacultural Engineering 52 (2013) 65-72.

[11] Palstra, A. P., Mes, D., Kusters, K., Roques, J. A. C., Flik, G., Kloet, K., Blonk, R. J. W., Forced sustained swimming exercise at optimal speed enhances growth of yellowtail kingfish (Seriola lalandi), Frontiers Physiology 5 (2015) No. 506.

[12] Papáček, Š., Petera, K., Císař, P., Stejskal, V., Saberioon, M., Experimental & computational fluid dynamics study of the suitability of different solid feed pellets for aquaculture systems, Applied Sciences 10 (19) (2019) No. 6954.

On prediction of non-uniform temperature fields in heat analysis of aero engines using machine learning approach

J. Pařez[a,c], P. Kovář[b,c]

[a]*Department of Mechanics, Biomechanics and Mechatronics, Faculty of Mechanical Engineering, Czech Technical University in Prague, Technická 4, 160 00 Prague 6, Czech Republic*

[b]*Department of Technical Mathematics, Faculty of Mechanical Engineering, Czech Technical University in Prague, Karlovo náměstí 13, 121 35 Prague 2, Czech Republic*

[c]*Center of Aviation and Space Research, Faculty of Mechanical Engineering, Czech Technical University in Prague, Technická 4, 160 00 Prague 6, Czech Republic*

1. Introduction

A fundamental task in the development process of modern aircraft engines is to ensure the effective cooling of highly thermal stressed engine components. The lifetime of components, and therefore the lifetime of the entire engine, is strongly dependent on material cyclic warming up and therefore it is required a reliable temperatures prediction in materials for specific operation conditions. Conjugated heat transfer, first formulated by Perelman [8], considers the interaction between a solid and fluid. Flow conditions strongly influence material temperatures and thermal interactions. Thus, secondary flows can occur in the concentric annular cavities of compressors and turbines. For an optimal design, transient processes and the solid-fluid interaction as well as the thermal time mismatch for the solid and the fluid must be considered.

In transient analyses of temperature and stress distributions in turbine components, the finite element method (FEM) is usually used. The resulting thermal loads are described by simplified boundary condition models from empirical correlations using advective one-dimensional models as presented by Fiedler et al. [3]. Heselhaus and Vogel [5] have shown that by using transient simulations, conjugate flow and heat transfer that account for three-dimensional effects, a significant improvement in accuracy can be achieved without relying on empirical correlations. This can significantly improve the prediction of component temperatures. Conversely, inappropriate modelling of transients during flight changes can lead to critical clearances or thermal stresses, as reported by Sun et al. [9]. Thermal differences in time make conjugate simulations of the heat transfer with respect to all time scales extremely expensive, as convective heat transfer in a fluid is up to $104\times$ faster than heat conduction through a solid body.

In order to reduce the computational complexity, Errera and Baqué [1] and Sun et al. [9] introduced coupled aerothermal and mechanical methods where optimized programs are used to independently simulate heat transfer in a fluid and in a solid. This so-called weak coupling allows the thermal behaviour of the solid to be calculated using a FEM code, while the adjacent flow is calculated using computational fluid dynamics (CFD). To ensure a physical, accurate and stable solution of the conjugate system, the FEM and CFD codes must exchange information on a common interface. Different strategies exist in the literature for this purpose. Errera and Duchaine [2] investigated different coupling coefficients and continuity of the exchange variables for aerothermal simulations. They showed that if a criterion based on the ratio of thermal resistances at the interface is satisfied, the Dirichlet-Robin transfer procedure leads to

stable and fast convergence. Gimenez et al. [4] presented approaches updating the boundary conditions between the coupling points. They showed that the quasi-dynamic coupling method with transient calculations for solids and steady-state calculations for fluids is the most promising in terms of accuracy and efficiency. Gimenez et al. [4] further showed that a value of the relaxation parameter close to the heat transfer coefficient is advantageous.

This paper is devoted to the study of novel numerical coupling approach between CFD and FEM in conjugated heat transfer for steady-state and possibly transient analysis of aero-engine applications and similar applications in turbomachinery. The coupling is made using a correlation based on CFD data postprocessed by a novel artificial higher order neural network approach. Temperature field prediction can be prescribed on the boundary nodes of the FEM mesh and the observed overall deformation in time can be determined.

2. An approach

The problem is solved on the single annular geometry, which is key geometry in turbomachinery, specifically in compressors and turbines section. The considered geometry is shown in Fig. 1.

Initial conditions entering the CFD analysis are based on the thermodynamic cycle of an aircraft engine in *CRUISE* flight mode that is discussed in detail by Pařez et al. [7]. Temperature field distribution on outer tube is calculated by CFD and the correlation is determined using artificial neural network. This temperature distribution is non-uniform on the outer annular tube due to ongoing natural convection caused by the steady-state homogeneous heating of the inner tube, which is representing hot gases flowing through the turbine. Since the outer tube represents the case of the gas turbine, this temperature distribution is important for the electronic components placement or the overall engine deformation, that can be calculated by FEM.

Presented approach allows a quick estimation of the temperature distribution with no need to perform time demanding CFD simulations that can rapidly accelerate design and development
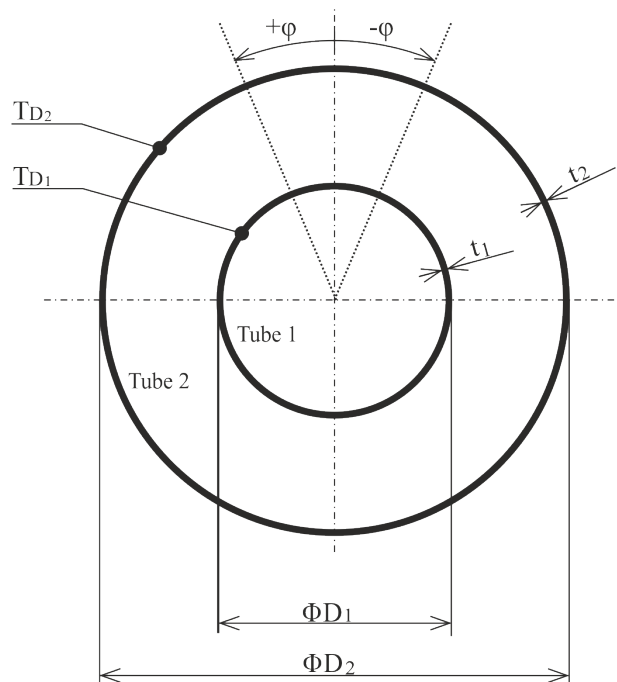
Fig. 1. Sketch of the computational domain

Table 1. Input parameters for CFD analysis

Parameter	Values	Unit
D_1/D_2	$\{0.5, 0.6, 0.7, 0.8, 0.9\}$	[1]
t_2	$\{1, 2, 3\}$	[mm]
T_{D_1}	$\{500, 600, 700\}$	[°C]
φ	$\{0, 1, \ldots, 358, 359\}$	[°]

of the device. This is essential for transient FEM analysis where deformation is determined in every time step with time-depend parameters change. The goal is to determine a limited number of the most important parameters that affect the outer tube temperature distribution. The values of the dependent parameters are listed in Table 1. The influencing angular position parameter φ is considered to be equally spaced around the tube wall.

The correlation function is obtained using an extensive set of CFD simulations under different operational conditions and geometrical setups as it is shown in Fig. 2. A machine learning approach is applied to results of the CFD simulation and the only correlation function is obtained for a range of input variable parameters. The correlation function can be expressed as

$$T_{D_2} = \mathcal{N}(\bullet) = f(D_1/D_2, t_2, T_{D_1}, \varphi). \tag{1}$$

The calculation of deformations is then carried out using the standard FEM calculation, which has been presented, for example, in the paper by Pařez and Kovář [6], where a computational tool developed in the MATLAB environment was presented.
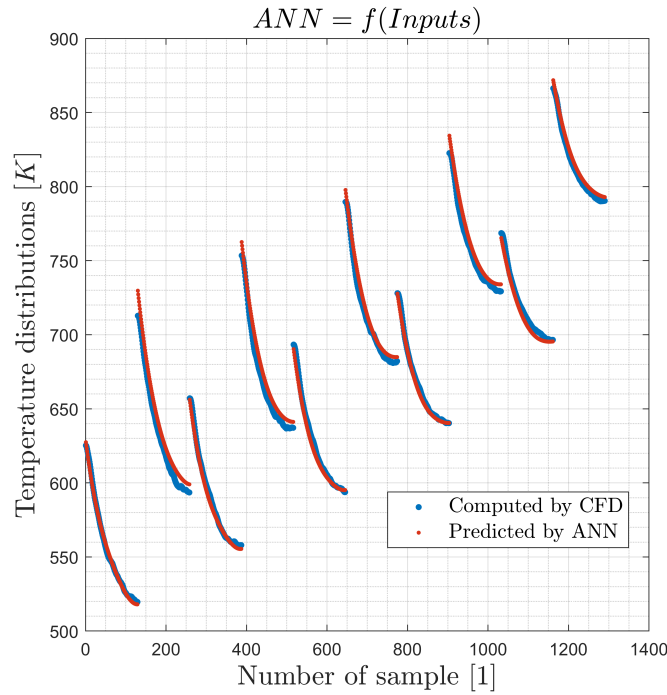
Fig. 2. Resulting correlation function: Comparison of the ANN prediction and CFD simulations

3. Summary

An approach how the temperature field on the case of the aircraft engine can be modelled based on the neural networks has been presented. This approach can make deformation analysis using FEM much faster due to no need to compute time demanding CFD. Instead of the simulation, boundary conditions can be obtained by learned neural network.

Acknowledgments

References

[1] Errera, M. P., Baqué, B., A quasi-dynamic procedure for coupled thermal simulations, International Journal for Numerical Methods in Fluids 72 (2013) 1183-1206.

[2] Errera, M. P., Duchaine, F., Comparative study of coupling coefficients in Dirichlet-Robin procedure for fluid-structure aerothermal simulations, Journal of Computational Physics 312 (2016) 218-234.

[3] Fiedler, B., Muller, Y., Voigt, M., Mailach, R., Comparison of two methods for the sensitivity analysis of a one-dimensional cooling flow network of a high-pressure-turbine blade, Proceedings of the ASME Turbo Expo 2020: Turbomachinery, American Society of Mechanical Engineers, New York, 2020.

[4] Gimenez, G., Errera, M.P., Baillis, D., Smith, Y., Pardo, F., A coupling numerical methodology for weakly transient conjugate heat transfer problems, International Journal of Heat and Mass Transfer 97 (2016) 975-989.

[5] Heselhaus, A., Vogel, D., Numerical simulation of turbine blade cooling with respect to blade heat conduction and inlet temperature profiles, Proceedings of the 31st Joint Propulsion Conference and Exhibit, San Diego, 1995.

[6] Pařez, J., Kovář, P., Development and application of a 3D FEM model for rotor thermal bow prediction, Proceedings of the 24th International Scientific Conference APPLIED MECHANICS 2023, Strojnícka fakulta STU v Bratislave, Bratislava, 2023, pp. 93-96.

[7] Pařez, J., Tater, A., Kovář, P., Polanský, J., Vampola, T., Investigation of temperature fields during turboprop engine cooling simplified to the 3D double annulus, Proceedings of the 15th European Conference on Turbomachinery Fluid dynamics & Thermodynamics, The European Turbomachinery Society, 2023.

[8] Perelman, T., On conjugated problems of heat transfer, International Journal of Heat and Mass Transfer 3 (4) (1961) 293-303.

[9] Sun, Z., Chew, J. W., Hills, N. J., Lewis, L., Mabilat, C., Coupled aerothermomechanical simulation for a turbine disk through a full transient cycle, Journal of Turbomachinery 134 (1) (2011) No. 011014.

Feature selection for high-order neural unit based identification

V. Pawlik[a], P. Steinbauer[a], I. Bukovský[a]

[a] *Faculty of Mechanical Engineering, CTU in Prague, Technická 4, 160 00 Praha 6, Czech Republic*

1. Introduction

The main challenge of using learning systems is the selection of input data. In the field of system identification, the input vector usually consists of a combination of the plant's inputs and outputs. With high-order neural units (HONUs) as the model, the input vector can also contain said quantities in higher powers and combinations of products, however, not all contribute to the model's output, and selecting the features to include by hand is inefficient. This paper shows the use of the Boruta package for feature selection in the task of dynamic system identification with HONUs as a model.

2. High-order neural units

The structure of HONU is as follows

$$y_m = \sum_{i=0}^{n} w_i x_i = \mathbf{w}^T \mathbf{x}, \tag{1}$$

where y_m is the model's output, $\mathbf{x}$ is the input vector and $\mathbf{w}$ is the neural weights vector [1].

The general HONU output formula is

$$y_m = \mathbf{w}^T \operatorname{col} \mathbf{x}, \tag{2}$$

where $\mathbf{w}$ and $\operatorname{col} \mathbf{x}$ are both column vectors. The neural weights $\mathbf{w}$ can be adapted using a gradient descent algorithm and optimizing the criterion

$$J = \frac{1}{2} e(k)^2, \tag{3}$$

where the error e is the difference between the desired and the current output

$$e(k) = y(k) - y_m(k). \tag{4}$$

The gradient of the criterion J with respect to $\mathbf{w}$, which is the steepest direction, is

$$\frac{\partial J}{\partial \mathbf{w}} = e(k) \left(\frac{\partial J}{\partial \mathbf{w}} y(k) - \frac{\partial J}{\partial \mathbf{w}} y_m(k) \right) = e(k) \left(0 - \operatorname{col} \mathbf{x} \right) = -e(k) \operatorname{col} \mathbf{x}. \tag{5}$$

The weights are then adjusted toward the minimum of the criterion using the algorithm for stochastic optimization Adam [3].

To assess the performance of HONU, the sum of squared errors (SSE) over a certain horizon N_e might be used

$$\text{SSE} = \sum_{i=k-N_e}^{k} e(i)^2. \tag{6}$$

3. Boruta

An approach of feature selection using the Boruta package [4] was explored in [5] for data with many input variables. During the process, the original features are shuffled randomly and a new dataset of shadow features is created. The new dataset is then used for training a Random Forest Regressor [2] and the feature importance is checked. The original features with higher importance than the most important shadow feature are marked. This is done in multiple iterations and the results are combined and the original features are ranked using statistical metrics.

4. Plant and simulation

The plant used for testing in simulation is a non-linear oscillating plant with time-variant parameters

$$\ddot{z} + b|\dot{z}|\dot{z} + cz = u. \tag{7}$$

The parameters of the plant start changing randomly at halftime, the input is a square wave with varying amplitude. The plant is simulated continuously with Runge-Kutta method integration and then sampled with zero-order-hold at 100 Hz, resulting in a history of $z(k\Delta t) = z_k$, $\Delta t = 0.01$ s, $k = 0, 1, \ldots$ An example of the plant's input and parameters is shown in Fig. 1.
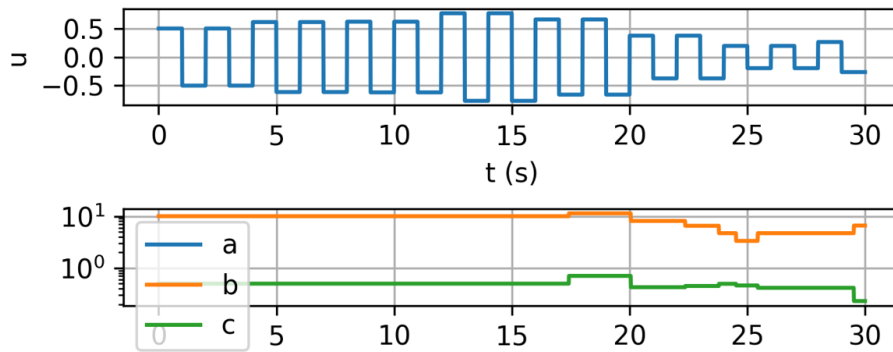
Fig. 1. The input and output of the testing plant

A dataset of plant outputs z_k and HONU inputs $\mathrm{col}\, \mathbf{x}_k$ from the simulation history was assembled and used for the feature selection. For ease of presentation, a quadratic cubic unit with $n_y = 2$ and $n_u = 2$ was selected. In Fig. 2, the inputs, outputs, and parameters of the plant and HONU process are shown. In Table 1, the results of the Boruta method are shown. The features with rank 1 are to be kept and others are to be discarded.

Table 1. The result of the Boruta algorithm. The features with the lowest rank are the most important

Feature	Rank	Feature	Rank	Feature	Rank	Feature	Rank	Feature	Rank
u0u0y0	1	u1u1y0	1	y0y1y1	1	u1y0	1	u1u1u1	5
y0y0y1	1	u0y1y1	1	y1y1y1	1	u0y1	1	u0u0u1	6
y0y0y0	1	u0y0y1	1	y1y1	1	y1	1	u1	7
u1y1y1	1	u0y0y0	1	y0y1	1	u0y0	1	u0	8
u1y0y1	1	u0u1y1	1	y0	1	u0u0	2	u0u0u0	9
u1y0y0	1	u0u1y0	1	y0y0	1	u0u1	3	u0u1u1	10
u1u1y1	1	u0u0y1	1	u1y1	1	u1u1	4	1	11
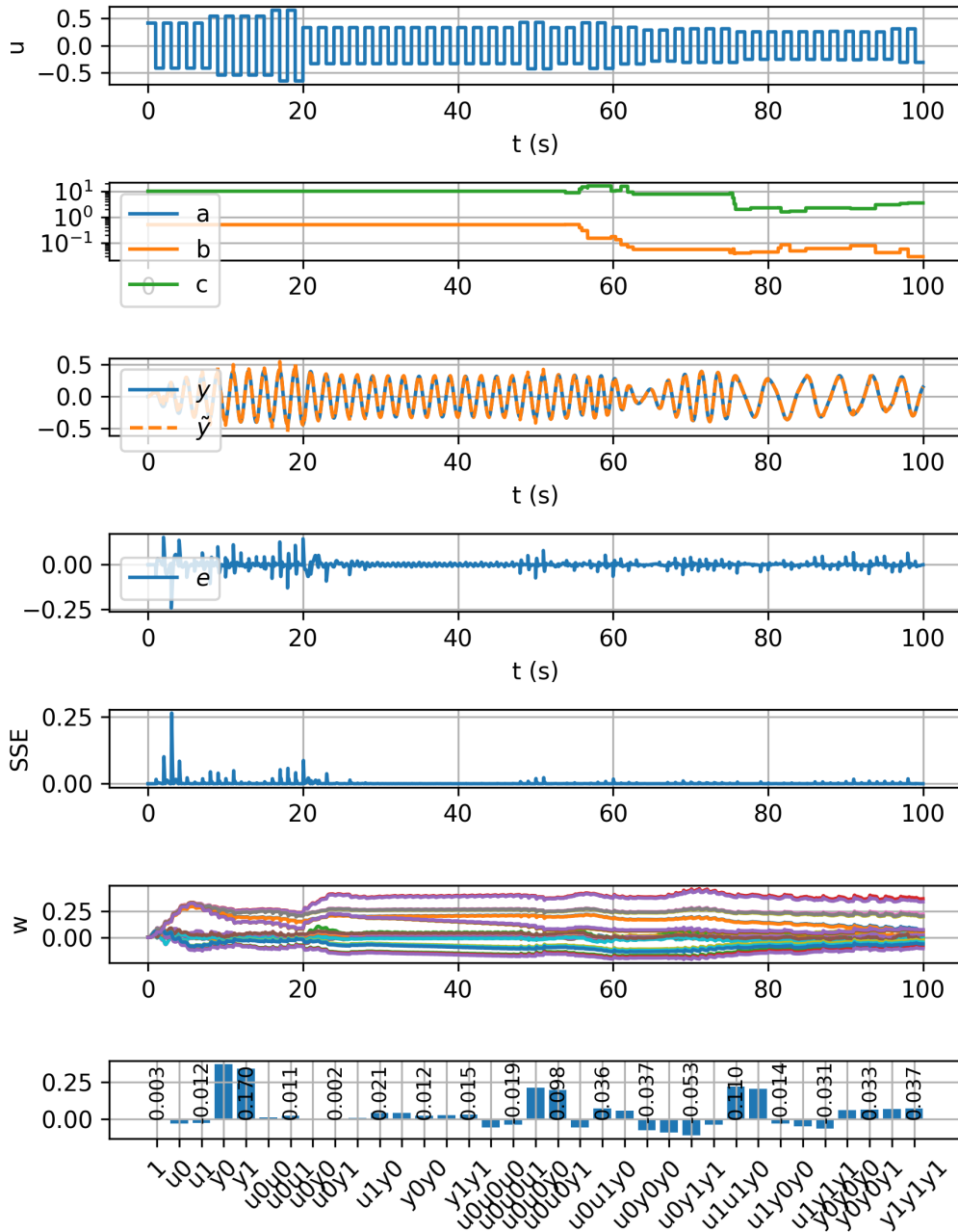
Fig. 2. Training of a HONU. The plant input u, plant's parameters b and c, plant's and HONU's outputs y and $\tilde{y}$ and the error e and criterion SSE are shown. In the last plot two plots, the history of neural weights w and the final weights of the HONU are shown

5. Conclusion

The Boruta algorithm was able to select features to be disregarded. This selection is confirmed by comparing the neural weight values after the training process with the rank from Boruta. The features with high rank have low weight and do not contribute to the output of the HONU.

Therefore, Boruta can be used to a priory disregard features and speed up the computationally intensive learning process of HONUs with higher orders.

Further research shall focus on evaluating the speed-up by feature elimination and feature selection for HONUs used in a control process.

Acknowledgement

References

[1] Bukovsky, I., Voracek, J., Ichiji, K., Homma, N., Higher order neural units for efficient adaptive control of weakly nonlinear systems, Proceedings of the 9th International Joint Conference on Computational Intelligence, Funchal, Madeira, Portugal, 2017, pp. 149-157.

[2] Breiman, L., Random forests, Machine Learning 45 (2001) 5-32.

[3] Kingma, D. P., Ba, J., Adam: A method for stochastic optimization, 2014. doi: 10.48550/arXiv.1412.6980

[4] Kursa, M. B., Rudnicki, W. R., Feature selection with the Boruta package, Journal of Statistical Software 36 (11) (2010) 1-13.

[5] Marzova, K., Bukovsky, I., Feature selection and uncertainty analysis for bubbling fluidized bed oxy-fuel combustion data, Processes 9 (10) (2021) No. 1757.

Periodic homogenization of structural metamaterials

G. Pokatilov[a,b], P. Henyš[a]

[a]Institute of New Technologies and Applied Informatics, Faculty of Mechatronics, Informatics and Interdisciplinary Studies, Technical University of Liberec, Studentská 1402/2, 461 17 Liberec 1, Czech Republic
[b]Institute of Plasma Physics of Czech Academy of Sciences, TOPTEC, Sobotecká 1660, 511 01 Turnov, Czech Republic

1. Introduction

This paper focuses on the periodic homogenization of structural metamaterials and methods of parametric control of the geometry of individual patterns. Based on the selection of 6 parameters, it will be possible to create a wide range of derived shapes of the original geometry and then continue to homogenize these patterns. The upcoming task will be based on the implementation of this method using neural networks. Homogenization of structural materials is a process that aims to simplify the description of their complex structure into efficient continuous material models.

2. Formulation of liner elasticity for pattern

In this section, we formulate the equations governing linear elasticity for single pattern with conventional material (metal, polymer). The governing equations are as follows:

$$-\nabla \cdot \boldsymbol{\sigma} = \mathbf{0} \quad \text{in } \Omega, \tag{1}$$

$$\boldsymbol{\sigma} \cdot \mathbf{n} = \mathbf{0} \quad \text{on } \Gamma, \tag{2}$$

where $\boldsymbol{\sigma}$ is the stress tensor, $\mathbf{n}$ is the outward unit normal vector on the boundary Γ, and Ω represents the spatial domain.

The strain tensor $\boldsymbol{\varepsilon}(u)$ is defined as:

$$\boldsymbol{\varepsilon}(u) = \hat{\boldsymbol{\varepsilon}} + \frac{1}{2} \left(\nabla u + \nabla u^T \right), \tag{3}$$

where $\hat{\boldsymbol{\varepsilon}}$ denotes the given macroscopic strain, and u represents the micro displacement field.

The stress-strain relationship is given by

$$\boldsymbol{\sigma}(\boldsymbol{\varepsilon}) = \lambda \cdot \operatorname{tr}(\boldsymbol{\varepsilon} + \hat{\boldsymbol{\varepsilon}}) \cdot \mathbb{I} + 2\mu(\boldsymbol{\varepsilon} + \hat{\boldsymbol{\varepsilon}}) = \bar{\boldsymbol{\sigma}}(\boldsymbol{\varepsilon}) + \hat{\boldsymbol{\sigma}}(\hat{\boldsymbol{\varepsilon}}), \tag{4}$$

where λ and μ are the Lamé parameters, and $\mathbb{I}$ is the identity tensor. Periodic conditions admit rigid translation, therefore, an additional constraint on fluctuation field was imposed

$$\int_{\Omega} u \, \mathrm{d}\Omega = 0. \tag{5}$$

To obtain the weak form of the equations together with constraints above satisfied, we can use either Lagrange multipliers or a penalty method [1]. Using Lagrange multipliers g (and test function δg), we arrive at the following variational formulation:

$$\int_{\Omega} \boldsymbol{\varepsilon}(v) : \bar{\boldsymbol{\sigma}}(u) \, \mathrm{d}\Omega + \int_{\Omega} g \cdot v \, \mathrm{d}\Omega + \int_{\Omega} \delta g \cdot u \, \mathrm{d}\Omega = - \int_{\Omega} \hat{\boldsymbol{\sigma}} : \boldsymbol{\varepsilon}(v) \, \mathrm{d}\Omega. \tag{6}$$

We discretized this scheme with mixed finite elements with linear basis functions for both displacement and multipliers and their test functions v and δg. Alternatively, employing a penalty method, we have

$$\int_\Omega \boldsymbol{\varepsilon}(v) : \bar{\boldsymbol{\sigma}}(u)\,\mathrm{d}\Omega + \int_\Omega u \cdot v\,\mathrm{d}\Omega = -\int_\Omega \hat{\boldsymbol{\sigma}} : \boldsymbol{\varepsilon}(v)\,\mathrm{d}\Omega. \qquad (7)$$

It is worth noting that a necessary condition for applying periodic boundary conditions is the requirement for identical node positions on opposite periodic boundaries.

3. Homogenization

In the study of homogenization, we establish the relation between macroscale ($\hat{\boldsymbol{\sigma}}$, $\hat{\boldsymbol{\varepsilon}}$) and microscale ($\boldsymbol{\sigma}$, $\boldsymbol{\varepsilon}$) quantities. The relationships are defined as follows:

$$\hat{\boldsymbol{\sigma}} = \frac{1}{\Omega}\int_\Omega \boldsymbol{\sigma}\,\mathrm{d}\Omega, \qquad \hat{\boldsymbol{\varepsilon}} = \frac{1}{\Omega}\int_\Omega \boldsymbol{\varepsilon}\,\mathrm{d}\Omega. \qquad (8)$$

Here, $\hat{\sigma}$ represents the macroscopic stress averaged over the entire domain Ω and $\hat{\varepsilon}$ represents the prescribed macroscopic strain. The connection between macroscopic stress $\hat{\sigma}$ and macroscopic strain $\hat{\varepsilon}$ is expressed as

$$\hat{\boldsymbol{\sigma}} = \mathbb{C}^{hom} : \hat{\boldsymbol{\varepsilon}}. \qquad (9)$$

In this context, tensor $\mathbb{C}^{hom}$ is formed by elastic constants characterizing the homogenized medium. The components of the tensor $\mathbb{C}^{hom}$ can be determined through the solution of standardized strain $\hat{\varepsilon}$ load cases (six load cases).

This homogenization process (Fig. 1) enables us to bridge the gap between the macroscopic behavior of a material and its underlying microstructure, allowing for the characterization of effective properties on a larger scale [2].
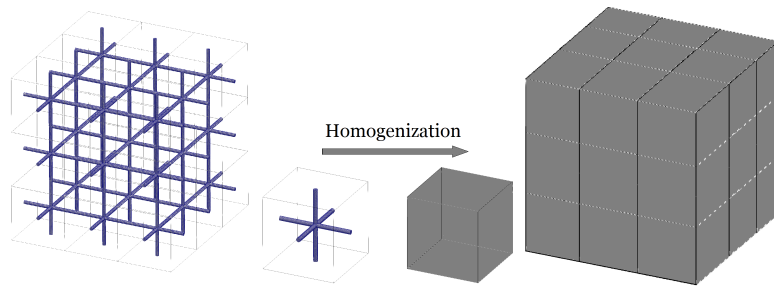
Fig. 1. Structural homogenization scheme

4. Geometry control

Our research focuses on parametric control of explicit geometries using two methods: numerical and analytical. In the numerical approach, we assign structural properties to the original model and induce controlled deformations by rotation and translation along specified axes. The resulting deformed mesh is homogenized. In the analytical approach, we use transformation functions to project nodes from the original mesh into the new coordinates, ensuring that there is no overlapping of nodes or violation of mesh connectivity. We use the following function for the translational transformation:

$$f_i(x,y,z) = T_i \frac{(K^2 - x^2)(K^2 - y^2)(K^2 - z^2)}{2K^4}\left[e^{\left(\frac{-x^2}{1+K}\right)} + e^{\left(\frac{-y^2}{1+K}\right)}\right], \ i \in \{\mathrm{X, Y, Z}\}, \quad (10)$$

where T_i are three control parameters for analytical transformation in the axis direction. For rotational transformation, the following function was chosen:

$$f_{\varphi_Z}(x, y) = \frac{(K - |x|)(K - |y|)(x + y)}{K^3},$$ (11)

$$Rot_Z = \begin{bmatrix} x - [x \cdot cos(R_Z \cdot f_{\varphi_Z}) - y \cdot sin(R_Z \cdot f_{\varphi_Z})] \\ y - [y \cdot sin(R_Z \cdot f_{\varphi_Z}) + y \cdot cos(R_Z \cdot f_{\varphi_Z})] \\ z \end{bmatrix},$$ (12)

where R_Z is control parameter for analytical rotation by corresponding axis. The remaining 2 parameters (R_X, R_Y) are similarly defined. Figs. 2–3 show the behavior of the functions for a particular case.
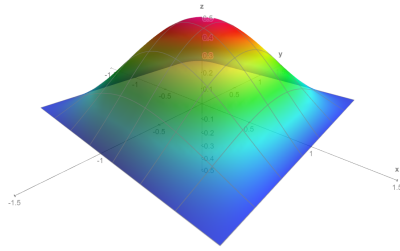
| Fig. 2. Translation function | Fig. 3. Rotation function | Fig. 4. Basic pattern |
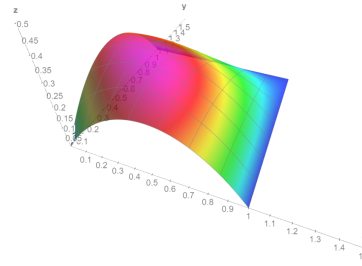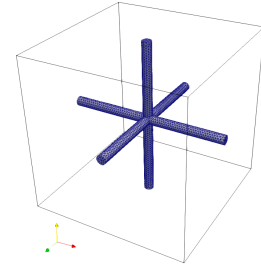
A simple cross-patern was chosen for development purposes, Fig. 4. Numerical and analytic methods guide this mesh in the following way, the resulting geometry of which can be seen in Fig. 5.
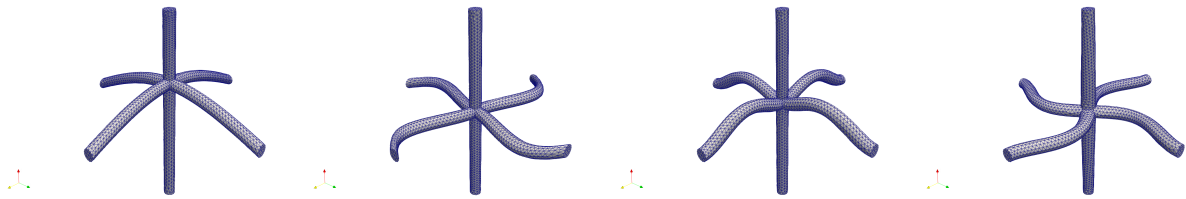
(a) Analytic translation   (b) Analytic rotation   (c) Numerical translation   (d) Numerical rotation

Fig. 5. Deformation of basic pattern by individual methods

5. Results

Homogenized values obtained for specific geometries using different methods. Fig. 6 illustrates the homogenized values of E_{22} for 4 different types of transformation: analytic (translation and rotation), see Fig. 6a,b,e,f, and numerical (translation and rotation), see Fig. 6c,d,g,h.

We obtained similar homogenized results by analytical and numerical methods, but the analytical approach provides a wider range of geometry control and is less computationally intensive. The results show that using the developed methods we are able to control the material properties of the metastructures using 6 parameters.

(a) Analytic translation   (b) Analytic rotation   (c) Numerical translation   (d) Numerical rotation

(e) Analytic translation   (f) Analytic rotation   (g) Num. translation   (h) Num. rotation
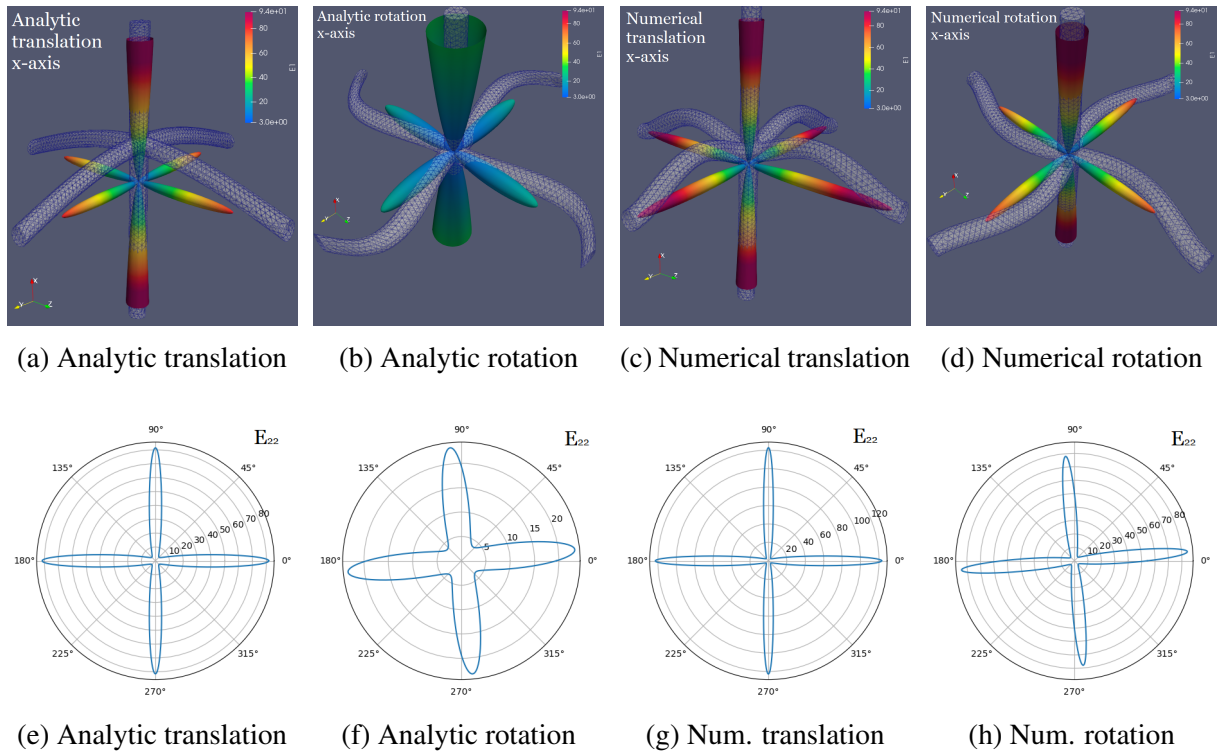
Fig. 6. Homogenised values of E_{22} for the corresponding geometries (spherical and polar)

6. Conclusions

Appropriate methods have been developed to quantify the elastic constants of the designed metamaterials and an effective method to control their geometry. These assumptions are essential for further optimization of metamaterials using neural networks.

Acknowledgements

References

[1] Henyš, P., Čapek, L., Březina, J., Comparison of current methods for implementing periodic boundary conditions in multi-scale homogenisation, European Journal of Mechanics-A/Solids 78 (2019) No. 103825.

[2] Wang, C., Gu, X., Zhu, J., Zhou, H., Li, S., Zhang, W., Concurrent design of hierarchical structures with three-dimensional parameterized Lattice microstructures for additive manufacturing, Structural and Multidisciplinary Optimization 61 (3) (2020) 869-894.

On a stepladder model walking (with and without a decorator)

P. Polach[a], R. Prokýšek[b], Š. Papáček[c]

[a] *Research and Testing Institute Plzen Ltd., Tylova 1581/46, Plzeň, Czech Republic*
[b] *The Department of Mechanics, Biomechanics and Mechatronics, CTU, 160 00 Prague, Czech Republic*
[c] *The Czech Academy of Sciences, Institute of Information Theory and Automation, Pod vodárenskou věž 4, 182 08 Prague, Czech Republic*

1. Introduction

This work is related to our previous studies on underactuated biped robot models and has been motivated by the need to implement the previously developed sensor and control algorithms for the real-time movement of the laboratory walking robot, designed and built at the Department of Control Theory of the Institute of Information Theory and Automation of the Czech Academy of Sciences [1, 6, 7].

Underactuated biped robots with an upper body form a subclass of legged robots, see, e.g., [4] for a review on the control of underactuated mechanical systems and [2] for a study of an asymptotically stable walking for biped robots. It is obvious that in general, the walking control of underactuated walking robots is a more challenging problem than walking control of fully actuated walking robots.

As follows, we examine the well-known mechanical system of the stepladder model with and without a decorator, whose role is substituted by an external inertial force according to the D'Alembert principle. It is well known, that stepladder walking is possible due to the periodic movement (pendulating) of an operator – decorator[1] The rigorous dynamical analysis of stable cyclic walking of a class of stepladder models is presented in the next section.

2. Stepladder model formulation

The stepladder model with, respectively without a decorator is schematically depicted in Fig. 1. It is similar to the so-called Compass gait biped walker (with neither ankles nor knees), which is the simplest underactuated mechanical system hypothetically able to walk, see, e.g., [3] and references therein. This three or two-link planar mechanism with two rigid legs, each one with a lumped mass (no inertia), connected at the revolute (hip) joint, is alternatively called the Acrobot (with or without an upper body). It has, in general, four or five degrees of freedom in 2-dimensional space. More precisely, using the notation introduced in Fig. 1: There are 2 degrees for the angles of two legs of equal length (θ_1, θ_2), 2 degrees for the position of hips (position of the center of mass O_H, and one degree of freedom for the angle θ_3 describing the angular position of a decorator (an upper body), respectively.

There is an important difference between the general Compass gait biped and stepladder walking: While the Compass gait usually switches the legs, stepladder walking resides in preserving the leg order.

---

[1] One curious case of a 'self-induced' stepladder walking on a sloped plane is reported in YouTube (https://www.youtube.com/watch?v=v5yRvop08t0).
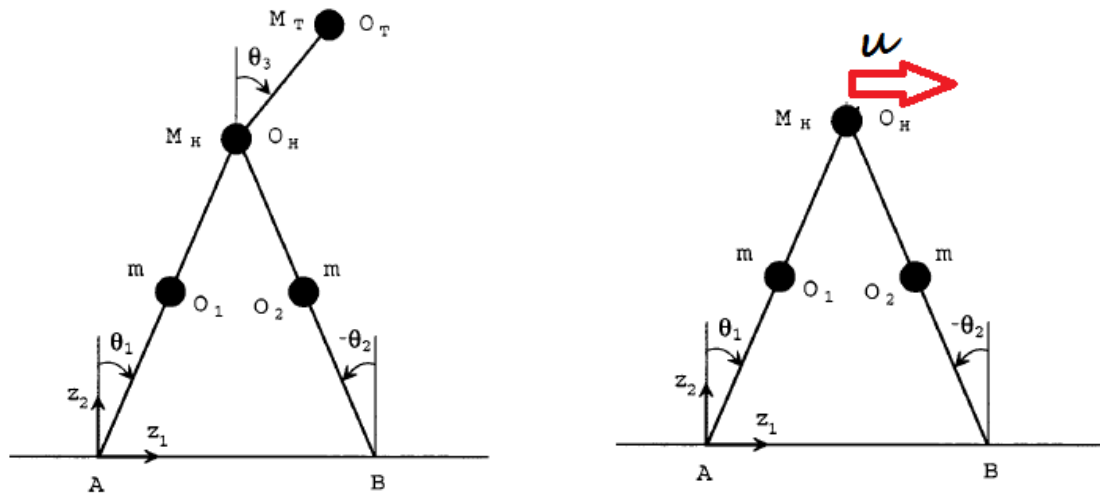
Fig. 1. (left) The stepladder model (with a decorator), (right) Compass gait biped walker (Acrobot) with external force applied on hip joint: parameters and coordinates

Next, we set up the system model for both the swing phase of the motion and the impact model, which has to be applied when both legs touch the ground.

First, the swing phase of the motion where either the forward or backward leg touches the ground: a dynamic equation, in the well-known form for mechanical systems obtained from the usual Lagrangian approach, follows

$$\mathbf{D}(\theta)\ddot{\theta} + \mathbf{C}(\theta,\dot{\theta})\dot{\theta} + \mathbf{G}(\theta) = \mathbf{u}, \tag{1}$$

where $\mathbf{D}(\theta)$ is the inertia matrix, $\mathbf{C}(\theta,\dot{\theta})$ contains Coriolis and centrifugal terms, $\mathbf{G}(\theta)$ contains gravity terms, $\mathbf{u}$ stands for the vector of external (and inertial) forces, θ, and $\dot{\theta}$ are 3-dimensional configuration vectors of angular positions and velocities, $\ddot{\theta}$ is the vector of accelerations.

Second, the very short, phase of the motion for the velocities just before (x^-) and just after (x^+) the impact, is governed by the impact model. The result of solving the corresponding equations yields an expression

$$x^+ = \Delta x^-, \tag{2}$$

which should then be used to re-initialize the model (1) with appropriate use of coordinates since the former swing leg is now in contact with the ground. The function Δ and other details are given, e.g., in [2].

Finally, the overall model can be expressed as a system with impulse effects. Striving for a (stable) cyclic walking, four consecutive time intervals can be distinguished:

1. Swing phase A: Point A is moving forward, and the governing equations are (1) with suitable initial conditions (of type A).
2. Impact A: Point A is touching ground, the governing equations are (2) with a suitable form of the compact operator (of type A).
3. Swing phase B: Point B is moving forward, and the governing equations are (1) with suitable initial conditions (of type B).
4. Impact B: Point B is touching the ground, the governing equations are (2) with a suitable form of the compact operator (of type B).

Two variants of the stepladder model are derived. The more complex one with a decorator (an upper body) with an autonomous movement $\theta_3 = f(t)$, and the simpler one, for the special form of the external force $u = g(t)$. The implementation is made in the computer algebra system *Mathematica.*

3. Conclusion

In this work, we formulated a model for stable cyclic walking for the stepladder with and without an operator. We used the idea of substituting the dynamic effects of the operator with the inertial forces applied to the revolving joint connecting both legs (center of mass O_H).

Now, encouraged by the successful implementation of the model, we are open to the possibility of running a study on the stability of cyclic walking for different values of model parameters and the operator movement. Here, the expected result is to find in some sense optimal (e.g., minimizing the energy input) stepladder walking regime.

Acknowledgments

References

[1] Anderle, M., Čelikovský, S., On the controller implementation in the real underactuated walking robot model, Proceedings of the 12th Asian Control Conference (ASCC), Kitakyushu, Fukuoka, Japan, 2019, pp. 91-99.

[2] Grizzle, J. W., Abba, G., Plestan, F., Asymptotically stable walking for biped robots: Analysis via systems with impulse effects, IEEE Transactions on Automatic Control 46 (1) (2001) 51-64.

[3] Jadlovská, A., Jadlovská, S., Koska, L., Modeling, Analysis and control of the compass gait biped robot and extensions: A review, Acta Electrotechnica et Informatica 21 (4) (2021) 14-22.

[4] Krafes, S., Chalh, Z., Saka, A., A review on the control of second order underactuated mechanical systems, Complexity 2018 (2018) NO. 9573514.

[5] McGeer, T., Passive dynamic walking, International Journal of Robotics Research 9 (2) (1990) 62-82.

[6] Polach, P., Anderle, M., Papáček, Š., On the design and modeling of a trainer for the underactuated walking robot without ankles, Proceedings of the 27/28th International Conference Engineering Mechanics 2022, Milovy, Czech Republic, Institute of Theoretical and Applied Mechanics of the CAS, v. v. i., 2022, pp. 309-312.

[7] Polach, P., Papáček, Š., Anderle, M., Development of underactuated biped robot models with upper body, Book of Abstracts of the 11th ECCOMAS Thematic Conference on Multibody Dynamics, IDMEC – Instituto Superior Técnico, Lisbon, Portugal, 2023, p. 210.

Optimization of wheel suspension geometry using a genetic algorithm

J. Rágulík[a], M. Sivčák[a]

[a]*Department of Applied Mechanics, Faculty of Mechanical Engineering, Technical University of Liberec, Studentská 2, 461 17 Liberec, Czech Republic*

1. Introduction

This work deals with the optimization of the geometry of the independent wheel suspension, which is part of an experimental chassis with air springs. These springs, specifically the pressure inside their bellows, are controlled by deep reinforcement learning (DRL) algorithm. This chassis platform does not allow turning and driving, it is used exclusively for the research and application of DRL algorithms to control non-linear suspension elements on a system with multiple degrees of freedom. The geometry of the chassis, specifically the length and position of the individual arms, is optimized by a genetic algorithm (GA) in order to achieve the smallest possible displacement of the bottom edge of the tire and appropriate tilting of the wheel. Manufacturing possibilities are taken into account during the optimization, since the assembled suspension consists of steel rods and components produced by 3D printing technology, which can only have limited dimensions.

2. Genetic algorithms

Unlike traditional optimization techniques that rely on mathematical derivations and gradient-based methods, GA are inspired by the principles of natural selection and evolution. They work by evolving a population of potential solutions over multiple generations, gradually improving the quality of solutions until an optimal or near-optimal solution is found. GA are well-suited for finding global optima in complex and multi-modal search spaces but can be computationally expensive, especially for large-scale problems [1]. The following paragraph will describe the operation of the GA, which is also shown in the (Fig. 1).

The first step is initialization, in which an initial generation of randomly generated solutions is created. The second step is the evaluation of the solutions, i.e., the calculation of the fitness value of all solutions in the population, after which the given number of solutions with the highest fitness values is selected in the third step during selection. The fitness function is a crucial element of a genetic algorithm. It quantifies how well a particular solution performs with respect to the optimization problem's objectives. The higher the fitness value, the better the solution. The fourth step is the crossover of the solutions selected in the previous step, and mutation is applied to them in the fifth step, i.e., random percentage changes of the individual solutions. It adds diversity to the population and prevents premature convergence. In the sixth step, a new generation of solutions is created, which may include parents, offspring, or a combination of both. Then steps 2 to 6 are repeated until the desired fitness value is reached.

Setting appropriate parameters, such as population size and mutation rates, can be challenging and may require experimentation. If these parameters are set incorrectly, GAs may converge to suboptimal solutions [2].
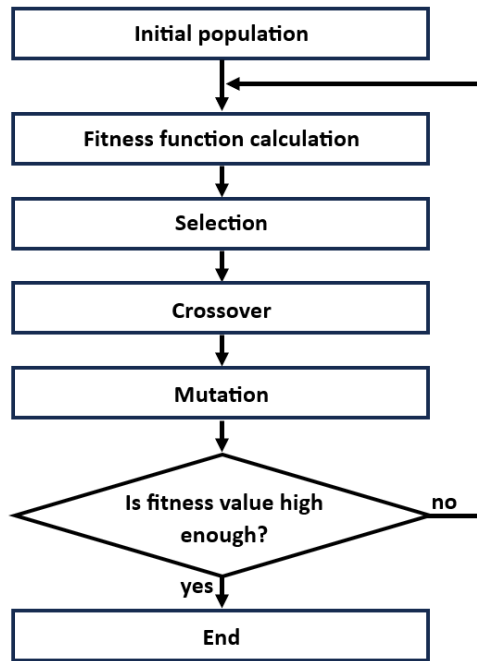
Fig. 1. Flowchart of the genetic algorithms

3. Wheel suspension geometry

The geometry of a wheel suspension system refers to the lengths and positions of various components, such as control arms, springs, shock absorbers, spindles and wheel hubs. Proper suspension geometry is crucial for achieving the desired balance between ride comfort and handling stability. It plays a pivotal role in determining a vehicle's ride quality, handling characteristics, and overall performance. All optimized dimensions are shown in the diagram (Fig. 2). These are the length of the upper and lower arms, the length of the spindle and the relative position of the bearings that ensure the connection of the suspension to the vehicle frame.
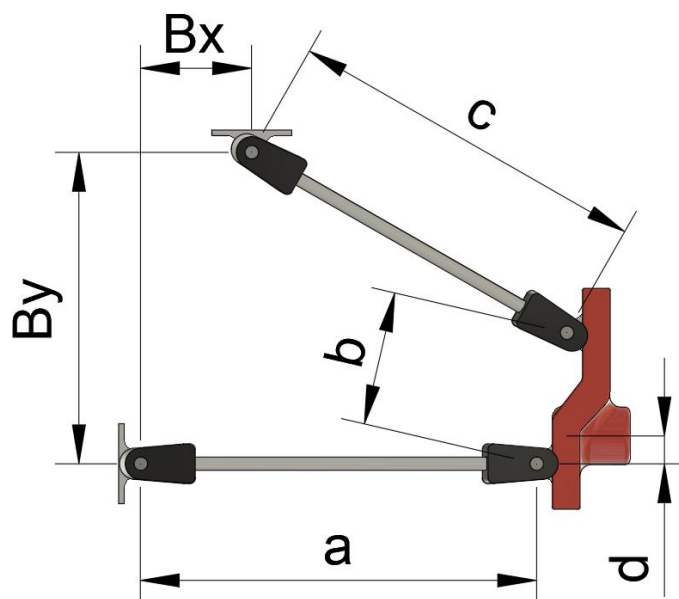
Fig. 2. Wheel suspension dimensions

The aim of the optimization is to achieve the smallest possible displacement of the bottom edge of the tire and appropriate tilting of the wheel. The resulting suspension must allow the installation of an air spring, which will be located between the upper arm and the frame. Tilting of the upper arm with respect to the height of the spring in its working area is 25 to 35 degrees to the horizontal part of the frame. In this angle range, the horizontal displacement of the lower edge of the tire will therefore be required to be minimised.

The relationship for calculating the vertical displacement of the lower edge of the tire was obtained by solving a vector loop with the angle between the frame and the upper arm as the independent variable.

4. Results

The parameters of the GA have been optimized to achieve a minimum vertical displacement of the bottom edge of the tire. Experimenting with these parameters, it was found that a sufficient size of the population is 100, and its changes do not have a noticeable effect on the course of optimization, unless there was a substantial reduction. Increasing the size of the population increases the computational complexity of the optimization, which would not be a problem given the speed of the optimization in the order of seconds. The parameters that had an influence on the course are crossover and mutation rates. The crossover rate indicates the probability of two solutions crossing over, and the mutation rate indicates the probability of mutation of a solution. Crossover rate was set to 0.9 and mutation rate was set to 0.05. Increasing these parameters encourages exploration, while lowering them favours exploitation. In this case, the set parameters ensure sufficient exploration and at the same time prevent convergence to a sub-optimal solution.

The most important aspect of genetic algorithm optimization is the use of an appropriate fitness function, which was created in such a way that the optimization process is terminated when the lower edge of the wheel moves less than 1 mm. A higher value of the fitness function means a better solution, so the inverse of the deviation was used. A value corresponding to the desired displacement was calculated, and when it was reached, the best solution from the current population was declared as the result.

The resulting dimensions achieved with this fitness function could not be realized, therefore the fitness function was supplemented with a member that penalizes the algorithm if the length of the upper arm does not allow the installation of an air spring. Furthermore, the initial population was initialized so that the length of the upper arm is a random number from the interval of values at which spring installation is possible. The algorithm adapted in this way provides a resulting geometry that is feasible and at the same time achieves the desired displacement of the bottom edge of the wheel. The obtained dimensions were rounded to whole millimetres and according to this geometry, the wheel spindle, red component in the (Fig. 3), was created using 3D printing technology and the steel bars that make up the wheel suspension arms were cut.

Wheel displacement calculated for rounded optimized dimensions is 0.5 mm. A displacement of 1.4 mm was measured for the assembled suspension. For the purposes for which this experimental chassis is made, such displacement is very acceptable.

The measurement of the distance of the lower edge of the wheel was done with a laser length sensor optoNCDT 1420, and the angle between the frame and the upper arm was set with a digital protractor INSIZE 2179-360. The resulting deviation is mainly caused by the inaccuracy of the dimensions produced on the 3D printer.
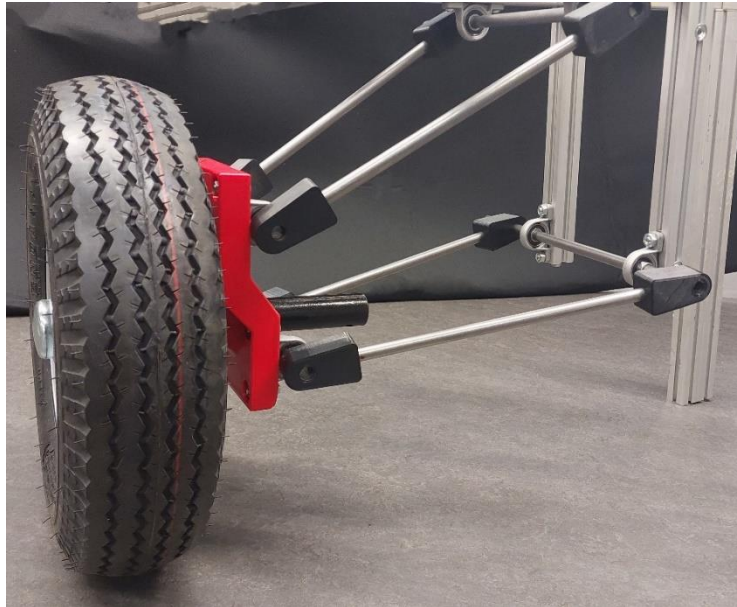
Fig. 3. Assembled wheel suspension

Acknowledgement

References

[1] Bartz-Beielstein, T., Branke, J., Mehnen, J., Mersmann, O., Overview: Evolutionary algorithms, SchriftenreiheCIplus Band, 2015.

[2] Goldberg, D. E., Genetic algorithms in search, optimization and machine learning, Addison-Wesley Professional, 1989.

Influence of static unbalance on rotors with various journal bearing types

J. Rendl[a], M. Byrtus[a], Š. Dyk[a], L. Smolík[a]

[a]*NTIS – New Technologies for the Information Society, Faculty of Applied Sciences, University of West Bohemia, Univerzitní 8, 301 00 Plzeň, Czech Republic*

A mathematical model of the rotor operating at angular velocity ω and supported on the journal bearing is written in the following form:

$$\begin{bmatrix} m & 0 \\ 0 & m \end{bmatrix} \begin{bmatrix} \ddot{y}_J \\ \ddot{z}_J \end{bmatrix} = \begin{bmatrix} -mg \\ 0 \end{bmatrix} + \begin{bmatrix} F_{hd,y} \\ F_{hd,z} \end{bmatrix} + \begin{bmatrix} \Delta mE\, \omega^2 \sin(\omega t) \\ \Delta mE\, \omega^2 \cos(\omega t) \end{bmatrix}, \tag{1}$$

where g is the gravitational acceleration of applied gravity load, $F_{hd,y}, F_{hd,z}$ are the components of hydrodynamic force and ΔmE is the rotor static unbalance. Employing substitutions

$$\tau = \omega t, \quad \bar{y}_J = \frac{y_J}{c}, \quad \text{and} \quad \bar{z}_J = \frac{z_J}{c}, \tag{2}$$

where τ stands for non-dimensional time and $\bar{z}_J$ and $\bar{y}_J$ are non-dimensional coordinates of the journal centre related to radial bearing clearance c, allows to transform the equations of motion into the dimensionless form which is more suitable for deeper numerical analyses. The equations of motion can be further rewritten as

$$\begin{bmatrix} \bar{y}_J'' \\ \bar{z}_J'' \end{bmatrix} = -\frac{1}{\bar{\omega}^2} \begin{bmatrix} 1 \\ 0 \end{bmatrix} + \frac{1}{mc\omega^2} \begin{bmatrix} F_{hd,y} \\ F_{hd,z} \end{bmatrix} + \begin{bmatrix} A_u \sin\tau \\ A_u \cos\tau \end{bmatrix}, \tag{3}$$

where the temporal derivatives, i.e., $\dot{\square} = \square'\omega$ etc., where $\dot{\square} = \frac{d}{dt}\square$ and $\square' = \frac{d}{d\tau}\square$, are held and the following non-dimensional parameters are defined:

$$\bar{\omega} = \omega\sqrt{\frac{c}{g}}, \quad A_u = \frac{\Delta mE}{mc}. \tag{4}$$

The design parameters of the rotor-bearing system are summarised in the non-dimensional parameter λ based on [3]

$$\lambda = \frac{\mu R L^3}{mc^{2.5}g^{0.5}}, \tag{5}$$

where R is the inner shell bearing radius and L is the bearing length.

The presented model (3) of the rotor-bearing model was analysed by the numerical continuation method employed in the open-source software MATCONT [1]. Using this method allows for tracing solution branches [2] of limit cycle oscillation (LCO) solution based on chosen bifurcation parameters $\bar{\omega}, A_u$, checking the stability criteria and revealing bifurcation points such as period-doubling (PD) and Neimark-Sacker (NS) bifurcation points. The obtained results (adopted from [3]) for two systems with various λ parameters of cylindrical journal bearing and
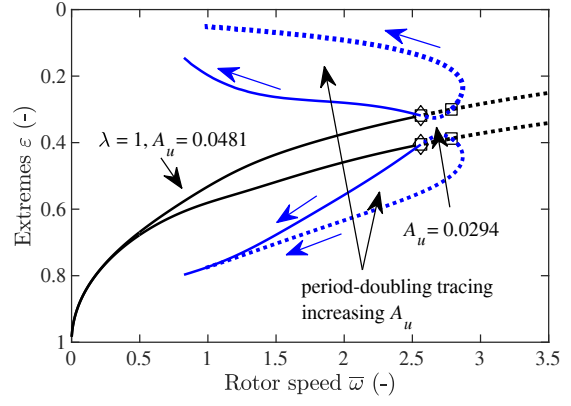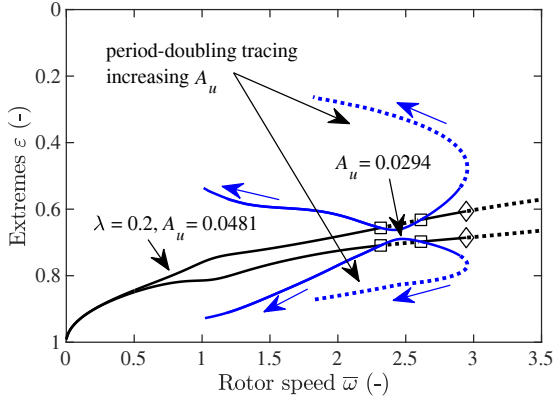
Fig. 1. Bifurcation diagram of the system response: synchronous LCO branches (stable '—', unstable '···'); codim-2 branch of PD bifurcation points in $(\overline{\omega}, A_u)$ space (stable '—', unstable '···'); NS bifurcation point '◇', PD bifurcation point '□'
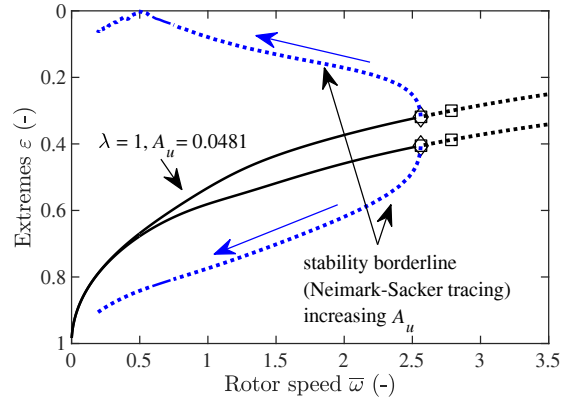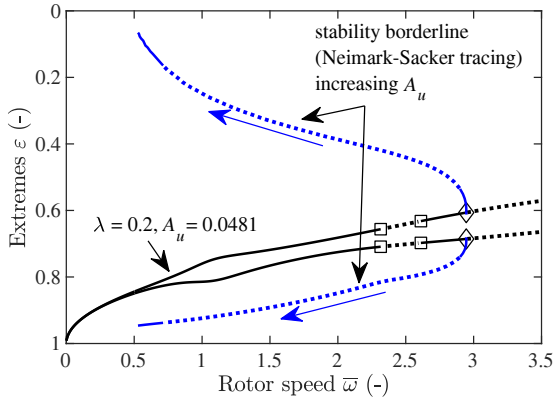
Fig. 2. Bifurcation diagram of the system response: synchronous LCO branches (stable '—', unstable '···'); codim-2 branch of NS bifurcation points in $(\overline{\omega}, A_u)$ space (stable '—', unstable '···'); NS bifurcation point '◇', PD bifurcation point '□'

tracing the bifurcation points for varying static unbalance A_u are depicted in Figs. 1–2. The hydrodynamic force is calculated based on the infinitely short bearing theory. The system stability is globally lost after crossing the NS bifurcation point. Moreover, there is an area between PD points when the 1-periodic stable solution is locally lost and new 2-periodic solution is born.

Acknowledgement

References

[1] Dhooge, A., Govaerts, W., Kuznetsov, Y. A., MATCONT: A MATLAB package for numerical bifurcation analysis of ODEs, ACM Transactions on Mathematical Software 29 (2) (2003) 141-164.

[2] Nayfeh, A. H., Balachandran, B., Applied nonlinear dynamics, John Wiley & Sons, 1995.

[3] Rendl, J., Byrtus, M., Dyk, Š., Smolík, L., Subcritical behaviour of short cylindrical journal bearings under periodic excitation, Nonlinear Dynamics 111 (2023) 9957-9970.

Acoustic streaming in homogenized deformable porous media

E. Rohan[a], F. Moravcová[b]

[a]*Department of Mechanics, Faculty of Applied Sciences, University of West Bohemia, Univerzitní 8, 301 00 Plzeň, Czech Republic*
[b]*NTIS – New Technologies for the Information Society, Faculty of Applied Sciences, University of West Bohemia,
Univerzitní 8, 301 00 Plzeň, Czech Republic*

1. Introduction

In microfluidic devices, nonlinear acoustic phenomena, namely the acoustic radiation, acoustic streaming are employed to manipulate particles and actuate fluid flow. These principles have attracted much interest of the research focused on developing new tissue engineering technologies since the acoustic wave are highly biocompatible, providing a non-contact controlable handle to manipulate bioparticles, or cells.

This paper deals with the acoustic streaming (AS) in periodic poroelastic media, see [2] where the AS in a bulk fluid was studied in response to vibrating walls of a channel. The fluid-structure interaction problem is imposed in elastic scaffolds. To capture the acoustic streaming phenomenon in response to propagating acoustic wave, nonlinearities originating in the divergence of the Reynolds stress, the advection acceleration term in the Navier Stokes equation, and the nonlinearity generated by deforming pore geometry must be retained. The perturbation with respect to a small parameter proportional to the inverse Strouhal number is applied. This yields the first and the second order sub-problem enabling to linearize the Navier-Stokes equations governing the barotropic viscous fluid dynamics in deforming scaffolds. Subsequent treatment by the asymptotic homogenization leads to a two scale problem where the macroscopic model provides the vibro-acoustic analysis in the Biot-type medium. It yields the AS source term for the second order problem which attains the form of the Darcy flow.

2. Micromodel of the heterogeneous structure

Flow of the barotropic viscous fluid (parameterized by the 1st and the 2nd viscosities, μ_f and η_f, and the reference sound speed c_0) is described by the velocity, pressure and density $(\boldsymbol{v}^f, p, \rho^f)$ satisfying the Navier-Stokes equations in the pores Ω_f. The fluid interacts with the deforming solid skeleton Ω_s, such that its displacement field $\boldsymbol{u}$ is governed by the elastodynamic (wave) equation involving the elasticity tensor $\mathbb{D}_s$ and the density ρ_s. A nonlinear problem is constituted by the following system of equations:

$$
\begin{aligned}
\rho_s \partial_{tt}^2 \boldsymbol{u} - \nabla \cdot \mathbb{D}_s \boldsymbol{e}(\boldsymbol{u}) &= 0 \quad \text{in } \Omega_S , \\
\rho_f \left(\partial_t \boldsymbol{v}^f + \boldsymbol{v}^f \cdot \nabla \boldsymbol{v}^f \right) &= -\nabla p + \nabla \cdot \mathbb{D}^f \nabla \boldsymbol{v}^f + \boldsymbol{f}^f \quad \text{in } \Omega_f , \\
\partial_t \rho_f + \nabla \cdot (\rho \boldsymbol{v}^f) &= 0 \quad \text{in } \Omega_f
\end{aligned}
\tag{1}
$$

with the state equation $p = c_0^2 \rho_f + c_0 c_0' (\rho_f)^2$ and the standard continuity of the stress tractions and velocities considered on the interface Γ_{fs},

$$
\dot{\boldsymbol{u}} = \boldsymbol{v}^f, \quad \text{and} \quad \boldsymbol{n} \cdot \mathbb{D}_s \boldsymbol{e}(\boldsymbol{u}) = \boldsymbol{n} \cdot (\mathbb{D}_f \boldsymbol{e}(\boldsymbol{v}^f) - p\boldsymbol{I}) \quad \text{on } \Gamma_{fs} .
\tag{2}
$$

It is of advantage to introduce a smooth extension $\widetilde{\boldsymbol{u}}^f$ of the solid displacements to Ω_f, such that $\boldsymbol{v}^f$ can be expressed using the seepage $\boldsymbol{w}$, as follows: $\boldsymbol{v}^f = \boldsymbol{w} + \widetilde{\boldsymbol{u}}^f$, whereby $\boldsymbol{w} = 0$ on Γ_{fs}.

Following the approach suggested by Nyborg [1] based on the successive approximations, the nonlinear problem represented by (1)–(2) can be decomposed into 2 subproblems:

- 1st order: Fast time–periodic dynamics: acoustic waves propagating in the two-phase medium, $(\boldsymbol{u}, \boldsymbol{w}_1, p_1)$ satisfy (with boundary conditions imposing an incident acoustic wave; recall the "tilde" notation denoting the displacement extension to Ω_f)

$$
\begin{aligned}
\rho_s \partial_{tt}^2 \boldsymbol{u} - \nabla \cdot \mathbb{D}_s \boldsymbol{e}(\boldsymbol{u}) &= 0 \quad \text{in } \Omega_s, \\
\partial_t \rho_1 + \rho_0 \nabla \cdot (\boldsymbol{w}_1 + \widetilde{\boldsymbol{u}}^f) &= 0 \quad \text{in } \Omega_f, \\
\rho_0(\partial_t \boldsymbol{w} + \partial_t \widetilde{\boldsymbol{u}}^f) + \nabla p_1 - [\mu \nabla^2 + (\mu/3 + \eta)\nabla(\nabla \cdot)](\boldsymbol{w}_1 + \widetilde{\boldsymbol{u}}^f) &= 0 \quad \text{in } \Omega_f, \\
p_1 &= c_0^2 \rho_1 \quad \text{in } \Omega_f .
\end{aligned}
\tag{3}
$$

- 2nd order: Slow flow streaming in Ω_f described by $(\boldsymbol{w}_2, p_2.\rho_2)$ with given $\boldsymbol{v}_1 := \boldsymbol{w}_1 + \widetilde{\boldsymbol{u}}^f$,

$$
\begin{aligned}
\partial_t \bar{\rho}_2 + \rho_0 \nabla \cdot \bar{\boldsymbol{w}}_2 &= -\nabla \cdot \overline{(\rho_1 \boldsymbol{v}_1)}, \\
\rho_0 \partial_t \bar{\boldsymbol{w}}_2 + \nabla \bar{p}_2 - \mu \nabla^2 \bar{\boldsymbol{w}}_2 + (\mu/3 + \eta)\nabla(\nabla \cdot \bar{\boldsymbol{w}}_2) &= -\rho_0 \left(\overline{(\boldsymbol{v}_1 \cdot \nabla)\boldsymbol{v}_1} + \overline{\boldsymbol{v}_1(\nabla \cdot \boldsymbol{v}_1)} \right), \quad (4) \\
\bar{p}_2 &= c_0^2 \bar{\rho}_2 + c_0 c_0' \overline{(\rho_1)^2},
\end{aligned}
$$

where all the "over-bar" designates the time-average over the time period of the acoustic waves described by the 1st order problem.

3. Homogenized model

We consider periodic porous structures, such that the characteristic pore scale is proportional to a small parameter $\varepsilon = \ell/L$ defined by the ratio of the micro- and macroscopic characteristic lengths, denoted by ℓ and L, respectively. The periodic structures of the poroelastic medium are generated by the so-called representative periodic cell (RPC) $Y = Y_s \cup Y_f \cup \Gamma_{fs}^Y$ which consists of the solid and fluid parts correspondingly to the decomposition of Ω, see Fig. 1. The homogenization procedure applied to derive an effective model of the two-phase medium consists in the asymptotic analysis $\varepsilon \to 0$ of the micro-models (3) and (4) presented above, where all the unknowns and model parameters depending on the scale ε. Homogenization of (3) yields the standard Biot model of the poro-elastodynamics, cf. [3] For a given frequency ω, the acoustic waves are represented by the amplitudes $(\boldsymbol{u}_1^0, \boldsymbol{w}_1^0, p_1^0)$ which satisfy the following
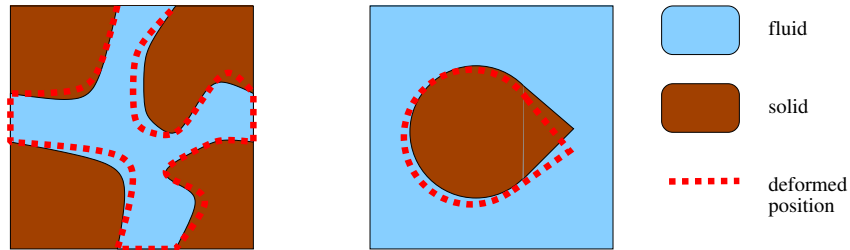
Fig. 1. The representative cells Y for the case of solid skeleton Y_s constituting a connected domain Ω_s^ε (left) and the case of suspended particles Y_s which can be rigid (right). In the latter case, the "suspension" can be realized due to a very thin (negligible) elastic network

set of equations which hold in Ω:

$$-\omega^2 \hat{r} \boldsymbol{u}_1^0 + \mathrm{i}\omega \boldsymbol{w}_1^0 - \nabla \cdot \left(\widehat{\mathbb{D}}^H \boldsymbol{e}_x(\boldsymbol{u}_1^0) - p_1^0 \widehat{\boldsymbol{B}}^H \right) = 0,$$

$$\mathrm{i}\omega \widehat{\boldsymbol{B}}^H : \boldsymbol{e}_x(\boldsymbol{u}_1^0) + \nabla \cdot \boldsymbol{w}_1^0 + \mathrm{i}\omega \widehat{M}^H p_1^0 = 0,$$

$$\boldsymbol{w}_1^0 + \widehat{\mathcal{K}}(\nabla_x p_1^0 - \omega^2 \omega^2 \boldsymbol{u}_1^0) = 0.$$

The effective coefficients $\widehat{\mathbb{D}}^H, \widehat{\boldsymbol{B}}^H, \widehat{M}^H$ and $\mathcal{K}$ are computed using the characteristic responses of the so-called cell problems solved in Y_s and Y_f. The dynamic permeability $\widehat{\mathcal{K}}$ depending on ω can be expressed in terms of eigenvalues $\{\eta_r\}_r$ and eigenfunctions $\{\boldsymbol{w}^r\}_r$ of the Stokes flow problem in Y_f.

In order to evaluate the AS source (force), the fluid velocity must be reconstructed at the microscopic level (for any $x \in \Omega$). For this, the decomposition using the extended velocity of the solid and the fluid seepage are employed, as follows

$$\boldsymbol{v}_1^{\mathrm{mic}} = \hat{\boldsymbol{w}}_1 + \widetilde{\dot{\boldsymbol{u}}_1^{\mathrm{mic}}}^f \quad \text{in the fluid } Y_f \times \Omega,$$

$$\dot{\boldsymbol{u}}_1^{\mathrm{mic}} = \dot{\boldsymbol{u}}_1^1 + \boldsymbol{\Pi}^{rs} e_{rs}^x(\dot{\boldsymbol{u}}_1^0) \quad \text{in the solid } Y_s \times \Omega$$

$$\text{with} \quad \dot{\boldsymbol{u}}_1^1 = \boldsymbol{\chi}^{rs} e_{rs}^x(\dot{\boldsymbol{u}}_1^0) + \boldsymbol{\chi}^P \dot{p}_1^0 \,,$$

where $\dot{\boldsymbol{u}}_1^1$ is the solid velocity corrector (the two-scale function defined in $Y_s \times \Omega$, being expressed in terms of $\boldsymbol{\chi}^{rs}$ and $\boldsymbol{\chi}^P$, the characteristic responses of the microstructure, i.e., the skeleton displacements with respect to the unit strain modes and the unit pore pressure, respectively. Further, $\boldsymbol{\Pi}^{rs} e_{rs}^x(\boldsymbol{u}_1^0)$ provides the affine displacement in Y due to the macroscopic strain $e_{rs}^x(\boldsymbol{u}_1^0)$. Then, the seepage velocity is expressed using the convolution integral with the kernel associated with the dynamic permeability through the eigenpairs $\{\eta_k, \boldsymbol{w}^k\}_k$ and $\boldsymbol{\beta}^k$ denoting the mean of $\boldsymbol{w}^k$ in Y_f, so that

$$\hat{\boldsymbol{w}}_1(t, y, x) = -\sum_k \rho_0^{-1} \int_0^t \hat{\alpha}_k \boldsymbol{w}^k(y) \otimes \boldsymbol{\beta}^k \exp\{-\eta_k(t - \tau)\} \boldsymbol{p}_1^{\mathrm{dyn}}(\tau, x) \mathrm{d}\tau \quad \text{in fluid}$$

$$\text{with} \quad \boldsymbol{p}_1^{\mathrm{dyn}} = \nabla_x \dot{p}_1^0 - \rho_s \ddot{\boldsymbol{u}}_1^0 \,.$$

The streaming source $\boldsymbol{S}$ (also called the "acoustic force") is defined by virtue of the 2nd ordered problem (4)

$$\boldsymbol{S}(\boldsymbol{v}_1^{\mathrm{mic}}) = (\hat{\boldsymbol{w}}_1 + \widetilde{\dot{\boldsymbol{u}}_1^{\mathrm{mic}}}^f) \cdot \nabla_y(\hat{\boldsymbol{w}}_1 + \widetilde{\dot{\boldsymbol{u}}_1^{\mathrm{mic}}}^f) + (\nabla_y \cdot \widetilde{\dot{\boldsymbol{u}}_1^{\mathrm{mic}}}^f)(\hat{\boldsymbol{w}}_1 + \widetilde{\dot{\boldsymbol{u}}_1^{\mathrm{mic}}}^f) \,.$$

Thus, in the limit, $\boldsymbol{S}(\boldsymbol{v}_1^{\mathrm{mic}})$ depends on the characteristic responses Ξ of the fluid and solid parts of the microstructure, and on the 1st order macroscopic response — the acoustic waves described by $\mathbf{U}(x, t) := (\ddot{\boldsymbol{u}}_1^0, e_{rs}^x(\dot{\boldsymbol{u}}_1^0), \dot{p}_1^0, \nabla_x \dot{p}_1^0)$. In general, the streaming force (acceleration) is defined by the mapping $\mathcal{F}_{AS} : (\Xi, \mathbf{U}) \mapsto \boldsymbol{S}$.

Homogenization of the 2nd order problem describing the AS in the fluid (obviously, no streaming in the solid) leads to the same result as the one obtained for the case of a rigid solid. Micro-response in Y_f is presented by the couple $(\boldsymbol{w}_2, p_2^1)$ satisfying

$$-\rho_0 \frac{\partial}{\partial t} \boldsymbol{w}_2 + \nabla_y \cdot (\bar{\mu} \nabla_y \otimes \boldsymbol{w}_2) - \nabla_y p_2^1 = \nabla_x p_2^0 + \rho_0 \boldsymbol{S}^*(\boldsymbol{v}_1^{\mathrm{mic}}),$$

$$\nabla_y \cdot \boldsymbol{w}_2 = 0 \quad \text{in } Y_f \,, \quad \boldsymbol{w}_2 = 0 \quad \text{on } \Gamma_{fs} \,.$$

This problem can be solved using the spectral decomposition, which leads to the same spectral problem as the one solved to solve the the 1st order problem. It enables to express the macroscopic "streaming source", velocity $\boldsymbol{w}^{AS}$ which constitutes the driving force in the AS equation governing the pressure field $\bar{p}_2^0$,

$$-\nabla_x \cdot \overline{\mathcal{K}} \nabla_x \bar{p}_2^0 = \nabla_x \cdot \boldsymbol{w}^{AS} \quad \text{in } \Omega.$$

As for the boundary conditions for $\bar{p}_2^0$ on $\partial\Omega$, clearly a fixed wall Γ_w of a waveguide yields $\boldsymbol{n} \cdot \overline{\mathcal{K}} \nabla_x \bar{p}_2^0 = 0$, whereas $\bar{p}_2^0 = 0$ can be considered on the open surfaces $\Gamma_o = \partial\Omega \setminus \Gamma_w$. In Fig. 2, the AS induced flow around the suspended rigid obstacles is reconstructed at two macroscopic positions $x \in \Omega$ of the waveguide.
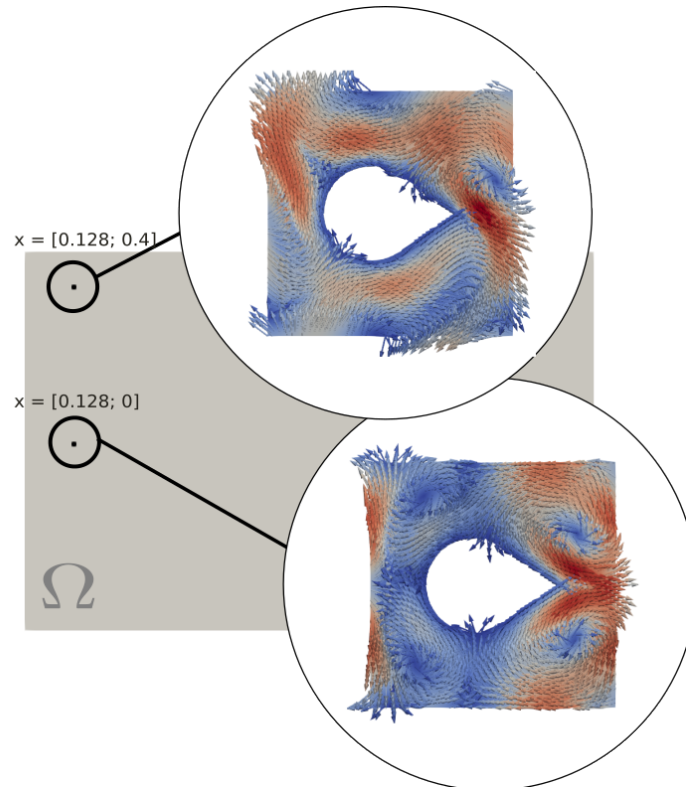
Fig. 2. Illustration of the AS in response to the acoustic waves in the fluid saturating rigid scaffolds (periodically distributed droplet-shaped obstacles). The AS flow is displayed in terms of streamlines (arrows) and $|\boldsymbol{w}_2|$ (color) at two macroscopic position $x \in \Omega$

Acknowledgement

References

[1] Nyborg, W. L., Acoustic streaming due to attenuated plane waves, Journal of the Acoustical Society of America 25 (1) (1953) 68-75.

[2] Moravcová, F., Rohan, E., Acoustic streaming of viscous fluid in a confining layer with vibrating walls – numerical simulations, Proceedings of the conference Computational Mechanics 2021, Srní, University of West Bohemia, 2021, pp. 157-160.

[3] Rohan, E., Naili, S., Homogenization of the fluid-structure interaction in acoustics of porous media perfused by viscous fluid, Zeitschrift für angewandte Mathematik und Physik 71 (2020) No. 137.

Crack growth prediction of mixer shaft

M. Růžička[a], K. Doubrava[a], M. Nesládek[a], J. Kuželka[a]

[a]*Department of Mechanics, Biomechanics and Mechatronics, Faulty of Mechanical Engineering, Czech Technical University in Prague; Technická 4, 166 07 Prague, Czech Republic*

1. Introduction

The subject of the assessment was a drive shaft of the horizontal chemical agitator mixer, which is used to produce polypropylene powder. The scheme of the equipment as well as the beam model of the assembly is depicted in Fig. 1 (left). The Zapex® gear coupling is mounted with the keyed joint connection on the agitator drive shaft. During operation, this joint proved to be a critical point of the structure and showed the appearance of fatigue cracks and insufficient service life. A detail of the shaft with a keyed joint and the area of an initiated crack from the keyway is shown in Fig. 1 (right) [2]. The goal of the analysis was to predict the crack rate of this damage under operating conditions and safe life of the shaft.
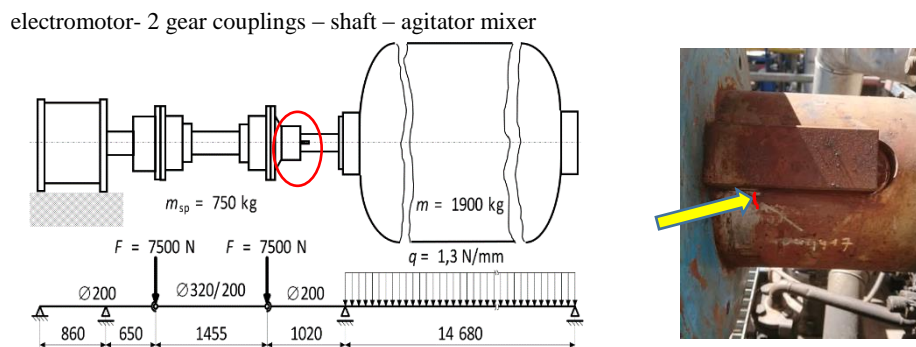
Fig. 1. The drive assembly of the mixer as well as the beam model of the assembly (left) and detail of the shaft with the keyed joint and the area of the initiated crack from the keyway (right)

2. Experimental analysis realized on the agitator mixer equipment

First, a strain-gauge analysis on the shaft was performed with the aim to obtain the nominal bending and shear strains and stresses, as well as the local strains near the found crack tip, see Fig. 2. These strain-gauge measurements were realized on four different power input levels. Mean strains and stress levels as well as amplitudes/ranges were averaged from measured time histories to evaluate the calibration lines between electric power input and nominal or local strains and stresses.

The correlation relationship between the long-time monitored electrical power input of the electromotor against the nominal normal bending stress and the shear stress on the agitator shaft is depicted in Fig. 3. It has been shown that these dependencies could be linearized and can be used to calculate bending and shear stresses for archived or currently acquired operational records power input of the electromotor.

Fig. 2. The scheme of the location of the installed strain gauges (left) and detail of the strain gauge rose at the crack tip (right)
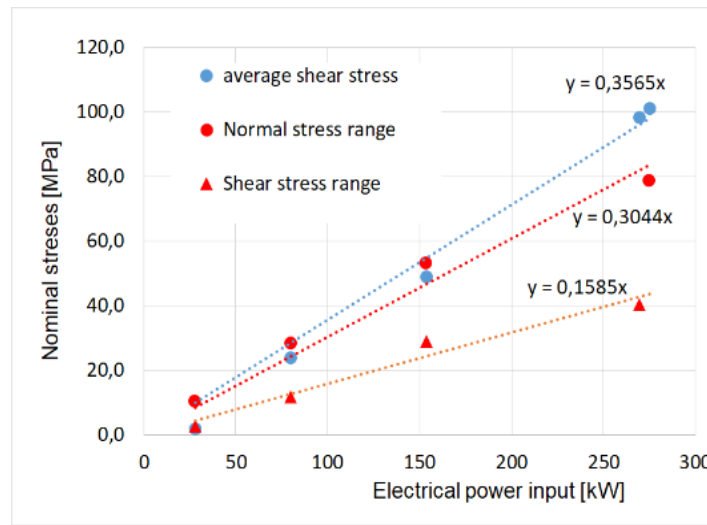
Fig. 3. Calibration lines: dependency between the electro motor power input and nominal normal bending and shear stresses on the shaft

3. Analytical and numerical analysis

Second, the FEM calculations on keyed joint connection model was performed to determine the stress concentration factors as well as crack length correction functions. These functions were subsequently used for an analytical calculations of stress intensity factors (SIF) *K* serving as a basis for the analytical crack growth models for a residual life prediction. Fig. 4 (right) shows the FE models of the keyed joint connection with selected crack length from the reconstructed geometry of the crack front in successive steps according to fractographic analysis. The SIF were calculated during cracks numerical propagation to determine the SIF correction functions $f_{K_i}\left(\frac{a}{d}\right) = \frac{K_i}{\sigma\sqrt{\pi a}}$ for the analytical predictions calculations. All three crack loading modes *I, II* and *III* were taken into account and correction functions were calculated from the relations

$$f_{K_i}\left(\frac{a}{d}\right) = \frac{K_i}{\sigma\sqrt{\pi a}}, \qquad i = I, II, III, \tag{1}$$

where *a* is the crack length, *d* is the shaft diameter and σ is nominal bending or shear stress.

The resulting range value of the stress intensity factor taking into account all three crack loading modes was determined according the relation

$$\Delta K_{eff} = \sqrt{\Delta K_I{}^2 + \Delta K_{II}{}^2 + \Delta K_{III}{}^2/(1-\nu)}. \tag{2}$$

181

Fig. 4. The fractographic reconstruction of the crack front in different damage time and FEM model geometry for selected crack lines for calculation of the SIF and geometric correction functions [2]

Finally, the residual fatigue life analysis was done according to the Paris-Erdogan, Klesnil-Lukáš and NASGRO crack growth models [3]. The type of model depends on the form of the function g in the crack growth equation

$$v = \frac{da}{dN} = g(\Delta K_{eff}).$$ (3)

Material parameters of these models were investigated for the used material (36NiCrMo16 steel) experimentally on the small specimens [1]. For crack propagation studies, the NASGRO model according the next equation (4) with the following experimentally determined parameters was finally chosen, see Table 1

$$v = v = C(\Delta K_{eff})^n \frac{\left(1 - \frac{\Delta K_{th}}{\Delta K}\right)^p}{\left(1 - \frac{K_{max}}{K_c}\right)^q}.$$ (4)

Table 1. NASGRO model equation parameters

C	n	p	q	ΔK_{th}	K_0	ΔK_c
	-	-	-	MPa√m	MPa√m	MPa√m
1.90E-11	2.7	0.85	0.5	8.94	4.62	110

Fig. 5 (top) shows the time history of the electrical power input of the machine for which a fatigue crack growth of the initiated crack was simulated. Predictions of further crack growth were subsequently calculated for repeated typical three-months operational loading until the limited crack length before formation of a quasi-brittle fracture in the whole shaft cross-section. The crack length curve in Fig. 5 shows the predicted growing of the primary detected crack (12 mm in the length) and a limited service life for further operation of the agitator mixer.
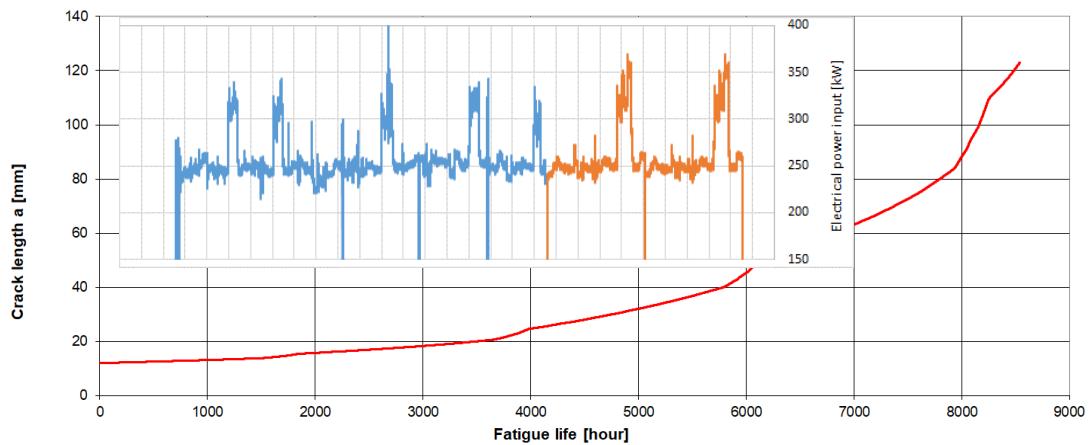
Fig. 5. The time history of the electrical power input of the machine (top) and predicted crack length growth curve according the NASGRO model (bottom)
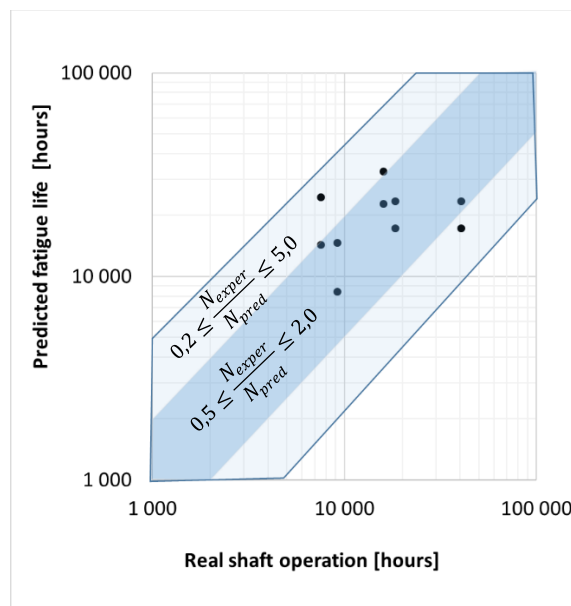
Fig. 6. Calibration of the power input and nominal stresses on the shaft (left) and FEM model geometry of the FE crack lines models for calculation of the SIF and geometric correction function (right) [2]

4. Conclusion

Based on the findings presented above, the following conclusions can be drawn:

- The fatigue life of this type of joint under the given operating loadings is insufficient.
- Operation leads to the formation and propagation of fatigue cracks and there is a risk of operational failure.
- When a short fatigue crack is found, its further growth can be predicted.
- For further safe life designs, a fatigue life factor of $k = 5$ should be recommended.
- It would be appropriate to reconstruct the given type of keyway connection.

References

[1] Kovářík O., Kunz J., Study of the crack grow rates in steel 1.6773, Internal report, Faculty of Nuclear Sciences and Physical Engineering, CTU in Prague, 2020.
[2] Růžička, M., at all, Fatigue life assessment of the agitator mixer shaft, In 60th Annual Conference on Experimental Mechanics, CTU Prague, 2022.
[3] Růžička, M., Fidranský, J., Strength and fatigue life of aircrafts, CTU Prague, 2000. (in Czech)

Simulation of mechanism with frictional effects combining physical models and machine learning regression models

Z. Šika[a], K. Kraus[a], P. Kočandrle[b],

[a]*Faculty of Mechanical Engineering, Czech Technical University in Prague, Technická 4, 160 00 Praha 6, Czech Republic*
[b]*Amadeus Czech Republic & Slovakia, Sokolovská 100, 186 00 Praha 8, Czech Republic*

Within the design process of a new machine it is necessary to harmonize the properties of mechanical parts, joints, sensors, actuators and control algorithms. Kinematic joints are essential components of the machine structure. Especially in various robotic devices with the required large range of motion and at the same time high accuracy, they are difficult to replace. Kinematic joints are necessary e.g. also for active multi-dimensional absorber investigated in CTU [4] in order to allow relatively large motions which bring possibility of non-linear behaviour. Usage of flexible pseudo-joints is only possible for small motions and in addition it brings many other problems, such as fatigue damage, problematic integration with accurate sensor of relative motions, etc. The ability to overcome the harmful effects of imperfections and friction in the joints of machine is one of the key issues of computed aided design. Although the use of virtual prototypes or digital twins is an established part of mechatronic design, the sufficiently reliable modelling of the joint imperfections and friction effects is still an open problem. Unfortunately, the late detection of insufficient suppression of these phenomena often leads to the need for a complete overhaul of the machine concept almost from the beginning.

Research and ways to model and compensate these nonlinearities are very current, for example, the use of LuGre models [3] and their combinations with advanced observers [5] can be mentioned. For detailed research of suitable models of passive effects, an experimental stand equipped with accurate motion measurement is important for a detailed comparison of the real mechanism and its models. An experimental demonstrator of above mentioned absorber was used for the research purpose. It includes three controlled legs with voice-coil actuators, linear ball bearings, accurate built-in linear encoders and precise revolute/spherical joints.

Fig. 1. Scheme of identification of LuGre models and other parameters by optimization

$$F = \sigma_o z + \sigma_1 \dot{z} + \sigma_2 v$$

$$\dot{z} = v \cdot \left(1 - \frac{\sigma_o z}{g(v)} sgn(v) \right) \tag{1}$$

$$g(v) = F_d + (F_s - F_d)e^{-(v/v_{Stribeck})^{\gamma}}$$

Fig. 1 schematically shows the procedure used to identify the mechanism model equipped with well known LuGre models (1) of passive effects in joints based on training and testing experiments. During these identifications, the repeatability of the results and the degree of uncertainty of the obtained models were also determined.
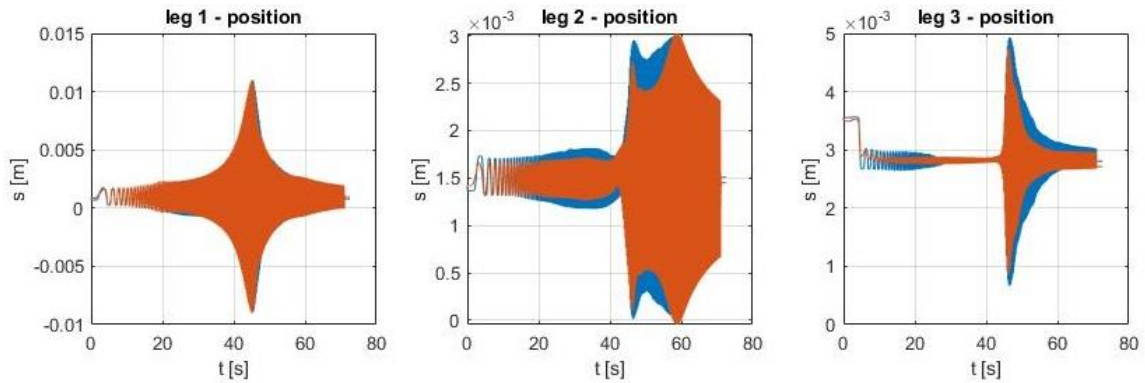

Fig. 2. Reality-model comparison after identification of LuGre models and other parameters

As can be seen from the Fig. 2, even after the optimization tuning of LuGre model parameters in kinematic joints and other mechanism parameters, the match between experiment and simulation is not perfect, especially for the second leg of the mechanism. This is due to significant frictional and adhesive effects.

Therefore, it is advisable to look for new auxiliary tools for supplementing the physical models and improving the accuracy of simulation and/or prediction with respect to reality. To further improve the model of mechanisms with frictional effects two state of the art machine learning methods are used – deep learning [2] and XGBoost [1]. The input data are divided into the training set and testing set. The training set is used for fitting the model while the model performance is evaluated on the testing set. The values of key hyperparameters of both methods are tuned to further increase the predictive power of the models.

Acknowledgement

References

[1] Chen, T., Guestrin, C., XGBoost: A scalable tree boosting system, KDD '16: Proceedings of the 22nd ACM SIGKDD International Conference on Knowledge Discovery and Data Mining, 2016, pp. 785–794.
[2] Goodfellow, I,, Bengio, Y., Courville, A., Deep learning, An MIT Press book, 2016.
[3] Huang, S., Liang, W., Intelligent friction compensation, IEEE-ASME Trans. Mechatron. 24 (4) (2019) 1763-1774.
[4] Kraus, K., et al., Mechatronic robot arm with active vibration absorbers, J. Vib. Control 26 (13-14) (2020) 1145-1156.
[5] Sancak, K. V., Bayraktaroglu, Z. Y., Observer-based friction compensation in heavy-duty parallel robot, J. Mech. Sci. Technol. 35 (8) (2021) 3693-3704.

COMPUTATIONAL MECHANICS 2023

Complex simulation procedure to predict flutter of steam turbine rotor blades

V. Sláma[a], D. Hron[b], A. Macálka[c]

[a]Department of Research and Development, Doosan Skoda Power, Tylova 1/57, 301 28 Plzeň, Czech Republic
[b]Department of Mechanics, Faculty of Applied Sciences, University of West Bohemia, Univerzitní 8, 301 00 Plzeň, Czech Republic
[c]NUM solution s.r.o., U Pergamenky 1145/12, 170 00 Praha 7 - Holešovice, Czech Republic

1. Introduction

The need for robust numerical tools to predict the flutter of rotor blades is a crucial aspect of the aeromechanical design of new modern last-stage blades for steam turbines. Therefore, a reliable flutter calculation procedure has been developed and validated in Doosan Skoda Power. As a result, a unique and úowerful tool FLTR was developed. It also automates the generation of transient input files and the evaluation described in this paper.

In general, the aerodynamic instability of blades, known as flutter, has been a crucial subject of many studies. Measurements were performed to identify the critical flutter parameters, and numerical solvers were used to predict turbine blade flutter and effective ways to keep steam turbine last stage blades' vibration amplitudes low were also proposed [1]. In this paper, the presented flutter calculation procedure is shown for the case of an 1100 mm long last-stage rotor blade, see Fig. 1 on the left, which was created for high backpressures [3].
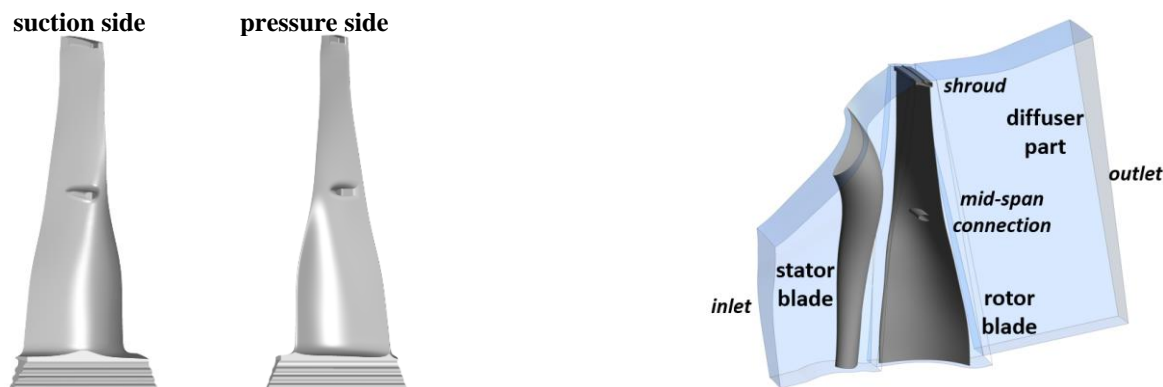

Fig. 1. 1100 mm long last stage rotor blade (left), CFD (right)

2. Flutter calculation procedure

The numerical investigation of flutter is performed using a one-way decoupled method with the workflow shown in Fig. 2 on the left. Higher fidelity CFD models [5] would be more precise. They could help to validate the currently used approach further. However, such models still need to be fully prepared, tested, and validated for such a complex geometry, which is a last-stage blade that includes all detailed features like a mid-span connection and a shroud and operates under different boundary conditions from transonic to supersonic cases.

The reliability of the used commercial code ANSYS CFX was proved by detailed studies described e.g. in [4]. Besides, the calculation procedure has been refined in recent years, as

shown in Fig. 1 on the right. The analysis is defined as a transient blade row with the time integration method. This flutter calculation procedure provides following advantages: (i) pressure and other variables distributions are more precise at the rotor blade domain inlet which is crucial, especially for transonic flow cases which are very often for ultra-long LSBs (last stage blades), (ii) effects such as shock waves going from the stator domain to the rotor domain and vice versa are included, (iii) a calculation is stable.
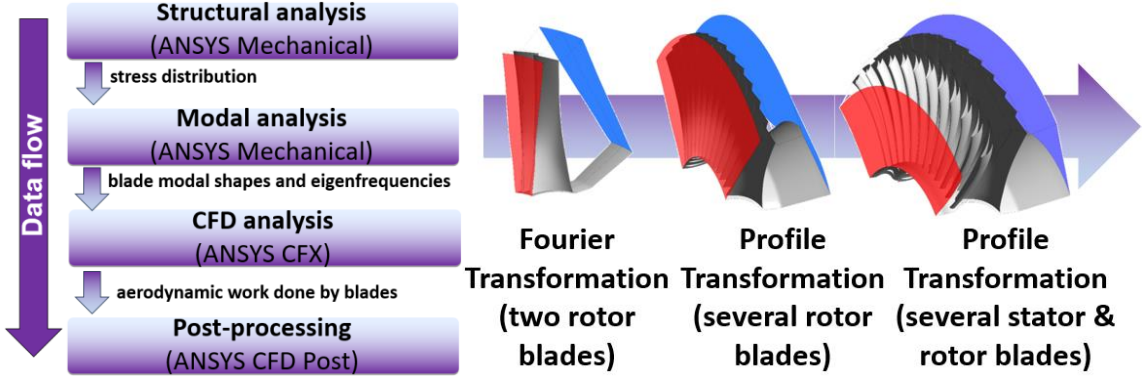

Fig. 2. Flutter analysis workflow, one way decoupled method (left), flutter calculation procedure development (right)

The structural analysis with defined periodic conditions is carried out concerning large deformations using element SOLID 186 with a defined contact at coupling elements consisting of a straight fir tree at the hub, a mid-span connection (also called a tie-boss) and an untwisted integrated shroud. It is shown in Fig. 3 on the left. This modal analysis respects all crucial phenomena, such as deformations of the blade caused by the operation speed, an imperfect blade root-disc groove connection, spin softening, and tensile stress softening. Further details are published in [2]. Besides the required modal analysis, other essential analyses are also carried out: (i) natural frequencies sensitivity to the size of contact areas of the connecting elements, which can differ due to the imperfect manufacturing, (ii) low cycle fatigue for an estimation of an allowed number of start-ups concerning a nonlinear material behavior, (iii) a rotor coupled analysis to investigate the interaction of the blades with the rotor.

Fig. 3. Details of the structural model parts (left), CFD mesh (right)

The model for CFD analysis, Fig. 1 on the right, is created for ANSYS CFX using a mesh of finite volumes. The detail of the mesh is in Fig. 3 on the right. In order to reduce computation time, only fully structured meshes are used. It means that a hexahedral mesh with an appropriate boundary layer on the blades and the adjacent walls is created, ensuring that a maximum value of y+ is lower than 5. It is a recommended value for the used turbulent model.

The CFD analysis consists of two steps: the steady-state analysis and the unsteady analysis. For the steady-state analysis, the Reynolds stresses terms of the RANS equations are computed using the two-equation eddy-viscosity SST k-ω turbulence model with an AWF (automatic wall

function). The equilibrium steam model based on the IAPWS-IF97 steam properties database is used. A total pressure profile, a total enthalpy profile, vectors of flow velocity components, and turbulence intensity define the inlet boundary condition. An average static pressure and a radial equilibrium condition define the outlet boundary condition.

A convergence of the steady-state analysis is said to be achieved when averaged residuals of momentum and mass variables reach the target value of $1 \cdot 10^{-4}$, and the monitored thermodynamic efficiency oscillations are lower than 0.01%. Furthermore, the global imbalances have to be lower than 0.01%. The unsteady analysis uses a full-scale time-marching 3D viscous model to obtain the solution of the URANS equations in the time domain. A high-resolution scheme deals with the advection term, and a second-order backward Euler scheme is used for the transient term. The time period is specified as the reciprocal value of the blade eigenfrequency according to the relevant ND (nodal diameter). The total time duration of each simulation is defined as the total number of periods per run. The blade motion is defined according to physical deformations obtained from the modal analysis results.

3. Post-processing

The energy method is used to compute aerodynamic forces during the unsteady simulation. It assumes that flutter occurs with the blade's natural mode shape and makes a flutter prediction by calculating the energy exchanged between the blade and the flow field. The required aerodynamic work W per one vibration cycle is calculated as

$$W = - \int_{t_0}^{t_0+T} \int_A p\mathbf{Vn}\, \mathrm{d}A\mathrm{d}t \tag{1}$$

where T is the period of one vibration cycle, t_0 is the time at the start of the cycle, p is the static fluid pressure, V is the velocity of the blade due to the imposed vibrational displacement, A is the surface of the blade and n is the normal unit vector to the surface A.

In order to generalize the results, the aerodynamic work W has to be normalized. There are two basic types of normalization: the normalization using the inlet flow energy or the normalization using the blade average kinetic energy. In this case, the second option is used. It means that the damping ratio ξ is calculated as:

$$\xi = \frac{-W}{8 \cdot \pi \cdot E} = \frac{-W}{2 \cdot \pi \cdot m \cdot \omega^2 \cdot a^2} \tag{2}$$

where E is the blade´s average kinetic energy, m is the blade (equivalent) modal mass, a is the modal amplitude (maximal displacement), and ω is the angular frequency. When the damping ratio is negative, it indicates that the blade is unstable and there can be a danger of flutter.

In this numerical method, mechanical and material damping of the blade is not considered. It means that the blade can be stable even for some negative values of the damping ratio. Therefore, the flutter onset was defined from the results of on-site vibration measurement during the turbine shut-down operations where atypical operating conditions were allowed. The flutter threshold was determined when the vibration limit was close to the defined maximal values. However, in practice, it is not the threshold of flutter. It appears later. In other words, if the values of the damping ratios of the newly designed blade are greater than those of the measured referential blade, the new blade can be considered flutter-free and, hence, safe.

Fig. 4 on the left shows the damping ratio results according to Eq. (2) for various NDs for one turbine operating point. The positive NDs stand for the forward traveling waves, and the negative ones for the backward traveling waves. Results show that the damping ratios are negative for a few negative NDs. In this region, the new blade damping ratios are greater than the ratios of the referential blade. It means that no problems with flutter are expected for the presented operating point of the new blade.
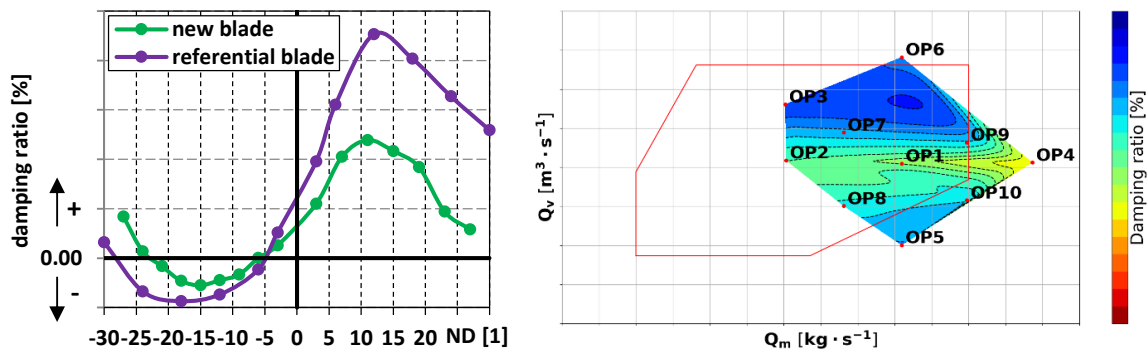
Fig. 4. Damping ratio dependence on nodal diameter (left), flutter map for the newly developed LSB (right)

The results presented in Fig. 4 on the left are just for one operating condition. However, it is necessary to perform flutter analyses for a wider range to avoid the danger of flutter for all turbine operating conditions. Therefore, in order to evaluate and clearly show the blade sensitivity to flutter, the flutter maps were developed. An example of one such flutter map can be seen in Fig. 4 on the right. It shows the dependence of the damping ratio on the mass flow Q_m going through the last stage and the volumetric flow rate Q_v. The red lines depict the region of the LSB operating range. The flutter map is created for the NDs with the most negative values. As a result, the areas of damping ratios with low negative values can be found. Hence, a potential danger of flutter can be detected in the preliminary design phase. If the values inside the operation range were lower than the referential value, using the blade for such operating points would be dangerous. In this case, the blade must be redesigned.

4. Conclusion

The in-house flutter calculation procedure (FLTR tool), which is based on a commercial numerical code ANSYS, has been developed and validated to predict a danger of flutter. Details of this procedure, along with all crucial settings, were shown. Using the S-shaped curves and the flutter maps, which are supposed to be an original and complex approach developed by Doosan Skoda Power Company in cooperation with NUM Solution Company, all required areas in the operating range of the blade were investigated. By comparing the damping ratio results with the referential blade results, it was shown that the new blade satisfies the safety requirements from the flutter occurrence point of view in the required operating range. Thanks to this procedure, any blade can be checked whether it is flutter-free or not.

Acknowledgement

References

[1] Drozdowski, R., Völker, L., Häfele, M., Vogt, D. M., Experimental and numerical investigation of the nonlinear vibrational behavior of steam turbine last stage blades with friction bolt damping elements, ASME Turbo Expo 2015, GT2015-42244, Montreal, Canada, 2015.
[2] Misek, T., Kubin, Z., Duchek, K., Static and dynamic analysis of 48" steel last-stage blade for steam turbine, ASME Turbo Expo 2009, GT2009-59085, Orlando, USA, 2009.
[3] Novak, O., Bobcik, M., Slama, V., at al., Development of highly efficient and robust ultra-long last stage blade for high backpressure, ASME Turbo Expo 2019, GT2019-90350, Phoenix, USA, 2019.
[4] Slama, V., Eret P., Pinelli, F., at al., Experimental and numerical study of controlled flutter testing in a linear turbine blade cascade, Acta Polytechnica 20 (2018) 98-107.
[5] Zorn, J., Davis, R., Clark, J., High fidelity simulation of fluid-structure interaction in a 1½ stage axial turbine, ASME Turbo Expo 2019, GT2019-90972, Phoenix, USA, 2019.

Modelling of pulse-triggered running waves on a blade cascade

P. Šnábl[a], L. Pešek[a]

[a]*Institute of Thermomechanics of the CAS, v. v. i., Dolejškova 1402/5, 182 00 Praha 8, Czech Republic*

An experimental cascade of five NACA 0010 blades with pitch degrees of freedom is excited by a moment pulse to one of the blades. Depending on the flow conditions, such as wind speed and the angle of attack of the wind on the blades, the vibration of the excited blade is transmitted by the wind to the other blades. This can result in a running wave that diminishes over time or in a flutter running wave.

A simplified spring-mass-damper model with inter-blade connections and non-linear van der Pol dampers is tuned to match experimentally obtained stability curves and tested to see if it can qualitatively model the response of the cascade to the pulse excitation.

The motion equations of all five blades with inertia $\mathbf{I}$, damping $\mathbf{B}$ and stiffness $\mathbf{K}$ and blade displacement $\boldsymbol{\varphi}$ can be written as

$$\mathbf{I}\ddot{\boldsymbol{\varphi}} + \mathbf{B}\dot{\boldsymbol{\varphi}} + \mathbf{K}\boldsymbol{\varphi} + \mathbf{g}(\boldsymbol{\varphi},\ \dot{\boldsymbol{\varphi}}) = \mathbf{m_E}, \tag{1}$$

where the additional nonlinear term $\mathbf{g}(\boldsymbol{\varphi},\ \dot{\boldsymbol{\varphi}})$ describes the aeroelastic couplings between the blades and the right-hand vector $\mathbf{m_E}$ adds the moment of the pulse excitation.

The question is how to mathematically describe the complex fluid-structure interaction that is present in the experimental blade cascade. In our previous works, e.g., [1], we used the van der Pol damping term, which can be written for the pitch motion of the blade i as

$$g_i(\boldsymbol{\varphi},\ \dot{\boldsymbol{\varphi}}) = -\mu \left[1 - \left(\frac{\varphi_i}{r} \right)^2 \right] \dot{\varphi}_i. \tag{2}$$

It is a negative damping with an intensity μ that becomes positive when the displacement of the blade exceeds the threshold value set by r. This change of sign causes excitation of the blades at low amplitudes and damping at high amplitudes which is advantageous in simulations because the amplitudes do not grow to infinity. It also corresponds to the experiment with only one blade installed - at certain flow conditions the blade starts to self-oscillate, but after a short transition period the amplitude settles at certain value. However, equation (2) for blade i does not contain any information about adjacent blades. Thus, each blade can oscillate independently which is not the case in experiment with multiple blades.

To interconnect the blades, the van der Pol damping equation (2) was modified in [2] to act on the relative motion of the adjacent blades

$$g_i(\boldsymbol{\varphi},\ \dot{\boldsymbol{\varphi}}) = -\mu_R \Bigg\{ \left[1 - \left(\frac{\varphi_i - \varphi_{i-1}}{r_R} \right)^2 \right] (\dot{\varphi}_i - \dot{\varphi}_{i-1}) + $$
$$+ \left[1 - \left(\frac{\varphi_i - \varphi_{i+1}}{r_R} \right)^2 \right] (\dot{\varphi}_i - \dot{\varphi}_{i+1}) \Bigg\}. \tag{3}$$

190

Equation (3) reaches a minimal value when the adjacent blades oscillate in opposite phase, at an inter-blade phase angle (IBPA) of 180°, which forces the blades to oscillate at this IBPA. However, this is not the case in our experiments.

This is shown graphically in Fig. 1 where the aerodynamic damping (AD) parameter, which corresponds to the work done by the moment acting on the blade during one period of blade motion, is plotted as a function of IBPA. Negative AD means that the moment is exciting the blade, positive AD means that the moment is damping the blade. While in the experiment the AD follows a typical so-called S-curve with a minimum around -90° and a maximum around 90°, the AD provided the by relative motion van der Pol damping from (3) together with the viscous damping term $\mathbf{B}\dot{\varphi}$ from (1) actually shows a minimum at 180°.

The aim of this paper is to introduce such a term $\mathbf{g}(\varphi, \dot{\varphi})$ that would add damping to the system corresponding to the experiment. The suggested term for the blade i is

$$g_i(\varphi) = k_{AE} \left[r_1 r_2 \varphi_{i-1} + (r_2^2 - r_1^2)\varphi_i - r_1 r_2 \varphi_{i+1} \right]. \tag{4}$$

This equation is based on a virtual spring attached between the i-th blade trailing edge at arm r_1 from the blade axis and the $(i + 1)$-th blade leading edge at arm r_2 from the blade axis. However, this would only create an elastic connection with no ability to damp or excite the system. Therefore, the sign of the virtual spring force acting on the trailing edge of each blade was reversed, resulting in a non-conservative force. Equation (4) can then be tuned to match the experimentally obtained S-curve with the aeroelastic "stiffness" parameter k_{AE}, as shown in Fig. 2. The values of the arm lengths are set according to the blade cascade geometry: $r_1 > r_2$.

Both the experimental and numerical S-curves in Fig. 2 were obtained using the travelling wave mode approach with a blade oscillation amplitude of 1° and frequency of 25 Hz. The experiment was carried out at a wind speed of 25 m/s and an angle of attack of $-8°$ (negative sign corresponds to the turbine configuration).
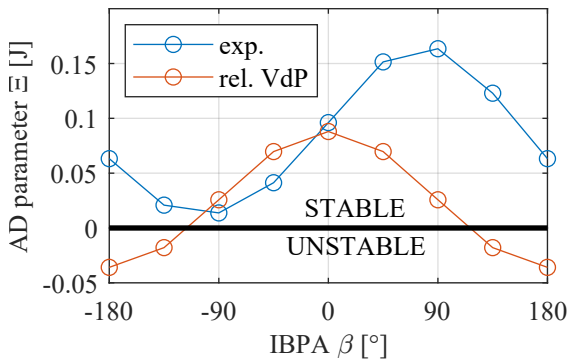

Fig. 1. Experimentally measured aerodynamic damping in comparison with simulated aerodynamic damping using relative motion van der Pol damping equation
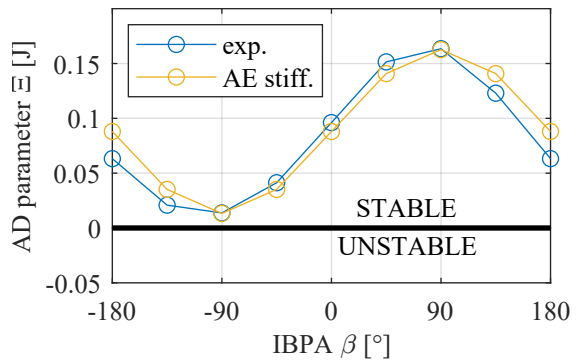
Fig. 2. Experimentally measured aerodynamic damping in comparison with simulated aerodynamic damping using herein proposed aeroelastic stiffness

The next step is to simulate the behaviour of the blade cascade behaviour when one of the blades is excited by a moment pulse. This was done experimentally with the first and last blade fixed. The experimental results are shown in Figs. 3a, 4a and 5a, where the pulse was applied to the blades $+1$, 0 and -1, respectively. The displacement of all three non-fixed blades can be observed and the most important is the IBPA between the blades. It can be seen that in all three cases the blade $+1$ is followed by blade 0 and blade 0 is followed by blade -1. This means that a backward running wave was excited which is consistent with the S-curve in Figs. 1 and 2,
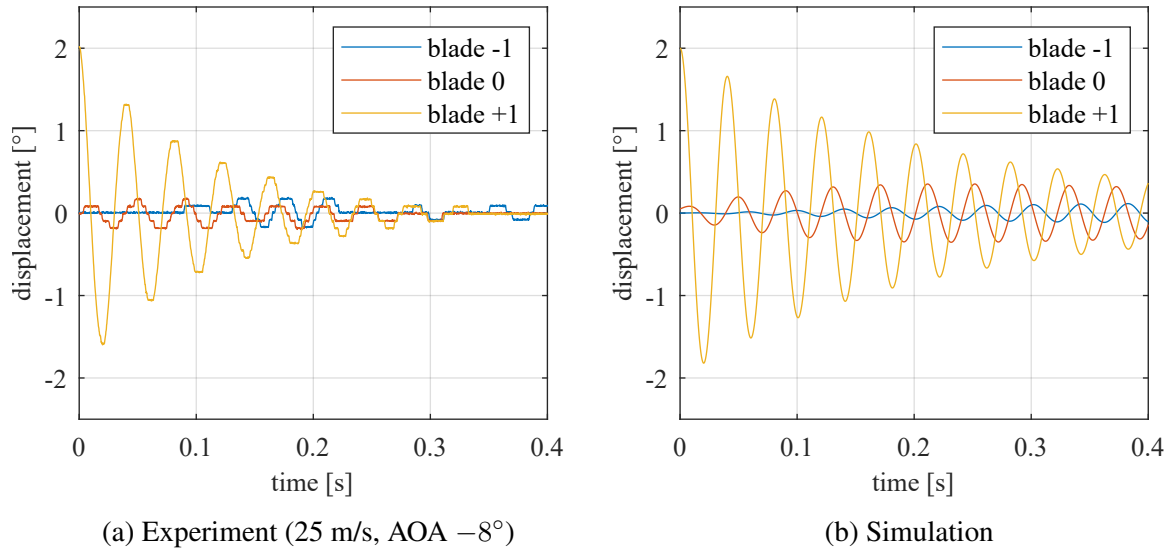
(a) Experiment (25 m/s, AOA −8°)   (b) Simulation

Fig. 3. Behaviour of the blade cascade after pulse excitation of the blade +1

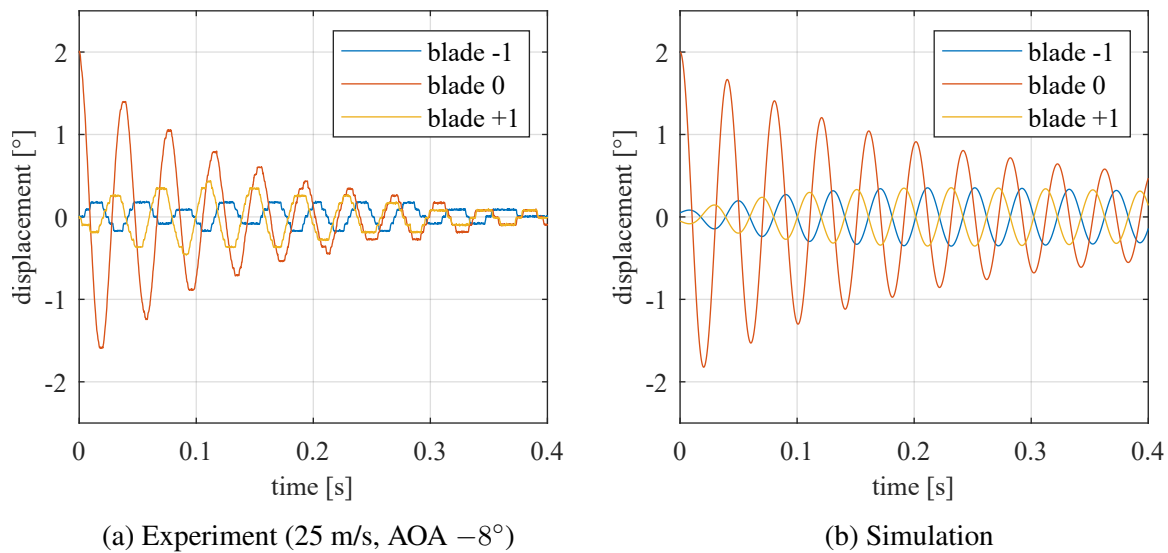(a) Experiment (25 m/s, AOA −8°)   (b) Simulation

Fig. 4. Behaviour of the blade cascade after pulse excitation of the blade 0

where negative IBPA corresponds to the backward running wave. The minimal AD is at IBPA −90° and this is the most likely phase angle at which the blade cascade starts to oscillate.

Simulations of the system described by (1) with the aeroelastic term (4) tuned to match the experimental S-curve as shown in Fig. 2 were carried out in Simulink and the results are shown in Figs. 3b, 4b and 5b with pulses to the blades +1, 0 and −1, respectively.

With the pulse applied to the blades +1 and 0 in Figs. 3 and 4, we can see qualitatively very similar behaviour in the experiment and simulation. After the pulse, the adjacent blades start to oscillate, creating the backward running wave. In the simulation the IBPA is always −90°. However, in the experiment this is not always true, e.g., in Fig. 4a the IBPA of the blade −1 with respect to the blade 0 is somewhere in between 0° and −90°. There is also a noticeable difference in the overall damping. Although the damping in simulation is also tuned to match the experimental S-curve, the oscillations decay faster in the experiment than in the simulation.

A different scenario can be seen when the pulse is applied to the blade −1 in Fig. 5. While the simulation behaves similarly to the previous cases and in accordance with the S-curve in
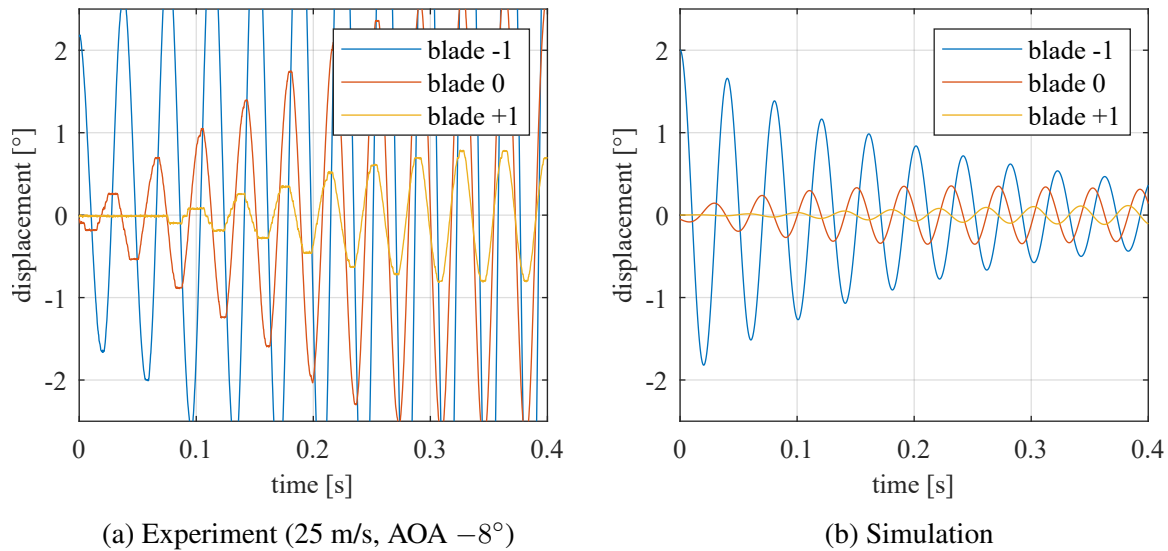
(a) Experiment (25 m/s, AOA $-8°$) (b) Simulation

Fig. 5. Behaviour of the blade cascade after pulse excitation of the blade -1

Fig. 2 where the AD is always positive and no self-excitation should occur, the reality in the experiment is different. After the pulse in Fig. 5b we can see the onset of the cascade flutter with diverging amplitudes of all the blades.

It must be noted that the case at 25 m/s and AOA $-8°$ is right at the flutter boundary. At AOA $-7°$ the flutter does not start after the pulse to the blade -1, at AOA $-9°$ the cascade starts to flutter even without any pulse. Also, at AOA $-8°$ the flutter will not start if the pulse to the blade -1 is smaller.

Although the cascade model with the proposed aeroelastic term (4) could not capture the on-set of the flutter, which is understandable due to the enormous complexity of the fluid-structure interaction, it was able to very realistically interconnect the blades and simulate the blade cascade behaviour in non-flutter regimes which is a great achievement. To simulate the rapid increase in amplitudes when the flutter occurs, another term in the motion equations is needed, possibly a variant of the van der Pol damping equation. Further experiments and simulations will be carried out in the future to model the aeroelastic coupling even more accurately and possibly even capture the flutter behaviour.

Acknowledgement

References

[1] Pešek, L., Šnábl, P., Prasad, C. S., Modal synthesis method for inter-blade dry-friction surface angle design of turbine wheel for vibration suppression, Proceedings of the ASME 2022 International Design Engineering Technical Conferences and Computers and Information in Engineering Conference, 2022, V010T10A022.

[2] Pešek, L., Šnábl, P., Prasad, C. S., Delanney, Y., Numerical simulations of aeroelastic instabilities in turbine-blade cascade by a modified Van der Pol model at running excitation, Applied and Computational Mechanics 17 (1) (2023) 35-52.

COMPUTATIONAL MECHANICS 2023

Circular representative volume element
for discrete model of concrete

M. Středulová[a], J. Eliáš[a]

[a]*Institute of Structural Mechanics, Faculty of Civil Engineering, Brno University of Technology, Veveří 331/95, Brno, Czech Republic*

1. Introduction

Representative volume element (RVE) is a concept used in homogenization schemes, which potentially allows the reduction of computational costs of highly detailed simulations [6]. In essence, it is a small-scale (micro or mesoscale) model, which statistically represents a material used for a macroscale simulation. In a computational scheme (for example the Finite Element Method), it acts as a constitutive function substitution: An RVE is attached to an integration point, loaded by proper displacement or traction and its response is obtained. Subsequently, the results are used in the macroscale calculations [5].

Loading, whether displacement or traction, may be applied on the RVE in multiple ways, however, it has been shown that periodic boundary conditions are the most advantageous since the response they produce is the most realistic one [8]. RVE in combination with periodic boundary conditions is overwhelmingly used only for elastic response [6]. When applied to non-linear scenarios, for example a strain softening material with heterogenities, whose post-peak behavior is characterized by fracture, its use is also possible, albeit its statistical representativeness is questionable. It requires extensive modification to the original equations defining the boundary conditions and some transformation (rotation, translation) of the coordinate system so that a crack may emerge in an arbitrary direction. Apart from leading to complex implementations, such modifications inevitably add additional computational costs [2, 8–10].

One of the possible solutions proposed in literature, which builds on the concept of an RVE used in conjunction with periodic boundary conditions, is to substitute the conventionally used square / cubic RVE by a circular / spherical one [7, 9]. Such solution potentially offers seamless rotation of the coordinate system so that periodic boundary conditions allow the formation of a crack in arbitrary direction.

The present contribution is part of a larger effort to formulate a circular RVE formed by a lattice discrete particle model (LDPM) [3, 4] which could also account for a post peak strain softening behavior. It is concerned with the generation of a circular RVE geometry mimicking discrete setting which enables periodic placement of particles. We presume that the use of a discrete model does not allow the splitting of a particle and therefore necessarily leads to the generation of a irregular boundary. In the first part, the formation of a continuous circular RVE described in literature is shown. Subsequently a formation of a discrete circular RVE is mimicked by altering the boundary of a RVE. It is shown that this may lead to spurious strains being introduced into the RVE response. Possible modifications to the generation procedure are proposed and tested.

2. Circular RVE geometry generation

In an RVE formulation, periodic boundary conditions are prescribed for each opposing couple of nodes on the surface of an RVE. Each couple of points is allowed the same displacement and rotation. According to [7], the only requirement to which the shape of an RVE is subjected is that of opposing surface normals for each couple of nodes: $\boldsymbol{n}^+ = -\boldsymbol{n}^-$.

Upholding the periodicity of a material, geometry generation is according to [9] done by placing a periodic image of a particle with center (r, θ, ϕ) to a particle of the same diameter with center $(r - D, \theta, \phi)$, where D is the diameter of the RVE (Fig. 1a). In case of a circular RVE with particles created by continuous model, such requirement is naturally fulfilled, because the heterogeneities may be split and thus the surface of a RVE is kept regular (Fig. 1b). In the case of a discrete model with physical discretization [1], such split of particles is not possible by the nature of the model, hence the periodicity of the material must be upheld by allowing irregular boundary (Fig. 1c).
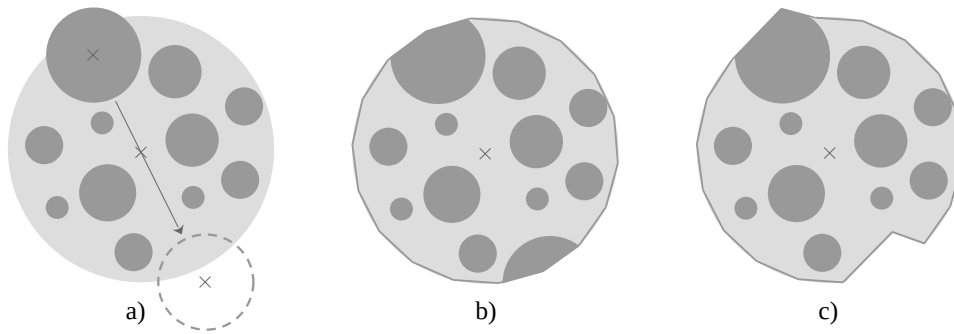

Fig. 1. (a) Geometry generation of a circular RVE with periodically placed particles, (b) a schematic boundary of a continuous RVE and (c) a schematic boundary of a discrete RVE

2.1 Simulations

Both of the scenarios described above have been tested in simulations, in order to asses its performance in elastic regime. To see the effect of the boundary manipulation, only the position of one node couple was altered (Figs. 1b and 1c). Elastic material of given parameters was used. No heterogeneities were incorporated. Periodic boundary conditions are applied to the opposing node couples. An in-house Finite Element Method preprocessor and solver, named OAS (Open Academic Solver), was used. The RVEs are loaded by uniaxial tension applied in the x direction $\boldsymbol{\varepsilon} = \{\varepsilon_{xx}\ 0\ 0\}^T$. Strain fields of the loaded RVEs are shown in Fig. 2.

The RVEs were both loaded by a strain $\varepsilon_x = 0.001$. The strain field of a RVE with regular boundary shows constant distribution of strains, with magnitude being equal to that of the applied loading. On the contrary, the RVE with irregular boundary shows that by the irregularities, strain magnitude differs by as much as 50 %, ranging up to 0.0015 magnitude. The difference lowers by decreases meshing of the RVE, but it remains present.

Upon closer inspection, the second RVE with irregular boundary does not abide by the condition of opposing normals. Fig. 3a illustrates the mismatch in supposedly parallel boundary segments. Segments of the same style (either solid or dotted line) are centrally symmetric and therefore should be parallel to allow for opposing normals. Clearly, that is not the case. To allow the segments to be parallel, the boundary needs to be changed in a centrally symmetric manner as well (Fig. 3b and 3c).

Results of the simulations performed in the same manner as described at the beginning of this subsection are shown in Fig. 4. The results show that by generating the geometry in a
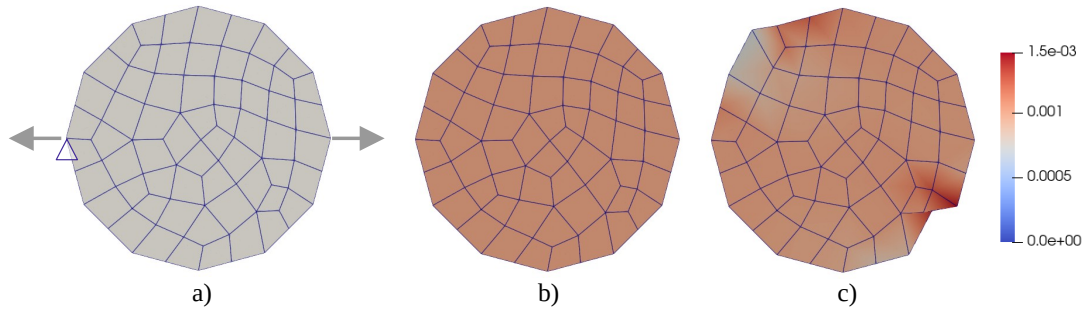
Fig. 2. (a) Scheme of the loaded circular RVE, (b) strain field (magnitude) of a circular RVE with regular boundary, (c) strain field of a circular RVE with irregular boundary (mimicking discrete RVE)
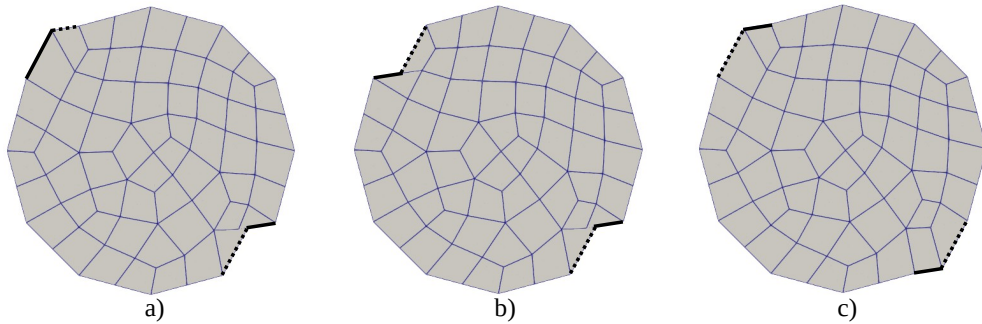

Fig. 3. Part of the RVE boundary which are joined to the deviated node of the boundary. Lines of the same pattern should be parallel to satisfy the opposing normals equation: (a) not parallel lines of the RVE generated based on the procedure used in [7,9], (b) and (c) suggested modifications to the geometry to maintain constant distribution of strains
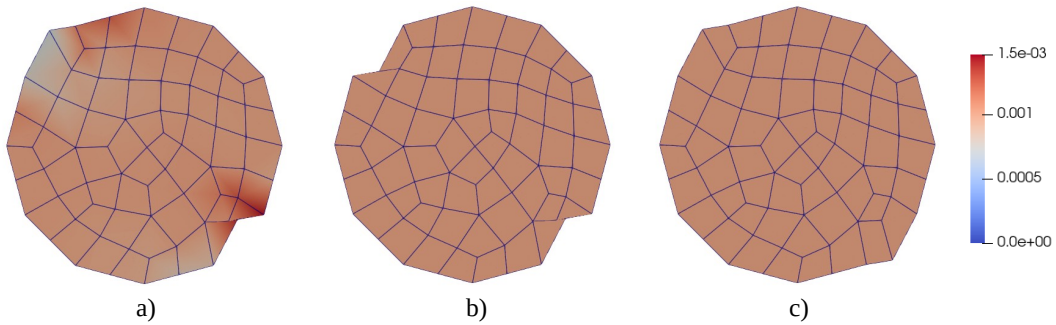

Fig. 4. (a) Strain distribution of the first geometry generation with not parallel boundary segments, (b) and (c) results obtained by a centrally symmetric geometry generation

centrally-symmetric manner (Fig. 3b and c), the distribution of strains is equivalent to that of the RVE with regular boundary.

3. Conclusion

It was shown to what extent geometry generation may influence the distribution of stresses in a circular RVE upon which periodic boundary conditions are applied. Following the procedure suggested for the geometry generation of a continuous RVE, the boundary irregularity oriented inward to the RVE behaves as a concentrator, raising the strain magnitude by as much as 50 %.

The strains are lower by the boundary distorted outside of the RVE. The phenomena may be attributed to the effect of periodic boundary conditions, which are in this case applied in a centrally symmetric manner to a non-symmetric node pair.

However, by distorting the boundary in a centrally symmetric manner, that is in the same direction with respect to the centroid of the RVE, the strain distribution is constant as in the case of the regular RVE. Although successful for the present analysis, it is left upon further discussion whether such a geometry generation produces geometrically periodic sample of a material, upholding the original concept of a representative volume element.

Acknowledgements

References

[1] Bolander, J. E., Eliáš, J., Cusatis, G., Nagai, K., Discrete mechanical models of concrete fracture, Engineering Fracture Mechanics 257 (2021) No. 108030.

[2] Coenen, E. W., Kouznetsova, V. G., Geers, M. G., Novel boundary conditions for strain localization analyses in microstructural volume elements, International Journal for Numerical Methods in Engineering 90 (2012) 1-21.

[3] Cusatis, G., Mencarelli, A., Pelessone, D., Baylot, J., Lattice discrete particle model (LDPM) for failure behavior of concrete. II: Calibration and validation, Cement and Concrete Composites 33 (9) (2011) 891-905.

[4] Cusatis, G., Pelessone, D., Mencarelli, A., Lattice discrete particle model (LDPM) for failure behavior of concrete. I: Theory, Cement and Concrete Composites 33 (9) (2011) 881-890.

[5] Eliáš, J., Cusatis, G., Homogenization of discrete mesoscale model of concrete for coupled mass transport and mechanics by asymptotic expansion, Journal of the Mechanics and Physics of Solids 167 (2022) No. 105010.

[6] Gitman, I. M., Askes, H., Sluys, L. J., Representative volume: Existence and size determination, Engineering Fracture Mechanics 74 (2007) 2518-2534.

[7] Glüge, R., Weber, M., Bertram, A., Comparison of spherical and cubical statistical volume elements with respect to convergence, anisotropy, and localization behavior, Computational Materials Science 63 (2012) 91-104.

[8] Goldmann, J., Brummund, J., Ulbricht, V., On boundary conditions for homogenization of volume elements undergoing localization, International Journal for Numerical Methods in Engineering 113 (2018) 1-21.

[9] Hofman, P., Ke, L., van der Meer, F. P., Circular representative volume elements for strain localization problems, International Journal for Numerical Methods in Engineering 124 (2023) 784-807.

[10] Toro, S., Sánchez, P. J., Huespe, A. E., Giusti, S. M., Blanco, P. J., Feijóo, R. A., A two-scale failure model for heterogeneous materials: Numerical implementation based on the finite element method, International Journal for Numerical Methods in Engineering 97 (2014) 313-351.

Conceptual study of non-cylindrical tank for gaseous fuels

O. Uher[a], J. Brabec[a], K. Barák[a], M. Růžička[b]

[a]Department of Aerospace Engineering, Faculty of Mechanical Engineering, Czech Technical University in Prague, Karlovo náměstí 13, 121 35 Praha, Czech Republic
[b]Department of Mechanics, Biomechanics and Mechatronics, Division of Strength and Elasticity, Faculty of Mechanical Engineering, Czech Technical University in Prague, Technická 4, 166 07 Praha 6, Czech Republic

1. Motivation

There is increased pressure from regulatory organs to move to greener and lower emission propulsion systems in aviation. That is possible thanks to recent development of electric propulsion systems. The biggest problem of such system is the energy source, most common type are lithium batteries, which are difficult to manufacture and the process is not ecological. The biggest problem of batteries however is their low gravimetric energy density compared to the standard aviation gas. In the figure [1] below (see Fig. 1), a graph of gravimetric energy densities compared to the volumetric energy densities is seen. From this graph the best gravimetric energy density is achieved by hydrogen compressed to either 30 or 70 MPa. Lithium Ion batteries have the worst energy densities of all listed substances. After hydrogen goes through the fuel cell, the only emission is water vapor and excess heat, making it the most ecologic of the listed energy sources.
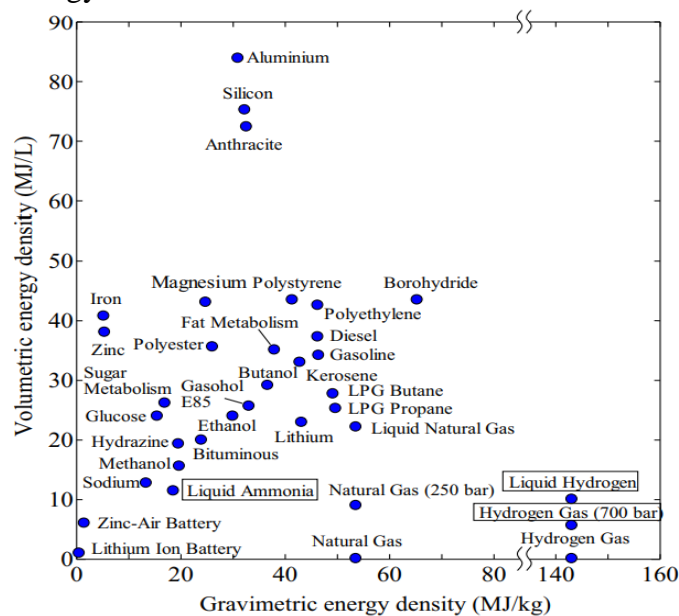

Fig. 1. Graph of energy densities [1]

The biggest problem of hydrogen is its low volumetric energy density, meaning it occupies larger volume to contain the same amount of energy as other sources with higher volumetric energy densities. In aircraft applications nowadays, the hydrogen tanks are attached outside of the airplane. This is hindering flight performance, because of increased drag. To mitigate this problem, tanks mounted inside the airframe can be used. However typical cylindrical tanks do

not fit inside with sufficient volume. Thus, noncylindrical tanks, that can efficiently use internal free space, are proposed. In addition, to save weight, tanks can be designed to bear external loads such as torsion for example.

2. Mass of tanks and amount of fuel determination

Calculation is based on principle of "constant" amount of energy stored in gas. It is calculated for small motor glider developed by the Department of Aerospace Engineering. For reference a similar aircraft of the same category was selected. Amount of gas in tanks: $V_f = 2 * 50\,l = 100\,l$, [3]. Gas: Avgas – volumetric energy density $\rho_{Evf} = 30.81$ MJ/l, [1]. The equation

$$E_G = V_f * \rho_{Evf} = 100 * 30.81 = 3081 \text{ MJ} \tag{1}$$

determines amount of energy of the gas carried by similar aircraft. Next energy "on the shaft" is defined by equation

$$E_{G\ shaft} = E_G * \eta_{combustion} = 3081 * 0.35 = 1078.35 \text{ MJ}. \tag{2}$$

The efficiency of hydrogen fuel cell based propulsion is calculated by equation

$$\eta_H = \eta_{fc} * \eta_{mc} * \eta_{em} = 0.85 * 0.99 * 0.9 = 0.757 \text{ [1]}, \tag{3}$$

where η_H is the overall efficiency of the system, η_{fc} is the efficiency of fuel cell [4], η_{mc} is the efficiency of motor controller and η_{em} is the efficiency of electric motor of similar power as a corresponding combustion engine used in similar category aircraft. Equation

$$E_{\mathrm{H}} = E_{G\ shaft}/\eta_H = 1078.35/0.757 = 1424.5 \text{ MJ} \tag{4}$$

determines the amount of energy needed to be stored in the compressed hydrogen. E_{H} is the energy stored in hydrogen, $E_{G\ shaft}$ is energy "on the shaft" defined by equation (2) and η_H is the efficiency of hydrogen fuel cell based propulsion system defined by (3). V_H is the volume of compressed hydrogen at 70 MPa to contain the energy as calculated in (4):

$$V_H = \frac{E_H}{\rho_{EvH}} = \frac{1424.5}{5} = 284.5\ l, \tag{5}$$

where ρ_{EvH} is the volumetric energy density of compressed hydrogen [MJ/l], was found in [2].

Based on the density of hydrogen compressed at 70 MPa as seen in Fig. 2, it is possible to determine the mass of needed hydrogen.
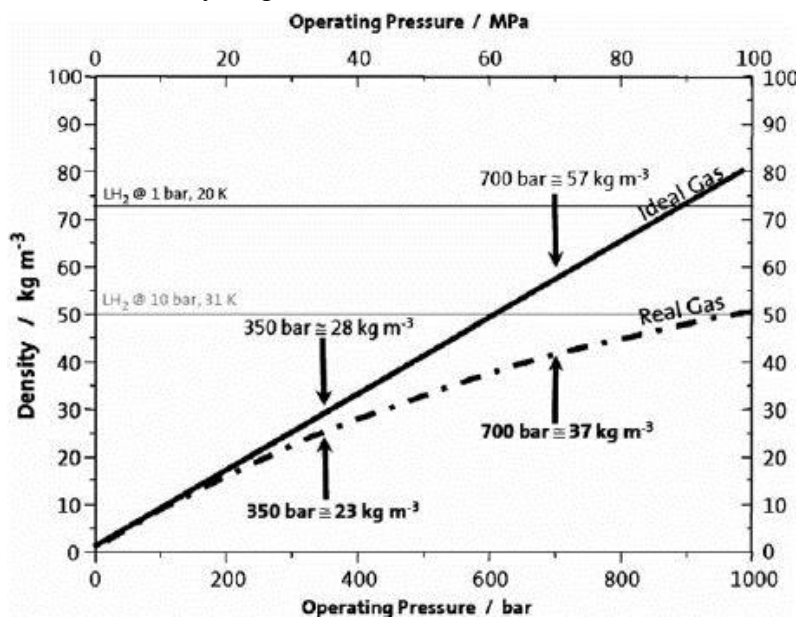

Fig. 2. Graph of hydrogen density based on pressure [1]

The mass of hydrogen needed

$$m_H = V_H * \rho_{H70} = 0.2845 * 37 = 10.53 \text{ kg}, \qquad (6)$$

where V_H is the volume of hydrogen (converted to m^3) and ρ_{H70} is the density of hydrogen compressed at 70 MPa.

$$m_f = V_f * \rho_f = 0.1 * 690 = 69 \text{ kg} \qquad (7)$$

defines the mass of petrol fuel m_f, V_f is the volume of fuel (converted to m3) carried by the aircraft and ρ_f is the density of petrol. Next, the mass of the whole propulsion system using petrol is defined as

$$m_{ps} = m_{ft} + m_f + m_e = 4 + 69 + 80 = 153 \text{ kg}, \qquad (8)$$

where m_{ft} is the mass of fuel tanks, m_f is the mass of petrol fuel defined by (7) and m_e is the mass of a combustion engine. Rotax 912 UL is considered. Based on weight of the whole propulsion, it is possible to determine the maximal weight of the compressed hydrogen tank. The goal is to keep the aircraft's maximal take-off weight the same as with a combustion engine propulsion system, to keep the aircraft in the same regulatory category. Maximal available mass of tank m_{tH} is determined as

$$m_{tH} = m_{ps} - m_H - m_{fc} - m_{mc} - m_{em} = 153 - 10.53 - 41 - 4.2 - 15.3 = \qquad (9)$$
$$81.97 \text{ kg},$$

where m_{ps} is the mass of petrol propulsion system as calculated (8), m_H is the mass of compressed hydrogen as calculated (6), m_{fc} is the mass of fuel cell, m_{mc} is the mass of motor controller and m_{em} is the mass of electric engine.

Based on knowledge of the mass of combustion engine propulsion system and the amount of petrol carried by the aircraft, maximal available mass of hydrogen tanks has been determined. The mass of the propeller or reduction gear, if used, is assumed the same as for a combustion engine and thus has not been calculated with. Furthermore, the mass of piping and hoses for routing gas or hydrogen has been neglected, as their length is yet to be determined. According to a 3D model of the proposed aircraft it is possible to store up to 400 l of hydrogen inside the structure of the wings, however the mass of the tanks would probably exceed the maximal allowable mass in its regulatory category.

3. Conceptual designs

So far, four conceptual designs of a tank for compressed hydrogen have been designed (see Fig. 3) and analysed. All of these are integrated into the wing structure, meaning they need to fit inside the airfoil envelope. The goal is to select the best concept for further more detailed design and analysis. The main criterion is minimal mass compared to the volume of gas it can store. Technology is also considered. All concepts have been analysed by membrane stress theory

$$t_n = \frac{p*k*R_n}{\sigma_{max}} \qquad (10)$$

for given radiuses R_n, the wall thickness t_n has been calculated, maximum strength has been empirically selected to $\sigma_{max} = 1000$ MPa. Working pressure p has been multiplied by a safety factor $k = 2.3$. This value is given by regulations for composite pressure vessels. The wall thickness is different for each concept variant and each radius. Radius values have been obtained from CAD. For mass evaluation, the length of curve of each part in each concept variant has been obtained from CAD as well. These are used to calculate the section area of composite by a simple multiplication of curve lengths and wall thicknesses. In the Table 1 are

wall thicknesses of each concept as well as their relative volume, i.e. volume per unit of mass. Concept number 1 does not have the wall thickness of vertical walls between cells displayed in the table. These were calculated analogically. FEM analysis shows good overall compliance with analytical examination, however FEM shows stress spikes on the edges of the membranes see Fig. 4. These regions would have to be reinforced.
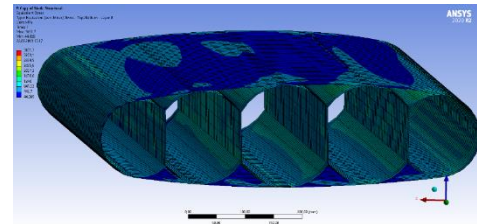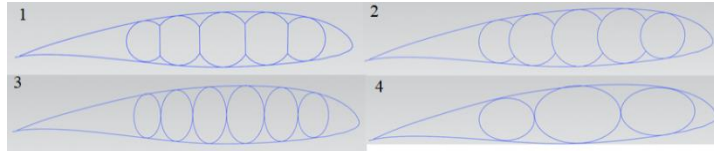

Fig. 3. Overview of evaluated concepts, fitted inside airfoil envelope   Fig. 4. FEM simulation of concept 1

Table 1. Wall thicknesses and relative volume of each concept

Concept Nr.	t_1 [mm]	t_2 [mm]	t_3 [mm]	t_4 [mm]	t_5 [mm]	t_6 [mm]	Relative volume [l/kg]
1	10.787	13.041	14.49	13.846	11.592	-	1.370357
2	10.787	13.041	14.49	13.846	11.592	-	1.348574
3	11.109	12.88	14.168	14.49	13.524	11.27	0.802497
4	14.49	22.54	19.32	-	-	-	0.797562

4. Conclusion

Due to increased demand for carbon neutral propulsion systems in aviation, hydrogen is highly considered. To use compressed hydrogen efficiently it is needed to design tanks that can conform to airframe structure and use internal volume. First, the necessary amount of hydrogen compressed to 70 MPa is calculated based on the energy stored and transferred to the propeller. Thanks to the knowledge of conventional propulsion system using combustion engine, the mass of both systems was compared and maximum allowable mass of the hydrogen tank has been calculated. Next, 4 concepts of conformal hydrogen tank fitted inside the airfoil envelope have been designed and analytically evaluated, FEM analysis was further performed to confirm the results. Both analyses show good agreement, however FEM shows stress spikes in places where membrane stresses connect. Concept 1 has the best relative volume and is the most promising for further optimization and development.

Acknowledgement

References

[1] Felderhoff, M., Weidenthaler, C., Helmolt, R., Eberle, U., Hydrogen storage: The remaining scientific and technological challenges, Physical chemistry chemical physics 9 (2007) 2643-2653.
[2] Prewitz, M., Bardenhagen, A., Beck, R., Hydrogen as the fuel of the future in aircrafts – Challenges and opportunities, International Journal of Hydrogen Energy 45 (2020).
[3] UFM 13/15 Lambáda, available from: https://www.distar.cz/ufm-13-15-lambada/ (online)
[4] Types of Fuel Cells, U.S Department of energy, Available from: http://www1.eere.energy.gov/hydrogenandfuelcells/fuelcells/fc_types.html, https://web.archive.org/web/20100609041046/http://www1.eere.energy.gov/hydrogenandfuelcells/fuelcells/fc_types.html (online)

The magic of angles

M. Valášek[a], V. Bauma[a]

[a]Department of Mechanics, Biomechanics and Mechatronics, Faculty of Mechanical Engineering, Czech Technical University in Prague, Technická 4, 160 00 Praha 6, Czech Republic

1. Introduction

The calibration of robots and machine tools requires the measurement of position of points in space. The modern devices for such measurements are laser trackers and laser tracers. The precision of measurements of position of points is quite high. However, the calibration of robots requires to determine the position of body (robot gripper) based on measurements of several points.

The paper describes the surprising result that the subsequent determination of body position only from position of points is possible only with low accuracy. The accuracy of determination of body position can be significantly (more than 10 times) increased if there are measured not only the position of points but also some angles. The influence of measurements of angles on the determination of body position is magic. The paper describes the simulation and then resulting patented calibration device for robots.

2. Problem formulation

The industrial robots especially with translation on the 7th axis require calibration. For stationary robots the suitable device for calibration is the laser tracker. Laser tracker looses its precision for longer distances given for example by movement on the 7th axis and besides that it is quite expensive. Therefore a new calibration device was proposed (Fig. 1) [2] that should be capable to calibrate long robot workspace around the 7th axis and achieve similar accuracy as laser tracker for shorter distances.
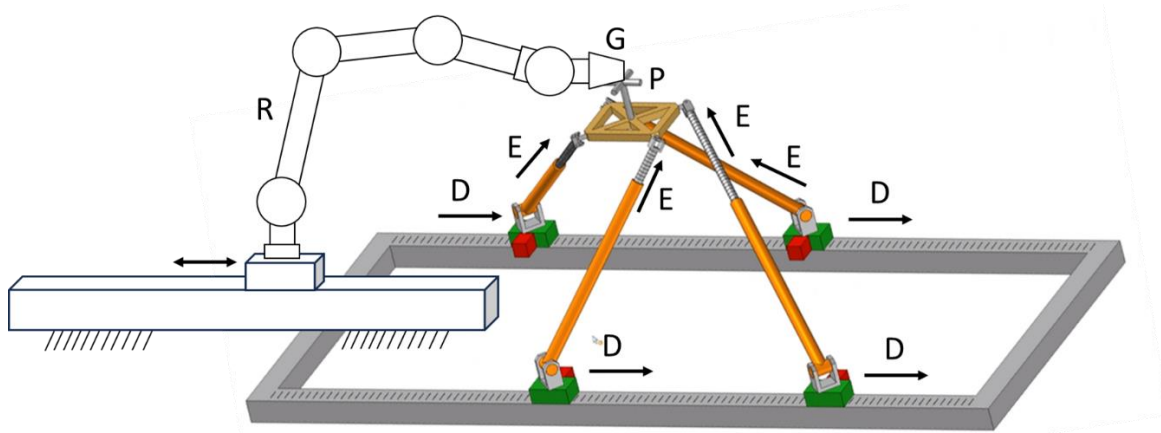

Fig. 1. Calibration concept of robot with new calibration device

Its concept is derived from the similar calibration device RedCaM (Redundant Calibration and Measuring Machine) [3, 1]. The industrial robot R using its gripper G is firmly connected with the platform P. The platform P is suspended through spherical joints on four legs with measured extensions E that are by joints with azimuth and elevation angles connected to four carriages with measured displacements D. The carriages move on two parallel sliding guides. The positions of displacements of carriages on these sliding guides are individually and independently driven by drives and measured. Such device uses redundant measurements that was successfully applied to RedCaM. The redundancy is given by usage of four legs instead of necessary minimum three legs and by usage of multiple (unlimited) positions of carriages. In each measured positions (that means the certain position of the robot gripper G and the positions of carriages D) the four displacements D and corresponding four extensions E are measured. The redundancy is quite big as multiple positions of each carriage is used. Therefore it was expected that similar accuracy would be achieved as RedCaM did. RedCaM besides self-calibration is capable to measure the position of its platform with accuracy equal to uncertainty of one single sensor, i.e. no addition of errors from sensors for determination of 6 DOFs of platform occurs.

Thus it was quite surprising that the accuracy of determination of 6 DOFs of robot gripper was quite poor. The analysis showed that the accuracy of determination of positions of centres of spherical joints between the legs and the platform P can be due to redundant measurement quite high but then the accuracy of determination of the position of the platform P (6 DOFs – 3 translations and 3 rotations) is at least 10 times lower than the accuracy of determination of positions of centres of spherical joints. The experience with laser tracers justifies that the accuracy of determination of positions of centres of spherical joints is high but the rest is mysterious.

Several modifications of the calibration device from Fig. 1 were proposed: usage of intersecting sliding guides, usage of skew sliding guides, usage of displacement of carriages not only along the sliding guides but also orthogonal side. Nothing helped.

Finally it was proposed to use the measurement of angles in azimuth, elevation or in both of them. This helped immediately and fully solved the problem. The determination of positions of platform from the positions of centres of spherical joints between the platform and four legs achieved accuracy 10 times better than previously. It was emotionally called the magic of angles. This paper is devoted to computational explanation of this reality.

3. Planar analyses

The planar variant of the calibration device is in Fig. 2. Two coordinate systems were chosen to calculate the position of the platform. The first, fixed, basic coordinate system x_1, y_1 and the second coordinate system x_p, y_p rigidly connected to the platform see Fig. 2. The carriage moves along the x_1 axis. The platform is rectangular with dimensions p by q. The centers of the rotational joints on the carriages are marked Si, the centers of the rotational joints on the platform are marked Ri. The lengths of the legs are $l_1 = \overline{S_1 R_1}$ and $l_2 = \overline{S_2 R_2}$.

Coordinates of the centers of rotational joints in the basic coordinate system x_1, y_1 are $S_1 = [\, x_1 \,;\, 0\,]$, $R_1 = [\, x_{R1} \,;\, y_{R1}\,]$, $S_2 = [\, x_2 \,;\, 0\,]$, $R_2 = [\, x_{R2} \,;\, y_{R2}\,]$. The essential constraints are

$$(x_{R1} - x_1)^2 + y_{R1}^2 = l_1^2, \tag{1}$$

$$(x_{R2} - x_2)^2 + y_{R2}^2 = l_2^2, \tag{2}$$

$$(x_{R2} - x_{R1})^2 + (y_{R2} - y_{R1})^2 = p^2. \tag{3}$$

The carriages S_1, S_2 are in multiple (at least two) different positions. The position of the platform is described by coordinates x_{1Op}, y_{1Op}, φ bounded by transformation equations

$$\mathbf{T}_{1p} = \mathbf{T}_x(x_{10p})\,\mathbf{T}_y(y_{10p})\,\mathbf{T}_\varphi(\varphi)$$

$$\mathbf{r}_{1Ri} = \mathbf{T}_{1p}\mathbf{r}_{pRi}, \quad i = 1,2 \tag{4}$$

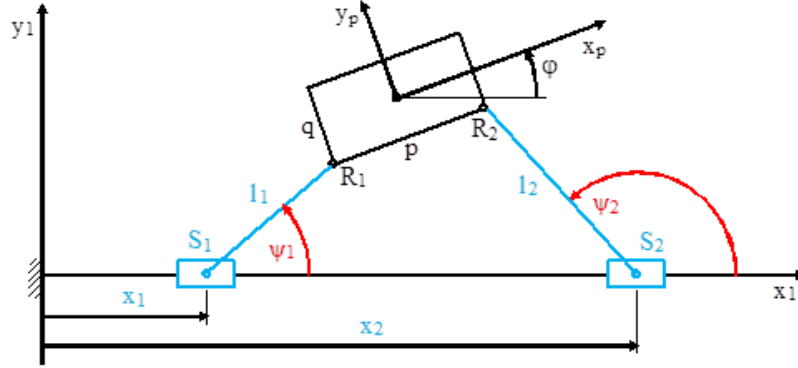

Fig. 2. Planar variant of calibration device

Ten different sets of equations and particular unknowns (e.g. $\sin(\varphi), \cos(\varphi)$ instead of φ) were used for determination of platform coordinates x_{1Op}, y_{1Op}, φ.

Then the concurrent measurement of angles ψ_1 and ψ_2 was considered. It leads to the constraints

$$x_{R1} = x_1 + l_1 \cos\psi_1, \tag{5}$$

$$y_{R1} = l_1 \sin\psi_1, \tag{6}$$

$$x_{R2} = x_2 + l_2 \cos\psi_2, \tag{7}$$

$$y_{R2} = l_2 \sin\psi_2. \tag{8}$$

And again ten different sets of equations and particular unknowns were used for determination of platform coordinates x_{1Op}, y_{1Op}, φ.

The solution of the constraint equations was done not only with precise measured values but also with varied values due to the influence of errors within the measurement. The ideal leg lengths were gradually shortened by $1 \cdot 10^{-5}$ m and corresponding errors in angles. The best results were obtained for unknowns x_{1Op}, y_{1Op}, $\sin\varphi$ and $\cos\varphi$.

The resulting deviations were for the case without measurements of angles $\Delta x_{1Op} = 18{,}38 \cdot 10^{-6}$ m, $\Delta y_{1Op} = 55{,}0 \cdot 10^{-6}$ m, $\Delta\varphi = 366 \cdot 10^{-6}$ rad and for the case with measurements of angles $\Delta x_{1Op} = 4{,}66 \cdot 10^{-6}$ m, $\Delta y_{1Op} = 2{,}22 \cdot 10^{-6}$ m, $\Delta\varphi = 30{,}4 \cdot 10^{-6}$ rad. This means 10 times improved accuracy.

4. Spatial analyses

The spatial variant of the calibration device is in Fig. 3. Similar description as in the case of planar variant is used. And again ten different sets of equations and particular unknowns were used for determination of platform coordinates x_{1Op}, y_{1Op}, z_{1Op}, Cardan angles φ_x, φ_y and φ_z.

The solution of the constraint equations was done not only with precise measured values but also with varied values due to the influence of errors within the measurement. The ideal leg lengths were gradually shortened by $1 \cdot 10^{-5}$ m and corresponding errors in angles. It was considered the variant of measurement of both azimuth and elevation for all legs, the variant of angular measurement of only azimuth or only elevation. The results of accuracy for variant of measurement of both angles and just measurement of elevation angles are similar. The case of only measurement of azimuths is worse. Therefore the variant with measurement of elevation

angles is favourite one. The dimensions were $d = 0,8$ m, $p = 0,24$ m, $q = 0,18$ m and leg lengths $\langle 0,8 ; 1,3 \rangle$ m.
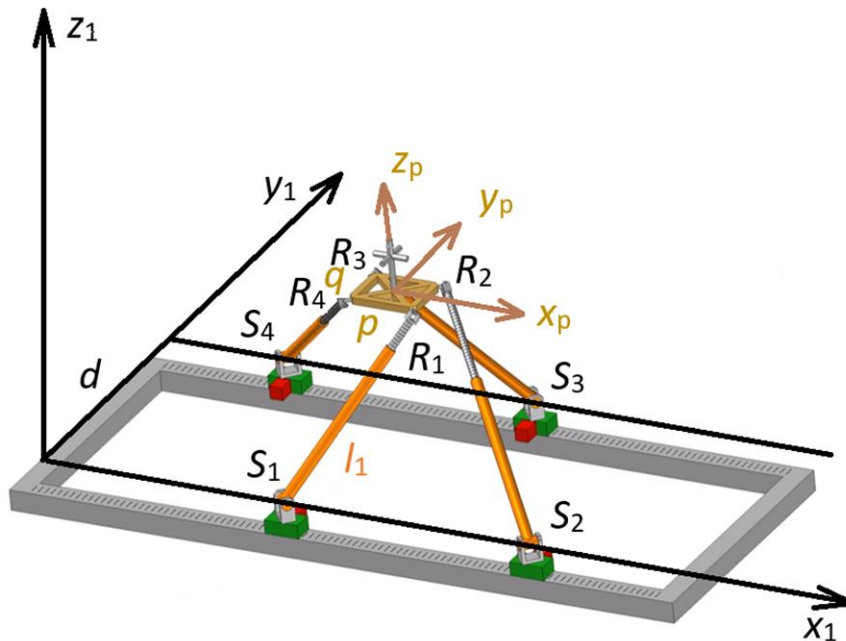

Fig. 3. Spatial variant of calibration device

The resulting deviations were for the case without measurements of angles $\Delta x_{1Op} = 123,8 \cdot 10^{-6}$ m, $\Delta y_{1Op} = 4740,0 \cdot 10^{-6}$ m, $\Delta z_{1Op} = 333,0 \cdot 10^{-6}$ m, $\Delta\varphi_x = 9380 \cdot 10^{-6}$ rad, $\Delta\varphi_y = 31600 \cdot 10^{-6}$ rad, $\Delta\varphi_z = 1858 \cdot 10^{-6}$ rad, for the case with measurements of both azimuth and elevation angles $\Delta x_{1Op} = 8,54 \cdot 10^{-6}$ m, $\Delta y_{1Op} = 7,86 \cdot 10^{-6}$ m, $\Delta z_{1Op} = 5,73 \cdot 10^{-6}$ m, $\Delta\varphi_x = 68,2 \cdot 10^{-6}$ rad, $\Delta\varphi_y = 82,0 \cdot 10^{-6}$ rad, $\Delta\varphi_z = 61,0 \cdot 10^{-6}$ rad and for the case with measurements of only elevation angles $\Delta x_{1Op} = 11,1 \cdot 10^{-6}$ m, $\Delta y_{1Op} = 19,42 \cdot 10^{-6}$ m, $\Delta z_{1Op} = 5,93 \cdot 10^{-6}$ m, $\Delta\varphi_x = 75,4 \cdot 10^{-6}$ rad, $\Delta\varphi_y = 43,2 \cdot 10^{-6}$ rad, $\Delta\varphi_z = 68,2 \cdot 10^{-6}$ rad. This means 10 to 100 times improved accuracy.

5. Conclusion

The measurement by the described calibration device requires the measurement of some angles besides the displacements. The particular suitable variants are described above.

This can be generalized. The determination of positions of points is possible with good precision just from measurement of lengths, i.e. in our case the lengths of legs from different displacements. But the determination of positions of bodies requires the measurement of some angles. The measurement of only displacements is not sufficient for reasonable accuracy.

Acknowledgement

References

[1] Beneš, P., Valášek, M., Šika, Z., et al., Experiments with redundant parallel calibration and measuring machine RedCaM, Applied and Computational Mechanics 1 (2007) 387-392.
[2] Valášek, M., Petrů, F., Šika, Z., et al., A device for measuring and/or calibrating the position of a body in space, Utility pattern, UPV 37244.
[3] Valášek, M., Petrů, F., Šika, Z., et al., Method and apparatus for measurement and/or calibration of position of an object in space, European Patent EP 1968773B1.

Assessment of solid lubricants for the wheel–rail interface

P. Voltr[a], S. Liberová[b]

[a]*Educational and Research Centre in Transport, Faculty of Transport Engineering, University of Pardubice, Doubravice 41, 533 53 Pardubice, Czech Republic*
[b]*Subsidiary Česká Třebová, Faculty of Transport Engineering, University of Pardubice, Nádražní 547, 560 02 Česká Třebová, Czech Republic*

1. Introduction

One of the key concepts of railway transport mechanics is adhesion, which means the ability to transmit tangential forces at the wheel–rail interface under normal loading. Tangential forces can act as traction or braking forces, and they take part in the guiding of a vehicle on the track. They cause stress in the material and influence the wear of wheels and rails.

The ratio of tangential force to normal force is limited by the coefficient of friction, which constitutes the main characteristic of the tribological conditions of the wheel–rail interface. There have always been methods to influence the tribological conditions, such as sanding in case of low adhesion. Today, the problem is treated in a complex way and referred to as friction management (see e.g. [3]), and its tools can be generally characterized as friction modifiers. This paper is focused on friction modifiers designed to cause low coefficient of friction (LCF), i.e. lubricants of the flange/gauge corner zone, specifically in the solid state.

Information on the performance of the lubricants is important for the evaluation of their suitability for use in railway operation and also serves as an input for the simulation of vehicle dynamics and wear of wheel/rail profiles.

2. Test methodology

The methodology for comparative testing of solid lubricants using a twin-disc machine is defined in the standard EN 15427-2-1 [1], adopting the procedure of the previous standard EN 16028. The procedure can be briefly described as follows: after mounting the test discs and setting the load, the machine runs at the required speed without lubrication of the discs. When the coefficient of friction (COF) reaches the initial level of 0.4, a solid lubricant sample (stick) is applied and loaded against one of the discs. If the lubricant is effective, the COF drops. After 200 s, the lubricant sample is removed without stopping the machine and the COF gradually rises again. The test ends when the COF reaches the reference dry level of 0.4. The lubricant sample is weighed to assess the lubricant consumption.

The standard recommends keeping creepage at 10–20 %, rotational speed 230–400 rpm (without indication of the disc diameter) and pressure in the contact of the discs 800–1200 MPa (without specifying whether this is mean pressure or maximum Hertzian pressure). The lubricant stick loading is not prescribed in the standard. The discs should be cooled by air flow.

The following outputs are evaluated:
- rate of COF decrease after applying the lubricant,
- steady COF value during lubrication of the discs,
- duration of COF increase up to the reference dry level after the lubricant is removed,
- consumption of the lubricant during the test.

The test discs should be manufactured from real wheel and rail materials (cut from wheels and rails) and shaped so that the required Hertzian pressure is reached by applying the force by the twin-disc machine. The lubricant sample is obtained by cutting the supplied sticks to dimensions suitable for a small-scale applicator.

3. Results

After the start of the test, the COF usually starts to increase and soon reaches the dry reference value. When the lubricant is applied, the COF drops. Depending on the lubricant performance, the lubricated COF levels as well as the general shape of the COF history during the test can differ considerably; examples for two different materials are shown in Fig. 1 (the bottom example shows better performance than the top one).
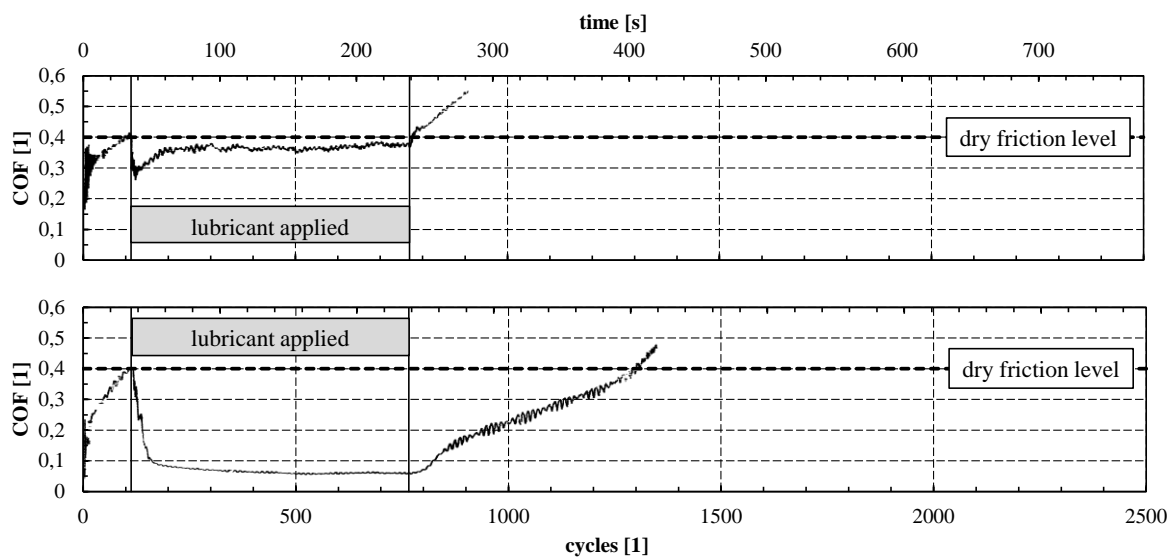

Fig. 1. Measured time histories of COF during twin-disc tests of two different solid lubricants

Evaluation of lubricant sample consumption, required by the standard, appears impracticable: weight loss after 200 s is extremely difficult to measure. If a particle is accidentally separated from the sample during manipulation or if a piece of metal debris from the disc is embedded in the stick, the result is significantly affected. It is suitable to depart from the standard and perform an additional test just to evaluate the lubricant consumption, where the weight loss is measured in multiple stages of a run taking about 100 000 cycles. The discs can be weighed during this test as well to find the effect of the lubricant on disc wear.

The methodology is designed for comparative testing, serving for comparison of various lubricant materials on a given test apparatus. Comparability of results obtained on different testing machines is not guaranteed. In the authors' experience, the methodology is not sufficiently specified and the results are not always consistent even with a single testing machine.

The study [2] shows that the performance in terms of COF may not be consistent with the effect on the wear of the discs (the wear can be sometimes reduced even if the COF stays quite high).

4. Factors influencing the results

Unsuitable thermal conditions (high temperature at the disc interface) can cause structural changes of the interface layer with the lubricant. It is also important that the discs should be cut out of such parts of wheels and rails that are not affected by plastic deformation of the surface

layers. Care must be taken to have high geometrical quality and surface roughness. Furthermore, loading of the lubricant sample is an important factor that influences lubricant performance and consumption. The standard requires a run-in shape of the stick end (conformal contact), but an alternative option has also been discussed that uses a flat end (line contact) which leads to more consistent conditions of transferring the lubricant particles to the disc surface.

5. Conclusions

The standardized testing methodology should be improved, which is the objective of the current research. A methodology that would produce absolutely valid and universally comparable results may not be possible to find. What can be done, however, is to provide such a test setup that the solid lubricant, together with the steel disc surfaces, operates in a mode relevant to real operation.

References

[1] EN 15427-2-1, Railway applications – Wheel/Rail friction management – Part 2-1: Properties and Characteristics – Flange lubricants, CEN, 2022.
[2] Evans, M., Lewis, R., Alternative twin-disc assessment of solid stick flange lubricants, 10th International Conference on Contact Mechanics, Colorado Springs, 2015.
[3] Tomeoka, M., et al., Friction control between wheel and rail by means of on-board lubrication, Wear 253 (1–2) (2002) 124–129.

Validation of thermoplastic composites forming simulations

V. Vomáčko[a,b,d], D. Brands[c,d]

[a]Faculty of Mechatronics, Informatics and Interdisciplinary Studies, Technical University of Liberec,
Studentská 1402/2, 46117, Liberec, Czech Republic
[b]Computations and Modeling Department, VÚTS, a.s., Svárovská 619, 46001, Liberec, Czech Republic
[c]Production Technology, Faculty of Engineering Technology, University of Twente, Drienerlolaan 5, 7522 NB Enschede, Netherlands
[d]ThermoPlastic Composites Research Center (TPRC), Palatijn 15, 7521 PN Enschede, Netherlands

1. Introduction

Press forming of thermoplastic continuous fiber composite materials is a high-efficiency manufacturing process enabled by the properties of thermoplastic matrices, which can be remelted multiple times. Flat laminates of desired layups are usually consolidated on large continual forming presses. The laminates are cut into blanks from which is then final part formed. These blanks undergo heating in an infrared oven, causing the thermoplastic matrix to melt. Subsequently, they are rapidly transported to the press area and formed. Tooling is heated to temperature that is lower than melting temperature of matrix, ensuring immediate cooling upon contact. This allows manufacturing cycle that can be done in a few minutes (depends on matrix material, part thickness, oven power, etc.), which is significantly lower time than for conventional manufacturing process utilizing thermoset prepregs and autoclave curing.

Numerical simulation tools, like AniForm [1], can be employed to design manufacturing process as they help in avoiding defects such as wrinkles or folds and optimizing mold geometry. The development of an appropriate mold design is a crucial element in the press forming process and typically follows an iterative process: The mold is manufactured, a part is press-formed, the part's geometry is examined, mold geometry is compensated, and so on. This is precisely where numerical simulations play a pivotal role.

Modelling of material behaviour during press forming is challenging due to interaction of several deformation mechanisms and dificulties with characterization of material in molten (matrix) state. The deformation of laminate in press forming process is driven by several mechanisms which can be divided to (i) Intra-ply mechanisms: in-plane shear, out-of-plane bending, fibre extension and compression and transverse extension and compression, (ii) Interface mechanisms: ply-ply, tool-ply friction and ply-ply, tool-ply separation.

These mechanisms can be described by various mathematical models. For example, intra-ply mechanisms can be modelled as (i) Elastic: linear/orthotropic, Mooney-Rivlin, etc. (ii) Viscous: Newtonian fluid, Cross-viscosity fluid, etc. Usually superposition of several models is employed, such that the total stress results from the addition of the selected models individual stress components. Furthermore, characterization methods for thermoplastic composites in processing temperatures are not standardized.

With wide array of choices, many simulation settings are possible. To evaluate the capabilities and accuracy of these simulations, a robust validation tool becomes essential. In this work, experimental campaign for validation of press forming simulations was carried out using double-curvature geometry.

2. Dome forming experiments

Two commercially available unidirectional thermoplastic composite materials, namely Toray TC1225 (T700 carbon fiber with low melt PAEK matrix) and Solvay APC (AS4D carbon fiber with PEKK matrix) were examined. The layup and width of specimens were varied to examine formability and wrinkling severity. The test matrix is summarized in Table 1, 0 fiber direction is aligned with specimen longer dimension and right hand rule is applied for other directions. For every specimen set were made 3 repetitions.

Table 1. Overview of specimen sets

Layup	Width [mm]
$[0, 45, 90, -45]_s$	40
$[0, 45, 90, -45]_s$	80
$[90, -45, 0, 45]_s$	80
$[0, 90]_{2s}$	80

The plies were cut from the role of material and stacked into mold according to desired layup and flat laminates were consolidated. Laminates were cut into rough dimensions and dot pattern for deformation tracking was applied. The dimensions of the pattern were: dot size 1 mm with 3 mm spacing. The dot pattern was applied by combination of exposure mask, photoresist film, sandblasting and heat resistant spray paint. The specimens were then machined to final dimensions $295 \times (40, 80)$ mm.

Dot pattern of flat laminate was digitized by photogrammetry technique. The setup consists of remote-controlled turntable, polarized lighting and digital camera. Photographs were captured at 16 equidistant angles. These photos were further analysed in PhotoModeler software [3] where dots are automatically marked, referenced and 3D position of dots with its precision can be exported. Photogrammetry is then repeated after press forming in the same manner. Example photos before and after press forming are depicted in Fig. 1.

Press forming experiments were carried out on 200-ton press from Pinette Emidecau Industries at the TPRC. Steel hemisphere tool was used. Laminates were placed in the shuttle frame, heated in infra-red oven, rapidly transported and press formed (see Fig. 2). The tooling was not fully closed but additional 2 mm gap was left to be able clearly observe wrinkles.

The digitized dot patterns are meshed in Matlab with a regular triangular mesh. Green-Lagrange strains, shear angles and fiber directions are calculated as in the previous publication by Brands et al. [2]. The results of 3 specimens are averaged.
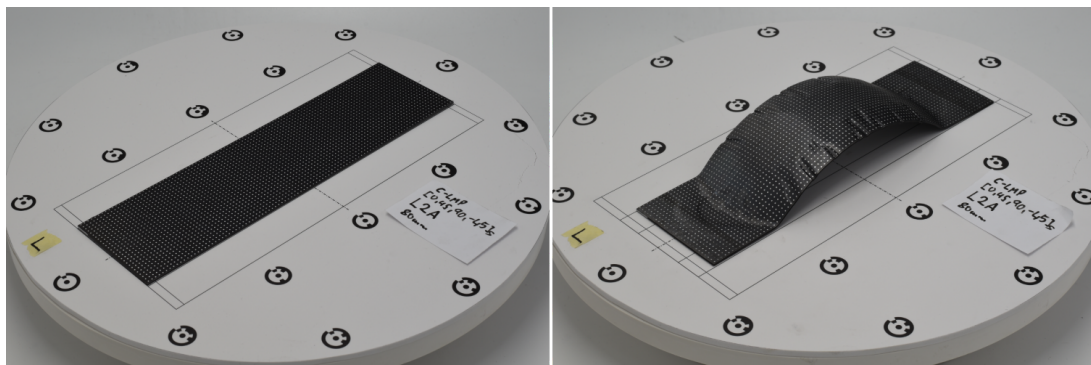

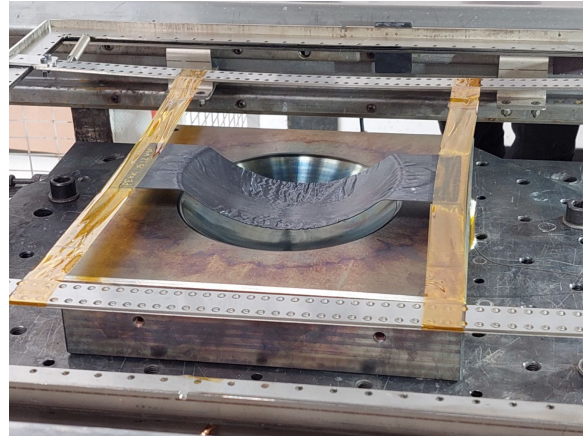Fig. 1. Example of photos for photogrammetry, before and after forming

Fig. 2. Lower tool, press formed specimen and laminate handling setup

3. Results and discussion

Fig. 3 shows one selected part per specimen set of 4 different layups for both materials. The Solvay APC material exhibits slightly better formability compared to the similar Toray TC1225 material.

For both 40 mm quasi-isotropic (QI) $[0/45/90/-45]_s$ specimens, we observe only minimal wrinkling, which is likely to disappear when the molds fully close. However, when the same layup is scaled to a width of 80 mm, we observe more pronounced wrinkles. Interestingly, when this layup is rotated 90 degrees clockwise, resulting in the $[90/-45/0/45]_s$ layup we still observe wrinkles, but they are less severe. This phenomenon may be attributed to the presence of the 90-degree layer on the laminate's surface, which has less resistance to bending compared to the outer 0-degree ply and may also experience some extension in the transverse direction (longitudinal direction of the specimen). The ply-ply friction is the main deformation mechanism for QI laminates and in-plane shear deformation is limited. In contrast, for cross-ply $[0, 90]_{2s}$ specimens, we observe a significantly higher degree of shear deformation compared to QI laminates. This results in lower levels of out-of-plane deformation and, consequently, fewer wrinkles in the material.
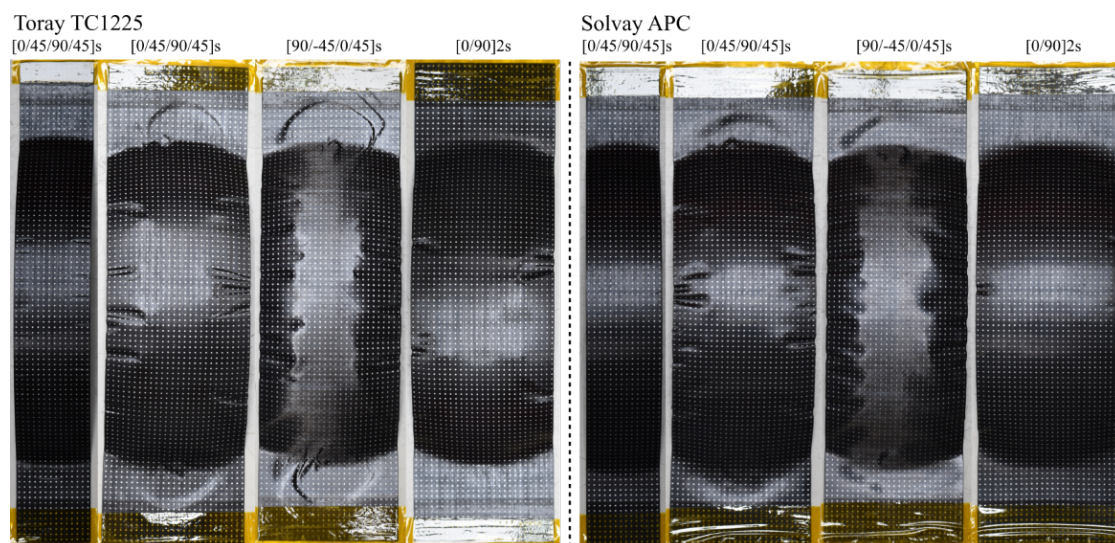

Fig. 3. Press formed specimens

Comparison of Green-Lagrange shear strain average over 3 specimens between QI and cross-ply specimens from TC1225 is visible in Fig. 4. This picture also shows Green-Lagrange shear strains of two AniForm simulations with different material models employed and demonstrates possible use of presented dataset for validation of press forming simulations.
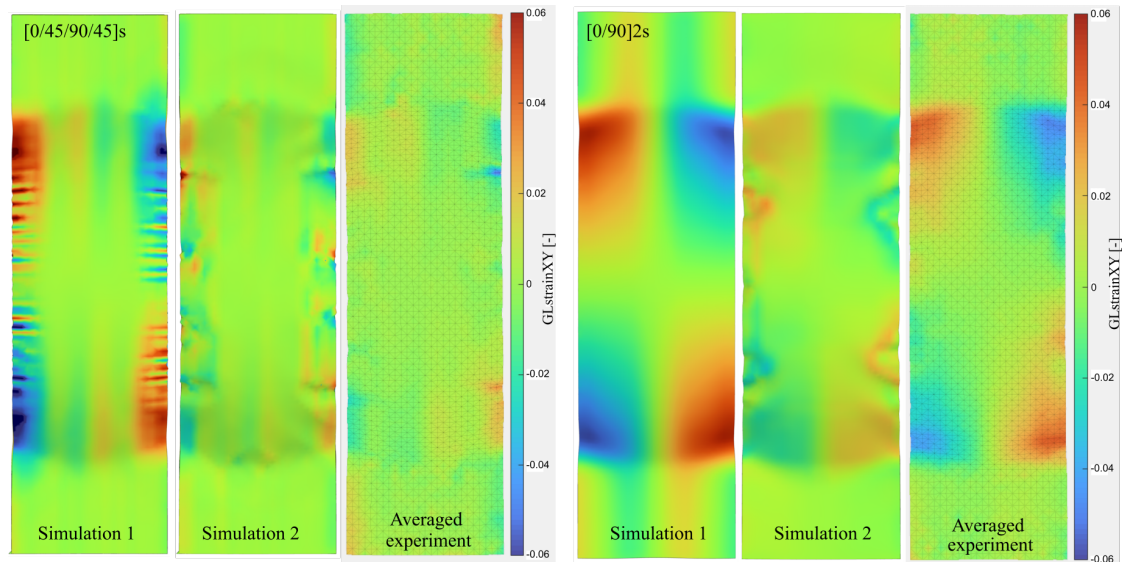

Fig. 4. Comparison of Green-Lagrange shear strains of two simulations with different material models employed and experimentally obtained Green-Lagrange shear strain for QI and cross-ply layups of TC1225 material

4. Conclusion

Press forming experiments of two unidirectional thermoplastic composite materials were performed. To track deformation during the forming process, a dot pattern was applied and subsequently digitized by photogrammetry technique and Green-Lagrange strains were calculated. This obtained dataset can serve as basis for validation of press forming simulations.

Acknowledgements

References

[1] AniForm Engineering B.V., AniForm Virtual Forming.
[2] Brands, D., van Kammen, K., Wijskamp, S., Grouve, W. J. B., Akkerman, R., In-plane deformation measurements for validation of composite forming simulations, Materials Research Proceedings 28 (2023) 293-304.
[3] PhotoModeler Technologies, PhotoModeler Premium.

Propensity assessment of tensile surface structures to water ponding

Z. Zajac^{a,b}, R. Lang^{a,b}, I. Němec^{a,b}

^{a}*Institute of Structural Mechanics, Faculty of Civil Engineering, Brno University of Technology, Veveří 331/95, 602 00 Brno, Czech Republic*
^{b}*FEM consulting, s.r.o., Veveří 331/95, 602 00 Brno, Czech Republic*

1. Introduction

Water accumulation on a tensile surface structure is a well-known phenomenon called the ponding effect. The risk of structure damage or failure is increased due to an accumulated load. Distinguishing whether the structure is sufficiently designed could be a highly demanding task even for professionals. The research published in [4] concluded that the accumulated load on a tensioned structure is more dangerous than on an inflatable structure. Hence, the ponding effect occurrence must be avoided.

In contrast with conventional buildings, periodic variable loading may affect the prestress level and thus change a force distribution in the structure [2]. Another reason for regular maintenance is the possibility of drainage blockage. The actual failures on structures caused by accumulated load were studied in [5]. The authors of research [1] summarized the recommendations for the basic shapes of tensile surface structures to avoid the undesired stress increase in the structure.

2. Methodology

To assess the structure of water accumulation propensity the algorithm for the lowest point and its catchment area detection was developed. The input for the algorithm is an arbitrary number of discretized surfaces, a specific weight of liquid and an amount of precipitation if required.

Firstly, the local lowest points on the finite element mesh are found. Each point is surrounded by its catchment area defined by the concentric slope. This area is found to determine the amount of water that may accumulate in this particular area called the pond. The whole process is based on physical laws and fluid behaviour. Two ponds are suitable for merging if they share a drainage point. Such a point is defined as the lowest point on the edge of the pond where water drains.

The level of the pond surface bounds the liquid volume. This volume could be calculated as a numerical integration over the region Ω. The region Ω is defined by the pond surface. The discretization of the volume is determined by the finite element mesh of the surface. Then the volume of each element is calculated as $dV_i = A_{p,i} \cdot dz$, where $A_{p,i}$ is the projected area of the finite element on the horizontal XY plane and dz is the height of the water column above the centre of gravity of the element. The total volume of water in the pond $V_{tot} = \sum_{i=1}^{n} dV_i$, where n is the number of flooded elements.

The real structure must withstand the always-changing climate loading. To assess the structure in real conditions every possible risk state of the load must be verified. That is possible only if the amount of water applied to the structure is controlled.

The amount of precipitation p consideration is essential because it affects the stress state in the structure significantly. Hence, it is the crucial input parameter of the algorithm and it is specified as a volume of water per collection area. The algorithm compares the total volume of the pond and the possible volume considering the precipitation. The subsequent process determines the level of the pond considering the possible amount of water on the structure. So the surface level of the pond is found iteratively by the bisection method.

The tool to facilitate a tensile surface structure design was developed and implemented in the finite element solver by FEM consulting, s.r.o. The basics of the algorithm described above were presented at the 20th International Conference of Numerical Analysis and Applied Mathematics at Heraklion, Crete. However, the complexity of the issue was high enough to initialize further development thus the algorithm was improved and new features developed.

The most important task to deal with was the pond regions merging. Subsequent development focused on the algorithm implementation, utilization and results evaluation.

The last but foremost issue to deal with was a proper load calculation and application to the finite element model. The principle of virtual work states that the variation of the external virtual work δW^{ext} equals the variation of the internal virtual work δW^{int}.

The virtual work of external forces $\mathbf{R}$ in the new configuration at time $(t + \Delta t)$ assuming the linearized equilibrium equations

$$^{t+\Delta t}\mathbf{R} = \int_{^tV} {}^{t+\Delta t}\mathbf{f}^V \, \delta\mathbf{u}^V \, {}^t\mathrm{dV} + \int_{^tS} {}^{t+\Delta t}\mathbf{f}^S \, \delta\mathbf{u}^S \, {}^t\mathrm{dS} + \sum {}^{t+\Delta t}\mathbf{F}\delta\mathrm{u}, \tag{1}$$

where ^tV is the volume and ^tS is the surface area, $\delta\mathbf{u}$ is the nodal displacement variation and $^{t+\Delta t}\mathbf{f}^V$, $^{t+\Delta t}\mathbf{f}^S$, $^{t+\Delta t}\mathbf{F}$ represents volume, surface and nodal forces. The integral $\int_{^tS} {}^{t+\Delta t}\mathbf{f}^S \, \delta\mathbf{u}^S \, {}^t\mathrm{dS}$ represents variable nonlinear external load dependent on deformation [3].

3. Results and discussion

Firstly, the algorithm was verified on a hemisphere filled with water. The specific weight of water γ was $10.0\,\mathrm{kN/m^3}$. The radius r of the rigid structure was $2.0\,\mathrm{m}$. The volume of the hemisphere can be calculated analytically as $V = 0.5 \cdot \frac{4}{3} \cdot \pi \cdot r^3 = 16.755\,\mathrm{m^3}$. Therefore, the sum of forces in the vertical direction Z is $F = V \cdot \gamma = 167.6\,\mathrm{kN}$. The analytically calculated force corresponds with the force numerically obtained. The water depth in the hemisphere filled with water is in Fig. 1a.

The amount of precipitation p was $0.5\,\mathrm{m^3}$ of water per square meter to verify the precipitation algorithm. The volume of water on the structure $V_w = p \cdot A = p \cdot (\pi \cdot r^2) = 2\pi\,\mathrm{m^3}$, where A is the hemisphere area projected in global Z. The volume of a spherical cap can be calculated as $V = \frac{\pi \cdot v^2}{3} \cdot (3 \cdot r - v)$, where v is the height of the spherical cap. Analytical solution equals $v = 1.11\,\mathrm{m}$ and corresponds to the results numerically obtained in Fig. 1b.

Secondly, a membrane surface in the shape of a hyperbolic paraboloid in Fig. 2 was studied. The shape was chosen due to its popularity and common problems with insufficiently designed structures. Despite the anticlastic curvature, the load applied to the structure may cause the change of the geometry to synclastic curvature [2].

Multiple computational models were created and analyzed to highlight the issue of poorly constructed or maintained structures. The corner nodes of the membrane surface form a square of the side length L equal to $5.0\,\mathrm{m}$. The height changes from $0.4\,\mathrm{m}$ to $1.2\,\mathrm{m}$. The fabrics
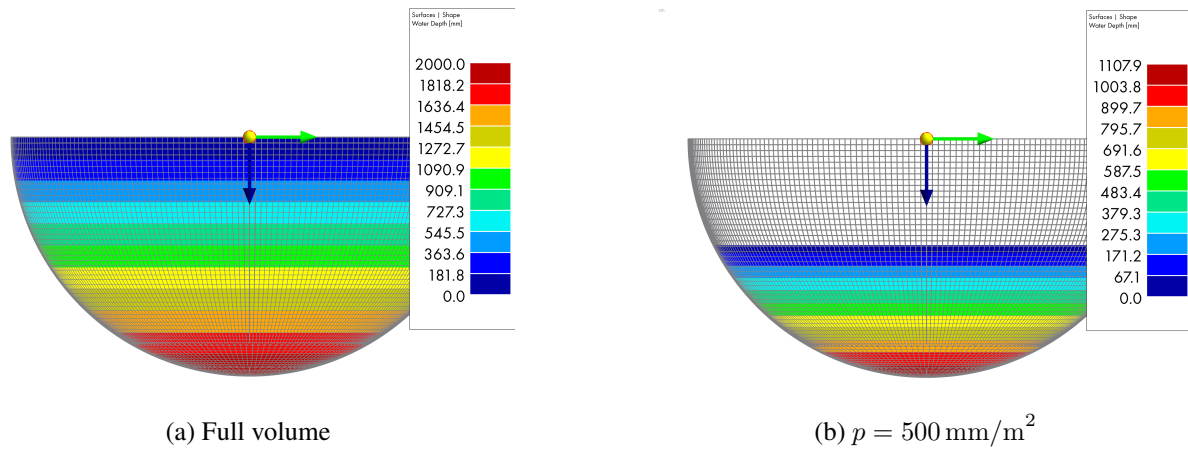
(a) Full volume

(b) $p = 500\,\mathrm{mm/m^2}$

Fig. 1. Water depth in hemisphere filled with water

(a) Hyperbolic paraboloid dimensions

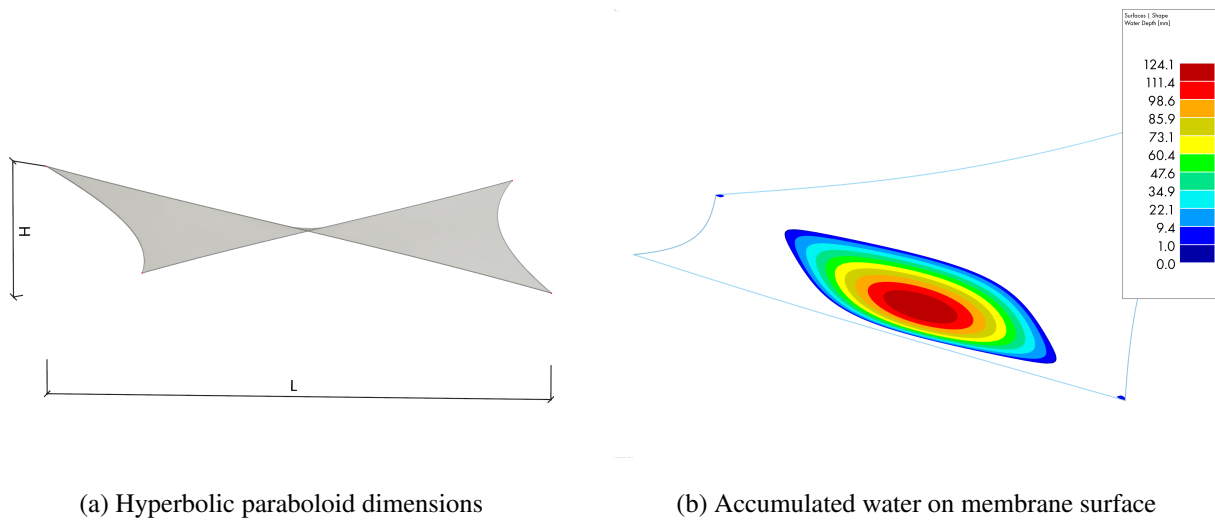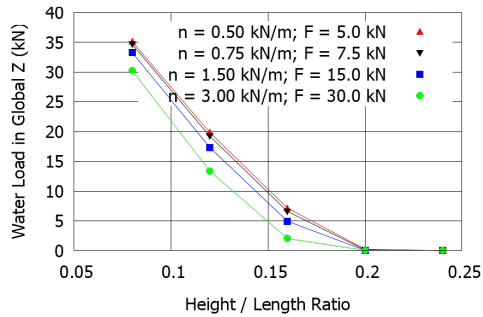(b) Accumulated water on membrane surface

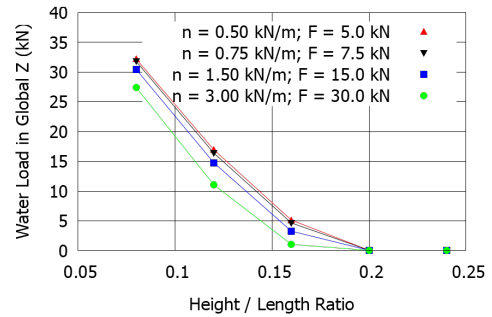Fig. 2. Water load accumulated on the membrane structure

coated with PVC type I and III for membrane surface represent common materials used for the tensile surface structures. Recommendations for the prestress level in the surface were intentionally violated to examine insufficiently designed structures. The level of prestress in the membrane changes from $0.50\,\mathrm{kN/m}$ to $3.00\,\mathrm{kN/m}$. There are prestressed cables on the edge of the membrane made of steel S235. The prescribed forces for the form-finding process vary from $5.0\,\mathrm{kN}$ to $30.0\,\mathrm{kN}$ to ensure the same curvature radii on the edge of the surface. To initialize the deformation the surface force $2.0\,\mathrm{kN/m^2}$ was applied.

There are sums of water loads accumulated on the structure in Fig. 3. The results imply the importance of the initial design of the support points. More prestressed structures do not show significantly higher resistance to water ponding. The amount of accumulated water on the surface was approximately the same in case of the same height-to-length ratio. As anticipated, the models with higher curvature in both directions were more resistant to load accumulation than those with flatter surfaces.

The influence of the fabric type is another important result of the case study. The stronger material may imply higher resistance against the ponding effect occurrence. However, the surfaces with the same topology show almost the same inclination to load accumulation. Stronger materials must be prestressed to higher levels so the supporting structure must withstand higher forces. Therefore, the financial costs may be reduced by using a cheaper material with a lower prestress level on the properly designed structure.

215

(a) PVC type I   (b) PVC type III

Fig. 3. Water load accumulated on the membrane structure

4. Conclusion

In conclusion, the usage of the algorithm for ponding effect detection and membrane surface evaluation was presented. The study focused on the proper structure dimensions determination. The influences on the tendency to load accumulation were evaluated in the case study.

The results imply that the initial dimensions affect the tendency for water accumulation the most. Hence, the proper structure dimensions may lower the internal forces and thereby reduce financial costs.

Acknowledgement

References

[1] Bridgens, B., Birchall, M., Form and function: The significance of material properties in the design of tensile fabric structures, Engineering Structures 44 (2012) 1-12.

[2] Forster, B., Mollaert, M., European design guide for tensile surface structures, Tansinet, Brussels, 2004.

[3] Lang, R., Algorithms for design and analysis of membrane structures, Ph.D. thesis, Brno University of Technology, Brno, 2019.

[4] Samy, A., Yuan, X., Zhang, Y., Zhang, W., Study on bagging effect and rupture failure of membrane structures, Engineering Structures 232 (2021) No. 111880.

[5] Weller, F., Common problems in the design and construction of membrane structures, Proceedings of the 8th International Conference on Textile Composites and Inflatable Structures – Structural Membranes 2017, Munich, 2018, pp. 147-177.

A short study on self-balancing of vertical rotors mounted in passive contactless bearings

J. Zapoměl[a,b], J. Kozánek[b]

[a]*Faculty of Mechanical Engineering, VŠB-Technical University of Ostrava, 17. listopadu 15, 708 00 Ostrava, Czech Republic*
[b]*Institute of Thermomechanics, Czech Academy of Sciences, Dolejškova 5, 182 00 Praha, Czech Republic*

1. Introduction

Energy losses and wear of the support elements of high-speed rotors can be reduced by mounting the rotors in stable passive contactless bearings, the operation of which is based on magnetic levitation. The goal of the conducted research was to investigate applicability of self-balancing device added to vertical rotors supported by bearings showing low stiffness and damping, which is a specific property of passive magnetic bearings.

Energy losses and wear of the support elements of high-speed vertical rotors can be reduced by mounting the rotors in passive contactless bearings, the operation of which is based on a stable magnetic levitation. This is offered by utilizing interaction between the activated superconducting material and a permanent magnet or interaction between two permanent magnets separated by diamagnetic material.

The dynamical response of rotors on unbalance excitation depends on stiffness and damping of the support elements and eccentricity of the rotor center of gravity. In cases when the unbalance is induced during running the rotating machine like due to occurrence of ice layers or liquid drops on rotating parts, sedimentation of dust particles, or by variable deformation of the rotor flexible components, the technical solution making its reduction possible consists in application of a self-balancing device. It consists of movable weights attached to the rotor that due to their inertia effects take such a position, at which they compensate the rotor unbalance [1], [2]. This paper deals with applicability and efficiency of self-balancing devices added to vertical rotors supported by bearings having very low stiffness and damping, which corresponds to the properties of magnetic frictionless bearings.

2. The investigated rotor system

The investigated system (Fig. 1) is an axisymmetric vertical rotor consisting of a shaft and one disc. The rotor is loaded by a driving moment acting on the rotor in the direction of its axis of rotation (axis x), and by the disc unbalance. The lateral movement of the rotor is affected by external damping. The driving moment sets the rotor into rotation of controlled angular velocity. The rotor bearings show very little stiffness and no damping. To eliminate lateral vibration of the rotor produced by the unbalance excitation, it is equipped with a self-balancing device formed by two balancing weights. The weights can move on circular trajectories in the plane perpendicular to the rotor axis. They are coupled with the rotor by contact couplings in the radial and axial directions and by a viscous one in the tangential direction.

In the computational model the rotor is considered absolute rigid, stiffness of the bearings linear, and external damping and damping between the disc and the balancing weights viscous and linear. Because of the rotor symmetry, the disc motion is planar.
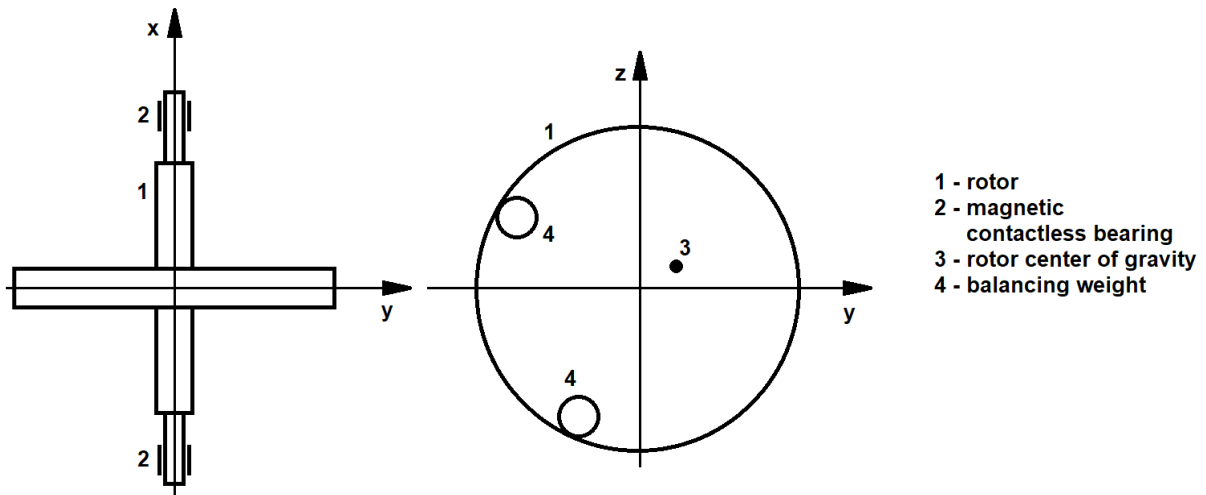
Fig. 1. The investigated rotor

The goal of the investigations was to determine time history of the disc center displacement after the rotor run-up to study efficiency of the self-balancing device.

3. Results of the simulations

The technological parameters of the investigated rotor are: mass of the rotor 130 kg, radial stiffness of one bearing 0.01 N/m, eccentricity of the disc center of gravity 50 μm, the number of balancing weights 2, mass of each balancing weight 21 g, radius of movement of each balancing weight 300 mm, and the damping coefficient of the coupling between the balancing weight and the rotor disc 1 Ns/m. The rotor angular velocity is time variable and approaches to the steady state value of 500 rad/s. Its time history is depicted in Fig. 2.
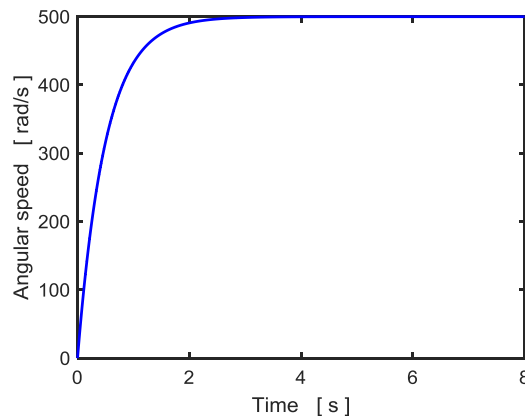

Fig. 2. Time history of angular velocity of the rotor rotation

The task was to analyze efficiency of the self-balancing device of a rotor supported by bearings of very low stiffness.

A simple analysis gives the undamped natural frequency of the rotor system 0.012 rad/s, which implies the rotor runs in the over-resonance area. If no self-balancing device were applied, the disc center would move after vanishing the transient component of the vibration on a circle, the radius of which would approach with rising speed to the disc eccentricity (50 μm).

No external damping was applied in the first investigated case. Fig. 3 shows the time history of the disc center displacements in the y and z directions. The simulation results indicate that no self-balancing effect can be observed.
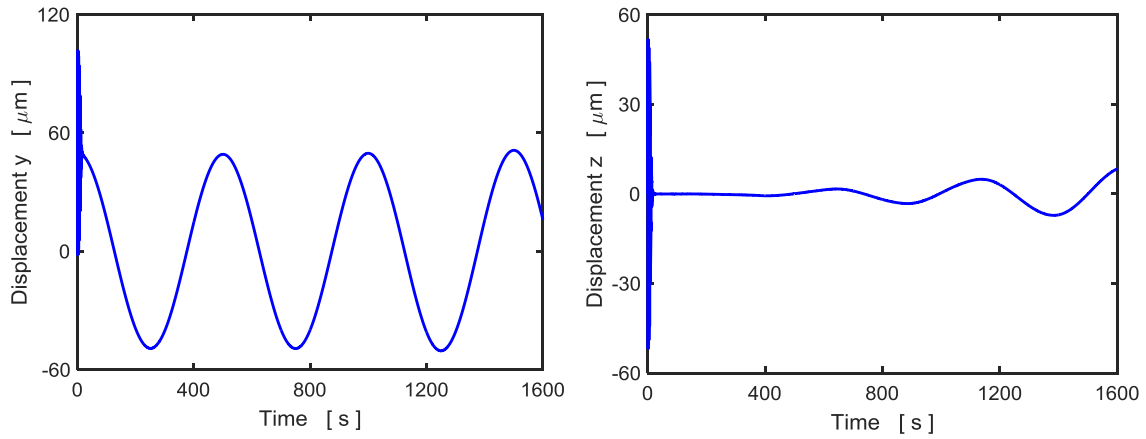
Fig. 3. Time history of the disc center displacements (no external damping)

In the second investigated case, the external damping of non-constant magnitude was added. Its initial value of 1000 Ns/m was reduced to zero during the time interval between 15 and 20 s from setting the rotor into rotation as depicted in Fig. 4.
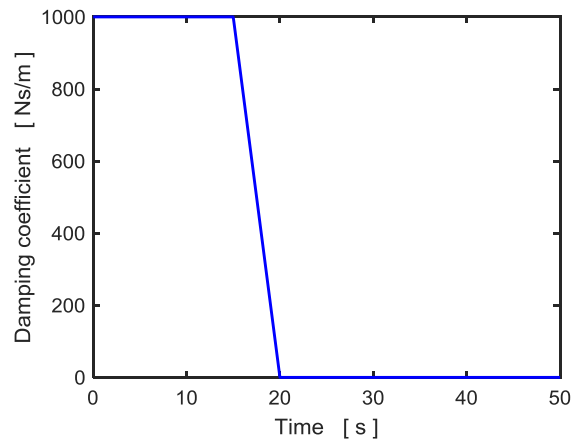

Fig. 4. Time history of viscous external damping coefficient

The time history of the disc center displacements in the y and z directions can be seen in Fig. 5. The steady state orbit is drawn in Fig. 6.
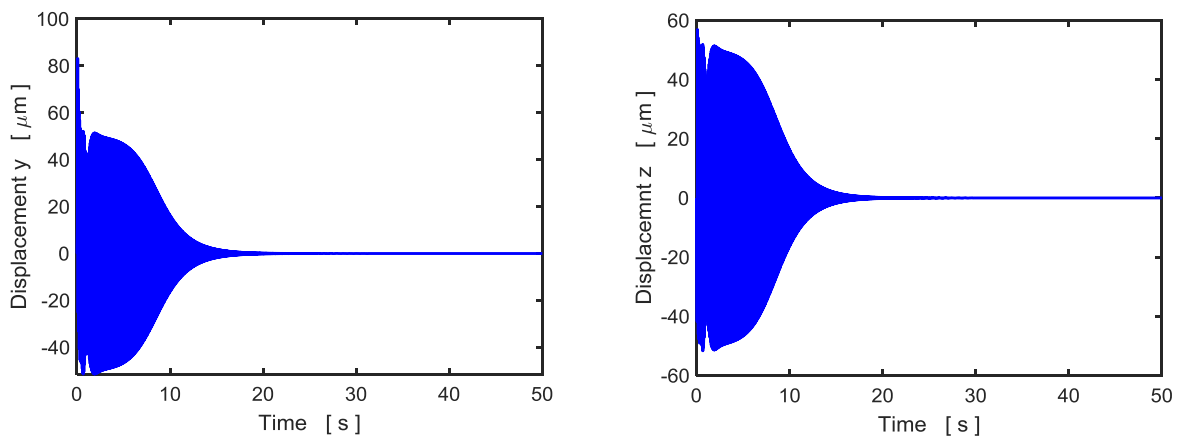

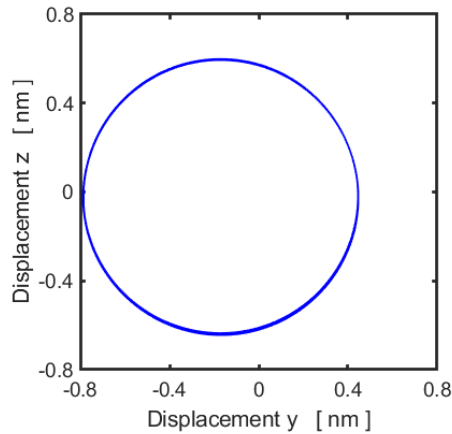Fig. 5. Time history of the disc center displacements (external damping applied)

Fig. 6. The steady state orbit of the disc center (external damping applied)

The simulation results show that after some period of the transient vibration the self-balancing effect starts, and the vibration amplitude of the disc center approaches to zero.

4. Conclusions

The results of the analysis of self-balancing of vertical rotors supported by bearings of low stiffness show that (i) the self-balancing effect can be achieved only if the rotor vibration is affected by some amount of external damping, (ii) if the external damping is applied the self-balancing device makes it possible to reduce the rotor vibration amplitude, (iii) because of low stiffness the steady state orbit can be slightly moved from the initial position of the disc center, and (iv) decrease of the external damping does not induce transient vibration of increased magnitude.

Acknowledgements

References

[1] Jung, D. Y., DeSchmidt, H., Limit-cycle analysis of planar rotor/autobalancer system supported on hydrodynamic journal bearings, Proceedings of the ASME 2011 International Design Engineering Conferences & Computers and Information in Engineering Conferences, 2011, pp. 1 - 12.
[2] Jung, D. Y., DeSchmidt, H., Nonsynchronous vibration of planar autobalancer/rotor system with asymmetric bearing support, Journal of Vibration and Acoustics, 139 (2017) 1-24.

Experimental identification of friction model parameters for selected materials

J. Zavřel[a], Z. Šika[a], M. Hajžman[b]

[b]*Department of Mechanics and Mechatronics, Faculty of Mechanical Engineering, Czech Technical University in Prague, Technická 4, 160 00 Praha 6, Czech Republic*
[b]*Department of Mechanics, Faculty of Applied Sciences, University of West Bohemia, Univerzitní 8, 301 00 Plzeň, Czech Republic*

Passive effects are present in all types of mechanisms, especially in imperfect joints. Their properties are reflected in all aspects of the system's behaviour. A mathematical models of imperfections are essential in not only modelling the behaviour of the system, but also in controlling it. Passive effects are based on various effects such as friction, slip-stick effect, adhesion and more.

Very often, simple models based on Coulomb friction are used. Such model considers the frictional force in the opposite direction of the velocity proportional to the normal force. These simplest models are independent on the relative speed of the moving parts, and the passive effects are directly proportional to the normal force. For more complex models of friction and non-linear effects, variant material properties and the influence of speed and damping of contact points or surfaces are considered. In the real cases, it is often a combination of several effects [1]. There is considered the sticking, sliding and Striebeck effect. One of the advanced models of friction with nonlinear effects is the LuGre model [3].

LuGre model can be expressed as follows

$$\mu = \sigma_0 z + \sigma_1 \dot{z} + \sigma_2 v, \tag{1}$$

$$\dot{z} = v - \sigma_0 \frac{\|v\|}{g(v)} z, \tag{2}$$

$$g(v) = \mu_c + (\mu_s - \mu_c) e^{-\left(\frac{\|v\|}{v_s}\right)^2}, \tag{3}$$

where μ is the coefficient of friction, z is the average deformation of bristles, $\dot{z}$ is the relative velocity between two surfaces, σ_0 is the bristle stiffness coefficient, σ_1 is the micro-damping coefficient, σ_2 is the viscous coefficient, $g(v)$ is a velocity-dependent function that can reproduce both the Coulomb friction and Stribeck effect, v_s is the Stribeck velocity, μ_c is the coefficient of kinetic friction and μ_s is the coefficient of the static friction.

Correct setting of friction model parameters plays a key role. Although there are known coefficients of friction for basic materials, these are approximate values that do not reflect the individual composition of the material, the current state of the surface or local conditions. It is also not easy to find the right parameters for different combinations of materials. It is even more difficult for materials that are not common. This applies for composite materials, such as various types of plastics or rubbers filled with glass or carbon fibres. The parameters for friction models for such materials can be determined only experimentally [2]. The question is also how to determine the material parameters if only a smaller sample is available.

For the identifying the parameters of different friction models, a measuring device was made (Fig. 1). This measuring device consists of a non-rotating part and a motor-driven rotating part. Samples of the measured materials are placed between these two parts. When the first sample rotates and the surface with the second sample comes into contact, friction occurs. It is possible to change the axial pressure force and the rotation speed. It is also possible to apply a radial force for measurement of ball-bearing or sliding-bearing. The torque is transferred from the rotating part through the sample to the non-rotating part and is measured.
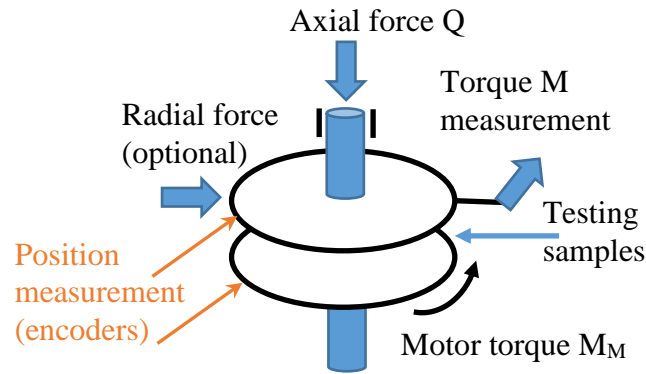

Fig. 1. Scheme of the measuring device principle

For two circular material samples with radius R, axial loading force Q and transmitted torque M, the friction coefficient μ can be evaluated for the Coulomb friction model from the equation

$$M = \frac{2}{3}Q\mu R \qquad (4)$$

To evaluate non-linear effects, the relative rotation of the samples must also be measured (Fig. 1). This makes it possible to evaluate such effects as adhesion or slip-stick effect. The coefficients of friction of a combination of different materials under different conditions were experimentally evaluated. Both new materials and after running-in, or in the presence of lubricant. The methodology for obtaining the LuGre model coefficient was proposed.

Acknowledgement

References

[1] Johanastrom, K., Canudas-de-Wit, C., Revisiting the LuGre friction model, IEEE Control Systems Magazine 28 (6) (2008) 101-114.
[2] Rizos, D. D., Fassios, D. S., Friction identification based upon the LuGre and Maxwell slip models, IEEE Transactions on Control Systems Technology 17 (1) (2009) 153-160.
[3] Zhen, Z., Xudong, Z., Qi, W., Zhang, Ch., Yiyong, S., Bin, L., Modeling and simulation of point contact multibody system dynamics based on the 2D LuGre friction model, Mechanism and Machine Theory158 (2021).

Modelling of bowed fuel assemblies vibration in mixed reactor core

V. Zeman[a], Z. Hlaváč[a], Š. Dyk[a]

[a]NTIS – New Technologies for the Information Society, Faculty of Applied Sciences, University of West Bohemia, Univerzitní 8, 301 00 Plzeň, Czech Republic

1. Introduction

A pressurized-water reactor core includes a large number of fuel assemblies (FAs) of the same or different types. During the reactor operation, FAs can be statically deformed in the lateral and/or torsional direction. This phenomenon is called FA bow [1, 3]. This contribution is focused on the mathematical modelling of the vibration of two different types bowed FAs in interaction. The aim of the modelling is a description of changes in FA's dynamic behaviour in the case of contacting FAs in the mixed reactor core.

2. Concept of the modelling

The presented method is based on the two-stage modelling concept, whose scheme is depicted in Fig. 1. The *first-stage model* represents the global nonlinear model of the VVER 1000 type reactor. The original reactor model [4, 5] with homogeneous reactor core (HCR) was modified
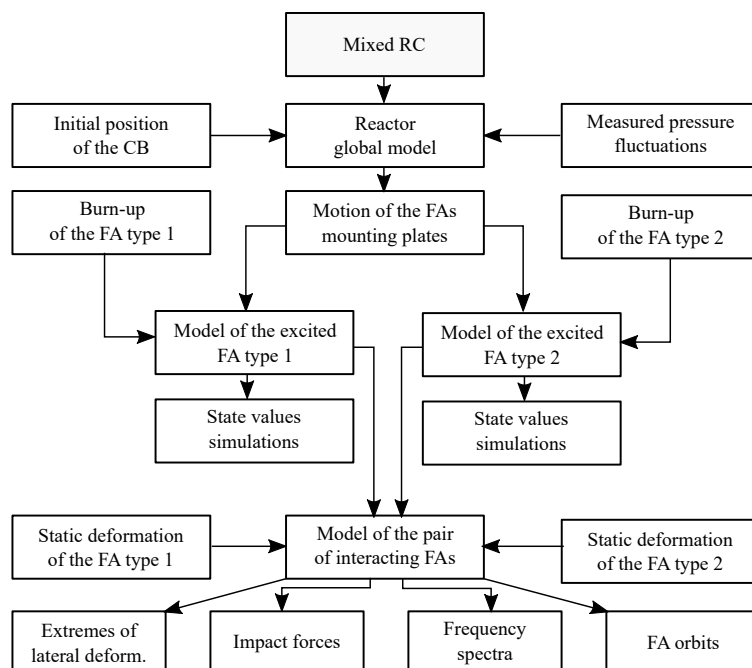

Fig. 1. Scheme of the two-stage modelling of the FAs vibration in the mixed reactor core (FA = fuel assembly, RC = reactor core, CB = core barrel)

for the mixed reactor core (MCR) containing FAs of two types. This new reactor model was created under the following assumptions:

1. FAs of both types were modelled as 1D beam-type continua based on the modal values of their detailed models.
2. An excitation of the reactor is based on time-series of the pressure fluctuations measured at the coolant inlet to reactor core [2] under standard operation.
3. Motion of the FAs mounting plates investigated on the global reactor model is the source of the FAs kinematic excitation.

In the *second-stage model*, both FA types are modelled more in detail (see Fig. 15 in [1]). The load-bearing skeleton (S) is made of six angles rigidly fixed with eight (type 1) or twelve (type 2) spacer grids. The spacer grids together with the rims and parts of the angles in the rim width are modelled as rigid hexagonal plates. Other FA components – fuel claddings (C), fuel pellets (FP) stacks, guide thimbles (GT) and central tube (CT) – are modelled as a beam-type continua. Interaction between the neighbouring FAs can occur due to their static deformations and kinematics excitation by mounting plates movement.

3. Mathematical model of the pair FAs inside the mixed reactor core

Considering a pair of neighbouring FAs composed of statically deformed FA_1 (type 1) and geometrically ideal FA_2 (type 2). Contact of the FAs can be assumed in the area of the vertices of the skeleton angles on the contact line (Fig. 2).

Let us denote normal contact forces $\bar{N}_{1,2}$ and $\bar{\bar{N}}_{1,2}$ at the contact line between FA_1 and FA_2. These forces can be written in the form

$$
\begin{aligned}
\bar{N}_{1,2} &= k_C(\bar{n}_{1,2} - \delta)H(\bar{n}_{1,2} - \delta), \\
\bar{\bar{N}}_{1,2} &= k_C(\bar{\bar{n}}_{1,2} - \delta)H(\bar{n}_{1,2} - \delta),
\end{aligned} \tag{1}
$$

where k_C is the contact stiffness between two skeleton angles and δ is the nominal clearance between FAs in the normal $n_{1,2}$ direction. Relative displacements $\bar{n}_{1,2}$ and $\bar{\bar{n}}_{1,2}$ of the vertices of FA_1 angles with respect to the vertices of FA_2 angles in the direction of normal $n_{1,2}$ are expressed using FAs generalized coordinates and static deformations parameters. A necessary condition for the activation of any normal contact forces is a positive argument of the Heaviside function H in (1).

Activated normal contact forces $N_{1,2} \in \{\bar{N}_{1,2}, \bar{\bar{N}}_{1,2}\}$ generate tangential an axial friction forces (see Fig. 2)

Fig. 2. Contact forces between FAs

$$
T_{1,2} = f(c_{1,2})N_{1,2}\frac{c_{1,2,t}}{c_{1,2}}, \qquad A_{1,2} = f(c_{1,2})N_{1,2}\frac{c_{1,2,ax}}{c_{1,2}}. \tag{2}
$$

The friction coefficient $f(c_{1,2})$ depends on the absolute sliding velocity $c_{1,2}$ between the vertices of the contacting angles [1]. The tangential sliding velocity $c_{1,2,t}$ is common to both contact points. The axial sliding velocity $c_{1,2,ax}$ in contact points at the contact line is given by the different expressions according to the mutual position of interacting FAs.
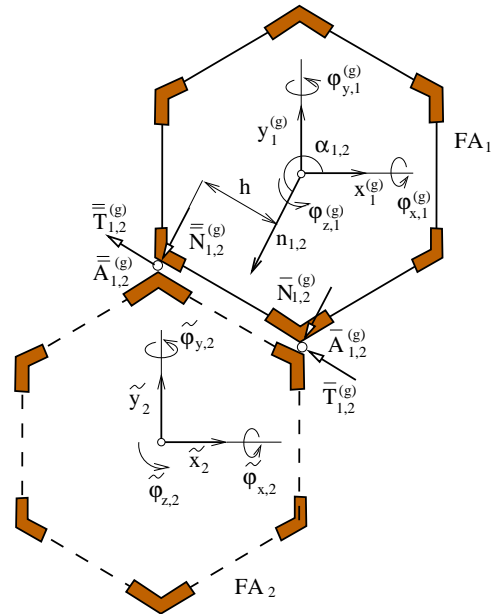
224

The mathematical model of a pair of neighboring FAs of different type can be written in the form

$$\begin{bmatrix} \boldsymbol{M}_1 & \boldsymbol{0} \\ \boldsymbol{0} & \boldsymbol{M}_2 \end{bmatrix} \begin{bmatrix} \ddot{\boldsymbol{q}}_1 \\ \ddot{\boldsymbol{q}}_2 \end{bmatrix} + \begin{bmatrix} \boldsymbol{B}_1 & \boldsymbol{0} \\ \boldsymbol{0} & \boldsymbol{B}_2 \end{bmatrix} \begin{bmatrix} \dot{\boldsymbol{q}}_1 \\ \dot{\boldsymbol{q}}_2 \end{bmatrix} + \begin{bmatrix} \boldsymbol{K}_1 & \boldsymbol{0} \\ \boldsymbol{0} & \boldsymbol{K}_2 \end{bmatrix} \begin{bmatrix} \boldsymbol{q}_1 \\ \boldsymbol{q}_2 \end{bmatrix} = \begin{bmatrix} \boldsymbol{f}_1^{KE}(t) \\ \boldsymbol{f}_2^{KE}(t) \end{bmatrix} + \begin{bmatrix} \boldsymbol{f}_{2,1}^{C} \\ \boldsymbol{f}_{1,2}^{C} \end{bmatrix}, \quad (3)$$

where $\boldsymbol{M}_j$, $\boldsymbol{B}_j$, $\boldsymbol{K}_j$, $j = 1, 2$ are the mass, damping, and stiffness square matrices of non-interacting FAs of order n_j. The kinematic excitation vectors $\boldsymbol{f}_j^{KE}(t)$, $j = 1, 2$ differ in the structure of FA types and in coordinates describing the position in the MRC. The vectors of contact forces $\boldsymbol{f}_{2,1}^{C}$, $\boldsymbol{f}_{1,2}^{C}$ between FAs are expressed by means of the normal and friction forces in (1) and (2). The dimension of global vector $[\boldsymbol{q}_1^T, \boldsymbol{q}_2^T]^T$ of generalized coordinates is way too large for nonlinear simulations in the time domain. Therefore, the modal reduction $\boldsymbol{q}_j = {}^m \boldsymbol{V}_j \boldsymbol{x}_j$, $j = 1, 2$ with modal submatrices ${}^m \boldsymbol{V}_j \in R^{n_j, m_j}$, $m_j < n_j$ of the undamped non-interacting FA$_j$ is used. The matrices ${}^m \boldsymbol{V}_j$ meet the conditions of orthonormality

$${}^m \boldsymbol{V}_j^T \boldsymbol{M}_j \, {}^m \boldsymbol{V}_j = \boldsymbol{I}_j, \quad {}^m \boldsymbol{V}_j^T \boldsymbol{K}_j \, {}^m \boldsymbol{V}_j = {}^m \boldsymbol{\Lambda}_j, \, j = 1, 2, \quad (4)$$

where $\boldsymbol{I}_j$ are the identity matrices of order m_j and ${}^m \boldsymbol{\Lambda}_j \in R^{m_j, m_j}$ are the diagonal spectral submatrices composed of FA$_j$ eigenfrequencies squares. Model (3) can be transformed into the form

$$\begin{bmatrix} \ddot{\boldsymbol{x}}_1 \\ \ddot{\boldsymbol{x}}_2 \end{bmatrix} + \begin{bmatrix} \boldsymbol{D}_1 & \boldsymbol{0} \\ \boldsymbol{0} & \boldsymbol{D}_2 \end{bmatrix} \begin{bmatrix} \dot{\boldsymbol{x}}_1 \\ \dot{\boldsymbol{x}}_2 \end{bmatrix} + \begin{bmatrix} {}^m \boldsymbol{\Lambda}_1 & \boldsymbol{0} \\ \boldsymbol{0} & {}^m \boldsymbol{\Lambda}_2 \end{bmatrix} \begin{bmatrix} \boldsymbol{x}_1 \\ \boldsymbol{x}_2 \end{bmatrix} = \begin{bmatrix} {}^m \boldsymbol{V}_1^T & \boldsymbol{0} \\ \boldsymbol{0} & {}^m \boldsymbol{V}_2^T \end{bmatrix} \begin{bmatrix} \boldsymbol{f}_1^{KE}(t) + \boldsymbol{f}_{2,1}^{C} \\ \boldsymbol{f}_2^{KE}(t) + \boldsymbol{f}_{1,2}^{C} \end{bmatrix}, \quad (5)$$

where the diagonal matrices $\boldsymbol{D}_j = \mathrm{diag}[2 D_\nu^{(j)} \Omega_\nu^{(j)}]$, $j = 1, 2$ are determined by FA$_j$ eigenfrequencies $\Omega_\nu^{(j)}$ and damping factors $D_\nu^{(j)}$, $\nu = 1, \ldots, m_j$.

To perform dynamic analysis, the reduced model (5) is transformed to the state space

$$\dot{\boldsymbol{u}} = \boldsymbol{A} \boldsymbol{u} + \boldsymbol{f}(\boldsymbol{u}, t). \quad (6)$$

The state vector $\boldsymbol{u}$ of dimension $2(m_1 + m_2)$ is defined as $\boldsymbol{u} = [\boldsymbol{x}_1^T, \boldsymbol{x}_2^T, \dot{\boldsymbol{x}}_1^T, \dot{\boldsymbol{x}}_2^T]^T$. The matrix $\boldsymbol{A}$ and the nonlinear vector $\boldsymbol{f}(\boldsymbol{u}, t)$ are defined as follows:

$$\boldsymbol{A} = - \begin{bmatrix} \boldsymbol{0} & \boldsymbol{I} \\ {}^m \boldsymbol{\Lambda} & \boldsymbol{D} \end{bmatrix}, \qquad \boldsymbol{f}(\boldsymbol{u}, t) = - \begin{bmatrix} \boldsymbol{0} \\ {}^m \boldsymbol{V} [\boldsymbol{f}_{KE}(t) + \boldsymbol{f}_C] \end{bmatrix}, \quad (7)$$

where $\boldsymbol{D}$, ${}^m \boldsymbol{\Lambda}$, ${}^m \boldsymbol{V}^T$, $\boldsymbol{f}_{KE}(t)$ and $\boldsymbol{f}_C$ are global matrices and vectors in (5). Model (6) is solved using a suitable numerical method in time-domain.

4. Application

To demonstrate the presented method, dynamic response of the statically deformed hexagonal FA$_1$ type 1 (eight spacer grids) and geometrically ideal hexagonal FA$_2$ type 2 (twelve spacer grids) in the MRC$_{132}$ (contains 132 FA$_2$ and 31 FA$_1$) was analysed. The FA$_1$ is statically deformed into a C-shape with forceless contact of both pairs of angles on the level of spacer grid $g = 5$ with the FA$_2$ between spacer grids 6 and 7 (see Fig. 2). The dynamic orbits of the FA$_1$ centre at the level of spacer grid $g = 5$ and the orbit of the FA$_2$ centre at the level of the spacer grid $g = 11$ are shown in Fig. 3. Dynamic orbits are shown for the FAs with the high fuel burn-up when gap between fuel pellets and FR cladding is closed. The orbits are depicted in a short time interval around extreme transverse FAs deformation.

Time-domain behaviour of normal contact forces $N_{1,2}$ ($N_{1,2} = N_{2,1}$) between FAs in time interval $t \in < 0; 5 > [s]$ are shown in Fig. 4. Two states of both FAs were considered with the low (state I) and the high (state II) fuel burn-up. The normal forces in contact phases are larger in state II.
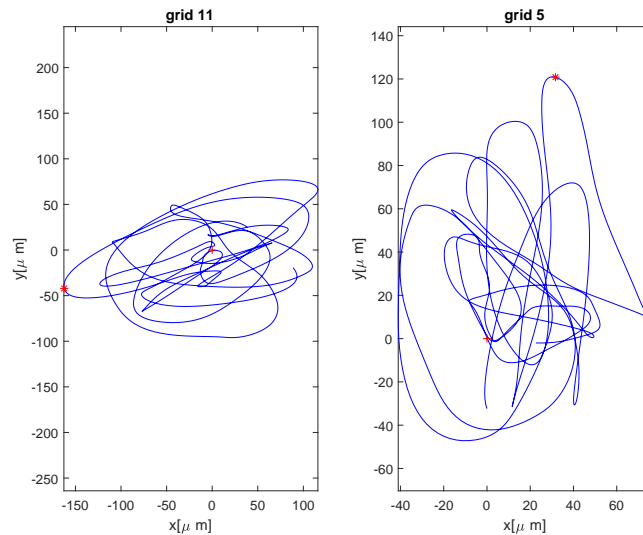
Fig. 3. Dynamic orbits of the FA$_j$'s load bearing skeleton centre at the level of maximally deformed spacer grids
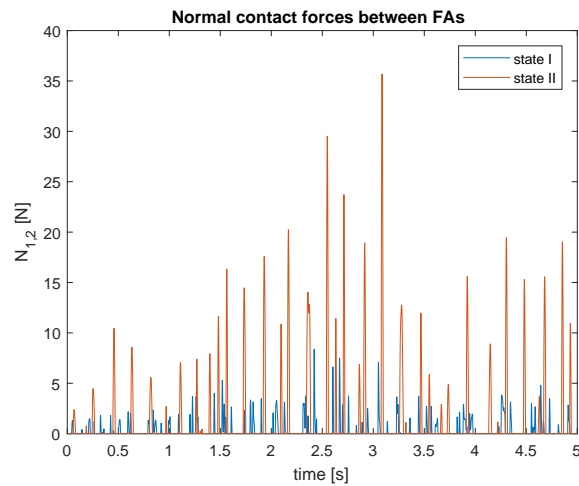

Fig. 4. Time-domain behaviour of the normal contact forces between FAs

References

[1] Dyk, Š., Zeman, V., Hlaváč, Z., Mechanical interaction of bowed hexagonal fuel assemblies in PWR core, Progress in Nuclear Energy 161 (2023) No. 104732.

[2] Stulík, P. et al., Mechanical behaviour of the nuclear fuel, its monitoring and validation using operation measurement, Internal Research Report, Nuclear Research Institute Řež, 2020. (in Czech)

[3] Wanninger, A., Seidel, M., Macián-Juan, R., Mechanical analysis of the bow deformation of a row of fuel assemblies in PWR core, Nuclear Engineering and Technology 50 (2) (2018) 297-305.

[4] Zeman, V., Hlaváč, Z., Dynamic response of VVER 1000 type reactor excited by pressure pulsations, Engineering Mechanics 15 (6) (2008) 50-59.

[5] Zeman, V., Hlaváč, Z., Modelling of the friction-vibration interactions in reactor core barrel couplings, Applied and Computational Mechanics 12 (2) (2018) 193-212.

Design, simulation and control of a biomechanical model of the upper limb

O. Zoufalý[a], V. Halamka[b], M. Daniel[a], Z. Šika[b]

[a]Division of biomechanics, Faculty of Mechanical Engineering, Czech Technical University in Prague,
Technická 4, 160 00 Prague, Czech Republic
[b]Division of mechanics and mechatronics, Faculty of Mechanical Engineering, Czech Technical University in Prague,
Technická 4, 160 00 Prague, Czech Republic

1. Introduction

Human musculoskeletal modelling is a complex discipline whose results can be applied to both robotics and medicine [4]. In robotics, these models can be used, for example, to design humanoid robots or supportive exoskeletons. In the medical field, these models can be used to investigate various movement limitations such as weakening of a specific muscle group, limited range of motion in joints, etc. The aim of this paper is to develop a comprehensive dynamic model of the upper limb that will become the basis for further research.

2. Musculoskeletal model

The dynamic model of the upper limb was built using Simscape (Matlab). This tool allows the direct application of physical solids and the definition of constraints between them, replacing the creation of differential equations of motion. Simscape also allows the visualization of the solved problem (Fig. 1) and the combination of multibody with electrical or fluid systems.

The skeletal dynamic model is based on the real geometry of the upper limb skeleton (thorax, scapula, clavicle and humerus) [3]. The individual bones were first placed in space and then connected in series using spherical constraints. The model also includes the geometry of
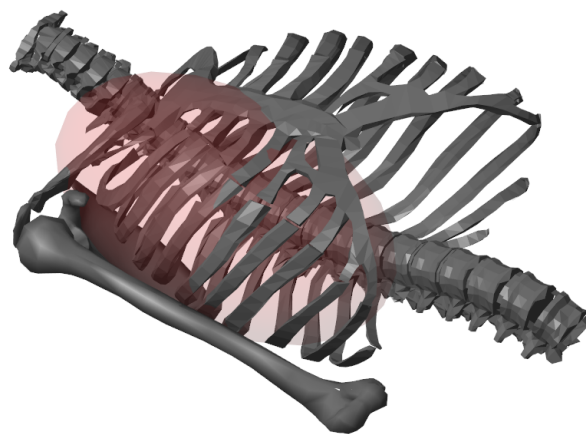

Fig. 1. Simscape visualisation of upper limb skeleton

scapular motion (including scapulohumeral rhythm), which is implemented by using an ellipsoid (Fig. 1) whose geometry approximates the shape of the thorax. The scapula then glides over the surface of this ellipsoid through one to three contact points.

Subsequently, the skeletal model was extended with a muscle model. The Hill and Huxley models are the most commonly used. The Hill model is based only on mechanical interaction and is easier to implement for models with a higher number of muscles. The muscle-tendon complex (Fig. 2) consists of a muscle part (contractile and passive elements) and an elastic tendon. The muscle force is then dependent on the contraction speed and the ratio of current to optimal muscle length. Huxley's model of muscle is slightly more complex and represents muscle contraction in both mechanical and metabolic terms.
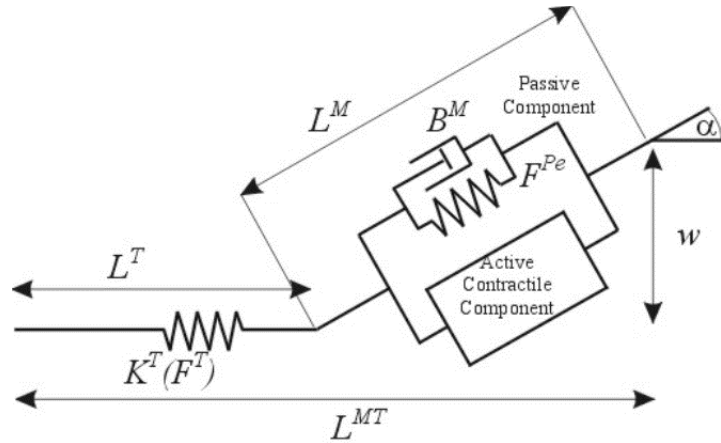

Fig. 2. Hill model scheme [2]

3. Computed muscle control

The Computed Muscle Control method was chosen to control the dynamic model (Fig. 3). This method combines the classical Computed Torque Control method and Static Optimization. In the first step, the desired acceleration of the model is modified using a PD controller based on the control deviation. In the second step, the moments acting at the joints are calculated from this acceleration to achieve the desired trajectory. And in the last step, these moments are converted to forces in each muscle by optimization.
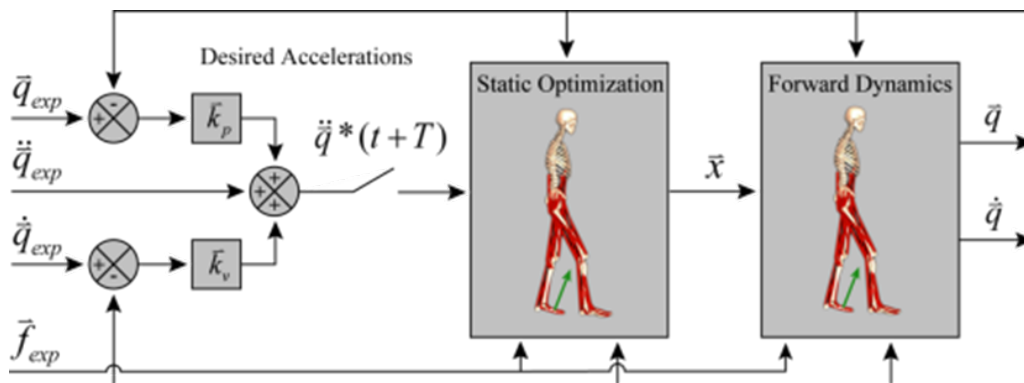

Fig. 3. Computed Muscle Control scheme [1]

Acknowledgements

References

[1] Thelen, D., Anderson, F., Using computed muscle control to generate forward dynamic simulations of human walking from experimental data, Journal of Biomechanics 39 (6) (2006) 1107-1115.

[2] Vilímek, M., Musculotendon forces derived by different muscle models, Acta of Bioengineering and Biomechanics 92 (2007) 41-47.

[3] Wu, W., Lee, P. V. S., Bryant, A. L., Galea, M., Ackland, D. C., Subject-specific musculoskeletal modeling in the evaluation of shoulder muscle and joint function, Journal of Biomechanics 49 (15) (2016) 36263634.

[4] Zajac, F. E., Muscle and tendon: Properties, models, scaling, and application to biomechanics and motor control, Critical Reviews in Biomedical Engineering 17 (4) (1989) 359-411.